A formalism for a consistent treatment of two-pion interactions in heavy meson decays

Dissertation

zur

Erlangung des Doktorgrades (Dr. rer. nat.)

der

Mathematisch-Naturwissenschaftlichen Fakultät

der

Rheinischen Friedrich-Wilhelms-Universität Bonn

vorgelegt von

Stefan Ropertz

aus

Waldbröl

Bonn 2020

Angefertigt mit Genehmigung der Mathematisch-Naturwissenschaftlichen Fakultät der Rheinischen Friedrich-Wilhelms-Universität Bonn

1. Gutachter:	Professor Dr. Christoph Hanhart
2. Gutachter:	Professor Dr. Dr. h.c. Ulf-G. Meißner
Tag der Promotion:	01.09.2020
Erscheinungsjahr:	2020

Abstract

The best-established theory of particle physics up to now is the Standard Model. The theory of strong interactions called quantum chromodynamics (QCD) is a part of it. QCD leads to a wide range of phenomena, which still need to be understood. For example, many experiments showed that the spectrum of QCD bound states contains many states that are inconsistent with the most simple quark model. To gain a better insight into their nature, theoretically sound studies are required, which preserve fundamental physical properties such as Lorentz invariance, causality and probability conservation. The problem is complicated because the standard perturbation theory approach in the strong coupling constant is not applicable at the hadronic scale. A proper alternative method is dispersion theory, which includes analyticity, unitarity and crossing by construction. However, its application is restricted to low energies due to the opening of inelastic channels. Therefore, this thesis aims to construct an effective high-energy extension of the dispersive framework in two subprojects.

The first project introduces a scattering matrix and form factor parametrization for $\pi\pi$-interactions, which is applicable from threshold to about 2 GeV. We focus primarily on the rich spectrum provided by the isoscalar, scalar final state rescattering of the channels $\pi\pi$ and $K\bar{K}$. In our method additional channels to those two are coupled by s-channel resonance exchange. An application to the decays $\bar{B}_s^0 \to J/\psi\pi\pi$ and $\bar{B}_s^0 \to J/\psi K\bar{K}$ allows for the extraction of the scalar, isoscalar form factor up to about 2.2 GeV. In this approach the J/ψ acts as a spectator and hence does not interact with the other final states. An analytic continuation of the form factor allows us to extract resonance poles for the $f_0(1500)$ and $f_0(2020)$.

The second project expands on providing a fully analytic and unitary solution to the three-particle decay amplitudes. While the previous project assumes one particle to be a spectator, we now allow for pairwise rescattering of all three particles. For this we consider the decay $\Upsilon(5S) \to \Upsilon(nS)\pi\pi$ with $n = 1, 2, 3$. While the $\pi\pi$ scalar spectrum is fixed by the previous analysis we include the exotic resonances $Z_b^{\pm}(10610)$ and $Z_b^{\pm}(10650)$ in the $\Upsilon(nS)\pi$ spectrum. Due to their closeness to the $B\bar{B}^\star$ and $B^\star\bar{B}^\star$ thresholds, respectively they are modeled as hadronic molecules by dynamic rescattering of these channels and further inelastic effects. Two approaches in order to determine the $\pi\pi$ S-wave amplitude for the $\Upsilon(1S)\pi\pi$ final state are employed. The first method is the standard integration along the Khuri-Treiman path. On the other hand, the second approach employs a spectral density integral for the crossed-channel amplitude to determine the partial-wave projection analytically. Both are consistent with each other, allowing us to use the second approach for the $\Upsilon(nS)\pi\pi$ final states with $n = 2, 3$. An application to the Dalitz plot data is in progress.

Parts of this thesis have been published in the following articles:

- S. Ropertz, C. Hanhart and B. Kubis, *A new parametrization for the scalar pion form factors*, Eur. Phys. J. **C78** (2018) 1000 [arXiv:1809.06867 [hep-ph]]

Contents

1. Introduction

The ultimate goal of particle physics is to find a theory that unifies the four fundamental forces the electromagnetic-, strong-, weak force and gravitation. The Standard Model of particle physics covers the first three, while the inclusion of gravitation has not been definitive yet. It is a local, Poincaré invariant locally gauge invariant quantum field theory that describes the interaction of quarks and leptons by the exchange of gauge bosons. These include the photon for electromagnetic interactions, the Z and $W^{\pm}$ for the weak interaction and the gluon for the strong force. Since the massive gauge bosons would spoil the gauge symmetry, their masses are introduced by spontaneous symmetry breaking. This mechanism at the same time leads to the Higgs boson.

Of primary interest in this thesis is the strong force, explained by the quantum field theory called quantum chromodynamics (QCD), which describes the interaction between quarks and gluons. In contrast to the theory of electromagnetic interactions, called quantum electrodynamics (QED), not only the fermions carry a (color) charge but also the gauge bosons. This allows for a self-interaction between the latter. The physical QCD bound states are color neutral objects formed by quarks and gluons. Therefore there are no colored asymptotic states. This property of QCD is called confinement. These QCD bound states, called hadrons, are categorized as either mesons (bosons) or baryons (fermions). In the conventional quark model mesons consist of a quark and an antiquark and baryons of three quarks. While this has been fairly successful in describing a large fraction of the spectrum, there are still exotic states which are not consistent with the model predictions. For such states more sophisticated models are required. These are e.g. states consisting of more than three quarks such as tetra- and pentaquarks. There are also candidates for glueballs, which consist only of gluons. Another model for exotics is a hybrid state containing constituent quarks and gluons, which contribute to the overall quantum numbers. Additionally, bound states of hadrons, so-called hadronic molecules, are excellent candidates to explain many of the exotic states. In order to understand the construction of QCD bound states, especially exotica, it is necessary to study the hadronic spectrum and strong transitions between different states.

Calculations in the standard model are often performed in a perturbation theory between fermions and gauge bosons as well as gauge bosons among themselves employing the strong coupling constant as an expansion parameter. As this parameter is subject to renormalization, it depends on the energy scale of the process. For the series to converge, the coupling constant needs to be small. While the perturbation theory works with astounding precision for QED, it is inadequate for QCD below 4 GeV due to a sizable coupling constant. At higher energies the theory is asymptotically free as the running coupling constant approaches zero. Since QCD shows a broad spectrum of states below

2 GeV experimentally, another framework is necessary for that energy region.

In order to describe hadronic interactions, effective field theories play an important role. They allow for perturbative calculations within a new power-counting scheme, while still retaining the symmetries of the original theory. However, this framework introduces several parameters, which either need to be matched to the underlying theory or extracted from experiments. Furthermore, its range of applicability is limited by non-perturbative effects at higher energies such as resonances. Using appropriate tools this problem can be alleviated, however a breakdown still occurs at higher energies.

Based on first principles, it is numerically possible to solve QCD by discretization of the space-time. This so-called Lattice QCD is another successful branch of hadron physics and shows promising results not only for light quarks but also in the charm and bottom sector. The trade-off, except for numerical artifacts such as finite lattice size and spacing, is that the calculations are very expensive. Furthermore, it requires a significant theoretical effort to extract the hadronic spectrum from Lattice QCD. On the other hand, this can give great insight into the nature of these states.

The last approach, which will be the focal point of this thesis, is S-matrix theory. It allows for a proper description of the amplitude and its analytic structure while retaining the constraints given by unitarity and crossing symmetry. This is not only useful to constrain Standard Model properties such as CP-violating phases but also for the particle identification in hadron spectroscopy. However, this approach is in principle limited by the prerequisite knowledge about the amplitude on the real axis, which needs to be determined separately.

The thesis is focused on three-particle heavy meson decays. They provide a large phase space, which allows for the extraction of a rich spectrum in the final state. We put much emphasis on the exotic meson states. In order to extract correct information about their nature, it is crucial to employ a proper parameterization of the amplitude. For example, the often-used sum of Breit-Wigner amplitudes violates unitarity and analyticity. Hence they are unfavorable for spectroscopy.

This thesis is structured as follows: Chapter 1 gives an introduction to the theoretical framework used in hadron physics. This not only includes an introduction to QCD and its effective field theories but also an introduction to S-matrix theory and its applications to hadron spectroscopy.

An effective parametrization for the isoscalar S-wave interaction of pions and kaons to higher energies is provided in chapter 2. The framework is then applied to extract isoscalar, scalar form factors from the decays $\bar{B}_s^0 \to J/\psi\pi\pi$ and $\bar{B}_s^0 \to J/\psi K\bar{K}$. The corresponding resonance poles are then extracted via Padé approximants.

Chapter 3 generalizes the framework to include crossed-channel rescattering, which is modeled by a unitary analytic function. We provide a proper analytic calculation for the partial-wave projection of an amplitude with a right-hand cut, which can be used in an inhomogeneous Omnès problem. As an example, we solve it for the decay $\Upsilon(5S) \to \Upsilon(nS)\pi\pi$ with $n = 1, 2, 3$ in two approaches, which are shown to be consistent with each other. While the previously determined amplitudes describe the $\pi\pi$ isoscalar S-wave spectrum, the $\Upsilon(nS)\pi$

spectrum shows two exotic resonances $Z_b^{\pm}(10610)$ and $Z_b^{\pm}(10650)$, which will be described by unitary B meson rescattering with additional inelastic contributions.

The thesis closes with a summary and an outlook.

1.1. Standard Model of particle physics

	Symbol	particle content	$SU(3)_c$	$SU(2)_L$
left handed quark	q_L	$\begin{pmatrix} u_L \\ d_L \end{pmatrix}$, $\begin{pmatrix} c_L \\ s_L \end{pmatrix}$, $\begin{pmatrix} t_L \\ b_L \end{pmatrix}$	[3]	[2]
right handed quark	q_R	u_R , c_R , t_R d_R , s_R , b_R	[3]	[1]
left handed lepton	ψ_L	$\begin{pmatrix} e_L \\ \nu_e \end{pmatrix}$, $\begin{pmatrix} \mu_L \\ \nu_\mu \end{pmatrix}$, $\begin{pmatrix} \tau_L \\ \nu_\tau \end{pmatrix}$	[1]	[2]
right handed lepton	ψ_R	e_R , μ_R , τ_R	[1]	[1]
gluon	g	g	[8]	[1]
W boson	W	$W^{\pm}$, W^0	[1]	[3]
Z boson	Z	Z	[1]	[1]
photon	γ	γ	[1]	[1]

Table 1.1.: Representation of the standard model particle content under $SU(3) \times SU(2)_L \times U(1)_Y$ symmetry

The Standard Model of particle physics [1, 2, 3, 4] is a quantum field theory, which simultaneously describes the electroweak and the strong interaction. The tremendous efforts to include gravitation into the scheme were so far unsuccessful.

Quarks and leptons are the fundamental fermionic particles. Whereas the latter only take part in the electroweak interaction, quarks are also subject to the strong one.

There are strong phenomenological evidences that quarks (q) and leptons (ψ) as well as their antiparticles come in three families. Each one consists of a doublet under the weak interaction. For leptons they are electron (e) and electron-neutrino (ν_e), muon (μ) and muon-neutrino (ν_μ) as well as tauon (τ) and tauon-neutrino (ν_τ). The quark families consist of up- (u) and down-quark (d), charm- (c) and strange-quark (s) as well as top- (t) and bottom-quark (b).

In the Standard Model, the strong, weak and electromagnetic force are combined into a $SU(3)_c \times SU(2)_L \times U(1)_Y$ gauge theory. The $SU(3)_c$ denotes the

color group corresponding to the strong interaction. On the other hand, the electroweak part is covered by the gauge group $\mathrm{SU}(2)_L \times \mathrm{U}(1)_Y$. Note that only left-handed particles transform non-trivially under the $\mathrm{SU}(2)_L$ group, which is the origin of the parity violation of the weak interaction.

In order to allow for local gauge symmetries, several gauge bosons need to be introduced. These correspond to the 8 gluons (g) for the strong, the $W^{\pm}$ and Z bosons for the weak and the photon (γ) for the electromagnetic interaction.

As a mass term of the $W^{\pm}$ and Z would break the $\mathrm{SU}(2)_L$-symmetry, masses need to be introduced dynamically via the Higgs mechanism [5, 6], which was experimentally confirmed in 2012 [7, 8]. In order to do that, a scalar Higgs field is introduced, which transforms as a doublet under $\mathrm{SU}(2)_L$. It is coupled via a Yukawa term to the quark and lepton fields. The Higgs potential has a non-trivial degenerate vacuum, which produces a spontaneously broken symmetry. Through this, the W and Z gauge bosons as well as the quarks and leptons gain an effective mass. Although some of the neutrinos have a non-vanishing mass, as indicated by e.g. neutrino oscillations [9, 10, 11], a mechanism to produce these is not yet clear.

1.2. Quantum chromodynamics

1.2.1. Introduction

The theory of strong interactions is governed by a quantum field theory named quantum chromodynamics (QCD) [4, 12]. It corresponds to the $\mathrm{SU}(3)_c$ gauge theory mentioned previously and thus considers the quarks q_i, antiquarks $\bar{q}_i$ and gluons A_μ^C as degrees of freedom.

The theory is described by the renormalizable Lagrangian density

$$\mathcal{L}_{\mathrm{QCD}} = \sum_{f=u,d,s,c,b,t} \bar{q}_f^a \left(i D_\mu^{ab} \gamma^\mu - m_f \delta^{ab} \right) q_f^b - \frac{1}{4} (G^a)_{\mu\nu} (G^a)^{\mu\nu} \,, \tag{1.1}$$

with the covariant derivative

$$D_\mu^{ab} = \partial_\mu \delta^{ab} - i g \lambda_c^{ab} A_\mu^c \tag{1.2}$$

and the gluonic field strength tensor

$$(G^a)_{\mu\nu} = \partial_\mu A_\nu^a - \partial_\nu A_\mu^a + g f^{abc} A_\mu^b A_\nu^c \,. \tag{1.3}$$

Here the λ_c^{ab} correspond to the adjoint representation of the $\mathrm{SU}(3)_c$ generators. The structure constants f^{abc} are defined through the algebra

$$[\lambda_a, \lambda_b] = i f^{abc} \lambda_c \,. \tag{1.4}$$

While the quarks transform under the fundamental representation

$$q_f \to \exp\left(-i \phi^a(x) \, \frac{\lambda_a}{2} \right) q_f = U[x] \, q_f \tag{1.5}$$

the antiquarks are transforming under the antifundamental representation

$$\bar{q}_f \to \bar{q}_f \exp\left(i\phi^a(x)\,\frac{\lambda_a}{2}\right) = \bar{q}_f\, U^\dagger[x]\,. \tag{1.6}$$

In order to yield a gauge invariant Lagrangian density the gluon field needs to transform as

$$A_\mu = \lambda_a A^a_\mu \to U[x] A_\mu U^\dagger[x] - \frac{i}{g}(\partial_\mu U[x]) U^\dagger[x]\,. \tag{1.7}$$

It is easy to proof, that the field strength tensor transforms according to the adjoint representation

$$G_{\mu\nu} = \lambda_a (G^a)_{\mu\nu} \to U[x] G_{\mu\nu} U^\dagger[x]\,. \tag{1.8}$$

Note that we omitted the QCD-Θ term defined by

$$\mathcal{L}_\Theta = \frac{g^2\Theta}{32\pi^2}\epsilon^{\mu\nu\rho\sigma}(G^a)_{\mu\nu}(G^a)_{\rho\sigma}\,. \tag{1.9}$$

This term is gauge invariant and of mass dimension four and thus in principle needs to be included in the standard QCD-Lagrangian. However due to the Levi-Civita-tensor it transforms odd under parity (P). As charge parity (C) is still conserved this term introduces a CP-violation, leading to e.g. a non-vanishing neutron electric dipole moment. A careful estimation of Θ leads to an upper limit $|\Theta| \leq 2.5 \cdot 10^{-10}$ [13]. The reason why CP-violating term is so small has not yet been understood. For all the following calculations it can be safely ignored.

The renormalization group dictates, that the strong coupling constant

$$\alpha_s = \frac{g_s^2}{4\pi^2} \tag{1.10}$$

depends on the transferred momentum Q of the interaction. This dependence can be extracted from several experiments. The corresponding results for different values of Q are shown in Fig. 1.1. It shows that at large Q α_s becomes smaller, such that a perturbation theory should converge for $Q > 4\,\mathrm{GeV}$. This phenomenon is called asymptotic freedom. However, at low momentum transfers it becomes large and a perturbation theory in the coupling constant can no longer be used.

As indicated by experiment and Lattice QCD, QCD at low temperatures is in its confining phase. This means that asymptotic states are formed only as bound states of quarks and gluons in a color singlet, whereas color charged objects are never observed. The usual qualitative explanation of this phenomenon is that the gluons, which are exchanged between two color charged objects, will form a narrow flux tube carrying energy. By increasing the distance between the charges or equivalently decreasing the momentum transfer, the energy density will increase to a point, such that it is eventually energetically more favorable to break the flux tube and generate a color-anti-color pair from the vacuum. Thus two color neutral objects are created. An analytical proof of confinement

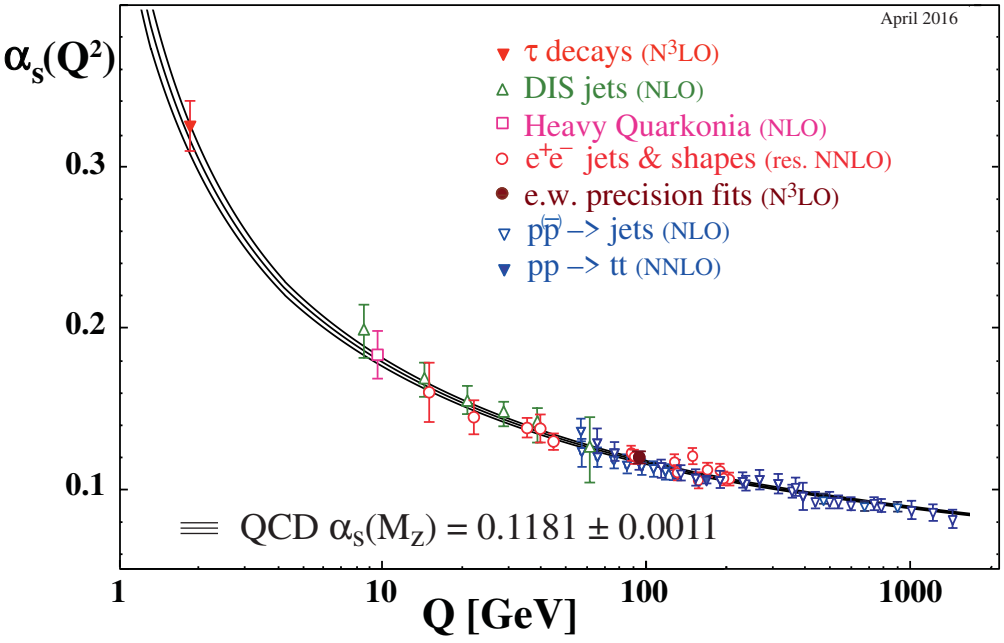

Figure 1.1.: Strong running coupling constant. The figure is taken from Ref. [14].

by non-abelian gauge theories such as QCD still remains to be shown. The intrinsic scale, which is set by renormalization, is the perturbatively calculated QCD Landau pole Λ_{QCD}, at which α_s diverges. It is found to be about 200 to 400 MeV. However, since its exact value is dependent on the loop order of the renormalization, it is nowadays not quoted anymore.

Since the asymptotic states of the theory are bound states of gluons and quarks, called either mesons (integer spin) or baryons (half-integer spin), an effective theory is needed describing their interaction, which is consistent with the underlying theory, namely QCD.

1.2.2. Global symmetries of the QCD Lagrangian

Scale separation

According to the Weinberg conjecture [15, 16] the S-matrix, calculated from the most general Lagrangian, containing all terms consistent with the assumed symmetry, will give the most general possible S-matrix consistent with perturbative unitarity, analyticity, cluster decomposition and symmetries. A first application to QCD has been done in Refs. [17, 18]. For a broader introduction to this topic we refer to Refs. [19, 20, 21], whose reasoning we follow.

As the quarks are not asymptotic states, their masses cannot be measured

directly. Thus they turn out to be scale-dependent quantities.

The PDG [14] quotes the most recent world averages for the light quarks u and d as

$$m_u = \left(2.16^{+0.49}_{-0.26}\right)\,\text{MeV} \,\text{and}\, m_d = \left(4.67^{+0.48}_{-0.17}\right)\,\text{MeV} \tag{1.11}$$

as well as s

$$m_s = (93^{+11}_{-5})\,\text{MeV}\,, \tag{1.12}$$

where the $\overline{\text{MS}}$-scheme fixed at a scale of 2 GeV was employed.

The top quark is so heavy that it decays before it can hadronize. However the other two heavy quarks, namely charm and bottom quark, build hadronic states. Their masses are

$$m_c = (1.27 \pm 0.02)\,\text{GeV} \,\text{and}\, m_b = (4.18^{+0.03}_{-0.02})\,\text{GeV}\,, \tag{1.13}$$

where the $\overline{\text{MS}}$-scheme at the scale of the heavy mass was employed.

The lightest mesons are the pseudoscalar pions, kaons and the eta. These are associated as the pseudo-Goldstone bosons of the spontaneously broken chiral symmetry, as will be explained later. A rough estimate for the chiral breakdown scale is given by $\Lambda_\chi \approx 4\pi F_\pi \approx 1170\,\text{MeV}$ [22], where F_π denotes the pion decay constant. The first hadronic resonances show up at roughly 1 GeV, such as the ρ meson at about 770 MeV. As resonances are genuine non-perturbative effects, which cannot be described by a pure perturbation theory using the Goldstone bosons, the breakdown scale might be even lower. Therefore using either of these scales, we can separate the physics of the light quarks u, d and s from those of the heavy quarks c and b.

Chiral symmetry

Projecting the quarks on their left- and right-handed components

$$q^{L/R} = P_{L/R}\, q \quad \text{with} \quad P_{L/R} = \frac{1}{2}(1 \mp \gamma_5) \tag{1.14}$$

allows us to rewrite the fermionic Lagrangian density as

$$\mathcal{L}^{\text{fermion}}_{\text{QCD}} = \sum_{f=u,d,s,c,b,t} \bar{q}^L_f D_\mu \gamma^\mu q^L_f - \bar{q}^R_f m_f q^L_f + (L \leftrightarrow R)\,. \tag{1.15}$$

Let us furthermore focus on the light quarks only. As discussed in Sect. 1.2.2 the mass of up and down quark is small compared to Λ_{QCD}. Although the corrections coming from the strange quark are larger we first assume $m_u = m_d = m_s = 0$. In this case the Lagrangian density reduces to

$$\mathcal{L}^{\text{fermion}}_{\text{QCD}} = \sum_{f=u,d,s} \bar{q}^L_f D_\mu \gamma^\mu q^L_f + \bar{q}^R_f D_\mu \gamma^\mu q^R_f\,. \tag{1.16}$$

This term shows a global $\text{U}(3)_L \times \text{U}(3)_R$ symmetry, which can be written as

$$\left(\begin{pmatrix} u_L \\ d_L \\ s_L \end{pmatrix}, \begin{pmatrix} u_R \\ d_R \\ s_R \end{pmatrix}\right) = (\vec{q}_L, \vec{q}_R) \to \left(e^{-i\Theta^L_a \frac{\lambda_a}{2}} e^{-i\Theta^L} \vec{q}_L, e^{-i\Theta^R_a \frac{\lambda_a}{2}} e^{-i\Theta^R} \vec{q}_R\right)\,. \tag{1.17}$$

In the following we refer to this as chiral symmetry. A more preferable way to write this global symmetry group is $\mathrm{U}(3)_L \times \mathrm{U}(3)_R \cong \mathrm{SU}(3)_V \times \mathrm{SU}(3)_A \times \mathrm{U}(1)_A \times \mathrm{U}(1)_V$. Here V stands for a vector-transformation and can be written in the following way

$$(\vec{q}_L, \vec{q}_R) \to (e^{-i\Theta_a^V \frac{\lambda_a}{2}} e^{-i\Theta^V} \vec{q}_L, e^{-i\Theta_a^V \frac{\lambda_a}{2}} e^{-i\Theta^V} \vec{q}_R)\,. \tag{1.18}$$

The axialvector transformation denoted with A on the other hand can be parametrized as

$$(\vec{q}_L, \vec{q}_R) \to (e^{+i\Theta_a^A \frac{\lambda_a}{2}} e^{+i\Theta^A} \vec{q}_L, e^{-i\Theta_a^A \frac{\lambda_a}{2}} e^{-i\Theta^A} \vec{q}_R)\,. \tag{1.19}$$

As a parity doubling of states is not observed experimentally, we need to assume that the chiral symmetry is spontaneously broken. Since the Vafa-Witten theorem [23] prevents vector-like symmetries from being broken, it follows that the only possible scenario is $\mathrm{U}(3)_L \times \mathrm{U}(3)_R \overset{SSB}{\to} \mathrm{SU}(3)_V \times \mathrm{U}(1)_V \times \mathrm{U}(1)_A$. In principle, this would produce nine Goldstone bosons. However, the $U(1)_A$ symmetry is broken by an anomaly, and thus we are left with $\pi^\pm$, π^0, $K^\pm$, K^0, $\bar{K}^0$ and η whereas the anomaly dominates the η' mass.

Note that the chiral symmetry is explicitly broken due to the non-vanishing quark masses. Thus the Goldstone bosons gain a non-vanishing mass. However as $m_s \gg (m_u + m_d)/2$ we also see a chiral symmetry concerning only u and d quarks works better than also including the s quark.

Chiral perturbation theory

In the following, we want to establish a quantum field theory describing the interactions of the Goldstone bosons among themselves. In this context, we apply the Weinberg conjecture [24], which states that any plausible quantum field theory does not contain anything else besides analyticity, unitarity, cluster decomposition and symmetries. To achieve this goal, we first need the transformation properties of the Goldstone bosons.

The QCD Lagrangian is invariant under the group $G = \mathrm{U}(3)_L \times \mathrm{U}(3)_R$ and thus every state Φ within its Hilbert space $\mathcal{H}$ will transform under a non-linear realization f of G. For every $g \in G$ we may now define it as

$$f(g, \Phi) = \tilde{\Phi} \in \mathcal{H}\,. \tag{1.20}$$

Let 0 denote the ground state of QCD. Then we know that it is invariant under $h \in H = \mathrm{U}(3)_V$ as defined in Eq. (1.18) or explicitly $f(h, 0) = 0$. However, every $g \notin H$ produces a non-trivial state $f(g, 0) = \pi_g$, which can be identified with the Goldstone bosons. In fact we may restrict ourselves to the left cosets $gH = \{gh | h \in H\}$ as every $\tilde{g} \in gH$ produces the same state from the ground state. Therefore we have a correspondence between the quotient $G/H = \{gH | g \in G\}$ and the Goldstone bosons.

Look now explicitly at $\tilde{g} \in G$ which can be defined through $\tilde{g} = (\tilde{L}, \tilde{R})$ with $\tilde{L}, \tilde{R} \in \mathrm{U}(3)_{L,R}$. The left coset may also be written as

$$\tilde{g}H = (\tilde{L}, \tilde{R})H = (1, \tilde{R}\tilde{L}^\dagger)(\tilde{L}, \tilde{L})H = (1, U)H \quad \text{with} \quad U = \tilde{R}\tilde{L}^\dagger\,. \tag{1.21}$$

Thus U represents the coset and can be used to specify the Goldstone bosons. Since $\tilde{L}$ and $\tilde{R}$ are both SU(3) matrices also U can be parametrized as such. A typical realization is given by

$$U(x) = \exp\left(i\frac{\phi(x)}{F_0}\right) \tag{1.22}$$

where F_0 denotes the meson decay constant in the chiral limit. The Goldboson matrix $\phi(x)$ is then expressed as

$$\phi(x) = \sum_{a=1}^{8} \lambda_a \phi_a(x) = \begin{pmatrix} \pi^0 + \eta/\sqrt{3} & \sqrt{2}\pi^+ & \sqrt{2}K^+ \\ \sqrt{2}\pi^- & -\pi^0 + \eta/\sqrt{3} & \sqrt{2}K^0 \\ \sqrt{2}K^- & \sqrt{2}\bar{K}^0 & -2\eta/\sqrt{3} \end{pmatrix} . \tag{1.23}$$

Furthermore it is easy to see that under chiral transformations $g = (L, R) \in G$ it transforms as

$$U \to U' = RUL^\dagger . \tag{1.24}$$

With this we have introduced the Goldstone boson fields and their transformation properties under chiral symmetry. Furthermore as they stem from axial transformations they have the quantum numbers $J^P = 0^-$. However, in order to obtain a systematically improvable effective field theory, we need to introduce a power counting scheme [15], which allows us to estimate the importance of different terms and thus also the accuracy of a perturbation calculation to a given order. Considering that the momenta of the Goldstone bosons are small compared to Λ_χ, an expansion in the ratio is sensible. In a theory with only Goldstone bosons, Lorentz symmetry restricts the Lagrangian to even powers in the momenta, thus the pure Goldstone boson Lagrangian may be ordered as

$$\mathcal{L}_\chi = \sum_{n=0}^{\infty} \mathcal{L}_\chi^{(2n)} \quad \text{with} \quad \mathcal{L}_\chi^{(2n)} = \mathcal{O}\left(\left(\frac{p^2}{\Lambda_\chi^2}\right)^n\right) . \tag{1.25}$$

The term $\mathcal{L}_\chi^0$ does not contain any momentum dependence and thus will give an offset, which can be safely ignored. Consequently the lowest order term starts at order $\mathcal{O}((p/\Lambda_\chi)^2)$ and can be written as

$$\mathcal{L}_\chi^{(2)} = \frac{F^2}{4}\left\langle \partial_\mu U \partial^\mu U^\dagger \right\rangle , \tag{1.26}$$

where $< \cdots >$ denotes a trace in flavor space.

Vector- v_μ and axial-vector sources a_μ can be included by replacing ∂_μ by the covariant derivative

$$\partial_\mu U \to D_\mu U = \partial_\mu U - i r_\mu U + i U l_\mu \tag{1.27}$$

with

$$r_\mu = v_\mu + a_\mu \quad \text{and} \quad l_\mu = v_\mu - a_\mu , \tag{1.28}$$

which ensures that it transforms under chiral symmetry covariantly

$$D_\mu U \to R D_\mu U L^\dagger . \tag{1.29}$$

Scalar s and pseudoscalar sources p on the other hand are included by

$$\chi = 2B(s + ip)\,, \tag{1.30}$$

which need to transform as

$$\chi \to R\chi L^\dagger \tag{1.31}$$

in order to preserve chiral symmetry.

Overall the full lowest order Lagrangian is then given as

$$\mathcal{L}_\chi^{(2)} = \frac{F^2}{4}\left\langle D_\mu U D^\mu U^\dagger \right\rangle + \frac{F^2}{4}\left\langle \chi U^\dagger + U\chi^\dagger \right\rangle . \tag{1.32}$$

The decay constant F can be determined to each order in p^2 by e.g. coupling the Goldstone boson fields to a an external axial-vector current $a^\mu = A_a^\mu \lambda_a$. Then the transition matrix element can be evaluated as

$$\langle 0\,|a^\mu|\,\phi_b(q)\rangle = \sum_a iq^\mu \delta_{ab} F_0\,. \tag{1.33}$$

Thus F_0 can be determined by the weak decays of the concerning meson such as $F_\pi = (92.3 \pm 0.1)$ MeV [14] from the decay $\pi^+ \to l^+\nu_l$.

By employing the spurion technique it is possible to introduce the explicit chiral symmetry breaking through the non-vanishing quark masses. The Gell-Mann-Oakes-Renner relations say that the squared pion mass is proportional to the quark mass [25]. Therefore chiral symmetry breaking will contribute to order $p^2 = m_\pi^2$ through the term $s = \mathrm{diag}(m_u, m_d, m_s) = \mathcal{M}$ resulting in

$$\mathcal{L}_\chi^{(2)} = \frac{F^2}{4}\left\langle \partial_\mu U \partial^\mu U^\dagger \right\rangle + \frac{F^2 B^2}{2}\left\langle \mathcal{M}U^\dagger + U\mathcal{M}^\dagger \right\rangle . \tag{1.34}$$

The free parameter B can be determined to leading order by comparing the energy density of the ground state between full QCD and the effective field theory with $U = 1$

$$\left.\frac{\partial \langle 0|H_{\mathrm{QCD}}|0\rangle}{\partial m_q}\right|_{m_u=m_d=m_s=0} = \left.\frac{\partial \left\langle 0|H_\chi^{(2)}|0\right\rangle}{\partial m_q}\right|_{m_u=m_d=m_s=0}, \tag{1.35}$$

which is equivalent to

$$3F^2 B = -\langle 0|\bar{q}q|0\rangle\ . \tag{1.36}$$

For an effective field theory it is important that the Weinberg power counting scheme [15] is not disturbed by renormalization. Hence it is necessary to determine the chiral dimension of each loop diagram. Following the discussion presented in Ref. [21], consider a loop diagram A involving only Goldstone bosons. It contains L loops with overall I internal lines and V_d vertices of chiral order d. In terms of momenta p it scales as

$$A \propto \int \frac{\left(\mathrm{d}^4 p\right)^L}{\left(p^2\right)^I} \prod_d \left(p^d\right)^{V_d} \tag{1.37}$$

By rescaling the momenta $p \to \Lambda p$ the amplitude transforms as

$$A \to \Lambda^{\nu} A \quad \text{with} \quad \nu = 4L - 2I + \sum_d d\, V_d \,. \tag{1.38}$$

Using momentum conservation at each vertex it is possible to relate the number of loops to the internal lines and vertices, which allows us to rewrite the chiral dimension of the diagram ν as

$$\nu = 2L + 2 + \sum_d V_d \,(d-2) \;. \tag{1.39}$$

As $d \geq 2$ the chiral dimension is always positive. Furthermore each additional loop suppresses the chiral order of the diagram by $(p/\Lambda_\chi)^2$. For a broader renormalization scheme involving also baryons we refer to Refs. [26, 27].

Heavy quark symmetries

Not only light quarks and their symmetries but also heavy ones are of interest. In correspondence to the large mass gap between m_q and m_Q with $q = u, d, s$ and $Q = c, b$ it is possible to derive a heavy quark effective theory (HQET) under the assumption $m_Q \to \infty$ [28, 29, 30, 31, 32] and include systeamtically the corrections of order $\mathcal{O}\,(\Lambda_{\mathrm{QCD}}/m_Q)$. For a more detailed introduction we refer to Refs. [33, 34, 35]. We will explicitly follow the construction presented in Ref. [36].

Consider a hadron composed of a heavy quark Q and some light quark content. Its momentum can be written as

$$p^{\mu}_{\mathrm{had}} = m_{\mathrm{had}}\, v^{\mu} \,, \tag{1.40}$$

where m_{had} is the hadron mass and v^{μ} is the hadron velocity with $v^2 = 1$. The momentum of the heavy quark on the other hand can be expressed as

$$p^{\mu}_{Q} = m_Q v^{\mu} + k^{\mu} \,. \tag{1.41}$$

Considering only strong interactions the hadron is bound by the exchange of soft gluons, which sets the scale $k^{\mu} \approx \Lambda_{\mathrm{QCD}}$. The quark velocity therefore can be obtained by

$$v^{\mu}_{Q} = v^{\mu} + \frac{k^{\mu}}{m_Q} \,. \tag{1.42}$$

Thus the heavy quark and hadron velocity are the same up to corrections of order $\Lambda_{\mathrm{QCD}}/m_Q$. For $m_Q \to \infty$ this factor is suitable for a perturbation theory.

It is possible to define the velocity eigenstates

$$Q_{\pm} = P^{\pm}_{v}\, Q \quad \text{with} \quad P^{\pm}_{v} = \frac{1}{2}\,(1 \pm \not{v}) \;. \tag{1.43}$$

The projectors have the property

$$\not{v} P^{\pm}_{v} = \pm P^{\pm}_{v} \,. \tag{1.44}$$

Therefore Q_+ can be interpreted as moving along the hadron state, while Q_- has a negative velocity.

In order to separate both contributions in a quantum field theory it is possible to apply a momentum boost in order to either obtain a solution for a heavy quark

$$h_v^+ = e^{im_Q(v\cdot x)}Q_+ \quad \text{and} \quad H_v^+ = e^{im_Q(v\cdot x)}Q_- \tag{1.45}$$

or a heavy anti-quark

$$h_v^- = e^{-im_Q(v\cdot x)}Q_- \quad \text{and} \quad H_v^- = e^{-im_Q(v\cdot x)}Q_+ \,. \tag{1.46}$$

Note that this procedure has also been applied to pion–nucleon interaction [19, 37, 38, 39, 40].

Using the particle solution the heavy quark Lagrangian

$$L_{\mathrm{HQ}} = \bar{Q}\left(i\not{D} - m_Q\right)Q \tag{1.47}$$

leads to

$$L_{\mathrm{HQ}} = \bar{h}_v^+ iv_\mu D^\mu h_v^+ - \bar{H}_v^+ \left\{iv_\mu D^\mu + 2m_Q\right\} H_v^+ + \bar{h}_v^+ i\not{D}^\perp H_v^+ + \bar{H}_v^+ i\not{D}^\perp h_v^+ \,, \tag{1.48}$$

where

$$\not{D} = \not{v} v_\mu D^\mu + \not{D}^\perp \quad \text{and} \quad \not{D}^\perp = \gamma_\mu \left(g_{\mu\nu} - v_\mu v_\nu\right) D^\nu \,. \tag{1.49}$$

As now the field H_v^+ contains the heavy scale m_Q it will be integrated out in the path integral formalism [36]. Therefore it leads to the non-local operator

$$L_{\mathrm{HQ}} = \bar{h}_v^+ iv_\mu D^\mu h_v^+ - h_v^+ \not{D}^\perp \frac{1}{iv_\mu D^\mu + 2m_Q - i\epsilon} \not{D}^\perp h_v^+ \,. \tag{1.50}$$

With the assumption that the eigenvalue of $v_\mu D^\mu$ is small compared to m_Q the operator can be expanded as the well-known terms [41, 42, 43, 44]

$$L_{\mathrm{HQ}} = \bar{h}_v^+ iv_\mu D^\mu h_v^+ + K_v + M_v + \mathcal{O}\left(\frac{\Lambda_{\mathrm{QCD}}^2}{m_Q^2}\right) \tag{1.51}$$

with

$$K_v = \frac{1}{2m_Q} h_v^+ D^\mu \left(g_{\mu\nu} - v_\mu v_\nu\right) D^\nu h_v^+ \tag{1.52}$$

and

$$M_v = \frac{g}{4m_Q} \bar{h}_v^+ \sigma^{\mu\nu} F_{\mu\nu} h_v^+ \,. \tag{1.53}$$

With $v = (1,0,0,0)^t$ the term K_v corresponds to the non-relativistic kinetic energy and M_v is the Pauli term, which describes the chromomagnetic coupling of the gluon to the heavy quark. As expected from comparison to QED the chromomagnetic moment scales with m_Q^{-1}. For heavy mesons containing one heavy quark the Lagrangian reads to leading order

$$L_{\mathrm{HQ}} = \bar{h}_v^+ iv_\mu D^\mu h_v^+ \,. \tag{1.54}$$

As this term does not contain any Dirac structure a heavy quark spin symmetry $\mathrm{SU}(2)_v$ arises, which is consistent with e.g. the small mass difference between the B and $B^\star$-meson. A heavy spin symmetry transformation can be applied as [35]

$$h_v \to h_v' = \exp\left(i\sum_{k=1}^{3}\epsilon_k S_k^v\right) h_v \tag{1.55}$$

and

$$\bar{h}_v \to \bar{h}_v' = \bar{h}_v \exp\left(-i\sum_{k=1}^{3}\epsilon_k S_k^v\right) \tag{1.56}$$

with the generators

$$S_k^v = \frac{i}{4}\epsilon_{kmn}\left[\not{e}_m, \not{e}_n\right] P_v^+ \,. \tag{1.57}$$

The vectors e_m^μ define a set of spacelike orthonormal vectors, which are orthogonal to v^μ

$$(e_m)_\mu (e_n)^\mu = -\delta_{mn} \quad \text{and} \quad v_\mu (e_m)^\mu = 0\,. \tag{1.58}$$

Furthermore as the Lagrangian also does not depend on m_Q it would introduce a heavy flavor symmetry. Limitations of heavy quark spin symmetry are shown by the mass difference of the heavy quark spin partners

$$m_{D^\star} - m_D \approx 140\,\mathrm{MeV} \quad \text{and} \quad m_{B^\star} - m_B \approx 45\,\mathrm{MeV}\,, \tag{1.59}$$

as they are supposed to vanish.

For heavy quarkonia, the delicate balance between potential and kinematic energy dictates that the term K_v cannot be neglected [45]. Therefore they break heavy flavor symmetry while still retaining heavy spin symmetry.

Heavy meson chiral perturbation theory

In the previous section we introduced heavy quark symmetries. However, as only hadrons, consisting of quarks and gluons, are observed in experiment, it is advantageous to formulate an effective field theory involving those. For this note that the operators $h_v^\pm$ defined in Eq. (1.45) and (1.46) interpolate an incoming heavy quark or antiquark with velocity v.

We will illustrate the construction of meson states according to the lectures of Georgi [35]. A B and a $B^\star$ meson consist of a b-quark and a light quark and gluon cloud with the quantum numbers of a light antiquark coupled in an S-wave. With $q_1 = u$, $q_2 = d$ and $q_3 = s$ it is possible to define a meson wave function for the B meson with velocity v as

$$B_a(v) \propto \langle 0\,|b_v \bar{q}_a|\,B_a, v\rangle \tag{1.60}$$

and for a $B^\star$ with velocity v and polarization ϵ

$$B_a^\star(v,\epsilon) \propto \langle 0\,|b_v \bar{q}_a|\,B_a^\star, v, \epsilon\rangle\ . \tag{1.61}$$

Note that since $b_v \bar{q}_a$ contains two open Dirac indices also $B_a(v)$ and $B_a^\star(v,\epsilon)$ need to be matrices in Dirac space. Furthermore the field operator transforms as a

reducible representation of the Lorentz symmetry and hence can be decomposed in the pseudoscalar B_a and the vector $B_a^\star$. Therefore these two states form a doublet with respect to heavy quark spin symmetry. Thus it is useful to define the generalized state in the Hilbert space

$$|H_a, v\rangle = b\,|B_a, v\rangle + \sum_\epsilon b_\epsilon\,|B_a^\star, v, \epsilon\rangle\ . \tag{1.62}$$

in analogy to coherent states of the harmonic oscillator. The coefficients b and b_ϵ determine if the state is either a B or $B^\star$ meson.

Its wave function reads

$$H_a(v) \propto \langle 0\,|b_v \bar{q}_a|\,H_a, v\rangle = bB_a(v) + \sum_\epsilon b_\epsilon B_a^\star(v,\epsilon)\,. \tag{1.63}$$

The transformation property

$$\not{v} b_v = b_v \tag{1.64}$$

directly relates to

$$\not{v} H_a = H_a\,. \tag{1.65}$$

Considering also Lorentz invariance and parity of the B and $B^\star$ the wave functions can be parametrized by

$$B_a(v) = -P_v^+\,\gamma_5 \tag{1.66}$$

and

$$B_a^\star(v,\epsilon) = P_v^+ \not{\epsilon}\,. \tag{1.67}$$

To summarize it is possible to define the field operator

$$H_a = P_v^+\,((B_a^\star)_\mu \gamma^\mu - B_a \gamma_5) \tag{1.68}$$

where the field operators $B_a^\star$ and B_a have the normalizations

$$\langle 0\,|B_a|\,B_a, v\rangle = \sqrt{m_B} \quad \text{and} \quad \langle 0\,|(B_a^\star)^\mu|\,B_a^\star, v, \epsilon\rangle = \epsilon^\mu \sqrt{m_{B^\star}}\,. \tag{1.69}$$

A generalization for higher spin states is given in Ref. [46]. The wave function transforms under heavy spin symmetry as

$$H_a \to \exp\left(i \sum_{k=1}^{3} \epsilon_k S_k^v\right) H_a \tag{1.70}$$

and under Lorentz symmetry as

$$H_a \to D(\Lambda)^{-1} H D(\Lambda)^{-1}\,, \tag{1.71}$$

where $D(\Lambda)$ is the Dirac representation of the Lorentz group.

As it contains the quantum numbers of a light antiquark it transforms under the antifundamental representation of chiral vector symmetry. The state is coupled to the pseudo-Goldstone bosons via non-linear realizations [47, 48].

Commonly for this the Goldstone boson realization U of Eq. (1.22) is written as

$$U(x) = u(x)^2 = \left(\exp\left(i\frac{\phi(x)}{2F_0}\right)\right)^2 . \tag{1.72}$$

Under the chiral transformation defined in Eq. (1.24) it transforms as

$$u(x) \to RuK^\dagger(x) = K(x)uL^\dagger \tag{1.73}$$

with the unitary matrix

$$K(x) = \sqrt{RU(x)L^\dagger}Ru(x)\,. \tag{1.74}$$

The transformation of the heavy field H_a is thus given as

$$H_a \to H_b K^\dagger_{ba}(x)\,. \tag{1.75}$$

Correspondingly, the wave function for the heavy antiparticle $\bar{H}_a$ is defined by

$$\bar{H}_a(v) \propto \left\langle H_a, v \left| q_a \bar{b}_v \right| 0 \right\rangle \tag{1.76}$$

and thus can be related to H_a by

$$\bar{H}_a(v) = \gamma^0 H^\dagger_a(v)\gamma^0\,. \tag{1.77}$$

Hence the corresponding field operator can be written as

$$\bar{H}_a = \left((\bar{B}^\star_a)_\mu \gamma^\mu - \bar{B}_a\gamma_5\right) P^-_v\,. \tag{1.78}$$

The most general Lagrangian involving the interaction of pions and heavy mesons [49, 50, 51, 52] to leading order in the momentum expansion is given by

$$L = i\left\langle H_b v^\mu(\delta_{ab}\partial^\mu + V^\mu_{ab})\bar{H}_a\right\rangle + ig\left\langle H_b\gamma_\mu\gamma_5 A^\mu_{ba}\bar{H}_a\right\rangle \tag{1.79}$$

with

$$V^\mu = \frac{1}{2}\left(u^\dagger\partial^\mu u + u\partial^\mu u^\dagger\right) \quad \text{and} \quad A^\mu = \frac{1}{2}\left(u^\dagger\partial^\mu u - u\partial^\mu u^\dagger\right)\,. \tag{1.80}$$

The terms $\langle \dots \rangle$ denote a trace in Dirac space.

For heavy quarkonia states this formalism can be adapted [53, 54]. Considering e.g. the pseudo-scalar bottomonium ground state $\eta(1S)$ and the corresponding vector state $\Upsilon(1S)$, which are both singlets under chiral rotations, the field operator can be written as

$$J = P^+_v\left(\Upsilon_\mu\gamma^\mu - \eta\gamma_5\right)P^-_v\,. \tag{1.81}$$

Contact terms for the transition between different bottomonia J and J' can be e.g. described by the Lagrangian [55, 56]

$$L = -2\left\langle J^\dagger J'\right\rangle\left(c_1\left\langle A_\mu A^\mu\right\rangle + c_2\left\langle A_\mu A_\nu\right\rangle v^\mu v^\nu\right) + \text{h.c.}\,. \tag{1.82}$$

Even exotic mesons such as the Z_b can be involved in this framework [57].

1.3. Dispersion theory

1.3.1. S-Matrix theory

The renormalization procedure in quantum field theories has been established for the singularities of quantum electrodynamics at the end of the forties [58, 59, 60, 61, 62, 63, 64, 65, 66]. However a proper understanding of the renormalization of quantum chromodynamics has only been provided in the seventies [12, 67, 68]. In the meantime a different approach to quantum field theory, which was named S-matrix theory, was investigated [69, 70, 71, 72, 73, 74]. For an introduction to dispersion theory, which we will follow here, we refer to Refs. [75, 76, 77]. Both methods are not in conflict with each other. However, the application of dispersion theory is most feasible in the low energy region, thus covering the problematic region for quantum field theoretical studies of QCD.

Consider an experiment with a short ranged interaction of the involved particles. An initial state is prepared in the distant past

$$|i, \text{in}\rangle = |i, t \to -\infty\rangle \ , \tag{1.83}$$

where t denotes the time. These states are normalized

$$\langle i, \text{in}|j, \text{in}\rangle = \delta_{ij} \tag{1.84}$$

and furthermore fulfill a completeness relation

$$1 = \sum_m |m, \text{in}\rangle \langle m, \text{in}| \ . \tag{1.85}$$

Here the sum runs over all the different states, which are allowed by symmetries and kinematics.

In analogy one can define the final state in the future

$$|f, \text{out}\rangle = |f, t \to \infty\rangle \ , \tag{1.86}$$

which involves a similar normalization and completeness relation.

The intent of S-matrix theory is to determine the so called S-matrix, which describes the probability for the transition from the initial state to the final state

$$|\langle f, \text{out}|i, \text{in}\rangle|^2 = |\langle f, \text{in}\,|S|\,i, \text{in}\rangle|^2 = |\langle f, \text{out}\,|S|\,i, \text{out}\rangle|^2 \ . \tag{1.87}$$

Due to probability conservation a proper definition of the S-matrix is given by

$$S = \sum\!\!\!\!\!\!\int_m |m, \text{in}\rangle \langle m, \text{out}| \ , \tag{1.88}$$

which implies, using Eq. (1.85), the **unitarity** of the S-matrix

$$SS^\dagger = S^\dagger S = 1 \, . \tag{1.89}$$

As the basis for the in and out states define the same Hilbert space, we will drop their notion in the following.

Since the momenta of relativistic particles are easier to measure than their position it is advantageous to work in momentum space. Each state $|i\rangle$ is a state consisting of n particles with quantum numbers κ_j and momenta p_j with $j = 1, \ldots, n$

$$|i\rangle = |\kappa_1, p_1\rangle \otimes |\kappa_2, p_2\rangle \otimes \cdots \otimes |\kappa_n, p_n\rangle \ . \tag{1.90}$$

The particles fulfill the on-shell condition

$$p_j^2 = m_j^2 \tag{1.91}$$

and thus the normalization for each single-particle state is

$$\langle \kappa_i, p | \kappa_j, k \rangle = 2p^0 \, \delta_{\kappa_i,\kappa_j} \, (2\pi)^3 \delta^3 \left(\vec{p} - \vec{k} \right) \ . \tag{1.92}$$

Also the completeness relation needs to be adjusted to

$$1 = \sum_{n=0}^{\infty} \prod_{k=1}^{n} \sum_{\kappa_k} \int \frac{\mathrm{d}^4 p_k}{(2\pi)^4} \, 2\pi \delta(p_k^2 - m_k^2) \, |\kappa_k, p_k\rangle \, \langle \kappa_k, p_k| = \sum\!\!\!\!\!\!\int_m |m\rangle \, \langle m| \ , \tag{1.93}$$

where n denotes the number of particles in each state.

As the particles have a defined momentum they are not localized in position space due to the Heisenberg uncertainty principle. Therefore it is highly likely that they will pass each other without interaction. The definition

$$S = 1 + iR \tag{1.94}$$

properly separates off the interaction part R.

Since the probability does not depend on the reference frame, S needs to be Lorentz invariant. To also preserve overall momentum conservation, R in is usually defined as a distribution

$$\langle f | R | i \rangle = (2\pi)^4 \delta^4(p_i - p_f) \, \langle f | T | i \rangle \ , \tag{1.95}$$

where p_i and p_f are the overall momenta of the initial and final state. The transition amplitude T on the other hand can only depend on Lorentz invariants.

Invoking the unitarity of the S matrix in Eq. (1.89) leads to

$$\langle f | R | i \rangle - \left\langle f \middle| R^\dagger \middle| i \right\rangle = i \left\langle f \middle| R^\dagger R \middle| i \right\rangle \ . \tag{1.96}$$

The most common form of the unitarity relation is obtained by inserting the completeness relation, the definition of the transition amplitude T and integrating out the overall momentum conservation $(2\pi)^4 \delta^4(p_f - p_i)$

$$\langle f | T | i \rangle - \langle i | T | f \rangle^\star = i \sum\!\!\!\!\!\!\int_m (2\pi)^4 \delta^4(p_i - p_m) \, \langle m | T | f \rangle^\star \, \langle m | T | i \rangle \ . \tag{1.97}$$

For strong interactions PT invariance and the Schwarz reflection principle leads to

$$\langle i | S | f \rangle = \langle f | S | i \rangle \ , \tag{1.98}$$

which simplifies the unitarity equation to

$$2i\,\mathrm{Im}\,\langle f|T|i\rangle = i\sum\!\!\!\!\!\!\int_m (2\pi)^4\delta^4(p_i - p_m)\,\langle f|T|m\rangle^\star\,\langle m|T|i\rangle\ . \tag{1.99}$$

Another important property of the S-matrix is **analyticity**. It is related to the micro-causality condition for some arbitrary field operator $\phi(x)$

$$[\phi(x),\phi(y)] = 0 \quad \text{if} \quad (x-y)^2 < 0\,, \tag{1.100}$$

which says that information cannot be transmitted faster than light speed. Greens functions calculated under this assumption can be related to the S-matrix via the Lehmann-Symanzik-Zimmerman reduction formula [78, 79]. A Fourier transform to momentum space ensures an extended range of applicability for complex momenta [80, 81].

To illustrate further properties of the S-matrix we restrict ourselves to the scattering process of four scalar particles

$$\phi_1(p_1) + \phi_2(p_2) \to \phi_3(p_3) + \phi_4(p_4)\,. \tag{1.101}$$

The initial momenta p_1 and p_2 as well as the final state momenta p_3 and p_4 are restricted by the mass-shell condition

$$p_a^2 = m_a^2 \quad \text{with} \quad a = 1,\ldots,4\,. \tag{1.102}$$

Considering only scalar particles the transition amplitude will only depend on the momenta

$$\langle\phi_3(p_3)\phi_4(p_4)|T|\phi_1(p_1)\phi_2(p_2)\rangle = T^{fi}\,(p_1,p_2;p_3,p_4)\ . \tag{1.103}$$

As discussed in Ref. [75, 82] the amplitude T can only depend on the Lorentz invariant products

$$s_{xy} = p_x\cdot p_y \quad \text{with} \quad x,y = 1,\ldots,4 \tag{1.104}$$

and

$$\epsilon_{abcd} = \epsilon_{\mu\nu\alpha\beta}\,p_a^\mu p_b^\nu p_c^\alpha p_d^\beta \tag{1.105}$$

in order to preserve Lorentz invariance. It is commonly written as

$$T^{fi}(p_1,p_2;p_3,p_4) = T_s^{fi}(s_{xy}) + \epsilon_{abcd}\,T_{abcd}^{fi}(s_{xy})\,. \tag{1.106}$$

While the first term T_s^{fi} transforms even under parity, the second term changes sign. Since the strong interaction is parity conserving, the last term can often be neglected. However, not all possible contractions s_{xy} are independent from each other. Due to the on-shell conditions and momentum conservation only two of them are necessary to describe the amplitude. A common choice are the Mandelstam variables [83] given by

$$s = (p_1+p_2)^2 \quad , \quad t = (p_1-p_3)^2 \quad \text{and} \quad u = (p_1-p_4)^2\,. \tag{1.107}$$

With these the transition amplitude can be expressed as

$$T^{fi}(p_1, p_2; p_3, p_4) = T^{fi}(s, t, u)\,, \tag{1.108}$$

where one of the Mandelstam variables can be expressed by the others through the equation

$$s + t + u = m_1^2 + m_2^2 + m_3^2 + m_4^2\,. \tag{1.109}$$

In the center-of-mass system (CMS) the momenta may be written as

$$p_1 = \begin{pmatrix} p_1^0 \\ \vec{p}_{12} \end{pmatrix} \;,\; p_2 = \begin{pmatrix} p_2^0 \\ -\vec{p}_{12} \end{pmatrix} \;,\; p_3 = \begin{pmatrix} p_3^0 \\ \vec{p}_{34} \end{pmatrix} \text{ and } p_4 = \begin{pmatrix} p_4^0 \\ -\vec{p}_{34} \end{pmatrix} \tag{1.110}$$

with

$$p_{1/2}^0 = \sqrt{|\vec{p}_{12}|^2 + m_{1/2}^2} \text{ and } p_{3/4}^0 = \sqrt{|\vec{p}_{34}|^2 + m_{3/4}^2}\,. \tag{1.111}$$

The center-of-mass three-momenta are defined by

$$|\vec{p}_{12}|^2 = \frac{\lambda(s, m_1^2, m_2^2)}{4s} \quad \text{and} \quad |\vec{p}_{34}|^2 = \frac{\lambda(s, m_3^2, m_4^2)}{4s}\,, \tag{1.112}$$

whereas the Källén function $\lambda(a, b, c)$ is given as

$$\lambda(a, b, c) = \left(a - \left(\sqrt{b} + \sqrt{c}\right)^2\right)\left(a - \left(\sqrt{b} - \sqrt{c}\right)^2\right)\,. \tag{1.113}$$

With this notation the Mandelstam variables t and u can be expressed through s and the scattering angle θ_s between $\vec{p}_{12}$ and $\vec{p}_{34}$ as

$$t = \frac{1}{2}\left(\sum_{i=1}^{4} m_i^2 - s + \left(m_2^2 - m_1^2\right)\left(m_3^2 - m_4^2\right) + 4\,|\vec{p}_{12}|\,|\vec{p}_{34}|\,\cos\,\theta_s\right) \tag{1.114}$$

and

$$u = \frac{1}{2}\left(\sum_{i=1}^{4} m_i^2 - s - \left(m_2^2 - m_1^2\right)\left(m_3^2 - m_4^2\right) - 4\,|\vec{p}_{12}|\,|\vec{p}_{34}|\,\cos\,\theta_s\right)\,. \tag{1.115}$$

The transition amplitude can be partial-wave projected - in case of scalar particles the resulting expression is

$$T^{fi}(s, t, u) = T(s, \cos\,\theta_s) = 16\pi S \sum_{\ell=0}^{\infty} (2\ell + 1) P_\ell(\cos\theta_s) t_\ell^{fi}(s)\,. \tag{1.116}$$

For a discussion of particles with spin we refer to Ref. [84]. Here S denotes the corresponding symmetry factor, $P_\ell(\cos\theta_s)$ the standard Legendre-polnomials and $t_\ell(s)$ the partial-wave amplitude. Considering only two-particle intermediate states with masses m_a and m_b the unitarity equation for partial-waves reads

$$\mathrm{Im}\, t_\ell^{fi}(s) = S \sum_{m=\{m_a, m_b\}} (t_\ell^{fm})^\star(s)\sigma(s, m_a, m_b) t_\ell^{mi}(s)\,, \tag{1.117}$$

with the phase space factor

$$\sigma(s, m_a, m_b) = \frac{\sqrt{\lambda(s, m_a^2, m_b^2)}}{s} \, \theta\left(s - (m_a + m_b)^2\right) . \tag{1.118}$$

Note that the symmetry factor can be absorbed by the redefinition

$$\tilde{t}_\ell^{fi} = S \, t_\ell^{fi} \tag{1.119}$$

leading to the equation

$$\operatorname{Im} \tilde{t}_\ell^{fi}(s) = \sum_{m=\{m_a, m_b\}} (\tilde{t}_\ell^{fm})^\star(s) \sigma(s, m_a, m_b) \tilde{t}_\ell^{mi}(s) . \tag{1.120}$$

Furthermore it is important that the presented derivation only applies for $s > \max\left\{(m_1 + m_2)^2, (m_3 + m_4)^2\right\}$ as the initial and final states were assumed to be asymptotic states.

The CPT-theorem [85, 86, 87, 88] in quantum field theory allows one to relate the s-channel process

$$\phi_1(p_1) + \phi_2(p_2) \to \phi_3(p_3) + \phi_4(p_4) \tag{1.121}$$

to the t-channel

$$\phi_1(p_1) + \bar{\phi}_3(-p_3) \to \bar{\phi}_2(-p_2) + \phi_4(p_4) \tag{1.122}$$

and the u-channel processes

$$\phi_1(p_1) + \bar{\phi}_4(-p_4) \to \phi_3(p_3) + \bar{\phi}_2(-p_2) \tag{1.123}$$

by replacing a particle in an incoming state with an antiparticle in the outgoing state with reversed momentum. If e.g. m_1 is heavy enough to decay into the other three, the decay amplitude

$$\phi_1(p_1) \to \bar{\phi}_2(-p_2) + \phi_3(p_3) + \phi_4(p_4) \tag{1.124}$$

can also be obtained. In a similar fashion in S-matrix theory they are related by requiring **crossing symmetry**. It says, that these different processes are described by the same amplitude $T(s, t, u)$, which is continued into different energy regions of the Mandelstam variables s, t and u. An example of the Mandelstam plane is shown in Fig. 1.2.

The partial-wave unitarity equation of Eq. (1.117) shown for the s-channel can be similarly applied to the t- and u-channel. While the s-channel produces imaginary parts for

$$s > \max\left\{(m_1 + m_2)^2, (m_3 + m_4)^2\right\} = s_{\text{thr}} \tag{1.125}$$

the t-channel gets contributions for

$$t > \max\left\{(m_1 + m_3)^2, (m_2 + m_4)^2\right\} = t_{\text{thr}} \tag{1.126}$$

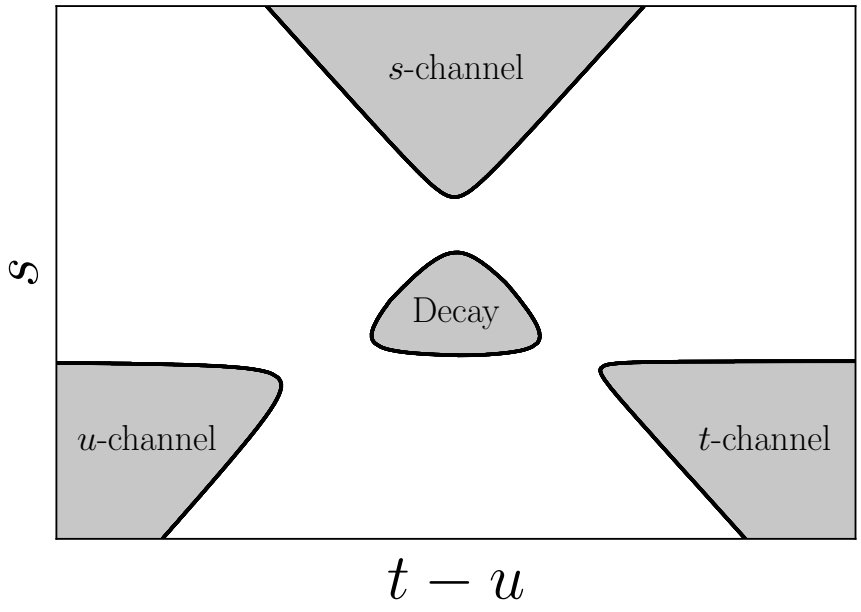

Figure 1.2.: Exemplary Mandelstam plane

and the u-channel

$$u > \max\left\{(m_1 + m_4)^2, (m_2 + m_3)^2\right\} = u_{\text{thr}}\,. \tag{1.127}$$

Accordingly the partial-wave amplitude in the s-channel does not only have an imaginary part for $s > s_{\text{thr}}$, which will denoted as **right-hand cut**, but also an imaginary part extending to $-\infty$, called **left-hand cut**.

Analyticity in terms of partial-waves means, that the partial-wave amplitude $t_\ell(s)$ can be analytically continued to the upper complex s-plane, without encountering singularities. Invoking the Schwarz reflection principle

$$t_\ell(s) = t_\ell^\star\left(s^\star\right) \tag{1.128}$$

it possible to define the partial-wave amplitude in the entire complex s-plane. The left- and right-hand cuts will show up as discontinuities

$$\operatorname{disc} t_\ell(s) = \lim_{\epsilon\to 0}\left(t_\ell(s + i\epsilon) - t_\ell(s - i\epsilon)\right) = 2i\,\operatorname{Im} t_\ell(s)\,. \tag{1.129}$$

Hence $t_\ell(s)$ is an analytic function in the entire first sheet of the complex s-plane, except for left- and right-hand cuts along the real axis and maybe bound states below the lowest threshold.

Furthermore, note that the Schwarz reflection principle in the decay region is broken, as left- and right-hand cuts may overlap. A proper description is then done e.g. by analytically continuing in the external masses m_i with $i = 1, \ldots, 4$ starting from a region, where the decay is not possible.

1.3.2. Dispersion integral

Consider an amplitude $f(s)$, which is holomorphic in the entire complex s-plane, except for a left-hand cut $C_L = \{s \in \mathbb{R} | s < s_L\}$, a right-hand cut $C_R = \{s \in \mathbb{R} | s > s_R\}$ and a bound state pole at s_p. Then for any $s \in \mathbb{C}$ with $s \notin C_L \cup C_R \cup \{s_p\}$ the amplitude $f(s)$ can be written with the residue theorem as

$$f(s) = \frac{1}{2\pi i} \int_{\mathcal{C}} \mathrm{d}z \, \frac{f(z)}{z - s} \,, \tag{1.130}$$

where $\mathcal{C}$ is any closed path with a mathematical positive orientation, which encircles $z = s$ but not any of the non-analyticities mentioned above.

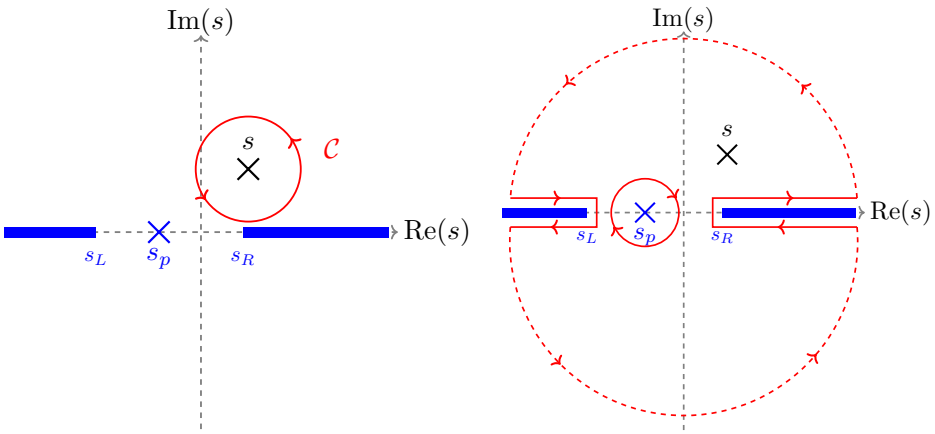

(a) Initial integration contour (b) Deformed integration contour

Figure 1.3.: Integration contours for the dispersive representation in the complex s-plane.

Using Cauchy's theorem it is possible to deform the integration path as long as the singularities such as the cuts and the pole are avoided. In order to obtain the integration path in Fig. 1.3b the residue

$$R\left(\frac{f(z)}{z-s}, s_p\right) = \mathrm{Res}\left(\frac{f(z)}{z-s}\right)\Big|_{z=s_p} \tag{1.131}$$

at s_p needs to be subtracted, due to the clockwise orientation of the integral around s_p. With a large but finite radius r the integral can be written as

$$f(s) = -R\left(\frac{f(z)}{z-s}, s_p\right) + I_c(s, -r, s_L) + I_c(s, s_R, r) + I_a(s, 0, \pi) + I_a(s, \pi, 2\pi) \,, \tag{1.132}$$

Here I_c is the integration along the real axis

$$I_c(s, a, b) = \lim_{\epsilon \to 0} \frac{1}{2\pi i} \int_a^b \mathrm{d}z \, \frac{f(z + i\epsilon) - f(z - i\epsilon)}{z - s - i\epsilon} \,, \tag{1.133}$$

which can be expressed through the discontinuity

$$I_c(s,a,b) = \lim_{\epsilon\to 0} \frac{1}{2\pi i} \int_a^b \mathrm{d}z \, \frac{\mathrm{disc}\, f(z)}{z - s - i\epsilon} \,. \tag{1.134}$$

The integration along the complex arc can be written as

$$I_a(s,\phi_1,\phi_2) = \frac{r}{2\pi} \int_{\phi_1}^{\phi_2} \mathrm{d}\phi \, e^{i\phi} \, \frac{f(re^{i\phi})}{re^{i\phi} - s} \,. \tag{1.135}$$

If $f(s)$ is sufficiently convergent, such that it behaves as

$$|f(s)| \to 0 \quad \text{for} \quad |s| \to \infty \tag{1.136}$$

the limit $r \to \infty$ is well defined. Furthermore this ensures, that the contribution of the complex arcs vanish, such that the dispersive representation of $f(s)$ is given as

$$f(s) = -R\left(\frac{f(z)}{z-s}, s_p\right) + \frac{1}{2\pi i}\left[\int_{-\infty}^{s_L} \mathrm{d}z \, \frac{\mathrm{disc}\, f(z)}{z-s} + \int_{s_R}^{\infty} \mathrm{d}z \, \frac{\mathrm{disc}\, f(z)}{z-s}\right] . \tag{1.137}$$

Note that the values on the cuts can be accessed by an analytic continuation of $f(s)$ by approaching with the prescription $s \to s + i\epsilon$. Hence the integral reads

$$f(s) = -R\left(\frac{f(z)}{z-s}, s_p\right) + \frac{1}{2\pi i}\left[\int_{-\infty}^{s_L} \mathrm{d}z \, \frac{\mathrm{disc}\, f(z)}{z-s-i\epsilon} + \int_{s_R}^{\infty} \mathrm{d}z \, \frac{\mathrm{disc}\, f(z)}{z-s-i\epsilon}\right] . \tag{1.138}$$

For the evaluation of s on either the left- or right-hand cut the Sokhotski-Plemelj theorem is required, which says

$$\int_a^b \mathrm{d}z \frac{h(z)}{z - s \pm i\epsilon} = \fint_a^b \mathrm{d}z \frac{h(z)}{z-s} \mp i\pi \int_a^b \mathrm{d}z \, h(z) \, \delta(z-s) \,. \tag{1.139}$$

The principal value integral is defined as

$$\fint_a^b \mathrm{d}z \, \frac{h(z)}{z-s} = \lim_{\epsilon\to\infty} \left[\int_a^{s-\epsilon} \mathrm{d}z \, \frac{h(z)}{z-s} + \int_{s+\epsilon}^b \mathrm{d}z \, \frac{h(z)}{z-s}\right] . \tag{1.140}$$

If $f(s)$ does not vanish fast enough so called **subtractions** can be introduced. For this consider a function

$$g(s) = \frac{f(s)}{P_n(s)} \,, \tag{1.141}$$

where $P_n(s)$ is a polynomial in s of order n, hence it can be expressed by its zeroes $\tilde{s}_i$ with $i = 1, \ldots, n$ as

$$P_n(s) = \prod_{i=1}^{n} (s - \tilde{s}_i) \,. \tag{1.142}$$

They are chosen, such that they do not coincide with either the left- or right-hand cut.

Since $P_n(s)$ does not have any discontinuities, the analytic structure of $g(s)$ is the same as $f(s)$ except for the poles at $z = \tilde{s}_i$. Additionally $g(s)$ shows an improved high energy behavior, such that for high enough n the limit $r \to \infty$ is well defined. Hence it can be reconstructed dispersively as shown above

$$\begin{aligned} g(s) = &-R\left(\frac{g(z)}{z-s}, s_p\right) - \sum_{i=1}^{n} R\left(\frac{g(z)}{z-s}, \tilde{s}_i\right) \\ &+ \frac{1}{2\pi i}\int_{-\infty}^{s_L} \mathrm{d}z\, \frac{\operatorname{disc} g(z)}{z-s-i\epsilon} + \frac{1}{2\pi i}\int_{s_R}^{\infty} \mathrm{d}z\, \frac{\operatorname{disc} g(z)}{z-s-i\epsilon}\,. \end{aligned} \tag{1.143}$$

Expressing the **dispersion relation** in terms of $f(s)$ leads to

$$f(s) = \tilde{P}(s) + \frac{P_n(s)}{2\pi i}\int_{-\infty}^{s_L} \frac{\mathrm{d}z}{P_n(z)}\, \frac{\operatorname{disc} f(z)}{z-s-i\epsilon} + \frac{P_n(s)}{2\pi i}\int_{s_R}^{\infty} \frac{\mathrm{d}z}{P_n(z)}\, \frac{\operatorname{disc} f(z)}{z-s-i\epsilon}\,. \tag{1.144}$$

The term

$$\tilde{P}(s) = -P_n(s)\left(R\left(\frac{g(z)}{z-s}, s_p\right) + \sum_{i=1}^{n} R\left(\frac{g(z)}{z-s}, \tilde{s}_i\right)\right) \tag{1.145}$$

is called **subtraction polynomial**. In exchange for an improved high energy behavior it contains information about the low energy regime, which cannot be restricted by dispersion theory alone. If $f(s)$ does not contain a pole $\tilde{P}(s)$ reduces to a polynomial

$$\tilde{P}(s) = \sum_{k=0}^{n-1} a_k s^k\,, \tag{1.146}$$

where the coefficients a_k are called **subtraction constants**.

1.3.3. Homogeneous Omnès problem

The simplest application of dispersion theory is the so called homogeneous Omnès problem [89] or homogenous Hilbert-type problem [90]. It considers a function, which contains only a right-hand cut starting at s_0 and is holomorphic otherwise. Its application to hadron physics is e.g. the transition of a source ψ with spin ℓ to a final state consisting of two particles ϕ_1 and ϕ_2

$$\langle f|S|i\rangle = \langle \phi_1(p_1), \phi_2(p_2)|T|\psi(p_1+p_2)\rangle \propto F_\ell^f\left((p_1+p_2)^2\right) \tag{1.147}$$

These so-called **form factors** have been studied extensively with the use of dispersion theory [89, 91, 92, 93, 94, 95, 96].

Consider as an example a vector of form factors $F_\ell^f(s)$, where $i = 1, \ldots, n$ denotes the open channels taking part in the rescattering process in a fixed partial-wave ℓ. According to Eq. (1.117) they fulfill the unitarity condition

$$\operatorname{Im} F_\ell^f(s) = \sum_{m=1}^{n} \left(t_\ell^{fm}(s)\right)^\star\, \sigma_m(s) F_\ell^m(s)\,, \tag{1.148}$$

where $\sigma_m(s)$ is a short-hand notation for the phase space of the channel m as defined in Eq. (1.118). The partial-wave scattering amplitude t_ℓ^{km} between channels k and m on the other hand serves as input to set up the dispersion relation.

Also define the Omnès matrix $\Omega_\ell^{fi}(s)$ which fulfills the unitarity condition

$$\operatorname{Im}\Omega_\ell^{fi}(s) = \sum_{m=1}^{n} \left(t_\ell^{fm}(s)\right)^\star \sigma_m(s)\Omega_\ell^{mi}(s) \tag{1.149}$$

and an unsubtracted dispersion relation

$$\Omega_\ell^{fi}(s) = \sum_{m=1}^{n} \frac{1}{\pi} \int_{s_0}^{\infty} \mathrm{d}z \, \frac{\left(t_\ell^{fm}(z)\right)^\star \sigma_m(z)\Omega_\ell^{mi}(z)}{z - s - i\epsilon} \tag{1.150}$$

with a normalization

$$\Omega_\ell^{fi}(0) = \delta_{fi}\,. \tag{1.151}$$

The function

$$f^i(s) = \sum_{k=1}^{n} \left(\Omega_\ell^{-1}(s)\right)^{ik} F_\ell^k(s) \tag{1.152}$$

is analytic and free of any discontinuities. Therefore a Taylor expansion of $f^i(s)$ converges for all s and it can be written as a polynomial $P^i(s)$. Hence the form factor is entirely determined by

$$F_\ell^i(s) = \sum_{k=1}^{n} \Omega_\ell^{ik}(s) P^k(s)\,. \tag{1.153}$$

Considering only a single channel as final and intermediate state, called elastic in the following, the Omnès function can be determined analytically. The partial-wave amplitude $t_\ell(s)$ above s_0 can be entirely described by the phase shift $\delta_\ell(s)$ as

$$t_\ell(s) = \frac{\sin\delta_\ell(s)}{\sigma_1(s)} e^{i\delta_\ell(s)}\,. \tag{1.154}$$

As the imaginary part is a real number the phase of both $F_\ell(s)$ as well as $\Omega_\ell(s)$ needs to be equal to the phase shift $\delta_\ell(s)$, which is called Watson theorem [97]. With the restriction $|\Omega_\ell(s)| > 0$ for all $s \in \mathbb{C}$ the unitarity condition can be expressed as

$$\operatorname{disc}\log\Omega_\ell(s) = 2i\delta_\ell(s)\,. \tag{1.155}$$

As $\delta_\ell(s)$ approaches a constant value for $s \to \infty$ one subtraction is enough to obtain a convergent dispersion integral. The unknown subtraction constant can be absorbed into the polynomial $P(s)$ of Eq. (1.153). Hence for the elastic Omnès function can be written as

$$\Omega(s) = \exp\left(\frac{s}{\pi}\int_{s_0}^{\infty} \frac{\mathrm{d}z}{z}\,\frac{\delta_\ell(z)}{z - s - i\epsilon}\right)\,. \tag{1.156}$$

In order to determine its high energy behavior assume that for $s \to \infty$ the phase shifts approaches a value δ_ℓ^∞. Using a cutoff Λ, such that $\Lambda \ll s$ but $\delta_\ell(\Lambda) \approx \delta_\ell^\infty$ allows to estimate the dispersion integral

$$\frac{s}{\pi} \fint_{s_0}^{\infty} \frac{\mathrm{d}z}{z} \frac{\delta_\ell(z)}{z-s} \approx \frac{1}{\pi} \int_{s_0}^{\Lambda} \frac{\mathrm{d}z}{z} \delta_\ell(z) + \frac{\delta_\ell^\infty}{\pi} \log\left(\frac{\Lambda}{s-\Lambda}\right) . \tag{1.157}$$

Hence the Omnès function scales at high energies like

$$\Omega(s) \propto \left(\frac{\Lambda}{s-\Lambda}\right)^{\frac{\delta_\ell^\infty}{\pi}} . \tag{1.158}$$

The multi-channel Muskhelishvili-Omnès problem (MO) [90] does not have a closed analytical expression. Therefore the integral equation (1.150) needs to be solved numerically. The common procedure [98, 99, 100, 101] is to approximate the principal value dispersion integral by a quadrature and solving the system of equations via singular value decomposition.

The unitarity equation (1.149) can be expressed as

$$\operatorname{Im} \Omega_\ell^{fi}(s) = \sum_{k=1}^{n} X_\ell^{fk}(s) \operatorname{Re} \Omega_\ell^{ki}(s) \tag{1.159}$$

with

$$X_\ell(s) = \left[1 - i t_\ell^\star(s) \hat{\sigma}(s)\right]^{-1} t_\ell^\star \hat{\sigma} . \tag{1.160}$$

Here $\hat{\sigma}(s)$ is a diagonal matrix containing the phase space factors as entries

$$\hat{\sigma}^{ij}(s) = \sum_{k=1}^{n} \delta_{ik}\delta_{jk}\sigma_k(s) . \tag{1.161}$$

Inserting the newly derived unitarity equation into the dispersion integral of Eq. (1.150) reads

$$\operatorname{Re} \Omega_\ell^{ij} = \sum_{k=1}^{n} \frac{1}{\pi} \fint_{s_0}^{\infty} \mathrm{d}z \, \frac{X_\ell^{ik}(z)}{z-s} \operatorname{Re} \Omega_\ell^{kj}(z) . \tag{1.162}$$

To proceed split the integral into two

$$\operatorname{Re} \Omega_\ell^{ij} = \sum_{k=1}^{n} \frac{1}{\pi} \fint_{s_0}^{\Lambda} \mathrm{d}z \, \frac{X_\ell^{ik}(z)}{z-s} \operatorname{Re} \Omega_\ell^{kj}(z) + \sum_{k=1}^{n} \frac{1}{\pi} \fint_{\Lambda}^{\infty} \mathrm{d}z \, \frac{X_\ell^{ik}(z)}{z-s} \operatorname{Re} \Omega_\ell^{kj}(z) \tag{1.163}$$

and discuss each integral separately.

The first integral takes on the generic form

$$I_1 = \fint_a^b \mathrm{d}z \, \frac{f(z)}{z-s} . \tag{1.164}$$

Using the substitution

$$z(y) = \frac{b-a}{2}\, y + \frac{a+b}{2} \tag{1.165}$$

with $y \in (-1, 1)$ the integral I_1 can be written as

$$I_1 = \fint_{-1}^{1} \mathrm{d}y\, \frac{g(y)}{y - \tilde{s}} \quad \text{with} \quad g(y) = f(z(y)) \quad \text{and} \quad \tilde{s} = \frac{2s - a - b}{b - a}\,. \tag{1.166}$$

The transformed function $g(y)$ on the other hand can expanded in terms of Legendre polynomials

$$g(y) = \sum_{k=0}^{\infty} c_k P_k(y) \quad \text{with} \quad c_k = \frac{2k+1}{2} \fint_{-1}^{1} \mathrm{d}y\, g(y) P_k(y) \tag{1.167}$$

To proceed use a Gauss-Legendre quadrature of order N for all coefficients c_k

$$c_k \approx \frac{2k+1}{2} \sum_{n=1}^{N} w_n^N g(y_n) P_k(y_n^N)\,, \tag{1.168}$$

where y_n^N with $n = 1, \ldots, N$ are the zeroes of $P_N(y)$ and w_n^N are the weights

$$w_n^N = \frac{2}{(1 - y_n^2)} \left[\frac{\partial P_N}{\partial y}(y_n) \right]^{-2}\,. \tag{1.169}$$

Truncating the series expansion of Eq. (1.167) at N leads to

$$g(y) \approx \sum_{k=0}^{N-1} P_k(y) \sum_{n=1}^{N} \frac{2k+1}{2} w_n^N g(y_n^N) P_k(y_n^N)\,, \tag{1.170}$$

as the order N vanishes by definition. Hence I_1 can be written as

$$I_1 = \sum_{n=1}^{N} W_n^N \left(\frac{2s - a - b}{b - a} \right) g(y_n^N) \tag{1.171}$$

with

$$W_n^N(\tilde{s}) = -\sum_{k=0}^{N-1} (2k+1) w_n^N P_k(y_n^N) Q_k(\tilde{s})\,. \tag{1.172}$$

The Legendre polynomials of second kind Q_k

$$Q_k(\tilde{s}) = -\frac{1}{2} \fint_{-1}^{1} \mathrm{d}y\, \frac{P_k(y)}{y - \tilde{s}} \tag{1.173}$$

are precisely determined and implemented in e.g. the GNU-GSL libraries [102] for all regions of $\tilde{s}$.

In a similar fashion the integral

$$I_2 = \int_c^{\infty} \mathrm{d}z\, \frac{f(z)}{z - s} \tag{1.174}$$

can be determined. The corresponding transformation

$$z = \frac{2c}{1-\hat{y}}\,. \tag{1.175}$$

leads to

$$I_2 = \int_{-1}^{1} \mathrm{d}\hat{y}\, \frac{2c}{1-\hat{y}}\, \frac{\hat{g}(\hat{y})}{\hat{y}-\hat{s}} \quad \text{with} \quad \hat{g}(\hat{y}) = f(z(\hat{y})) \quad \text{and} \quad \hat{s} = 1 - \frac{2c}{s}\,. \tag{1.176}$$

Following the same steps we obtain

$$I_2 = \frac{1}{s} \sum_{m=1}^{M} W_m^M \left(1 - \frac{2c}{s}\right) \frac{2c}{1-2y_m^M}\, \hat{g}(y_m^M)\,. \tag{1.177}$$

Considering N_1 Gauss-Legendre points for the finite range integral and N_2 for the other the full integral can be written as

$$\begin{aligned} \operatorname{Re}\Omega_\ell^{ij}(s) = {} & \frac{1}{\pi} \sum_{\alpha=1}^{N_1} W_\alpha^{N_1} \left(\frac{2s - s_0 - \Lambda}{\Lambda - s_0}\right) \sum_{k=1}^{n} X_\ell^{ik}(\tilde{z}_\alpha^{N_1}) \operatorname{Re}\Omega_\ell^{kj}(\tilde{z}_\alpha^{N_1}) \\ & + \frac{1}{\pi s} \sum_{\beta=1}^{N_2} W_\beta^{N_2} \left(1 - \frac{2\Lambda}{s}\right) \hat{z}_\beta^{N_2} \sum_{k=1}^{n} X_\ell^{ik}(\hat{z}_\beta^{N_2}) \operatorname{Re}\Omega_\ell^{kj}(\hat{z}_\beta^{N_2})\,. \end{aligned} \tag{1.178}$$

The grid points

$$\tilde{z}_\alpha^{N_1} = \frac{\Lambda - s_0}{2}\, y_\alpha N_1 + \frac{\Lambda + s_0}{2} \quad \alpha = 1, \ldots, N_1 \tag{1.179}$$

and

$$\hat{z}_\beta^{N_2} = \frac{2\Lambda}{1 - y_\beta^{N_2}} \quad \beta = 1, \ldots, N_2 \tag{1.180}$$

are defined by the zeros y_γ^N with $\gamma = 1, \ldots, N$ of the corresponding N^{th} Legendre polynomial $P_N(y)$.

In order to obtain a solution for the Omnès matrix evaluate Eq. (1.178) for all the different grid points $\tilde{z}_\alpha^{N_1}$ and $\tilde{z}_\beta^{N_2}$. Additionally evaluate it for $s = 0$, which gives the restriction of Eq. (1.151). The thus obtained system of equations is overdetermined and can by solved for $\operatorname{Re}\Omega^{ij}(\tilde{z}_\alpha^{N_1})$ and $\operatorname{Re}\Omega^{ij}(\hat{z}_\beta^{N_2})$ via singular value decomposition. The corresponding imaginary parts can then be determined by Eq. (1.159). In order to improve this procedure numerically it is possible to introduce more mesh points by either increasing the order of the Gauss-Legendre quadrature, or dividing the integration intervals into more subintervals.

1.3.4. Inhomogenous Omnès problem

The next more complicated application is the inhomogenous Omnès problem. Here the function does not only have a right-hand cut but also a left-hand

cut is considered. For example the decay amplitude of the particle Ψ into a three-particle final state with particles ϕ_1, ϕ_2 and Φ

$$\langle f\,|T|\,i\rangle = \langle \phi_1(p_1), \phi_2(p_2), \Phi(p_3)\,|T|\,\Psi(p)\rangle \propto A(s,t,u)\,, \tag{1.181}$$

where s is the invariant mass of the ϕ_1-ϕ_2 system, has such an analytic structure. The other two Mandelstam variables t and u can be expressed through s and the scattering angle θ between ϕ_1 and Ψ.

Assume that the scattering amplitude $A(s,t,u)$ is separated into two parts

$$A(s,t,u) = M(s,t,u) + K(s,t,u)\,. \tag{1.182}$$

Accordingly also the partial-wave amplitudes can be split in a similar manner

$$A(s,t,u) = 16\pi \sum_\ell (2\ell+1) f_\ell(s) P_\ell(\cos\theta) \tag{1.183}$$

with

$$f_\ell(s) = M_\ell(s) + K_\ell(s)\,. \tag{1.184}$$

Along the right-hand cut the partial-wave amplitude $f_L(s)$ fulfills the discontinuity equation

$$\mathrm{disc}_R\, f_\ell = 2i t_\ell^* \hat{\sigma} f_\ell\,, \tag{1.185}$$

where t_ℓ is the partial-wave meson-meson scattering amplitude as introduced in the previous section with the right-hand cut discontinuity

$$\mathrm{disc}_R\, t_\ell = 2i\, t_\ell^\star \hat{\sigma} t_\ell\,. \tag{1.186}$$

Furthermore assume that M_ℓ is free of left-hand cuts and all of those shall be explained through K_ℓ, which will be called **inhomogeneity** in the following. Using the Omnès matrix Ω_ℓ defined by the unitarity equation

$$\mathrm{disc}_R\, \Omega_L(s) = 2i\, t_\ell^\star(s) \hat{\sigma}(s) \Omega_\ell(s) \tag{1.187}$$

one may define

$$\zeta_\ell(s) = \Omega_\ell^{-1}(s) M_\ell(s) = \Omega_\ell^{-1}(s)(f_\ell(s) - K_\ell(s))\,, \tag{1.188}$$

which is an analytic function free of left-hand cuts. Its discontinuity along the right-hand cut is given by

$$\begin{aligned} \mathrm{disc}_R\, \zeta_\ell &= \Omega_\ell^{-1} M_\ell - (\Omega_\ell^{-1})^* M_\ell^* + \left(\Omega_\ell^{-1}\right)^\star M_\ell - \left(\Omega_\ell^{-1}\right)^\star M_\ell \\ &= -(\Omega_\ell^{-1})^* \left(\mathrm{disc}_R\, \Omega_\ell\right) \Omega_\ell^{-1} M_\ell + (\Omega_\ell^{-1})^* \mathrm{disc}_R (f_\ell - K_\ell) \\ &= 2i (\Omega_\ell^{-1})^* t_\ell^* \hat{\sigma} K_\ell - (\Omega_\ell^{-1})^* \mathrm{disc}_R\, K_\ell\,. \end{aligned} \tag{1.189}$$

With the assumption that $\mathrm{disc}_R\, K_\ell = 0$ it reduces to

$$\mathrm{disc}_R\, \zeta_\ell = 2i (\Omega_\ell^{-1})^\star t_\ell^\star \hat{\sigma} K_\ell\,. \tag{1.190}$$

Solving the discontinuity equation of Ω_ℓ and t_ℓ as

$$(\Omega_\ell^{-1})^\star = (1 - 2i t_\ell^\star \hat{\sigma}) \tag{1.191}$$

and

$$t_\ell^\star = (1 - 2it_\ell^\star \hat{\sigma})^{-1} t_\ell \tag{1.192}$$

allows us to rewrite the discontinuity of ζ_ℓ as

$$\mathrm{disc}_R\, \zeta_\ell = 2i\Omega_\ell^{-1} t_\ell \hat{\sigma} K_\ell \,. \tag{1.193}$$

The inhomogeneity K_ℓ may contain additional branch cuts, which will influence the chosen path for the dispersion integral. Assuming for now, that the branch points lie on unphysical Riemann sheets $\zeta_\ell(s)$ can be reconstructed dispersively as

$$\zeta_\ell(s) = P(s) + \frac{s^n}{\pi} \int\limits_{s_0}^{\infty} \frac{\mathrm{d}s'}{(s')^n} (\Omega_\ell^{-1})(s') \frac{t_\ell(s') \hat{\sigma}(s') K_\ell(s')}{s' - s - i\epsilon} \tag{1.194}$$

and thus

$$M_\ell(s) = \Omega(s) \left[P(s) + \frac{s^n}{\pi} \int\limits_{s_0}^{\infty} \frac{\mathrm{d}s'}{(s')^n} (\Omega_\ell^{-1})(s') \frac{t_\ell(s') \hat{\sigma}(s') K_\ell(s')}{s' - s - i\epsilon} \right] . \tag{1.195}$$

Here the subtraction polynomial $P(s)$ of order $n-1$ is a vector in channel space. To fix the subtraction constants additional input from either experiment or theory is needed.

For a single channel the inhomogeneous Omnès problem of Eq. (1.195) reduces to

$$M_\ell(s) = \Omega_\ell(s) \left[P(s) + \frac{s^n}{\pi} \int\limits_{s_0}^{\infty} \frac{\mathrm{d}s'}{(s')^n} \frac{\sin \delta_\ell(s')\, K_\ell(s')}{|\Omega_\ell(s')|\, (s' - s - i\epsilon)} \right] , \tag{1.196}$$

where δ_ℓ is the phase shift of the partial-wave amplitude t_ℓ.

1.4. Hadron spectroscopy

1.4.1. Introduction

In order to obtain a better insight into quantum chromodynamics, it is important to measure the interaction between quarks and gluons. However, since neither of them are directly observable in the experiment due to confinement, a different approach needs to be taken.

Similar to quantum electrodynamics, where information about the underlying theory can be inferred from the atomic spectra, it is possible to understand the strong interaction by observing the hadronic spectra. Therefore the first task is to identify proper hadronic states.

Another complication is that most of the states are short-lived and thus cannot be directly measured in a detector. But due to tremendous effort on the experimental side, it is possible to see the effect of these unknown states X in either production processes

$$I_1 + I_2 \to X + (S) \to F_1 + F_2 + \cdots + F_n + (S) \tag{1.197}$$

with or without a spectator particle S or in decays

$$I \to X + (S) \to F_1 + F_2 + \cdots + F_n + (S)\,. \tag{1.198}$$

While most states show up as bumps in the concerning cross-sections, for a proper understanding, a partial-wave amplitude analysis needs to be done, hence fixing particle properties such as spin, mass, width and transformation properties under internal symmetries. In order to avoid a strong bias, the amplitude should build only on the basic principles of scattering theory, such as unitarity, analyticity, Lorentz invariance and internal symmetries.

Physical states, produced by the dynamics of the underlying theory, show up as poles of the S-matrix. To be more specific, they lie in the complex s-plane of the partial-wave projection S_ℓ. A restriction by causality is that they can only appear on the real s-axis below the lowest threshold. They are called bound states and are stable under the concerned interaction, as dictated by energy conservation. A prime example is the deuteron, which is a proton-neutron bound state.

Also the unstable particles are proper hadronic states and thus must show up as poles of the S-matrix. While the causality restriction applies for the „physical“ complex s-plane, which is also called the first Riemann sheet, it does not apply to the analytic continuation of the S-matrix to unphysical Riemann sheets.

Consider a function $f(s)$, which is analytic in the entire complex s-plane, except for a cut between the branch points s_1 and s_2. For the sake of notation, assume that they lie on the real axis. Then for all $s_1 < s < s_2$ the function $f(s)$ can be smoothly continued to a second complex plane, the so called second Riemann sheet. Using Feynman $+i\epsilon$ prescription it is customary to approach the second Riemann sheet from below

$$\lim_{\epsilon\to 0} f^{II}(s + i\epsilon) = \lim_{\epsilon\to 0} f(s - i\epsilon) \quad \text{for } s_1 < s < s_2\,. \tag{1.199}$$

The analytic continuation is then done by subtracting the discontinuity

$$f^{II}(s + i\epsilon) = f(s + i\epsilon) - \operatorname{disc} f(s) \quad \text{for } s_1 < s < s_2\,. \tag{1.200}$$

Afterward $f^{II}(s)$ can be continued analytically into the entire second Riemann sheet. As it also has discontinuities the procedure can be repeated as many times as necessary. Note that since the two sheets are smoothly connected the location of the branch cut is arbitrary, while the branch points are fixed.

As an example consider the partial-wave amplitude $t_\ell(s)$ with a single channel consisting of two particles with mass m. Its discontinuity for $s > 4m^2$ is given by

$$\operatorname{disc} t_\ell(s) = \lim_{\epsilon\to 0} 2i\, t_\ell^\star(s + i\epsilon)\, \sigma(s + i\epsilon) t_\ell(s + i\epsilon)\,, \tag{1.201}$$

where

$$\sigma(s) = \sqrt{1 - \frac{4m^2}{s}}\,. \tag{1.202}$$

Its analytic continuation on the second Riemann sheet reads

$$t_\ell^{II}(s) = t_\ell(s) - 2i\, t_\ell^*(s + i\epsilon)\sigma(s + i\epsilon) t_\ell(s + i\epsilon)\,. \tag{1.203}$$

Using the Schwarz reflection principle and the smooth connection between first and second sheet above $s = 4m^2$

$$t_\ell(s - i\epsilon) = t_\ell^\star(s + i\epsilon) = t^{II}(s + i\epsilon) \tag{1.204}$$

leads to

$$t_\ell^{II}(s + i\epsilon) = [1 + 2i\, t_\ell(s + i\epsilon)\sigma(s + i\epsilon)]^{-1}\, t_\ell(s + i\epsilon)\,. \tag{1.205}$$

With a natural analytic continuation in s the final result reads

$$t_\ell^{II}(s) = [1 + 2it_\ell(s)\sigma(s)]^{-1}\, t_\ell(s) \tag{1.206}$$

where $\sigma(s)$ for complex s is defined as

$$\sigma(s) = \sqrt{\left|1 - \frac{4m^2}{s}\right|}\, \exp\left(\frac{i}{2} \arg\left(1 - \frac{4m^2}{s}\right)\right)\,. \tag{1.207}$$

Hence

$$\lim_{\epsilon \to 0} \sigma(s - i\epsilon) = -\sigma(s) \quad \text{for } s \in \mathbb{R} \text{ and } s > 4m^2\,. \tag{1.208}$$

The discontinuity of $t_\ell^{II}(s)$ for $s > 4m^2$ is

$$\operatorname{disc} t_\ell^{II}(s) = -2it_\ell^\star(s + i\epsilon)\sigma(s + i\epsilon)t_\ell(s + i\epsilon)\,. \tag{1.209}$$

Therefore analytically continuing $t_\ell^{II}(s)$ onto the next Riemann sheet leads to

$$t_\ell^{III}(s) = t_\ell^{II} + 2i\, t_\ell^*(s + i\epsilon)\sigma(s + i\epsilon)t_\ell(s + i\epsilon) = t_\ell(s)\,. \tag{1.210}$$

For this reason a partial-wave amplitude considering only two-particle intermediate states has only two Riemann sheets.

Poles show up at zeroes of the single-channel S-matrix

$$S_\ell(s) = 1 + 2it_\ell(s)\sigma(s)\,. \tag{1.211}$$

They are categorized as **virtual states**, if the pole lies on the real axis of the second Riemann sheet, or **resonances** which appear at complex s. While virtual states very close to threshold strongly influence threshold parameters, such as the scattering length for nucleon-nucleon scattering with isospin 1 and spin 0, resonances show up mostly as bumps in the cross-section. An example of such a resonance is shown in Fig. 1.4.

For a problem with N two-particle channels the formalism can be generalized, such that for each additional open channel the number of Riemann sheets doubles. The analytic continuation to the n^{th} sheet with $n = 2, 3, \ldots, 2^N$ is given by

$$\left(t_\ell^{(n)}(s)\right)_{ij} = \sum_{k=1}^{N} \left[1 + t_\ell(s)\sigma^{(n)}(s)\right]^{-1}_{ik} (t_\ell(s))_{kj}\,, \tag{1.212}$$

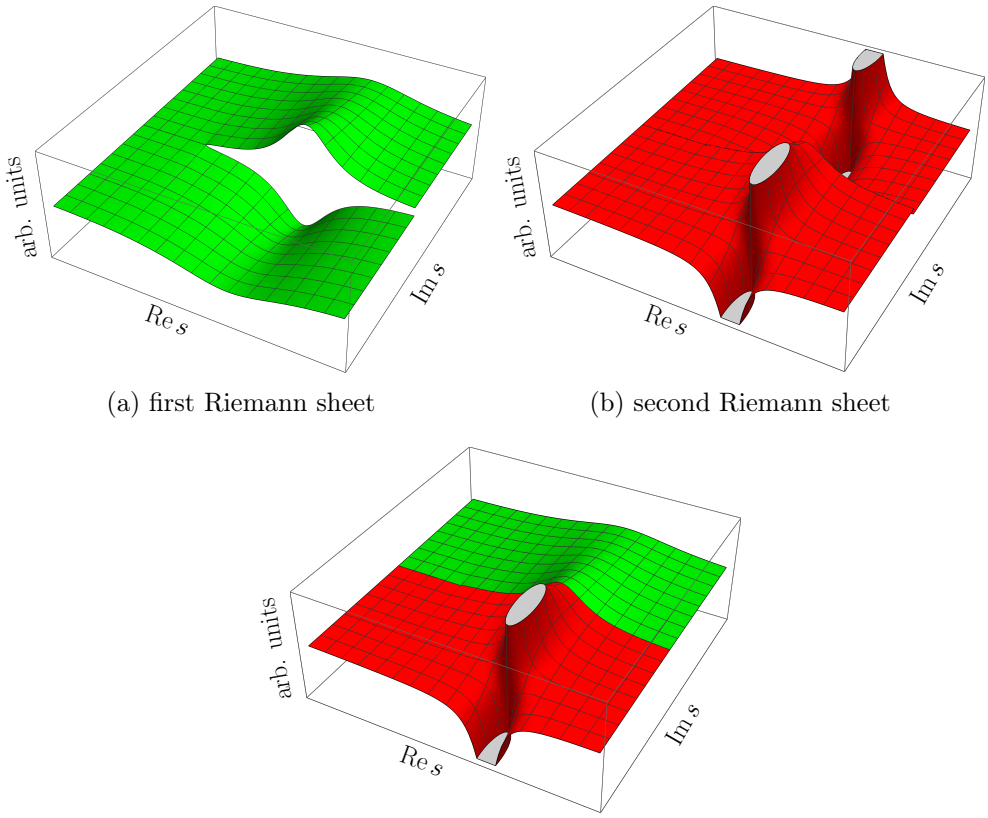

(a) first Riemann sheet

(b) second Riemann sheet

(c) transition from first to second Riemann sheet

Figure 1.4.: Exemplary scattering amplitude on the first Riemann sheet (green) with one pole on the second sheet (red).

where $\sigma^{(n)}(s)$ are $2^N - 1$ different matrices in channel space containing all combinations of corresponding phase space factors $\sigma_k(s)$ on its diagonal. As an example the two-channel problem with $\pi\pi$ and $K\bar{K}$ the matrices are given as

$$\sigma^{(2)}(s) = \begin{pmatrix} \sigma_{\pi\pi}(s) & 0 \\ 0 & 0 \end{pmatrix} \quad , \quad \sigma^{3}(s) = \begin{pmatrix} 0 & 0 \\ 0 & \sigma_{K\bar{K}}(s) \end{pmatrix} \tag{1.213}$$

and

$$\sigma^{4}(s) = \begin{pmatrix} \sigma_{\pi\pi}(s) & 0 \\ 0 & \sigma_{K\bar{K}}(s) \end{pmatrix} . \tag{1.214}$$

The same procedure can also be applied for a form factor $F(s)$ with the discontinuity

$$\operatorname{disc} F^i(s) = 2i \sum_{k=1}^{N} \left(t_\ell^{ik}(s) \right)^\star \sigma_k(s)\, F^k(s) . \tag{1.215}$$

Its analytic continuation on different Riemann sheets is defined by

$$\left(F^{(n)}(s) \right)^i = \sum_{k=1}^{N} \left[1 + 2i t_\ell(s) \sigma^{(n)}(s) \right]^{-1}_{ik} F^k(s) . \tag{1.216}$$

This illustrates, that the pole positions of $t_\ell^{(n)}(s)$ and $F^{(n)}(s)$ are the same, which allows one to postulate, that the pole positions are indeed universal and the same for every process.

In order to establish a particle, it is not enough to search for bumps in the cross-section, as also other kinematics, such as threshold cusps and triangle singularities, can produce similar effects [103]. A proper parametrization of the amplitude, consistent with analyticity, unitarity and crossing, that allows for the pole extraction is necessary.

1.4.2. QCD bound states

The conventional quark model [104, 105] is based on the assumption that a meson is described by a quark-antiquark system and baryons by three quarks in a color singlet. For a short introduction, we refer to the „Quark model“ review by the Particle Data Group [14]. The lightest mesonic states have the J^{PC} quantum numbers 0^{-+}, 1^{--}, 0^{++}, 1^{++}, 1^{+-} and 2^{++}. Considering also an $SU(3)$ flavor symmetry, they will show up as an octet and a singlet.

For baryons the group theory is a bit more complicated. The baryon wave function

$$|qqq\rangle = |\text{color}\rangle \otimes |\text{space}\rangle \otimes |\text{spin}\rangle \otimes |\text{flavor}\rangle \tag{1.217}$$

consists of a color, space, spin and flavor wave function. To fulfill the Fermi statistics it needs to be fully antisymmetric under the exchange of two quarks. As the color wave function always needs to be in an antisymmetric singlet the rest needs to symmetric. The spin wave function on the other hand can be decomposed into the subspaces

$$2 \otimes 2 \otimes 2 = (2)_M \oplus (2)_M \oplus (4)_S\,, \tag{1.218}$$

where M denotes mixed symmetry and S fully symmetric. Assuming SU(3) flavor symmetry the flavor wave function can be decomposed into

$$3 \otimes 3 \otimes 3 = (10)_S \otimes (8)_M \otimes (8)_M \otimes (1)_A\,. \tag{1.219}$$

By using Jacobi coordinates it is possible to identify the space wave function as a representation of SO(3) spacial symmetry, thus denoting it by an angular momentum L. For $L = 0$ this leads to the baryon octet with $J^P = \left(\frac{1}{2}\right)^+$ and the baryon decouplet with $J^P \left(\frac{3}{2}\right)^+$. Angular excitations can be calculated accordingly.

Any observed state that does not have the quantum numbers allowed by the quark model can safely be considered exotic. Examples are e.g. the $\pi_1(1400)$ and $\pi_1(1600)$ with $J^{PC} = 1^{-+}$ [106, 107, 108].

However, even with the allowed quantum numbers, there are states which do not agree with the quark model spectrum, given in e.g. the „Quark model“ review of the PDG [14], such as the baryon states $P_c^+(4380)$ and $P_c^+(4450)$ [109] or the $\Lambda(1405)$ [110]. We will give further mesonic examples in the next sections.

There are many different interpretations of these exotic hadrons. As already predicted by Gell-Mann [104], group theory allows color singlet states consisting

of more than three quarks or one quark and one antiquark. The simplest extensions of the quark model are tetraquarks, containing four quarks, for mesons or pentaquarks, containing five quarks, for baryons. However, also a bound state consisting only of gluons, the so-called glueball, has been predicted. On the other hand, hybrid states are bound states of quarks and gluons, where the latter also contribute to the hadron quantum numbers.

Another kind of state, which we want to advocate is a hadronic molecule. For an extensive review, we refer to Ref. [111]. The first proof for the existence of hadronic molecules was done by Weinberg [112]. The nowadays known Weinberg criterion was used to show that deuteron is not a compact quark state but consists of a neutron-proton bound state. By construction, it only considered a two-particle channel as well as one compact core. The criterion then allows one to relate the probability of finding a compact component in a physical state to its coupling constant to the continuum. However, the derivation is only applicable to shallow S-wave bound states with narrow constituents [113, 114] and therefore cannot be applied to resonances. Further generalizations of the criterion have already been considered [115].

Another approach is to count the number of corresponding poles. This pole-counting approach [116] says that a compact bound state has two near-threshold singularities. One of them lies on the first Riemann sheet, the other on the second. On the other hand, the molecular state only produces one pole close the threshold on the first Riemann sheet. The correspondence of the two approaches was first observed in Ref. [115].

This shows again the strength of a fully analytical approach. If it is possible to relate the amplitudes to QCD via e.g. an effective field theory, it is possible to track the pole trajectories as fundamental parameters such as the number of colors or quark masses get changed. For example in Ref. [117] a single channel S-matrix with two particles of mass m and two poles on the second Riemann sheet at

$$s_{1/2} = 4\left(k_p^2 + \xi(k_p)^2 + m^2 \pm i\sqrt{s-4m^2}\xi(k_p)\right) \tag{1.220}$$

has been considered. A given partial-wave L the width $\xi(k_p)$ contains a centrifugal barrier term

$$\xi(k_p) = \xi_0 k_p^{2L}\,. \tag{1.221}$$

They observed that for $L > 0$ the poles meet upon a continuation in k_p at threshold $s_{1/2} = s_{1/2}(k_p = 0) = 4m^2$. Decreasing k_p further lets one pole move through the unitarity cut to the first Riemann sheet, while the other stays on the second sheet. One of them will move on the positive s-axis and the other on the negative one. Therefore two near-threshold poles emerge. For $L = 0$ resonances, the position, where both poles meet, is not fixed but depends on the parameters k_p and ξ. Hence they can meet below the threshold, such that the pole on the first sheet will be close to threshold, while the other moves far away. In the context of the pole counting approach, this corresponds to a molecular state. The parameters ξ and k_p can be related to physical threshold parameters such as the scattering length and effective range.

For isolated near-threshold resonances the lineshape depends strongly on the nature of the resonance. A proper non-relativistic parameterization of the scat-

tering amplitude is given by

$$T(E) = \frac{g^2}{E - E_r + \frac{g^2}{2}(ik(E) + \gamma) + i\Gamma_0/2} \tag{1.222}$$

with the non-relativistic hadron momentum $k = \sqrt{2\mu E}$ and the generalized binding moment E_r. Inelastic effects due to other channels are all absorbed in the constant Γ_0. As already mentioned previously the coupling constant between physical state and vacuum g can be related to the possibility of a compact state. For a molecular state g^2 becomes very large, thus the line shape is asymmetric in E around $E = 0$ MeV. For a predominantly compact state g^2 is small, hence the amplitude will be symmetric.

The symmetries of QCD will translate to those of the QCD bound states. Therefore depending on the binding mechanism, it is possible to predict symmetry partners. This is especially useful for heavy mesons since heavy spin symmetry predicts in some cases that, when two heavy mesons form a molecule, also their spin partners need to do the same. If for example a molecular state is seen in $B\bar{B}^\star$ scattering, then there must also exist one in $B^\star\bar{B}^\star$ scattering.

1.4.3. Light meson spectroscopy

While the vector and tensor mesons at low energies have been widely observed and understood, the scalar mesons below 2 GeV show a rich spectrum with many unanswered questions. For an extensive review, we refer to the „Note on Scalar Mesons below 2 GeV“ and the „Non-$q\bar{q}$ Mesons“ by the Particle Data Group and references therein [14].

Although the isospin 1/2 and 1 channels show interesting features as well, we here will restrict ourselves to the scalar isoscalar channel. It is in particular interesting, because according to lattice calculations it should contain the glueball ground state [118, 119, 120, 121] between 1.6 and 1.7 GeV. It is important to note that these results are obtained by quenched Lattice QCD, such that the fermion determinant is set to a constant.

The problem is that the spectrum contains broad states that overlap with each other and are close to several thresholds that open up in a range over several hundred MeV.

The lowest state called $f_0(500)$ or σ for example is a very broad resonance. Furthermore the related peak position in a production rate is very reliant on the production mechanism. Hence the pole parameters extracted from data are very uncertain

$$\sqrt{s^\sigma_{\text{Pole}}} = ((400 - 550) - i\,(200 - 350))\ \text{MeV}\,. \tag{1.223}$$

As described by Refs. [92, 122] a Breit-Wigner parametrization for it is inappropriate. Since the pole position is also dependent on the left-hand cut a dispersive Roy-Steiner analysis for $\pi\pi$ scattering is the most precise [123, 124]. Averaging only the dispersive results [125, 126, 127] gives the very precise value [128]

$$\sqrt{s^\sigma_{\text{Pole}}} = \left(449^{+22}_{-16} - i\,(275 \pm 12)\right)\ \text{MeV}\,. \tag{1.224}$$

The σ-meson is not only considered exotic due to its large width, but also its non-$q\bar{q}$-like behavior in a large N_c expansion [129] as well as its deviation from the assumed Regge trajectory [130]. The most widely accepted interpretation is that it owes its existence to non-perturbative $\pi\pi$ interactions, but a definitive interpretation is still yet unclear [128, 131].

The next scalar resonance is the $f_0(980)$ with a pole at [126]

$$\sqrt{s_{\text{Pole}}^{f_0(980)}} = \left((996 \pm 7) - i(25^{+10}_{-6})\right) \text{ MeV}\,. \tag{1.225}$$

Due to its closeness to the $K\bar{K}$ the cusp effect needs to be taken into account. For this a standard Flatté parametrization is appropriate. However due to the overlap with the tail of the $f_0(500)$ a pure parametrization involving Breit-Wigner and Flatté would break unitarity. This is also one of the last states pure dispersion theory is able to describe, as further inelasticities need to be taken into account above this point. Its nature is still inconclusive as it can be described in the tetraquark picture [132, 133, 134, 135, 136] but also as a $K\bar{K}$ molecule [137].

The resonances $f_0(1370)$ and $f_0(1500)$ are shown to have strong contributions from the 4π decay mode [138, 139, 140]. Due to the large overlap between the two, a mass extraction is difficult. The last heavy scalar state below 2 GeV is the $f_0(1710)$, which mostly decays into $K\bar{K}$. While it is indicated [141, 142] that the $f_0(1370)$ is a non-strange quark model state, the $f_0(1710)$ a strange quark model state and the $f_0(1500)$ might be dominantly a glueball, further investigations are necessary. For a broader discussion of these three states, we refer to the „Non-$q\bar{q}$ Mesons“ as well as „Scalar Mesons below 2 GeV“ minireviews of the Particle Data Group [14] and the references therein.

1.4.4. Heavy meson spectroscopy

Experiments involving heavy quarks such as the charm or bottom quark are fascinating as they show a rich spectrum. Interestingly new exotic states show up above open flavor threshold, while below it is consistent with the conventional quark model. Advantageous for the study of those states is that most of the resonances are well separated from each other. However, various of them are measured in three-particle decays. Since the phase space is large, many crossed-channel resonances need to be taken into account. A thorough theoretical framework is necessary to describe the interference between the resonances in the different channels correctly. As always, it should be consistent with unitarity and analyticity to provide reasonable pole positions. The reviews used for this summary are Ref. [111] as well as the Particle Data Group reviews [14] about „Non-$q\bar{q}$ Mesons“ and „Spectroscopy of Mesons Containing Two Heavy Quarks“.

For the heavy-light sector for example the two narrow states $D_{s0}^{\star}(2317)^{\pm}$ and $D_{s1}(2460)^{\pm}$ seem to be exotic, as they are located well below the predicted mass for P-wave $c\bar{s}$ mesons. As they lie close to the DK and $DK^{\star}$ thresholds, they can be interpreted as the corresponding hadronic molecules [143, 144, 145, 146, 147]. But also an interpretation as four-quark states [148, 149, 150, 151] is advocated.

For the doubly heavy system, information about the QCD potential can be inferred, showing a great similarity to the positronium potential at small distances but a linear behavior at larger distances. For a broader discussion about different potential models we refer to Refs. [152, 153]. Interestingly, the B_c and its radial excitations also probe the interaction between different quark flavors.

In particular, in the doubly charmed or double bottom sector, many exotic resonances show up. In the new naming scheme of the Particle Data Group [14], they are named Y for isoscalar $J^{PC} = 1^{--}$ states and X or Z for the isoscalar or isovector states with other quantum numbers.

An example is the $X(3872)$ with the quantum numbers $J^{PC} = 1^{++}$ [154, 155]. It was observed in the $J/\psi\pi\pi$ invariant mass distribution. A particular feature is its closeness to $D\bar{D}^\star$ threshold. However further confirmation for its hadronic molecule [156] or tetraquark structure [150, 157] is still needed. It is also expected that a similar state X_b shows up in the bottominium sector. However, a search in the $\Upsilon(1S)\pi\pi$ invariant mass distribution [158] has not been fruitful. As pointed out in Refs. [159, 160, 161] this decay is suppressed by isospin violation, and hence they suggested better channels for the X_b search.

The vector resonances denoted by Y are directly accessible by e^+e^- annihilations. The first observed state with exotic features was the $Y(4260)$ seen in the $J/\psi\pi^+\pi^-$ invariant mass spectrum of the initial state radiation reaction $e^+e^- \to \gamma_{\rm ISR}\, J\psi\pi^+\pi^-$ [162]. Compared to conventional $c\bar{c}$ states it does not decay into a $D\bar{D}$ pair or give an enhanced contribution to the inclusive cross section $e^+e^- \to$ hadrons. It could be a hybrid charmonium state [163, 164, 165, 165, 166]. But also a $D_1\bar{D}$ molecular picture [167] as well as the tetraquark picture [168] are plausible.

The last states, which are of particular interest for us, are the Z states. The states in the charm sector are called $Z_c(3900)^\pm$ [169] and $Z_c(4020)^\pm$ [170]. They decay predominantly in a $D\bar{D}^\star$ and $D^\star\bar{D}^\star$ pair, respectively and thus contain a charm-anticharm pair. They are exotic in nature, since a quarkonium cannot be charged, hence they need to be in at least a $c\bar{c}q\bar{q}$ configuration. Their analog for the bottom sector are the $Z_b(10610)^{\pm,0}$ and $Z_b(10650)^\pm$ discovered in the reaction $\Upsilon(5S) \to \Upsilon(nS)\pi^+\pi^-$ and $\Upsilon(5S) \to h_b(mP)\pi^+\pi^-$ in the invariant mass spectrum of $\Upsilon(nS)\pi^+$ and $h_b(mP)\pi^+$ with $n = 1, 2, 3$ and $m = 1, 2$[171, 172]. Later it was shown that they predominantly decay into $B\bar{B}^\star$ and $B^\star\bar{B}^\star$ [173]. The rates of the $\Upsilon(nS)$ and $h_b(mP)$ final states are of the same order, indicating a heavy quark spin symmetry violation. This problem can be naturally avoided in a molecular picture. The transition to the $h_b(mP)$ final states is driven solely by the Z_b resonances, but those with $\Upsilon(nS)$ in the final states show additionally strong $\pi\pi$ dynamics. Thus the latter channels call for a proper description of the data the $\pi\pi$ interaction [56, 174]. Due to the closeness to the open charm and bottom thresholds a molecular picture was proposed [175]. But it also appears to be consistent with a tetraquark picture [176]. If the molecular picture is correct it leads to the prediction of spin partners W_{bJ} of the Z_b states [177, 178, 179, 180]. If they were measurable in the decays $\Upsilon(5S) \to W_{bJ}\gamma \to \chi_{bJ}(\eta_b)\pi\gamma$ it would be a strong confirmation of the hadronic molecule picture.

2. A new parametrization for the scalar pion form factors

2.1. Introduction

The scalar isoscalar sector of the QCD spectrum up to 2 GeV has been of high theoretical and experimental interest for many years. One of the main motivations for these investigations is the hunt for glueballs: their lightest representatives are predicted to occur in the mass range between 1600 and 1700 MeV with quantum numbers 0^{++} [118, 119, 120, 121]. The most straightforward way to identify glueball candidates is to count states with and without flavor quantum number and see if there are supernumerary isoscalar states; see, e.g., the minireview on non-$\bar{q}q$ states provided by the Particle Data Group (PDG) [14] or the reviews Refs. [181, 182]. Unfortunately, regardless of the year-long efforts, the scalar isoscalar spectrum is still not fully resolved: e.g. there is still an ongoing debate whether the $f_0(1370)$ exists or not [181]. One problem might be that most analyses of experimental data performed so far are based on fitting sums of Breit–Wigner functions, which can lead to reaction-dependent results. To make further progress, it therefore appears compulsory to employ parametrizations that allow one to extract pole parameters, for those by definition do not depend on the production mechanism. This requires amplitudes that are consistent with the general principles of analyticity and unitarity. In this paper we present a new parametrization for the scalar pion form factors that has these features built in, and in addition maps smoothly onto well constrained low-energy amplitudes.

The two-pion system at low energies is well understood from sophisticated investigations based on dispersion theory—in particular the $\pi\pi$–$K\bar{K}$ phase shifts and inelasticities can be assumed as known from threshold up to an energy of about $s = (1.1\,\text{GeV})^2$ [123, 124, 183, 184, 185, 186]. From this information, quantities like the scalar non-strange and strange form factors for both pions and kaons can be constructed, again employing dispersion theory [91, 98, 100, 187, 188, 189, 190, 191]. The resulting amplitudes, which capture the physics of the $f_0(500)$ (or σ) and the $f_0(980)$, were already applied successfully to analyze various meson decays, see, e.g., Ref. [190]. In particular the non-Breit–Wigner shape of these low-lying resonances [122] is taken care of automatically. However, to also include higher energies in the analysis, where additional inelastic channels become non-negligible and higher resonances need to be included, one is forced to leave the safe grounds of fully model-independent dispersion theory and to employ a model. Ideally this is done in a way that the amplitudes match smoothly onto those constructed rigorously from dispersion relations. Moreover, to allow for an extraction of resonance properties, the extension needs to be performed in a way consistent with analyticity.

A formalism that has all of these features was introduced for the pion vector form factor in Ref. [95]. In that case, the low-energy $\pi\pi$ interaction can safely be treated as a single-channel problem in the full energy range where high-accuracy phase shifts are available, since the two-kaon contribution to the isovector P-wave inelasticity is very small [185, 192].[1] However, this is not true for the isoscalar S-wave, clearly testified by the presence of the $f_0(980)$ basically at the $K\bar{K}$ threshold with a large coupling to this channel [127, 194]. Thus, in order to apply the formalism of Ref. [95] to the scalar isoscalar channel it needs to be generalized. This is the main objective of the present article. As an application we test the amplitudes on data for $\bar{B}_s^0 \to J/\psi\pi\pi/K\bar{K}$ recently measured with high accuracy at LHCb [195, 196], which allows us to extract the strange scalar form factor of pions and kaons up to about 2 GeV and to constrain pole parameters and branching fractions of two of the heavier f_0 resonances in that energy range.

This paper is organized as follows. In Sect. 2.2, we derive the unitary and analytic scalar form factor parametrization to be used. In Sect. 2.3 we illustrate its application in a coupled-channel analysis of the decays $\bar{B}_s^0 \to J/\psi\pi\pi$ and $\bar{B}_s^0 \to J/\psi K\bar{K}$. Specifically, we discuss the stability of our fits under changing assumptions for the parametrization concerning the number of resonances, the degree of certain polynomials, as well as the approximation in the description of the effective four-pion channel. In addition, in Sect. 2.4 we extract pole parameters, in particular for both the $f_0(1500)$ and the $f_0(2020)$, via the method of Padé approximants for the analytic continuation to the unphysical sheets. The paper ends with a summary and an outlook in Sect. 2.5.

2.2. Formalism

The derivation of the form factor parametrization is presented for the strange scalar isoscalar pion (kaon) form factor Γ_π^s (Γ_K^s). These are related to the matrix elements

$$\begin{aligned}\left\langle \pi^+(p_1)\pi^-(p_2)\,|m_s\bar{s}s|\,0\right\rangle &= \frac{2M_K^2 - M_\pi^2}{2}\,\Gamma_\pi^s(s)\,,\\ \left\langle K^+(p_1)K^-(p_2)\,|m_s\bar{s}s|\,0\right\rangle &= \frac{2M_K^2 - M_\pi^2}{2}\,\Gamma_K^s(s)\,,\end{aligned} \tag{2.1}$$

where $s = (p_1 + p_2)^2$. The $\Gamma_i^s(s)$, $i = \pi, K$, defined this way are invariant under the QCD renormalization group. Since the scalar isoscalar $\pi\pi$ system is strongly coupled to the $K\bar{K}$ channel via the $f_0(980)$ resonance, a coupled-channel description becomes inevitable even for energies around $s = 1\,\text{GeV}^2$. In this paper we present a parametrization for the scalar form factors valid at even higher energies. This becomes possible via the explicit inclusion of further inelasticities and resonances. Below 1 GeV the system is strongly constrained by dispersion theory using a coupled-channel treatment of $\pi\pi$ and $K\bar{K}$ [190].

[1] Note that a recent analysis of $N_f = 2$ and $N_f = 2 + 1$ lattice data revealed indications for the necessity to include a $K\bar{K}$ component for the ρ meson in the formalism [193].

At higher energies experimental data indicate that further inelasticities are usually accompanied by resonances. We thus derive a parametrization that allows for resonance exchange at higher energies. Those resonances also act as doorways for the coupling of the system to the additional channels. At the same time we make sure that their presence does not distort the amplitude at lower energies. To be concrete, here we consider in addition to $\pi\pi$ (channel 1) and $K\bar{K}$ (channel 2) an effective 4π channel (channel 3), modeled by either $\rho\rho$ or $\sigma\sigma$. Three-channel models with an effective $\sigma\sigma$ channel have been considered in the literature before [98, 197], while some of the f_0 states between 1.3 and 2 GeV have even been hypothesized to be dynamically generated by attractive interactions between ρ mesons [198, 199, 200, 201]. It should become clear from the derivation, however, that the formalism allows for the inclusion of additional channels in a straightforward manner.

The derivation starts from the scalar isoscalar scattering amplitude $T(s)_{if}$, where i and f denote the initial- and final-state channels. To implement unitarity and analyticity we use the Bethe–Salpeter equation, which reads

$$T_{if} = (V + VGT)_{if} = V_{if} + V_{im} G_{mm} T_{mf} \tag{2.2}$$

in operator form. Here V_{if} denotes the scattering kernel of the initial channel i into the final channel f. The loop operator G is diagonal in channel space and provides the free propagation of the particles of channel m. For example, at the one-loop level the above equation generates an expression of the form

$$\begin{aligned} V_{i1} G_{11} V_{1f} \propto \int \frac{\mathrm{d}^4 k}{(2\pi)^4} V_{i1}(k, \dots) \, \frac{i}{k^2 - M_\pi^2 + i\epsilon} \\ \times \frac{i}{(k-P)^2 - M_\pi^2 + i\epsilon} \, V_{1f}(k, \dots) \end{aligned} \tag{2.3}$$

for $\pi\pi$ rescattering, with P being the total 4-momentum of the system such that $P^2 = s$. For $m = 1$, 2, the discontinuity of the loop operator element G_{mm} reads

$$\operatorname{disc} G_{mm} = 2i\sigma_m \,, \tag{2.4}$$

where $\sigma_m(s) = \sqrt{1 - 4M_m^2/s}$ is the two-body phase space in the given channel, and M_m denotes the pion and kaon masses for channels 1 and 2, respectively. For the third channel, we need to include the finite width of the two intermediate (ρ and σ) mesons; we write

$$\operatorname{disc} G_{33}^k = 2i \int_{4M_\pi^2}^\infty \mathrm{d}m_1^2 \, \mathrm{d}m_2^2 \, \rho_k(m_1^2) \, \rho_k(m_2^2) \, \frac{\lambda^{1/2}(s, m_1^2, m_2^2)}{s} \,, \tag{2.5}$$

where $\lambda(a,b,c) = a^2 + b^2 + c^2 - 2(ab + ac + bc)$ is the Källén function. Here the spectral density for the state k, $\rho_k(m^2)$, is given as

$$\rho_k(q^2) = \frac{1}{\pi} \, \frac{m_k \Gamma_k(q^2)}{(q^2 - m_k^2)^2 + m_k^2 \, \Gamma_k^2(q^2)} \,, \tag{2.6}$$

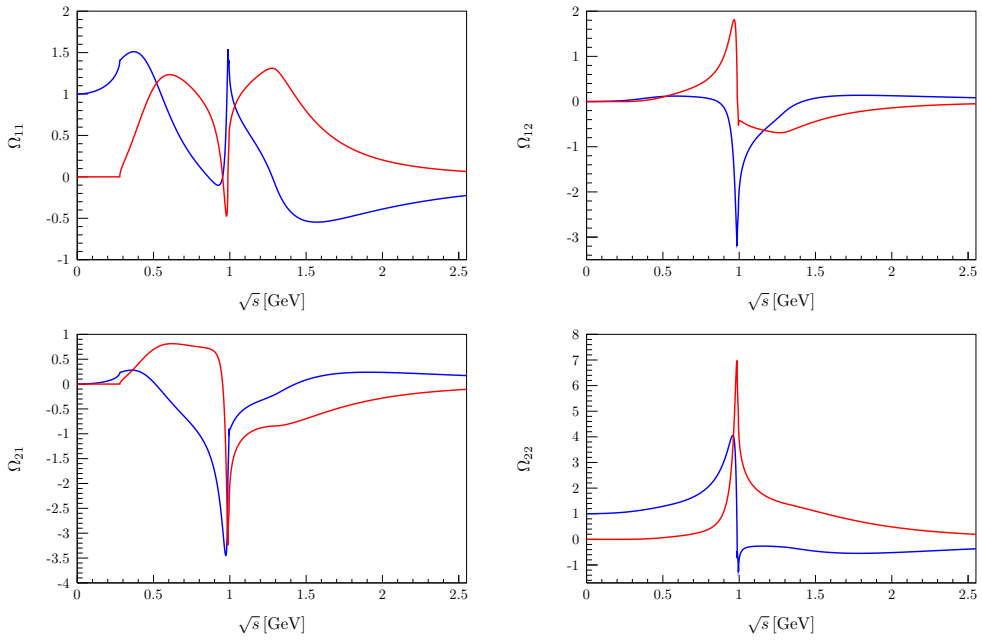

Figure 2.1.: Real (blue) and imaginary (red) parts of the Omnès matrix elements Ω_{11}, Ω_{12}, Ω_{21}, and Ω_{22}.

with the energy-dependent width

$$\begin{aligned} \Gamma_k(s) &= \frac{\Gamma_k\, m_k}{\sqrt{s}} \left(\frac{p_\pi(s)}{p_\pi(m_k^2)}\right)^{2L_k+1} \left(F_R^{(L_k)}(s)\right)^2 , \\ p_\pi(s) &= \frac{\sqrt{s}}{2}\sigma_\pi(s) , \end{aligned} \tag{2.7}$$

where Γ_k (m_k) denotes the nominal width (mass) of the resonance and L_k the angular momentum of the decay with $L_k = 1$ and 0 for the ρ and the σ, respectively. The $F_R^{(L)}(s)$ denote barrier factors that prevent the width from growing continuously. We employ the parametrization of Refs. [202, 203], where their explicit forms for $L = 0$, 1, 2 are given by

$$F_R^{(0)} = 1\,,\ F_R^{(1)} = \sqrt{\frac{1+z_0}{1+z}}\,,\ F_R^{(2)} = \sqrt{\frac{9+3z_0+z_0^2}{9+3z+z^2}}\,, \tag{2.8}$$

with $z = r_R^2\, p_\pi^2(s)$, $z_0 = r_R^2\, p_\pi^2(m_k^2)$, and the hadronic scale $r_R = 1.5\,\text{GeV}^{-1}$. Note that as long as no exclusive data are employed for the 4π final state, the amplitudes are not very sensitive to the details how, e.g., the spectral density of the σ meson is parametrized, since it enters only as the integrand in the self energies of the resonances. However, the analysis is somewhat sensitive to the differences between a $\rho\rho$ and a $\sigma\sigma$ self energy, since the energy dependence of the two is quite different, given the different resonance parameters and the different threshold behavior. We come back to this discussion later in this section.

To proceed with the derivation we split the scattering kernel into two parts, $V = V_0 + V_R$, conceptually following the so-called two-potential formalism [204].

The effect of V_0 will eventually be absorbed into the dispersive piece fixed by the low-energy $\pi\pi$–$K\bar{K}$ T-matrix input. Its explicit form is needed at no point; one may think of it as the driving term of a Bethe–Salpeter equation

$$T_0 = V_0 + V_0\, G\, T_0\,. \tag{2.9}$$

Since T_0 it is the solution of a scattering equation, T_0 is unitary. In particular, we may write

$$T_0 = \begin{pmatrix} \frac{\eta_0 e^{2i\delta_0}-1}{2i\sigma_\pi} & g_0 e^{i\psi_0} & 0 \\ g_0 e^{i\psi_0} & \frac{\eta_0 e^{2i(\psi_0-\delta_0)}-1}{2i\sigma_K} & 0 \\ 0 & 0 & 0 \end{pmatrix}, \tag{2.10}$$

where δ_0 is the scalar isoscalar $\pi\pi$ phase shift, ψ_0 the phase of the $\pi\pi \to K\bar{K}$ scattering amplitude, and g_0 its absolute value. The inelasticity η_0 is related to g_0 via

$$\eta_0 = \sqrt{1 - 4\,(g_0)^2\,\sigma_\pi\,\sigma_K\,\Theta\left(s - 4M_K^2\right)}\,. \tag{2.11}$$

The effects of resonances heavier than the $f_0(980)$ enter the amplitude via V_R. By means of V_R we can construct the resonance T-matrix T_R, related to the full T-matrix via $T = T_R + T_0$. Since T_0 is unitary by itself, T_R cannot be independent of T_0 in order to respect the Bethe–Salpeter equation (2.2). Solving for T_R we obtain

$$(1 - V_0 G - V_R G)\, T_R = V_R\,(1 + G T_0)\ . \tag{2.12}$$

To proceed, we define the vertex function Ω via

$$\Omega = 1 + T_0 G\,. \tag{2.13}$$

Its discontinuity is given by

$$\operatorname{disc}\Omega_{ij} = 2i\ (T_0)^*_{im}\ \sigma_m\,\Omega_{mj}\,, \tag{2.14}$$

which agrees with the discontinuity of the Omnès matrix derived from the scattering T-matrix T_0 [89, 90]. Therefore it can be constructed from dispersion theory:

$$\Omega = \begin{pmatrix} \Omega_{11} & \Omega_{12} & 0 \\ \Omega_{21} & \Omega_{22} & 0 \\ 0 & 0 & 1 \end{pmatrix},\ \Omega_{ij}(s) = \frac{1}{2\pi i}\int_{4M_\pi^2}^{\infty} \mathrm{d}z \frac{\operatorname{disc}\Omega_{ij}(z)}{z - s - i\epsilon}\,. \tag{2.15}$$

Numerical results for $\Omega_{ij}(s)$ based on the T-matrix of Ref. [205] are shown in Fig. 2.1. One observes in particular the signature of the $f_0(500)$ or σ-meson, i.e. the broad bump in the imaginary part of $\Omega_{11}(s)$ below 1 GeV, accompanied by a quick variation of the real part, which clearly cannot be parametrized by a Breit–Wigner form. For an earlier discussion about this fact see Ref. [122].

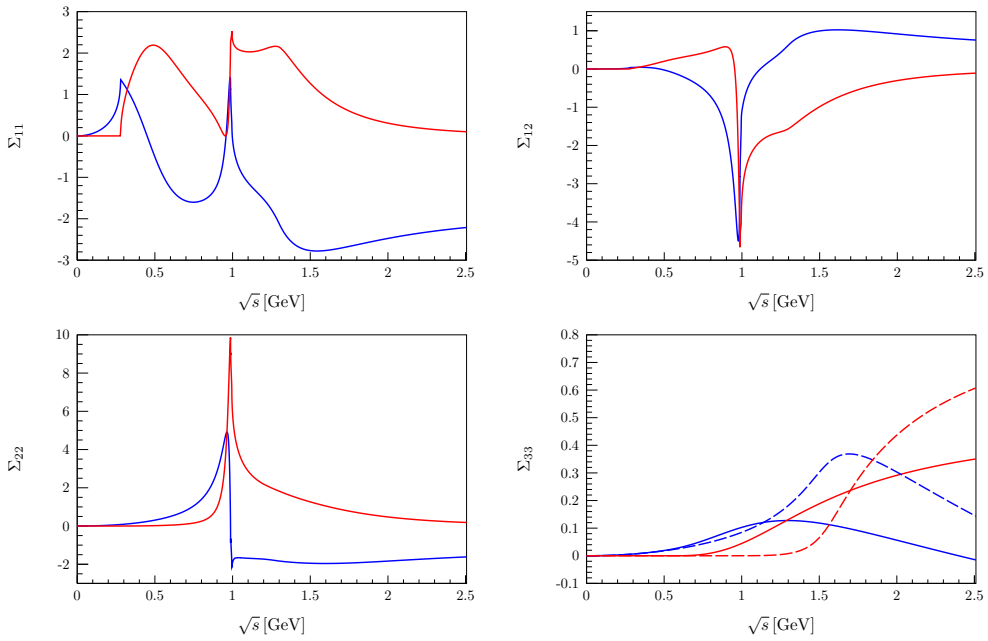

Figure 2.2.: Real (blue) and imaginary (red) parts of the self-energy functions Σ_{11}, $\Sigma_{12} = \Sigma_{21}$, Σ_{22}, and Σ_{33}, using the Omnès matrix displayed in Fig. 2.1. Note that Σ_{33} is a once-subtracted dispersion integral over the four-particle phase space factor taken as a $\sigma\sigma$ (solid) or a $\rho\rho$ (dashed) state.

Using $T_R = \Omega\, t_R\, \Omega^t$ and $V_0 G \Omega = \Omega - 1$, which follows from inserting Eq. (2.9) into Eq. (2.13), one obtains a Bethe–Salpeter equation for t_R,

$$t_R = V_R + V_R\ (G\Omega)\ t_R\,. \tag{2.16}$$

Note that Eq. (2.16) does not depend on V_0 explicitly. It appears only implicitly, since the loop operator G, describing the free propagation of the two-meson states, needs to be replaced by the dressed loop operator $(G\Omega)$, which describes the propagation of the two-meson state in the presence of the interaction T_0, in order to preserve unitarity. The discontinuity of this self-energy matrix $\Sigma = G\Omega$ is given by

$$\operatorname{disc}\Sigma_{ij}(s) = 2i\,\Omega^\dagger_{im}(s)\operatorname{disc} G_{mm}(s)\,\Omega_{mj}(s)\,. \tag{2.17}$$

The discontinuities of the loop functions for the two–body channels and the 4π channel were given in Eqs. (2.4) and (2.5), respectively. Equation (2.17) allows us to write Σ as a once-subtracted dispersion integral,

$$\Sigma_{ij}(s) = \Sigma_{ij}(0) + \frac{s}{\pi}\int \frac{\mathrm{d}z}{z}\frac{\operatorname{disc}\Sigma_{ij}(z)}{z - s - i\epsilon}\,. \tag{2.18}$$

The resulting self-energy functions $\Sigma_{ij}(s)$ are displayed in Fig. 2.2. The subtraction constants can be absorbed in a redefinition of the yet undefined potential V_R. Please observe that the component Σ_{33} looks very different for the two different model assumptions employed. For example, the self energy from $\sigma\sigma$ intermediate states rises very quickly right from the 4π threshold, while the one for $\rho\rho$ sets in significantly later. This difference reflects that the σ decays into two pions in an S-wave, while the ρ decays in a P-wave. On the other hand, since the discontinuity of G_{33} enters in the expression for Σ_{33} only as the integrand, this component of the self energy is not very sensitive to the details of the concrete parametrizations employed for the spectral functions.

The full solution for the scattering matrix is thus given by

$$T = T_0 + \Omega\,[1 - V_R\Sigma]^{-1}\,V_R\Omega^t\,. \tag{2.19}$$

In order to obtain a parametrization for the form factor, we adapt the P-vector formalism [206] to the system at hand. The isoscalar scalar form factor Γ^s_i is written as

$$\Gamma^s_i = M_i + T_{ij}G_{jj}M_j\,, \tag{2.20}$$

where M_i is an analytic term describing the transition from the source to the channel i. Inserting the parametrization of Eq. (2.19) we obtain, after some straightforward algebra,

$$\Gamma^s_i = \Omega_{im}\,[1 - V_R\Sigma]^{-1}_{mn}\,M_n\,. \tag{2.21}$$

As T_0 captures the physics in the $\pi\pi$ and $K\bar{K}$ channels at energies below 1 GeV including the $f_0(500)$, the $f_0(980)$, and the impact of the corresponding left-hand cuts (left-hand cuts in the other channel(s) are neglected by construction), the

potential V_R should predominantly describe the resonances above 1 GeV. In order to reduce their impact at low energies, we subtract V_R at $s = 0$ and arrive at

$$(V_R)_{ij} = \sum_r g_i^r \, \frac{s}{m_r^2 \, (m_r^2 - s)} \, g_j^r \, . \tag{2.22}$$

The bare resonance masses, m_r, as well as the bare resonance–channel coupling constants, g_i^r, are free parameters that need to be determined by a fit to data. The subtraction constants are effectively absorbed into T_0 that by construction captures all physics close to $s = 0$.

The most general ansatz for M reads

$$M_i = c_i + \gamma_i \, s + \cdots - \sum_r g_i^r \, \frac{s}{m_r^2 - s} \, \alpha_r \, , \tag{2.23}$$

where the parameters $c_i = \Gamma_i^s(0)$ provide the normalizations of the different form factors. Here the isospin Clebsch–Gordan coefficients were absorbed into the definition of the form factors. This means explicitly

$$\Gamma_2^s \to \frac{2}{\sqrt{3}} \Gamma_2^s \quad \text{and} \quad M_2 \to \frac{2}{\sqrt{3}} M_2 \, , \tag{2.24}$$

while for the third channel we absorb these factors into the coupling constants. The bare resonance masses and the corresponding couplings g_i^r are the same as before. The parameters α_r, which quantify the resonance–source couplings, and the slope parameters γ_i are additional free parameters.

This completely defines the formalism. Clearly, the number of inelastic channels can be extended in a straightforward way, however, for the concrete application studied in the following section, three channels turn out to be sufficient as long as no exclusive data for additional channels become available.

2.3. Application: $\bar{B}_s^0 \to J/\psi \, \pi^+\pi^-$ and $\bar{B}_s^0 \to J/\psi \, K^+K^-$

2.3.1. Parametrization of the decay amplitudes

As an example, we now apply the formalism introduced in the previous section to the decays $\bar{B}_s^0 \to J/\psi \, \pi^+\pi^-(K^+K^-)$, analyzing data taken by the LHCb collaboration [195, 196]. The dominant tree-level diagram for the corresponding weak transition on the quark level is displayed in Fig. 2.3.

It has been argued previously [190, 207] that the S-wave projection of the appropriate helicity-0 amplitude for $\bar{B}_s^0 \to J/\psi \, M_1 M_2$ transitions are proportional to the corresponding strange scalar form factors of the light dimeson system $M_1 M_2$; in particular, there are chiral symmetry relations between the different dimeson channels that fix the *relative* strengths to be equal to those of the matrix elements in Eq. (2.1) at leading order in a chiral expansion [207]. We conjecture here that the same will still hold true for the inclusion of the effective third (4π) channel. In this sense, the $\bar{B}_s^0$ decays allow to test the pion and kaon strange scalar form factors, up to a common overall normalization.

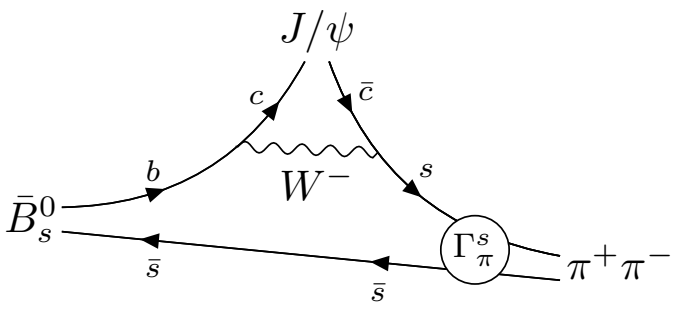

Figure 2.3.: Tree-level W-exchange diagram for the decay process $\bar{B}_s^0 \to J/\psi\,\pi^+\pi^-$. The hadronization of the $\bar{s}s$ quark pair into $\pi^+\pi^-$ (S-wave dominated) is given by the scalar form factor Γ_π^s.

A previous dispersive analysis [190], which considered the $\pi\pi$–$K\bar{K}$ coupled-channel system, worked well in the energy region up to 1.05 GeV. However, due to higher resonances and the onset of additional inelasticities the framework could not be applied beyond this energy. Our new parametrization allows us to overcome this limitation, while it guarantees at the same time a smooth matching onto the amplitudes employed in Ref. [190]. The data are provided in terms of angular moments $Y_L^0(\sqrt{s})$, which are given as angular averages of the differential decay rates

$$\left\langle Y_L^0 \right\rangle = \int \mathrm{d}\cos\Theta\, \frac{\mathrm{d}\Gamma}{\mathrm{d}\sqrt{s}\,\mathrm{d}\cos\Theta}\, Y_L^0(\cos\Theta)\,, \tag{2.25}$$

where Θ is the scattering angle between the momentum of the dipion system in the $\bar{B}_s^0$ rest frame and the momentum of one of the pions. We express the decay amplitude in terms of the partial-wave-expanded helicity amplitudes $\mathcal{H}_\lambda^L$, where L denotes the angular momentum of the pion or kaon pair, and $\lambda = 0, \parallel, \perp$ refers to the helicity of the J/ψ. The angular moments are then given as

$$\left\langle Y_0^0 \right\rangle = \frac{p_\psi p_\pi}{\sqrt{4\pi}} \left\{ \left|\mathcal{H}_0^0\right|^2 + \sum_{\lambda=0,\parallel,\perp} \left(\left|\mathcal{H}_\lambda^1\right|^2 + \left|\mathcal{H}_\lambda^2\right|^2 \right) \right\} \tag{2.26}$$

and

$$\begin{aligned} \left\langle Y_2^0 \right\rangle = \frac{p_\psi p_\pi}{\sqrt{4\pi}} \Bigg\{ & 2\mathrm{Re}\left[\mathcal{H}_0^0 \left(\mathcal{H}_0^2\right)^*\right] \\ & + \frac{1}{\sqrt{5}} \left[2\left|\mathcal{H}_0^1\right|^2 - \left|H_\parallel^1\right|^2 - \left|H_\perp^1\right|^2 \right] \\ & + \frac{\sqrt{5}}{7} \left[2\left|\mathcal{H}_0^2\right|^2 + \left|\mathcal{H}_\parallel^2\right|^2 + \left|\mathcal{H}_\perp^2\right|^2 \right] \Bigg\} \end{aligned} \tag{2.27}$$

for the moments of relevance for this work; see Refs. [190, 207] for details. In addition to the pion momentum in the dipion rest frame p_π introduced earlier, we also use the J/ψ momentum in the $\bar{B}_s^0$ rest frame, $p_\psi = \lambda^{1/2}(s, M_\psi^2, m_B^2)/(2m_B)$.

The scalar helicity amplitude $\mathcal{H}_0^0$ can be related to the scalar isoscalar form factor Γ_i^s as

$$\mathcal{H}_0^0 = \mathcal{N} p_\psi m_B \Gamma_i^s \,, \tag{2.28}$$

where the normalization factor $\mathcal{N}$ absorbs weak coupling constants and the pertinent Wilson coefficients, as well as meson mass factors and decay constants [190, 207]. Here i denotes the relevant channel. For the form factors we use the parametrization introduced in Sect. 2.2. Since the main focus of our analysis lies on the S-waves, we approximate the P- and D-waves as Breit–Wigner functions [208],

$$\begin{aligned}\frac{\mathcal{H}_\lambda^L}{\sqrt{2L+1}} = w_\lambda^L \sum_R h_\lambda^R \, e^{i\phi_\lambda^R} \mathcal{A}_R \\ \times F_B^{(J)} F_R^{(L)} \Big(\frac{p_\psi}{m_B}\Big)^J \Big(\frac{p_\pi}{\sqrt{s}}\Big)^L \,,\end{aligned} \tag{2.29}$$

for $L \geq 1$. The free parameters introduced here are the strength h_λ^R of the resonance R with helicity λ, its phase ϕ_λ^R, and a total rescaling factor w_λ^L for the helicity amplitude $\mathcal{H}_\lambda^L$. The factors $F_B^{(J)}$ and $F_R^{(L)}$ are the Blatt–Weisskopf factors of Eq. (2.8). Two different scales are employed therein: while $F_B^{(J)}$ depends on the argument $z = r_B^2 p_\psi^2$ with $r_B = 5.0\,\mathrm{GeV}^{-1}$, for $F_R^{(L)}$ we use $z = r_R^2 p_\pi^2$ with $r_R = 1.5\,\mathrm{GeV}^{-1}$ as in Eq. (2.8) [203]. The position as well as width of the corresponding resonance is then included in the Breit–Wigner function

$$\mathcal{A}_R(s) = \frac{1}{m_R^2 - s - i m_R \Gamma_R(s)} \tag{2.30}$$

with an energy-dependent width $\Gamma_R(s)$ (2.7). Since the only interference term in the angular moments considered, Eqs. (2.26) and (2.27), is the S-D-wave interference in $\langle Y_2^0 \rangle$, our fits are only sensitive to the relative phase motion of $\mathcal{H}_0^0$ and $\mathcal{H}_0^2$. To reduce the total number of free parameters for all partial-waves except the S-wave, we fix the resonance masses m_R as well as their respective widths to the central values found in Refs. [195, 196]. Furthermore we fix both h_λ^R as well as ϕ_λ^R with $\lambda = \parallel, \perp$ to the central values of the LHCb fits. However, since the phase motion of our S-wave will be different from the one of the LHCb parametrization [190], we allow w_λ^R to vary. For the helicity amplitude $\mathcal{H}_0^2$ we keep both h_0^R as well as ϕ_0^R flexible. To avoid unnecessary parameters we set $w_0^2 = 1$. The number of free parameters is discussed in more detail in Sect. 2.3.2.

2.3.2. Fits to the decay data

In this section we discuss the fit using the form factor parametrization of Eq. (2.21) to the data measured for $\bar{B}_s^0 \to J/\psi\pi^+\pi^-$ [195] and $\bar{B}_s^0 \to J/\psi K^+ K^-$ [196], which are presented as angular moments related to the helicity amplitudes via Eqs. (2.26) and (2.27). Note that these angular moments

have an arbitrary normalization and need to be rescaled to their physical values. The integrated partial width is given by

$$\begin{aligned}\Gamma\left(\bar{B}_s^0 \to J/\psi\,h^+h^-\right) &= \int \mathrm{d}\sqrt{s}\,\mathrm{d}\cos\Theta\,\frac{\mathrm{d}\Gamma}{\mathrm{d}\sqrt{s}\,\mathrm{d}\cos\Theta} \\ &= \sqrt{4\pi}\int \mathrm{d}\sqrt{s}\,\langle Y_0^0\rangle\ . \end{aligned} \tag{2.31}$$

The correctly normalized angular moments, $\langle Y_L^0\rangle_{\mathrm{norm}}$, can be obtained from those published, $\langle Y_L^0\rangle_{\mathrm{LHCb}}$, by

$$\langle Y_L^0\rangle_{\mathrm{norm}} = \frac{\Gamma\left(\bar{B}_s^0 \to J/\psi\,h^+h^-\right)}{\sqrt{4\pi}\int \mathrm{d}\sqrt{s}\,\langle Y_0^0\rangle_{\mathrm{LHCb}}}\,\langle Y_L^0\rangle_{\mathrm{LHCb}}\ . \tag{2.32}$$

We determine the partial decay rates $\Gamma\left(\bar{B}_s^0 \to J/\psi\,h^+h^-\right)$ via the total decay rate $\Gamma_{\bar{B}_s^0} = \tau_{\bar{B}_s^0}^{-1}$ with [14]

$$\tau_{\bar{B}_s^0} = (1.509 \pm 0.004)\,10^{-12}\,\mathrm{s} \tag{2.33}$$

and the branching ratios [14]

$$\begin{aligned}\mathcal{B}\left(\bar{B}_s^0 \to J/\psi\,\pi^+\pi^-\right) &= (2.09 \pm 0.23) \times 10^{-4}\,, \\ \mathcal{B}\left(\bar{B}_s^0 \to J/\psi\,K^+K^-\right) &= (7.9 \pm 0.7) \times 10^{-4}\,. \end{aligned} \tag{2.34}$$

The dispersive approach using the Omnès matrix already captures the physics of the $f_0(500)$ and $f_0(980)$ resonances. In order to extend the description further, we use N_R additional resonances. As outlined above, the S-wave contains in total up to $(N_c + N_s + 1)N_R + 2N_cN_s$ parameters, where N_c (N_s) denotes the number of channels (sources) included; in this study $N_s = 1$, $N_c = 3$, and N_R is either 2 or 3, depending on the fit. The last term in the sum above comes from the non-resonant couplings of the system to the source. The number of those parameters can be reduced from the observation that the normalizations of the pion and the kaon form factors can be fixed to $c_1 = 0$ and $c_2 = 1$ [190]. Since the four-pion channel is expected to couple similarly weakly to an $\bar{s}s$ source as the two-pion one (given OZI suppression at $s = 0$), we also set $c_3 = 0$. Thus the only free parameter from the constant terms in the sources M_i can be absorbed into the overall normalization $\mathcal{N}$ introduced in Eq. (2.28). Below we present fits without ($\gamma_i = 0$, resulting in $5N_R$ parameters) as well as with linear terms in the production vertex defined in Eq. (2.23) ($\gamma_i \neq 0$, providing three more free constants).

For the decay $\bar{B}_s^0 \to J/\psi\,\pi\pi$ the dipion system is in an isoscalar configuration; due to Bose symmetry the pions can therefore only emerge in even partial-waves. Since we restrict ourselves to a precision analysis of the S-wave, we adopt the D-waves of Ref. [195] and accordingly include two resonances, namely $f_2(1270)$ and $f_2'(1525)$. For the 0 polarization we introduce four new parameters given by the amplitude h_0^R and ϕ_0^R, while we fix $w_0^0 = 1$. For the other two helicity amplitudes we constrain h_λ^R and ϕ_λ^R while keeping w_λ^0 variable. This gives another two free parameters. In total we obtain six additional free parameters.

χ^2/ndf	$\sigma\sigma$	$\rho\rho$
Fit 1	$\frac{429.9}{384-30-1} = 1.22$	$\frac{376.2}{384-30-1} = 1.07$
Fit 2	$\frac{413.3}{384-33-1} = 1.18$	$\frac{361.4}{384-33-1} = 1.03$
Fit 3	$\frac{366.9}{384-35-1} = 1.05$	$\frac{335.4}{384-35-1} = 0.96$

Table 2.1.: Reduced χ^2 for the best fits. See main text for details.

Since K^+ and K^- do not belong to the same isospin multiplet, they do not follow the Bose symmetry restrictions. Thus the P-wave in the decay $\bar{B}_s^0 \to J/\psi\, K^+K^-$ is non-negligible and, in fact, dominant. It shows large contributions of the $\phi(1020)$ as well as of the $\phi(1680)$. Since the P-wave does not interfere with S- or D-waves in the angular moments $\langle Y_0^0 \rangle$ and $\langle Y_2^0 \rangle$, we adopt the parameters of LHCb [196]. In order to allow for some flexibility, we also fit w_λ^1, resulting in three parameters. The D-wave includes the resonances $f_2(1270)$, $f_2'(1525)$, $f_2(1750)$, and $f_2(1950)$. For $\lambda = 0$ we fit both h_0^R as well as ϕ_0^R with fixed $w_0^2 = 1$, resulting in eight free parameters. For the other helicity amplitudes we stick to the LHCb parametrization and keep w_λ^2 free, which results in two additional fit parameters. Therefore in total we have 13 additional free parameters for this channel.

All in all we have $5N_R + 20(+3)$ free parameters for $\gamma_i = 0$ ($\gamma_i \neq 0$). Clearly this number is larger than the number of parameters of two single-channel Breit–Wigner analyses, however, the advantage of the approach advocated here is that it allows for a combined analysis of all channels in a way that preserves unitarity, and for a straightforward inclusion of the 4π channel in the analysis. Note that the scalar resonances studied here are known to have prominent decays into four pions [14]; cf. also theoretical approaches modeling some of them as dynamically generated $\rho\rho$ resonances [198, 199, 200, 201].

The LHCb collaboration extracted two additional S-wave resonances from their data [195], namely $f_0(1500)$ and $f_0(1790)$. Since there is no $f_0(1790)$ in the listings of the Review of Particle Physics by the PDG [14], we use the name $f_0(2020)$ for the higher state, in particular since the parameters we extract below are close to those reported for that resonance. The first fit includes our parametrization with $N_R = 2$ and $\gamma_i = 0$ (Fit 1). To test the stability of this solution, we also include a fit with $N_R = 2$ and $\gamma_i \neq 0$ (Fit 2) as well as a fit with $N_R = 3$ and $\gamma_i = 0$ (Fit 3). In order to obtain an estimate of the systematic uncertainty, we repeat each fit with two different assumptions about the third channel, which we take to be dominated by either $\sigma\sigma$ or $\rho\rho$. The respective reduced χ^2 of the best fit results are listed in Table 2.1. We show the corresponding angular moments in Figs. 2.4 ($\rho\rho$) and 2.5 ($\sigma\sigma$). In principle we could have also investigated mixtures of $\sigma\sigma$ and $\rho\rho$ intermediate states or parametrizations representing the channels $\pi(1300)\pi$ or $a_1(1260)\pi$ reported to be relevant for the $f_0(1500)$ [14], however, since with the given choices we already find excellent fits to the data although the corresponding two-point function Σ_{33} look vastly different for the $\sigma\sigma$ and the $\rho\rho$ case (cf. the lower right panel of

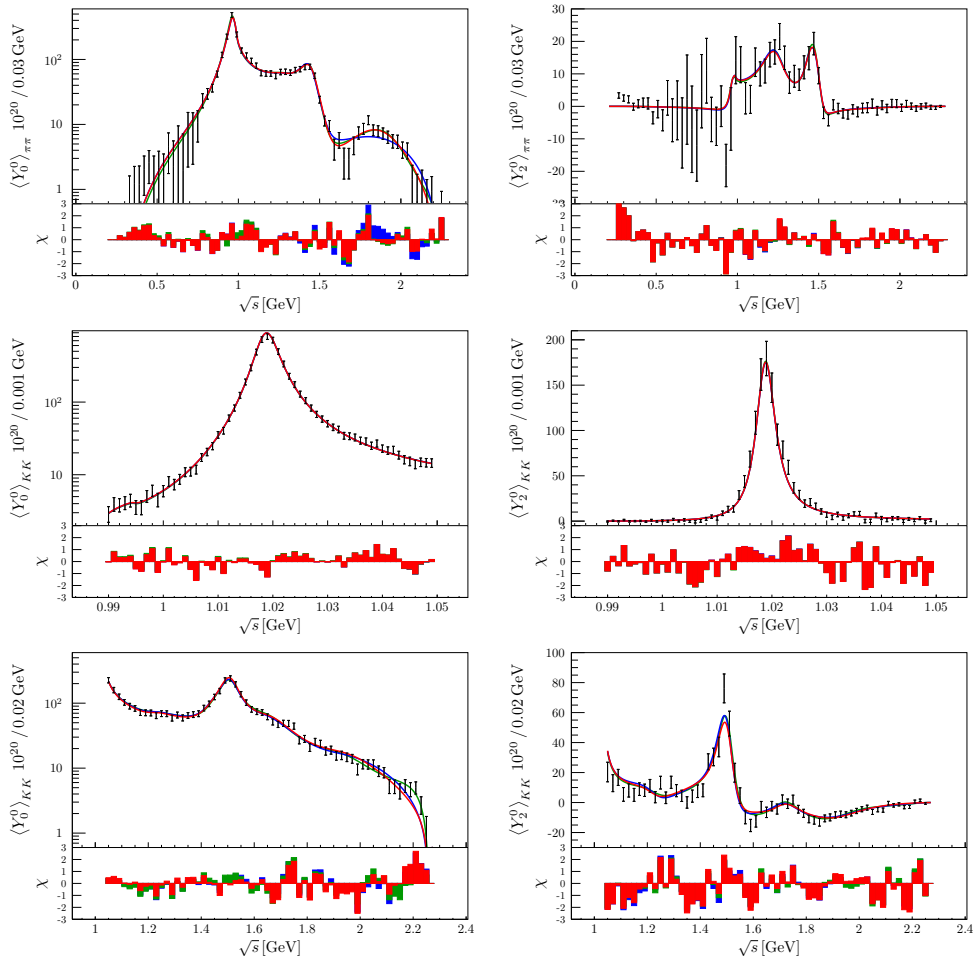

Figure 2.4.: Angular moments $\langle Y_0^0 \rangle$ and $\langle Y_2^0 \rangle$ for the decay $\bar{B}_s^0 \to J/\psi\,\pi^+\pi^-$ (top two) and $\bar{B}_s^0 \to J/\psi\,K^+K^-$ (bottom four) with an effective $\rho\rho$ channel. The picture shows Fit 1 in blue, Fit 2 in red, and Fit 3 in green. On the lower axis we show the fit residuals defined by $\chi = \left(\langle Y_L^0 \rangle_{\text{measured}} - \langle Y_L^0 \rangle_{\text{fit}}\right) / \sigma_{\text{measured}}$.

Fig. 2.2), studying other possible decays will be postponed until data for further exclusive final states become available.

We note first of all that the $\rho\rho$ fits have a lower reduced χ^2 compared to the $\sigma\sigma$ fits. Allowing for a linear term in the source further improves the data description, as witnessed by the differences of Fits 1 and 2. The overall best reduced χ^2 is obtained by including another, third, resonance.

For the $\rho\rho$ fit (see Fig. 2.4) we see that Fit 2 improves the description of $\langle Y_0^0 \rangle_{\pi\pi}$ in the energy region between 1.6 and 2.0 GeV. The biggest change between Fit 3 and the other ones is given by the better description of the high-energy tail in the decay $\bar{B}_s^0 \to J/\psi K^+K^-$.

For the $\sigma\sigma$ fit, Fig. 2.5, we observe a similar picture. Fit 2 provides a very slight overall improvement of Fit 1. However, here the main difference between Fit 3 and the rest resides in the better description of the $f_0(1500)$ especially

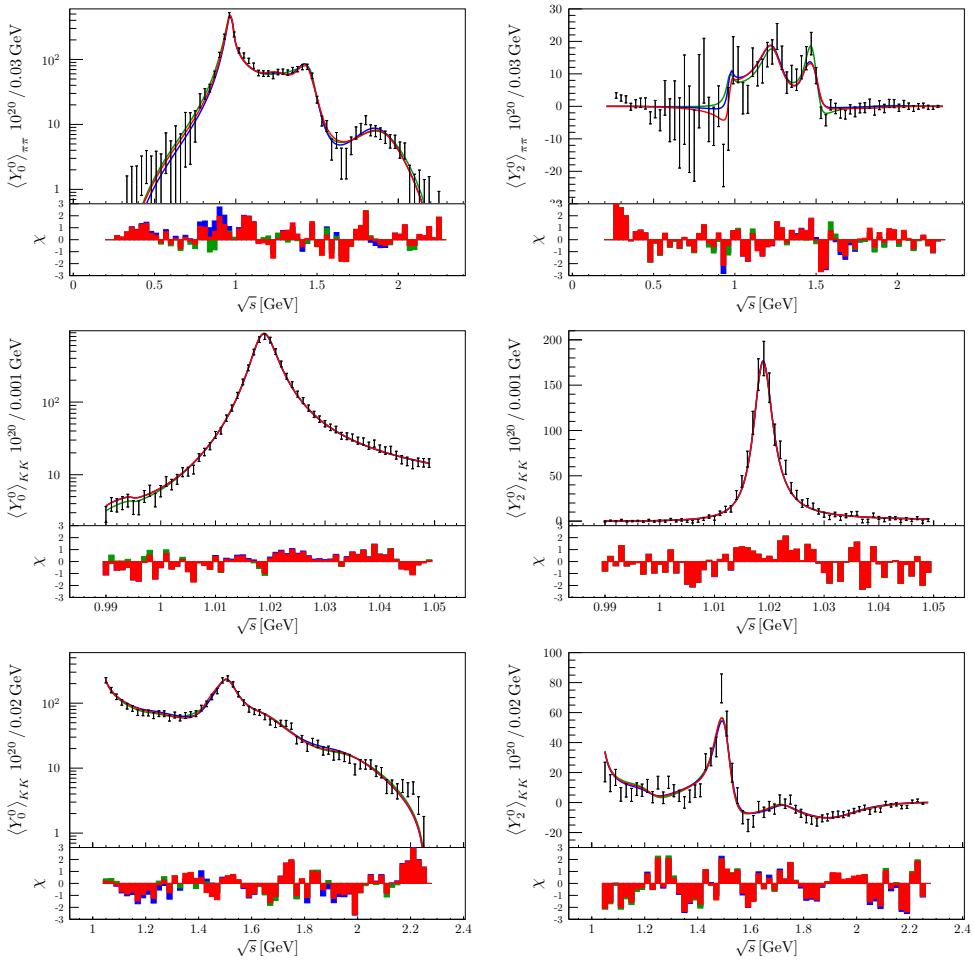

Figure 2.5.: Angular moments $\langle Y_0^0 \rangle$ and $\langle Y_2^0 \rangle$ for the decay $\bar{B}_s^0 \to J/\psi\,\pi^+\pi^-$ (top two) and $\bar{B}_s^0 \to J/\psi\,K^+K^-$ (bottom four) with an effective $\sigma\sigma$ channel. The picture shows Fit 1 in blue, Fit 2 in red, and Fit 3 in green. On the lower axis we show the fit residuals defined by $\chi = \left(\langle Y_L^0 \rangle_{\text{measured}} - \langle Y_L^0 \rangle_{\text{fit}}\right) / \sigma_{\text{measured}}$.

for the decay $\bar{B}_s^0 \to J/\psi\,\pi^+\pi^-$, while the high-energy tail of $\bar{B}_s^0 \to J/\psi\,K^+K^-$ remains nearly untouched.

For a better comparison of the different fits we discuss the resulting form factors Γ_i^s in some detail. We begin by comparing the strange scalar pion form factor Γ_1^s as shown in Fig. 2.6. In all fits three resonances are clearly visible, namely the $f_0(980)$, $f_0(1500)$, and a broad structure around 2 GeV related to the $f_0(2020)$ resonance. Furthermore we also know that the input contains the broad $f_0(500)$ resonance. Fit 3 contains an additional resonance: in the case of the $\rho\rho$ fit, it has its pole around 2.4 GeV and is relatively narrow. Notice that the maximum energy available for the $\pi\pi$ system in the decay studied is 2.27 GeV, thus this additional resonance in fact only contributes with its low-energy tail, giving small corrections for the high-energy parts of the angular moments. This is clearly visible in $\langle Y_0^0 \rangle_{KK}$ at high energies in Fig. 2.4, where Fit 3 can describe

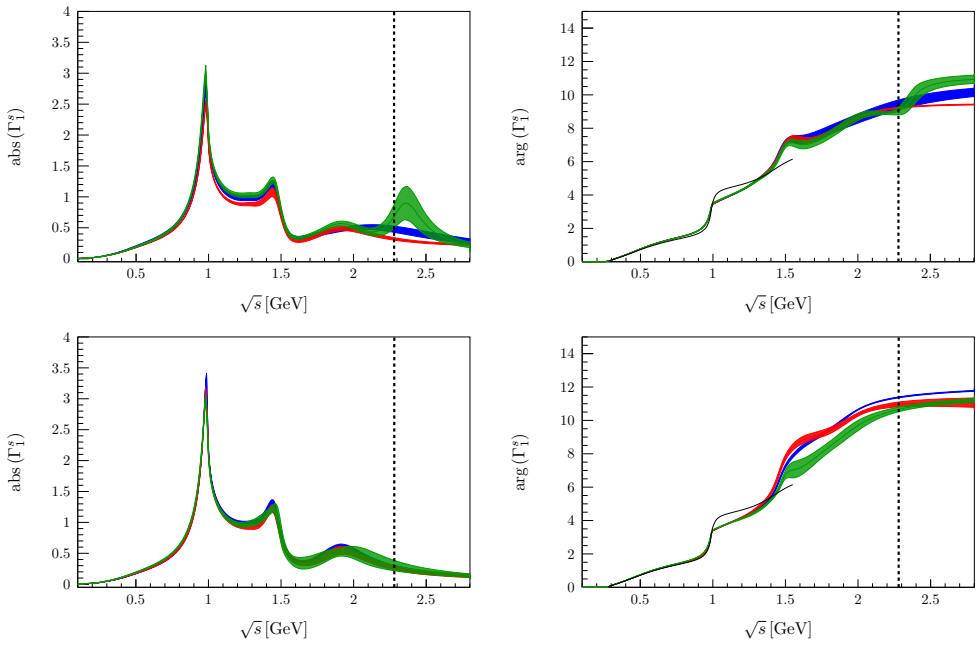

Figure 2.6.: Modulus (left) and phase (right) of the pion form factor Γ_1^s for the fits with an additional $\rho\rho$ (top) and $\sigma\sigma$ (bottom) channel. The input scalar isoscalar scattering phase δ_0 is depicted in black. Fit 1 is shown in blue, Fit 2 in red, and Fit 3 in green. The dotted vertical lines mark the kinematic upper limit for $\sqrt{s}$ in the $\bar{B}_s^0$ decay.

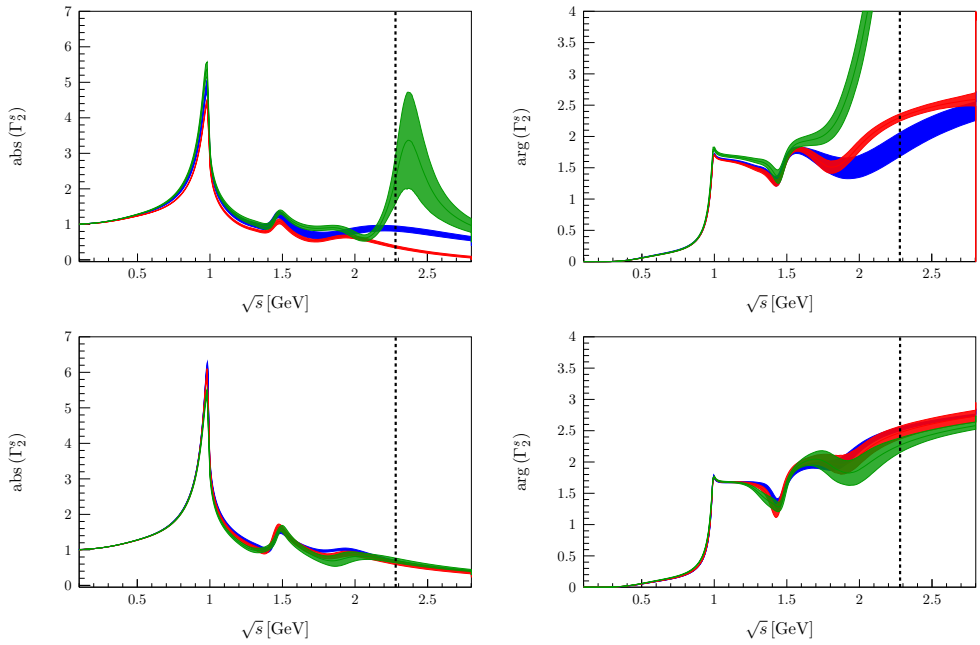

Figure 2.7.: Modulus (left) and phase (right) of the kaon form factor Γ_2^s for the fits with an additional $\rho\rho$ (top) and $\sigma\sigma$ (bottom) channel. Fit 1 is shown in blue, Fit 2 in red, and Fit 3 in green. The dotted vertical lines mark the kinematic upper limit for $\sqrt{s}$ in the $\bar{B}_s^0$ decay.

the last data points better than Fits 1 and 2. In comparison we see that the $\sigma\sigma$ fit lacks any such high-energy resonance. For this fit the difference between Fit 3 and the rest is only visible in the argument of Γ_1^s, showing a shift in the range $1.5 \ldots 2\,\text{GeV}$. This improves the description of $\langle Y_2^0 \rangle_{\pi\pi}$ near the $f_0(1500)$ resonance. From this discussion it becomes clear that the data analyzed here do not allow us to extract information on any further resonance beyond $f_0(500)$, $f_0(980)$, $f_0(1500)$, and $f_0(2020)$.

By comparing the extracted kaon form factors Γ_2^s in Fig. 2.7 we see very similar features as for the pion form factor. However, the $f_0(1500)$ couples more weakly to the $K\bar{K}$ channel than to $\pi\pi$, which is in line with what is reported about this state by the PDG [14]. The impact of the additional resonance in Fit 3 that appears outside the accessible data range is even more pronounced.

In Fig. 2.8 we compare the form factor of the additional, effective 4π, channel Γ_3^s. We see that the results of the fits with the 4π channel parametrized as $\rho\rho$ differ significantly from the ones employing the $\sigma\sigma$ variant. Moreover, also Fits 1–3 differ strongly from each other, even in the kinematic regime that can be reached in $\bar{B}_s^0$ decays. To further constrain these amplitudes it is compulsory to include data on $\bar{B}_s^0 \to J/\psi 4\pi$ in the analysis, which is so far unavailable in partial-wave-decomposed form [209].

Finally in Fig. 2.9 we show the phases, δ, and inelasticities, η, that result for T_{11} in the different fits, where we use the standard parametrization

$$T_{11} = \left(\eta e^{2i\delta} - 1\right) / (2i\sigma_\pi)\,. \tag{2.35}$$

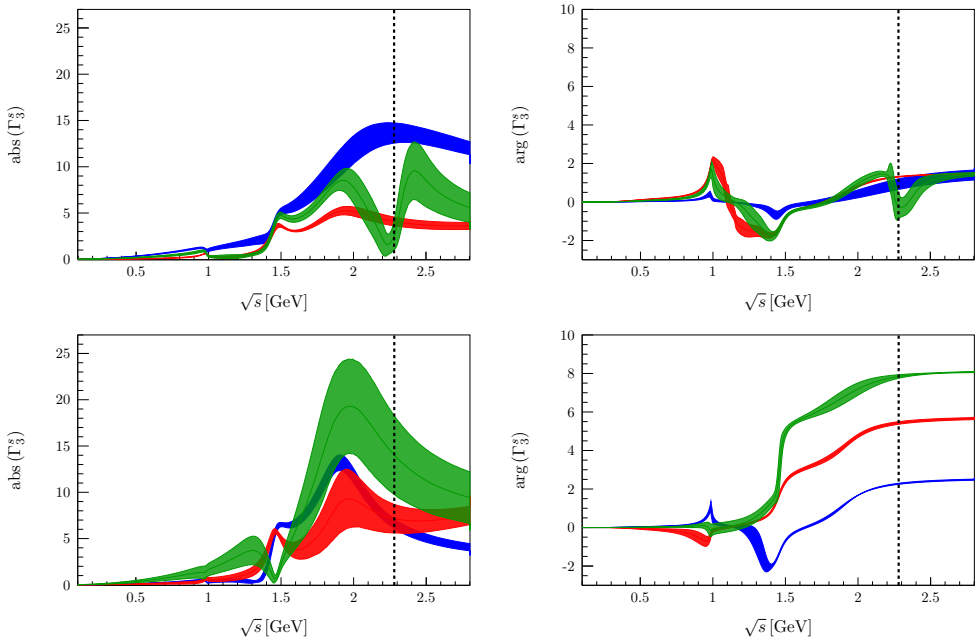

Figure 2.8.: Modulus (left, in arbitrary units) and phase (right) of the effective 4π form factor Γ^s_3 for the fits with an additional $\rho\rho$ (top) and $\sigma\sigma$ (bottom) channel. Fit 1 is shown in blue, Fit 2 in red, and Fit 3 in green. The dotted vertical lines mark the kinematic upper limit for $\sqrt{s}$ in the $\bar{B}^0_s$ decay.

In the figure we also show the two-channel input phase δ_0 and inelasticity η_0 introduced in Eq. (2.10) as black solid lines. The comparison of the different lines demonstrates that the high-energy extension maps smoothly onto the low-energy input, as it should. In the phases one clearly sees the effect of the $f_0(1500)$, which leads to a deviation of the phase of T_{11} from the input phase. In the inelasticity the full model starts to deviate from the input already at about 1.1 GeV as a consequence of the inclusion of the 4π channel. As in the phase the $f_0(1500)$ also leads to a pronounced structure in the inelasticity. It is interesting to observe that neither in the phase nor in the inelasticity there is a clear imprint of the $f_0(2020)$, which can be understood from its small coupling to the two-pion channel.

In Fig. 2.9 we also show a comparison of our phases and inelasticities to those extracted in Ref. [210] (plotted as purple dashed lines) and the preferred solution [182] of the CERN–Munich $\pi\pi$ experiment [211] (data points with error bars). As one can see in the phase shifts, all analyses agree up to about 1.5 GeV. However, the effect of the $f_0(1500)$, present in all analyses, is very different. Also for the inelasticity there is no agreement between our solution and those from the two other sources, but here the deviation starts basically with the onset of the $\bar{K}K$ channel; for a more detailed discussion of the current understanding of the inelasticity in the scalar isoscalar channel, we refer to Ref. [124]. Note that there is also no agreement between the amplitudes of Ref. [182] and Ref. [210]. Thus, at this time one is to conclude that T_{11} above 1.1 GeV is not yet known.

In a similar way, we can also compare the extracted $\pi\pi \to K\bar{K}$ scattering amplitude T_{12} with its absolute value g as well as its phase ψ, which are both shown in Fig. 2.10. While the resonance effects of the $f_0(1500)$ look qualitatively well-described by our high-energy extension, we see some differences to the actual data [212, 213]. Note that the shown results are a prediction based solely on the $\bar{B}_s^0$ decay data and could be improved upon by explicitly taking the phase motion into account in the fit.

2.4. Extraction of resonance poles

In this section we present the extraction of resonance poles in the complex s-plane from the parametrizations discussed above. Traditionally those are given in terms of a mass M and a width Γ, connected to the pole position s_p via [14]

$$\sqrt{s_p} = M - i\frac{\Gamma}{2}\,. \tag{2.36}$$

For narrow resonances located far from relevant thresholds, these parameters agree with the standard Breit–Wigner parameters. However, for broad and/or overlapping states, significant deviations can occur between the parameters derived from the pole location and those from Breit–Wigner fits. Since the analytic continuation to different Riemann sheets needs the on-shell scattering T-matrix as input, which, due to left-hand cuts induced by crossing symmetry, has a complicated analytic structure that cannot be deduced from the phase shifts straightforwardly, we use the framework of Padé approximants to search for the

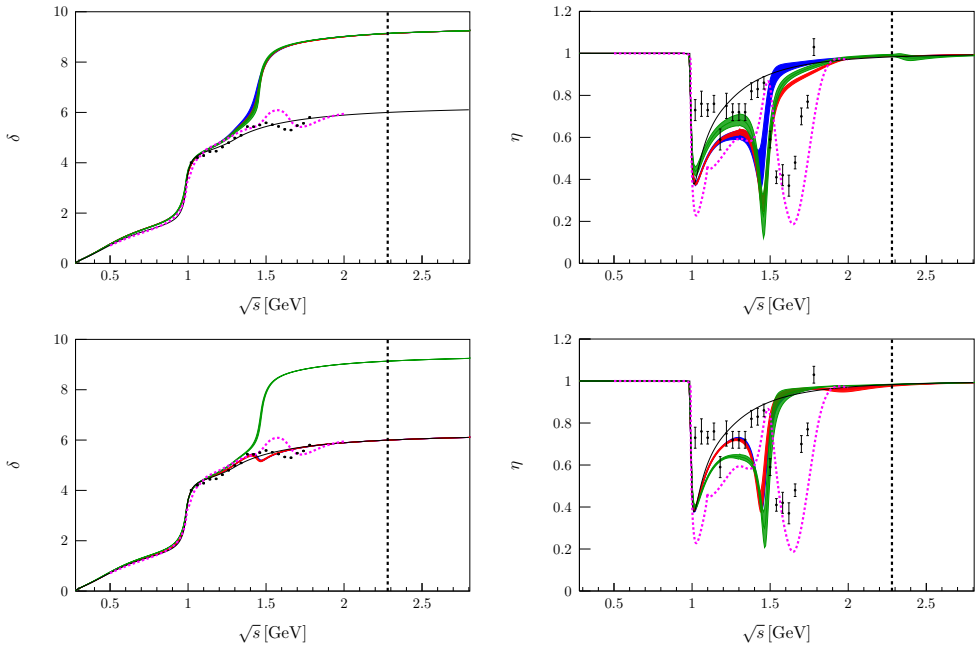

Figure 2.9.: Scalar isoscalar pion–pion scattering phase shift δ (left) and inelasticity η (right) defined by the $\pi\pi$ S-wave amplitude $T_{11} = \left(\eta e^{2i\delta} - 1\right)/(2i\sigma_\pi)$ for the fits with an additional $\rho\rho$ (top) and $\sigma\sigma$ (bottom) channel. Fit 1 is shown in blue, Fit 2 in red, Fit 3 in green, and the input δ_0 and η_0 [205] in black. The purple dashed line shows the K-matrix solution of Ref. [210]. In addition we plot the preferred phase shifts and inelasticities [182] of the CERN–Munich $\pi\pi$ experiment [211], which are denoted by data points with error bars.

poles on the nearest unphysical sheets. For a thorough introduction into this topic, see e.g. Refs. [214, 215, 216].

As the form factor $\Gamma_1^s(s)$ (Fig. 2.6) as well as $T_{11}(s)$ (Fig. 2.9) are smooth functions when moving from the upper complex s-plane of the first Riemann sheet to the lower complex s-plane of the neighboring unphysical sheet, we may expand both around some properly chosen expansion point s_0 according to

$$P_M^N(s, s_0) = \frac{\sum_{n=0}^{N} a_n (s - s_0)^n}{1 + \sum_{m=1}^{M} b_m (s - s_0)^m} \,. \tag{2.37}$$

The denominator allows for the inclusion of M resonance poles lying on the unphysical Riemann sheet. In the following we set M to 1, allowing for the extraction of the resonance that lies closest to the expansion point s_0. The numerator ensures the convergence of the series to the form factor or the scattering matrix for $N \to \infty$. In order to obtain the complex parameters a_n and b_n, we fit Padé approximants to both the form factor and the scattering matrix simultaneously. As both T_{11} and Γ_1^s have the same poles, the parameters b_n are the same for both, however, the a_n are different. Note furthermore that the a_0 parameters are constrained by $\Gamma_1^s(s_0)$ or $T_{11}(s_0)$, respectively.

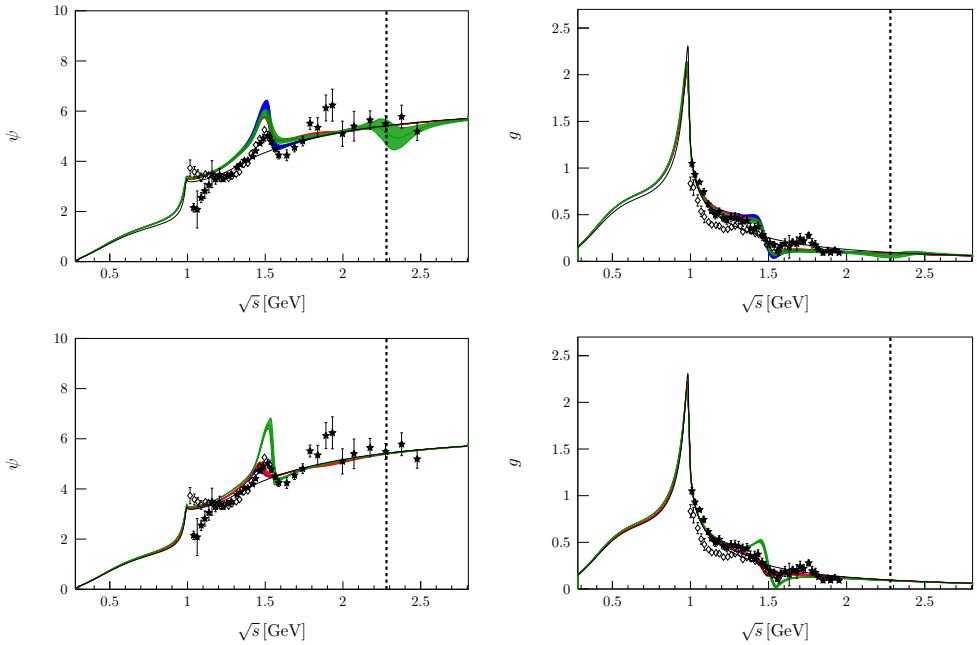

Figure 2.10.: Scalar isoscalar $\pi\pi \to K\bar{K}$ scattering phase shift ψ (left) and absolute value g (right) defined by the S-wave amplitude $T_{12} = g\,e^{i\psi}$ for the fits with an additional $\rho\rho$ (top) and $\sigma\sigma$ (bottom) channel. Fit 1 is shown in blue, Fit 2 in red, Fit 3 in green, and the input g_0 and ψ_0 [205] in black. For comparison we show the amplitude analyses of Refs. [212] (open diamonds) and [213] (filled stars).

For near-threshold poles such as the $f_0(500)$ and $f_0(980)$, we perform the Padé approximation not in s, but in the conformal variable

$$w(s) = \frac{\sqrt{s - 4M_\pi^2} - \sqrt{4M_K^2 - s}}{\sqrt{s - 4M_\pi^2} + \sqrt{4M_K^2 - s}} \tag{2.38}$$

instead [214]. This variable transformation maps the upper half complex s-plane of the first Riemann sheet to the inner upper half of a unit circle in the complex w plane, without introducing any unphysical discontinuities. The lower half of the second Riemann sheet is then mapped onto the lower half of the unit circle in the complex w-plane. This allows us to search for the two lowest poles within a circle around the expansion point s_0, without being limited by the proximity of the $\pi\pi$ and $K\bar{K}$ thresholds, which are automatically taken care of.

The statistical uncertainty is obtained through a bootstrap analysis of the fit results presented in Sect. 2.3.2. The systematic uncertainty coming from the Padé approximation on the other hand is estimated by [215]

$$\Delta^N = \left| \sqrt{s_p^N} - \sqrt{s_p^{N-1}} \right| , \tag{2.39}$$

		Fit	$\frac{\sqrt{s_0}}{\text{GeV}}$	$\text{Re}\sqrt{s_p}$/MeV	$-2\times\text{Im}\sqrt{s_p}$/MeV	$\lvert r_T\rvert/\text{GeV}^2$	$\arg(r_T)$	$\lvert r_\Gamma\rvert/\text{GeV}^2$	$\arg(r_\Gamma)$
$f_0(500)$	$\rho\rho$	1	0.481	441 ± 1	504 ± 2	0.204 ± 0.002	-145 ± 1	0.0309 ± 0.0028	-160 ± 3
$f_0(500)$	$\sigma\sigma$	1	0.466	440 ± 1	521 ± 1	0.205 ± 0.001	-149 ± 1	0.0254 ± 0.0010	-169 ± 2
$f_0(500)$	$\rho\rho$	2	0.483	441 ± 1	503 ± 1	0.204 ± 0.001	-145 ± 1	0.0275 ± 0.0010	-159 ± 2
$f_0(500)$	$\sigma\sigma$	2	0.486	443 ± 1	521 ± 2	0.205 ± 0.002	-147 ± 1	0.0279 ± 0.0032	-161 ± 4
$f_0(500)$	$\rho\rho$	3	0.481	441 ± 2	505 ± 3	0.202 ± 0.002	-145 ± 2	0.0279 ± 0.0039	-159 ± 4
$f_0(500)$	$\sigma\sigma$	3	0.485	442 ± 1	510 ± 1	0.203 ± 0.001	-146 ± 1	0.0284 ± 0.0023	-161 ± 3
$f_0(980)$	$\rho\rho$	1	0.941	998 ± 2	65 ± 3	0.099 ± 0.006	-164 ± 3	0.258 ± 0.016	107 ± 4
$f_0(980)$	$\sigma\sigma$	1	0.941	998 ± 1	48 ± 2	0.082 ± 0.007	-164 ± 5	0.258 ± 0.019	109 ± 5
$f_0(980)$	$\rho\rho$	2	0.941	1001 ± 2	65 ± 3	0.114 ± 0.011	-160 ± 6	0.270 ± 0.020	109 ± 5
$f_0(980)$	$\sigma\sigma$	2	0.941	998 ± 1	50 ± 2	0.082 ± 0.006	-166 ± 5	0.249 ± 0.014	108 ± 4
$f_0(980)$	$\rho\rho$	3	0.941	993 ± 3	65 ± 3	0.094 ± 0.005	-168 ± 3	0.261 ± 0.012	103 ± 3
$f_0(980)$	$\sigma\sigma$	3	0.941	998 ± 2	60 ± 2	0.099 ± 0.007	-163 ± 5	0.281 ± 0.016	109 ± 4
$f_0(1500)$	$\rho\rho$	1	1.459	1460 ± 6	109 ± 7	0.131 ± 0.017	-82 ± 3	0.18 ± 0.03	-53 ± 5
$f_0(1500)$	$\sigma\sigma$	1	1.449	1456 ± 4	107 ± 8	0.047 ± 0.005	-86 ± 3	0.23 ± 0.02	-74 ± 4
$f_0(1500)$	$\rho\rho$	2	1.517	1465 ± 4	116 ± 4	0.115 ± 0.007	-86 ± 2	0.18 ± 0.02	-50 ± 2
$f_0(1500)$	$\sigma\sigma$	2	1.449	1452 ± 5	103 ± 8	0.045 ± 0.005	-82 ± 6	0.23 ± 0.02	-54 ± 6
$f_0(1500)$	$\rho\rho$	3	1.466	1465 ± 5	105 ± 7	0.097 ± 0.018	-87 ± 3	0.18 ± 0.03	-57 ± 4
$f_0(1500)$	$\sigma\sigma$	3	1.476	1477 ± 6	90 ± 9	0.097 ± 0.010	-86 ± 7	0.12 ± 0.04	-51 ± 16
$f_0(2020)$	$\rho\rho$	1	2.145	1996 ± 67	998 ± 163	0.215 ± 0.407	4 ± 82	2.23 ± 0.62	18 ± 15
$f_0(2020)$	$\sigma\sigma$	1	1.900	1888 ± 9	344 ± 12	0.005 ± 0.002	-104 ± 24	0.48 ± 0.04	106 ± 4
$f_0(2020)$	$\rho\rho$	2	1.949	1869 ± 9	461 ± 15	0.026 ± 0.013	31 ± 33	0.51 ± 0.06	-10 ± 11
$f_0(2020)$	$\sigma\sigma$	2	1.900	1908 ± 10	344 ± 19	0.008 ± 0.006	-101 ± 64	0.41 ± 0.10	103 ± 13
$f_0(2020)$	$\rho\rho$	3	1.949	1919 ± 23	366 ± 47	0.011 ± 0.006	77 ± 51	0.45 ± 0.11	32 ± 15
$f_0(2020)$	$\sigma\sigma$	3	1.900	1910 ± 50	414 ± 42	0.014 ± 0.016	82 ± 69	0.72 ± 0.34	66 ± 34

Table 2.2.: Padé poles for $f_0(500)$, $f_0(980)$, and $f_0(1500)$ for $N = 5$, as well as $f_0(2020)$ for $N = 6$. The error is the uncorrelated sum of statistical and systematic uncertainty.

where s_p^N denotes the pole extracted by employing $P_1^N(s, s_0)$.

As in principle the results still depend on the expansion point s_0, we proceed as follows. We first calculate Padé approximants for a varying s_0; near the true pole position, the extracted Padé pole stabilizes. Finally we choose the s_0 that minimizes Δ^N for the maximum order of N employed.

Corresponding residues of the poles are then described by the coupling strength $g_{R\pi\pi}$ of the resonance R to $\pi\pi$ and the coupling g_{Rss} of the $\bar{s}s$ source to the resonance R. They are defined by the near-pole expansions [126, 127]

$$\begin{aligned} \lim_{s\to s_p} T_{11}(s) &= \frac{r_T}{s_p - s} = \frac{g_{R\pi\pi}^2}{32\pi(s_p - s)}\,, \\ \lim_{s\to s_p} \Gamma_1^s(s) &= \frac{r_\Gamma}{s_p - s} = -\frac{g_{R\pi\pi} g_{Rss}}{\sqrt{3}(s_p - s)}\,. \end{aligned} \tag{2.40}$$

The extracted poles and residues for the resonances are shown in Table 2.2.

As we did not include any variation of the input phases, we see that the statistical uncertainty coming from the fit parameters of the higher-mass resonances has only a small impact on the poles of $f_0(500)$ and $f_0(980)$. In fact the uncertainty is dominated by the systematic error coming from the Padé expansion.

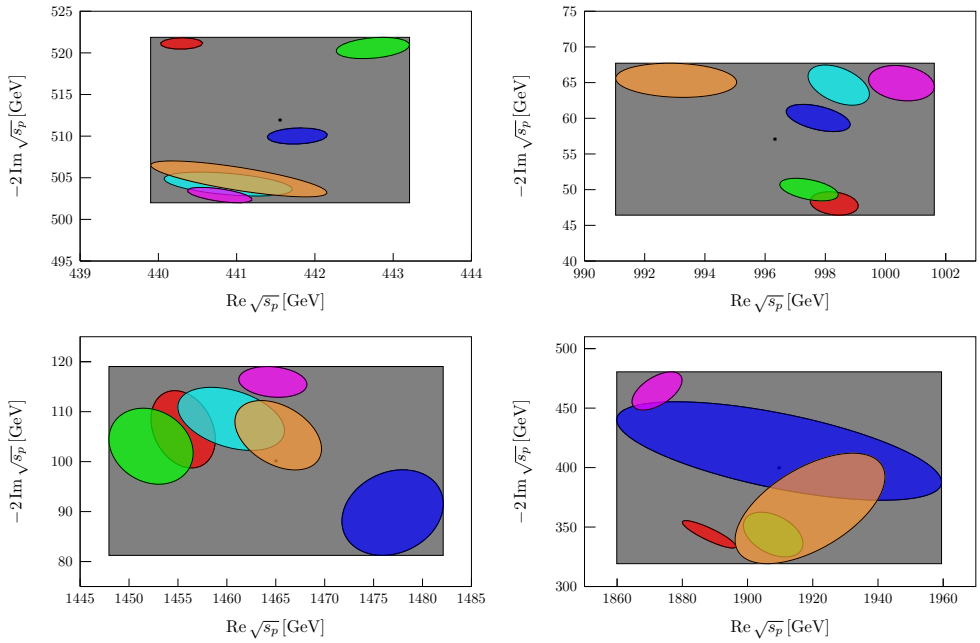

Figure 2.11.: Poles for the $f_0(500)$ (left top), $f_0(980)$ (right top), $f_0(1500)$ (left bottom), and $f_0(2020)$ (right bottom). We show the three fits with a $\sigma\sigma$ channel, namely Fit 1 (red), Fit 2 (green), and Fit 3 (blue), as well as the fits with the $\rho\rho$ channel with Fit 1 (cyan), Fit 2 (magenta), and Fit 3 (orange). The mean values are shown in black.

At higher energies the statistical uncertainty becomes more significant.

However, overall we have strong systematic effects due to the assumptions on the parametrization such as the number of additional resonances and the linear terms in the polynomials. As we do not have a criterion that allows us to decide which fits we should prefer, we keep them all and perform a conservative estimate of the uncertainty: we choose a range for the resonance parameters such that all poles with their corresponding errors are included. The quoted mean is the middle of the resulting box as illustrated in Fig. 2.11.

In order to see whether the pole extraction leads to sensible results, we first compare our findings for the $f_0(500)$ and $f_0(980)$ to the literature [125, 126, 127, 205]. In our parametrization the $f_0(500)$ has a mass of $(442 \pm 2)\,\mathrm{MeV}$ with a width of $(512 \pm 10)\,\mathrm{MeV}$. For the $f_0(980)$ we find a mass of $(996 \pm 6)\,\mathrm{MeV}$ and a width of $(57 \pm 11)\,\mathrm{MeV}$. As Ref. [205] serves as our input below 1 GeV, their pole positions are taken as a benchmark, which lie at $(441 - i\,544/2)\,\mathrm{MeV}$ and $(998 - i\,42/2)\,\mathrm{MeV}$, respectively. While the real parts are therefore perfectly consistent, we see that our parametrization slightly shifts the imaginary parts of the poles with respect to the input.

Furthermore we can compare the coupling strengths $g_{R\pi\pi}$ and g_{Rss} to the ones found in Ref. [127], which we adjust for the fact that the latter are quoted

for the complex conjugate poles. For the $f_0(500)$, we obtain

$$\begin{aligned} \left|g_{f_0(500)\pi\pi}\right| &= (4.53 \pm 0.03)\,\text{GeV}\,, \\ \arg\left(g_{f_0(500)\pi\pi}\right) &= (-73 \pm 2)^\circ\,, \\ \left|g_{f_0(500)ss}\right| &= (11 \pm 2)\,\text{MeV}\,, \\ \arg\left(g_{f_0(500)ss}\right) &= (90 \pm 7)^\circ\,. \end{aligned} \tag{2.41}$$

This is to be compared to $\left|g_{f_0(500)\pi\pi}\right| = 4.76\,\text{GeV}$ and $\arg\left(g_{f_0(500)\pi\pi}\right) = -76.4^\circ$ as well as $\left|g_{f_0(500)ss}\right| = \left(17 \pm 5^{+1}_{-7}\right)\,\text{MeV}$ and $\arg\left(g_{f_0(500)ss}\right) = 80.2^\circ$ [127]. With the exception of $|g_{f_0(500)\pi\pi}|$, which appears to be shifted by about 5%, these numbers are consistent with our findings. For the $f_0(980)$ pole, we find

$$\begin{aligned} \left|g_{f_0(980)\pi\pi}\right| &= (3.1 \pm 0.5)\,\text{GeV}\,, \\ \arg\left(g_{f_0(980)\pi\pi}\right) &= (-81 \pm 5)^\circ\,, \\ \left|g_{f_0(980)ss}\right| &= (147 \pm 14)\,\text{MeV}\,, \\ \arg\left(g_{f_0(980)ss}\right) &= (9 \pm 4)^\circ\,, \end{aligned} \tag{2.42}$$

in comparison to the reference values $\left|g_{f_0(980)\pi\pi}\right| = 2.80\,\text{GeV}$, $\arg\left(g_{f_0(980)\pi\pi}\right) = -85.3^\circ$, $\left|g_{f_0(980)ss}\right| = \left(146 \pm 44^{+14}_{-7}\right)\,\text{MeV}$, and $\arg\left(g_{f_0(980)ss}\right) = 14.2^\circ$ [127]. In this case therefore all parameters are consistent within uncertainties, with a small tension for the argument of $g_{f_0(980)ss}$. In particular, we reproduce the well-known hierarchy in the couplings to the $\bar{s}s$ current: the $f_0(980)$ couples to the strange scalar current an order of magnitude more strongly than the $f_0(500)$ does. Overall we find good agreement of our pole parameters for $f_0(500)$ and $f_0(980)$ with the literature. We see that, a posteriori, the subtraction of the additional term in the scattering amplitude that introduces the explicit resonances, cf. Eq. (2.22), suppresses its influence on the lower-mass poles sufficiently. The agreement between the reference parameters and ours gives us confidence for an extraction of the higher poles via Padé approximants.

As a reference for the higher resonance poles, we compare to the Breit–Wigner parameters of LHCb [203]. For the $f_0(1500)$, the collaboration quotes a resonance with mass $(1465.9 \pm 3.1)\,\text{MeV}$ and width $(115 \pm 7)\,\text{MeV}$. The pole we extract corresponds to a mass of $(1465 \pm 18)\,\text{MeV}$ and a width of $(100 \pm 19)\,\text{MeV}$, which lies within the previously quoted uncertainties of LHCb. The uncertainties we find are significantly larger: this is most likely due to the more flexible range of resonance parametrizations we employ; the masses and widths extracted using Breit–Wigner functions only are probably too optimistic. In addition we can extract the corresponding residues, which are given by

$$\begin{aligned} \left|g_{f_0(1500)\pi\pi}\right| &= (2.9 \pm 1.0)\,\text{GeV}\,, \\ \arg\left(g_{f_0(1500)\pi\pi}\right) &= (-42 \pm 4)^\circ\,, \\ \left|g_{f_0(1500)ss}\right| &= (125 \pm 76)\,\text{MeV}\,, \\ \arg\left(g_{f_0(1500)ss}\right) &= (167 \pm 21)^\circ\,. \end{aligned} \tag{2.43}$$

The main uncertainties stem from the assumptions made on the parametrization of the form factor, such as the number of resonances and the additional channels.

Nevertheless, we note that, despite a large uncertainty, the central value for $\left|g_{f_0(1500)ss}\right|$ seems to be comparable to $\left|g_{f_0(980)ss}\right|$. For further comparison, according to Refs. [127, 217] the $a_0(1450)$ couples to an isovector scalar $\bar{u}d$ current with $\left|g_{a_0(1450)ud}\right| = (284 \pm 54)\,\text{MeV}$, which is of the same order as our extracted value for $g_{f_0(1500)ss}$. The precise relation between the two couplings might be used to elucidate the structure of a scalar nonet around 1.5 GeV, which is however beyond the scope of the present study.

For broad, overlapping resonances a definition of branching ratios is not straightforward. Here we follow a prescription originally proposed to define the width of $f_0(500) \to \gamma\gamma$ [218] by using the narrow-width formula of the form

$$\mathcal{B}_{R\to\pi\pi} = \frac{\Gamma_{R\to\pi\pi}}{\Gamma_R} = \frac{|g_{R\pi\pi}|^2}{32\pi m_R \Gamma_R}\sqrt{1-\frac{4M_\pi^2}{m_R^2}}\,, \tag{2.44}$$

with the residues as coupling constants. With this we can deduce a branching ratio $\mathcal{B}_{f_0(1500)\to\pi\pi} = (58 \pm 31)\%$, where the main uncertainty stems from the difference between Fits 1 and 2 with an additional $\sigma\sigma$ channel compared to the rest of the fits. This is compatible with the (much more precise) branching ratio quoted by the PDG, $\mathcal{B}_{f_0(1500)\to\pi\pi} = (34.9 \pm 2.3)\,\%$ [14].

The last resonance identified by LHCb as the $f_0(1790)$ has a mass of $(1809 \pm 22)\,\text{MeV}$ with a width of $(263 \pm 30)\,\text{MeV}$. As we do not impose a Breit–Wigner line shape, our fits seem to prefer a significantly heavier and much broader resonance with mass $(1910 \pm 50)\,\text{MeV}$ and a width of $(398 \pm 79)\,\text{MeV}$. Note that for the average we neglected the pole extracted from Fit 1 with the $\rho\rho$ parametrization, since this fit describes the prominent resonance structure in the $\pi\pi$ spectrum less accurately than the rest of the fits. As the pole position of the higher pole extracted in our analysis is in better agreement with the $f_0(2020)$ of the PDG (which quotes a mass of $(1992 \pm 16)\,\text{MeV}$ and a width of $(442 \pm 60)\,\text{MeV}$ [14]), we will refer to it as such in the following. Furthermore we see that this pole allows for a stronger variance in the different fits. As its line shape does not only depend on the interference with other resonances, but also on further inelasticities, additional information about these channels would be appreciable.

Finally, we can also constrain the coupling strengths of this resonance to $\pi\pi$ and $\bar{s}s$, which are given as

$$\begin{aligned} \left|g_{f_0(2020)\pi\pi}\right| &= (1.2 \pm 0.9)\,\text{GeV}\,, \\ \arg\left(g_{f_0(2020)\pi\pi}\right) &= (2 \pm 89)^\circ\,, \\ \left|g_{f_0(2020)ss}\right| &= (1019 \pm 786)\,\text{MeV}\,, \\ \arg\left(g_{f_0(2020)ss}\right) &= (-72 \pm 149)^\circ\,. \end{aligned} \tag{2.45}$$

As we can see the coupling strength to the $\pi\pi$-channel is consistent with 0 within 1.5σ. The big uncertainty also strongly influences the extraction of $g_{f_0(2020)ss}$, which in addition is affected by a strong systematic uncertainty coming from the parametrization and can hardly be constrained in a meaningful manner. Using the narrow-width formula of Eq. (2.44), the branching ratio into $\pi\pi$ is

$\mathcal{B}_{f_0(2020)\to\pi\pi} = (1.3 \pm 1.8)\%$, which is obviously also consistent with zero. No meaningful branching ratios are quoted by the PDG in this case.

Since the bare resonance coupling strengths g_i^r as well as the bare resonance masses m_r are source-independent, we can use the same parameters for any decay with $\pi\pi$ S-wave final-state interactions and negligible left-hand cuts. Therefore a simultaneous study of $\bar{B}_s^0 \to J/\psi\pi\pi$ and $\bar{B}_d^0 \to J/\psi\pi\pi$ [219] should be useful to constrain the resonances in the scalar isoscalar channel further.

2.5. Summary and outlook

In this article, we have shown that the parametrization of Ref. [95] for the pion vector form factor can be adapted to the scalar form factors of pions and kaons, marrying the advantages of a rigorous dispersive description at low energies with the phenomenological success of a unitary and analytic isobar model beyond. For the scalar isoscalar channel, the low-energy part must already be provided in terms of a dispersively constructed coupled-channel Omnès matrix. We rely on the conjecture that the resulting strange scalar form factors can be tested in a simultaneous study of the S-waves in the helicity amplitudes for the decays $\bar{B}_s^0 \to J/\psi\pi\pi$ and $\bar{B}_s^0 \to J/\psi K\bar{K}$, whose leading angular moments we can describe successfully. In this way, we have in fact determined the corresponding strange scalar form factors up to $\sqrt{s} \approx 2\,\text{GeV}$, in particular for the pion with rather good accuracy. To quantify the uncertainties of the method, we compared fits based on different assumptions, such as different numbers of resonances as well as different final-state channels. Although they describe the data almost equally well, we see a significant systematic uncertainty at higher energies, which should be reduced significantly, however, once further information about the inelastic channels becomes available. For now, we only included an effective 4π channel modeled either by $\rho\rho$ or $\sigma\sigma$ intermediate states; for a more detailed description of the branching ratios of the heavier scalar isoscalar resonances, we might need to include further inelastic channels such as $a_1\pi$, $\eta\eta$, or $\eta\eta'$.

As the parametrization developed is fully unitary and analytic, we extracted resonance parameters as pole positions and residues in the complex energy plane, employing Padé approximants. In particular, we determined resonance poles as well as coupling constants for $f_0(1500)$ and $f_0(2020)$. While the pole location for the $f_0(1500)$ is consistent with the one derived from the LHCb Breit–Wigner extraction, we find a significantly shifted pole for the $f_0(2020)$. This shift ought to be tested experimentally in other processes with prominent S-wave pion–pion final-state interactions. Alternatively—or in addition—we might also include scattering data at higher energies in the fits explicitly [210, 220].

3. Z_b contributions to the decay of the $\Upsilon(5S)$

3.1. Introduction

While heavy meson decays involving pions have already been discussed in the previous chapter, we want to extend the applicability by allowing crossed-channel effects between the heavy meson-pion system. Therefore, the corresponding dispersion theory does involve not only a right-hand cut but also a left-hand cut. While the stable resonance exchange is often a good first approximation to capture the dominant left-hand cut effects, we want to consider a more sophisticated model. This is necessary since we aim for a detailed study of near-threshold line shapes that shall eventually reveal the nature of the studied states.

Especially interesting for this approach are exotic resonances such as the $Z_b^{\pm}(10610)$ and $Z_b^{\pm}(10650)$, which decay into a bottomonium and a pion. Since the $b\bar{b}$ pair in the final state cannot be produced in the decay, the Z_b resonances need to contain a bottom-antibottom quark system. However, since they are also charged, they need to consist of at least four quarks and thus are fundamentally not consistent with the conventional quark models that treat mesons as $Q\bar{Q}$ states.

The first measurements came from the Belle Collaboration for the decays $\Upsilon(5S) \to \Upsilon(nS)\pi\pi$ with $n = 1, 2, 3$ and $\Upsilon(5S) \to h_b(mP)\pi\pi$ with $m = 1, 2$ [172]. Here both of the Z_b resonances show up as peaks in the $\Upsilon(nS)\pi^+$ mass projections. Not only do tetraquark interpretations of the Z_b [157, 221, 222] but also hadronic molecule pictures [57, 175, 223, 224, 225, 226, 227, 228, 229, 230, 231] seem to be consistent with the data. However, since none of the mentioned studies involve a proper treatment of the $\pi\pi$ interactions a Dalitz plot analysis cannot be done so far. Dispersive analyses for the heavy bottominium decays have been applied for $\Upsilon(3S) \to \Upsilon(1S)\pi\pi$ [56] and $\Upsilon(4S) \to \Upsilon(nS)\pi\pi$ with $n = 1, 2$ [174], however those are only sensitive on the low-energy tail of the Z_b resonances. Therefore these ideas will be applied to the decay $\Upsilon(5S) \to \Upsilon(nS)\pi\pi$ with $n = 1, 2, 3$, where thanks to the larger masses of the $\Upsilon(5S)$ the Z_b states can be produced as physical states.

Due to the closeness of the Z_b resonances to the $B\bar{B}^\star$ and $B^\star B^\star$ thresholds, we proceed to model those resonances as hadronic molecules as presented in Ref. [223]. This involves a coupled-channel Lippmann-Schwinger equation with the channels $B\bar{B}^\star$, $B^\star\bar{B}^\star$, $\Upsilon(1S)\pi$, $\Upsilon(2S)\pi$, $\Upsilon(3S)\pi$, $h_b(1P)\pi$ and $h_b(2P)\pi$. The potential is modeled by heavy meson chiral perturbation theory. For simplicity, we take the easiest model, which only consists of an S-wave contact term between the elastic channels $B\bar{B}^\star$ and $B^\star\bar{B}^\star$ and a contact term between the

elastic channels and the others. With this assumption, the Lippmann-Schwinger equation can be solved analytically.

As in these decays the available dipion energy reaches up to 0.51 GeV for $\Upsilon(3S)$, 0.84 GeV for $\Upsilon(2S)$ and 1.40 GeV for $\Upsilon(1S)$ a multi-channel dispersive framework needs to be employed. We provide a two-channel Omnès matrix involving the scattering amplitude from Ref. [205], which is valid up to 1.05 GeV. For higher energies further inelasticities need to be taken into account. Thus we also provide a three-channel solution with the scattering amplitude from Ref. [232] in chapter 3.6.1, which also includes a $f_0(1500)$ resonance.

Afterward, we provide two different approaches to solve the inhomogenous Omnès problem for the decay $\Upsilon(5S) \to \Upsilon(1S)\pi\pi$. The first one involves the standard Khuri-Treimann path deformation [192, 233], while the second one employs a spectral density [234, 235, 236]. As both are consistent with each other, we apply the second formalism to the other two decays.

3.2. Kinematics

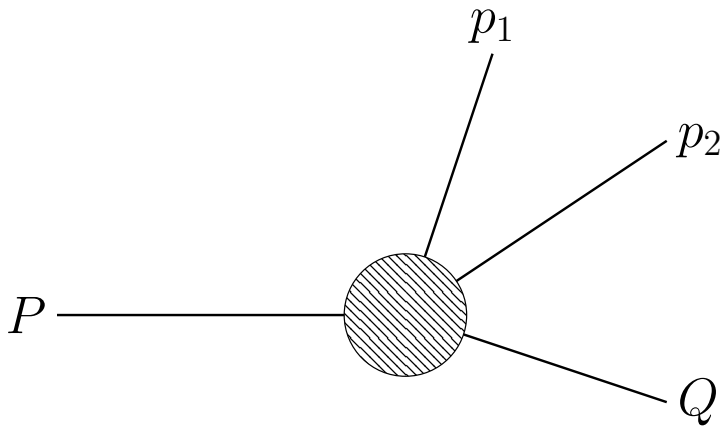

Figure 3.1.: Decay of a particle with mass $P^2 = m_i^2$ into one with mass $Q^2 = m_f^2$ and two with $p_1^2 = p_2^2 = m_\pi^2$.

Consider the decay

$$\Upsilon(5S)\,(P) \to \Upsilon(nS)\,(Q) + \pi\,(p_1) + \pi\,(p_2) \quad n = 1, 2, 3 \tag{3.1}$$

as depicted in Fig. 3.1. The particles have the masses

$$P^2 = m_i^2 \quad , \quad Q^2 = m_f^2 \quad \text{and} \quad p_1^2 = p_2^2 = m_\pi^2\,. \tag{3.2}$$

The Mandelstam variable s is given by the dipion center-of-mass energy

$$s = (p_1 + p_2)^2\,. \tag{3.3}$$

Then the other two Mandelstam variables may then be expressed in terms of s and the angle θ between $\vec{P}$ and $\vec{p}_1$ as

$$t(s, \cos\theta) = (P - p_1)^2 = \frac{1}{2}\left(m_i^2 + m_f^2 + 2m_\pi^2 - s + \kappa(s)\,\cos\theta\right) \tag{3.4}$$

and

$$u(s, \cos\theta) = (P - p_2)^2 = \frac{1}{2}\left(m_i^2 + m_f^2 + 2m_\pi^2 - s - \kappa(s)\,\cos\theta\right)\,. \tag{3.5}$$

Here the kinematic function $\kappa(s)$ is given by

$$\kappa(s) = \sigma(s, m_\pi^2)\sqrt{\lambda(s, m_i^2, m_f^2)} \tag{3.6}$$

with the pion phase space function

$$\sigma(s, m_\pi^2) = \sqrt{1 - \frac{4m_\pi^2}{s}} \tag{3.7}$$

and the Källén function

$$\lambda(s, m_i^2, m_f^2) = \left((m_i - m_f)^2 - s\right)\left((m_i + m_f)^2 - s\right)\,. \tag{3.8}$$

Note that in order to be consistent with the prescription $m_i^2 \to m_i^2 + i\epsilon$ and $m_f^2 \to m_f^2 + i\epsilon$ with an infinitesimal ϵ, we need to choose a branch of the square roots, that appear in Eq. (3.6). The proper choice

$$\kappa(s) = \sqrt{1 - \frac{4m_\pi^2}{s}}\sqrt{(m_i - m_f)^2 - s}\sqrt{(m_i + m_f)^2 - s} \tag{3.9}$$

shows two branch cuts. One coming from $\sigma_\pi(s)$ lies between the branch points 0 and $4m_\pi^2$. The other one is between the pseudo-threshold $(m_i - m_f)^2$ and the crossed-threshold $(m_i + m_f)^2$. Furthermore $\kappa(s)$ contains a pole at $s = 0\,\mathrm{GeV}^2$. An illustration of this is given in Fig. 3.2.

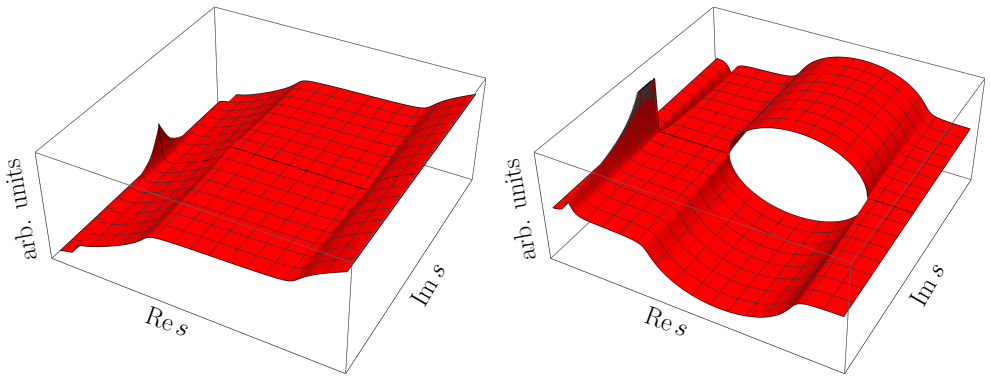

Figure 3.2.: Illustration of the real (left) and imaginary part (right) of $-\kappa(s)$ as given in Eq. (3.9) in the complex s-plane.

3.3. The decay amplitude

The full decay amplitude [56, 174] can be written as

$$\mathcal{M}^{\text{full}}(s,t,u) = \epsilon_{\Upsilon(5S)} \cdot \epsilon^{\star}_{\Upsilon(nS)}\, \mathcal{M}(s,t,u)\,, \tag{3.10}$$

where $\epsilon_{\Upsilon(5S)}$ and $\epsilon_{\Upsilon(nS)}$ are the polarization vectors of the $\Upsilon(5S)$ and $\Upsilon(nS)$, respectively. Note that contractions of the polarization vectors with momenta would contribute to higher order corrections in the heavy quark power counting scheme and hence are neglected in the following.

The scalar amplitude $\mathcal{M}(s,t,u)$ can then be partial-wave projected

$$\mathcal{M}(s,t,u) = \sum_{L=0}^{\infty} f_L(s)\, P_L(\cos\theta)\,, \tag{3.11}$$

where θ is the pion scattering angle as introduced in Sect. 3.2. The L^{th} Legendre polynomial is given by the standard representation $P_L(\cos\theta)$. Accordingly the partial-wave amplitude $f_L(s)$ can be extracted through

$$f_L(s) = \frac{1}{2L+1} \int_{-1}^{1} \mathrm{d}\cos\theta\, \mathcal{M}\left(s, t(s,\cos\theta), u(s,\cos\theta)\right)\, P_L(\cos\theta)\,. \tag{3.12}$$

Assume that each partial-wave can be decomposed into

$$f_L(s) = M_L(s) + K_L(s)\,, \tag{3.13}$$

where $K_L(s)$, which is called **inhomogeneity**, contains only a left-hand cut and $M_L(s)$ only a right-hand cut. Furthermore assume that we have a reliable model for $K_L(s)$, then concerning pion rescattering $M_L(s)$ can be reconstructed dispersively via an inhomogenous Omnès problem [237], namely

$$f_L(s) = \Omega(s) \left[P_L(s) + \frac{s^n}{\pi} \int_{4m_\pi^2}^{\infty} \frac{\mathrm{d}s'}{(s')^n} \frac{\Omega^{-1}(s') t_L(s') \hat{\sigma}(s') K_L(s')}{s'-s} \right] + K_L(s)\,. \tag{3.14}$$

As the available pion energy for $\Upsilon(5S) \to \Upsilon(1S)\pi\pi$ lies beyond the $K\bar{K}$ threshold it is inevitable to employ a coupled-channel formalism. In this case $K_L(s)$ is a vector containing the partial-wave projections

$$K_L(s) = \frac{1}{2L+1} \int_{-1}^{1} \mathrm{d}z \begin{pmatrix} K(s,t(s,z),u(s,z))_{\Upsilon(5s)\to\Upsilon(ns)\pi\pi} \\ K(s,t(s,z),u(s,z))_{\Upsilon(5s)\to\Upsilon(ns)KK} \end{pmatrix} P_L(z)\,. \tag{3.15}$$

The corresponding light-meson partial-wave amplitude t_ℓ, for e.g. isoscalar scalar $\pi\pi$-scattering, can be parametrized by the $\pi\pi$ scattering phase shift $\delta(s)$ [124, 184] as well as the $\pi\pi \to K\bar{K}$ modulus $g(s)$ and its phase $\psi(s)$ [185] as

$$t_L(s) = \begin{pmatrix} t_{\pi\pi\to\pi\pi} & t_{\pi\pi\to KK} \\ t_{\pi\pi\to KK} & t_{KK\to KK} \end{pmatrix} = \begin{pmatrix} \frac{\eta e^{2i\delta}-1}{2i\sigma(s,m_\pi^2)} & g e^{i\psi} \\ g e^{i\psi} & \frac{\eta e^{2i(\psi-\delta)}-1}{2i\sigma(s,m_K^2)} \end{pmatrix}. \tag{3.16}$$

Accordingly the Omnès matrix is given by the numerical solution of the Muskhelishvili-Omnès (MO) problem

$$\Omega(s) = \frac{1}{\pi} \int\limits_{4m_\pi^2}^{\infty} \mathrm{d}s' \, \frac{t_L^\star(s') \hat{\sigma}(s') \Omega(s')}{s' - s} \,, \tag{3.17}$$

where $\hat{\sigma}(s)$ is a diagonal matrix containing the phase space factors above threshold

$$\hat{\sigma}(s) = \begin{pmatrix} \sigma(s, m_\pi^2)\Theta(s - 4m_\pi^2) & 0 \\ 0 & \sigma(s, m_K^2)\Theta(s - 4m_K^2) \end{pmatrix} . \tag{3.18}$$

In case of a single channel the scattering amplitude reduces to

$$t_L(s) = \frac{\sin(\delta(s))}{\sigma(s, m_\pi^2)} e^{i\delta(s)} \,. \tag{3.19}$$

The corresponding Omnès-function can be determined analytically

$$\Omega(s) = \exp\left(\frac{s}{\pi} \int\limits_{4m_\pi^2}^{\infty} \frac{\mathrm{d}s'}{s'} \, \frac{\delta(s')}{s' - s} \right) . \tag{3.20}$$

Accordingly for a single channel the inhomogeneous Omnès problem of Eq. (3.14) can be written as

$$f_L(s) = \Omega(s) \left[P_L(s) + \frac{s^n}{\pi} \int\limits_{4m_\pi^2}^{\infty} \frac{\mathrm{d}s'}{(s')^n} \, \frac{\sin(\delta(s')) \, K_L(s')}{|\Omega(s')|(s' - s)} \right] + K_L(s) \tag{3.21}$$

3.4. Model for crossed-channel amplitude

Prominent resonances showing up in the $\Upsilon(nS)\pi$ amplitude are the $Z_b(10610)$, Z_b for short, and $Z_b(10650)$ or Z_b' for short. As they lie close to the $B\bar{B}^\star$ and $B^\star\bar{B}^\star$ thresholds, respectively, it is sensible to model them as dynamic bound states of these channels. In order to appropriately include their widths further inelastic channels such as $\Upsilon(nS)\pi$ with $n = 1, 2, 3$ and $h_b(mP)\pi$ with $m = 1, 2$ are taken into account. An illustration of the t- and u-channel diagrams is shown in Fig. 3.3.

Note that no charged bottomonium-like state with strangeness content, which may be identified with a Z_{bs}, has been measured yet. As such evidence is lacking, we do not include it as the primary contribution to the left-hand cut of the decay $\Upsilon(5S) \to \Upsilon(nS)K\bar{K}$. Furthermore, direct contributions coming from further inelastic channels such as 4π are also neglected. Therefore the inhomogeneity is only driven by the crossed-channel contributions of the Z_b and Z_b' to the decay $\Upsilon(5S) \to \Upsilon(nS)\pi\pi$.

The crossed-channel amplitude, which produces the left-hand cut, can thus be modeled by

$$K(s, t, u) = \phi(t) + \phi(u) \,, \tag{3.22}$$

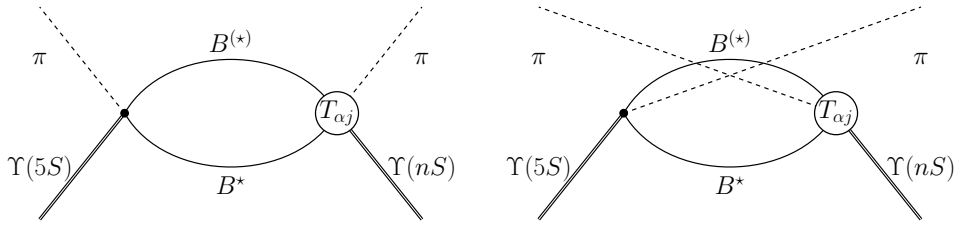

Figure 3.3.: Crossed-channel amplitudes coming from $B\bar{B}^\star$ and $B^\star\bar{B}^\star$ scattering in the t- (left) and u-channel (right).

where the single-variable amplitude $\phi(t)$ is given by

$$\phi(t) = A_{BB^\star\to\Upsilon(nS)\pi}(t) + A_{B^\star B^\star\to\Upsilon(nS)\pi}(t) \tag{3.23}$$

with

$$A_{BB^\star\to\Upsilon(nS)\pi}(t) = c_{BB^\star} J_{\mathrm{NR}}(t, m_B^2, m_{B^\star}^2) T_{BB^\star\to\Upsilon(nS)\pi}(t) \tag{3.24}$$

and

$$A_{B^\star B^\star\to\Upsilon(nS)\pi}(t) = c_{B^\star B^\star} J_{\mathrm{NR}}(t, m_{B^\star}^2, m_{B^\star}^2) T_{B^\star B^\star\to\Upsilon(nS)\pi}(t)\,. \tag{3.25}$$

Here the coupling constants for the transition $\Upsilon(5S)\pi \to B^{(\star)}B^\star$ given by $c_{B^{(\star)}B^\star}$ are free parameters. However employing heavy quark spin symmetry leads to

$$c_{BB^\star} = -c_{B^\star B^\star}\,. \tag{3.26}$$

The non-relativistic loop function $J_{\mathrm{NR}}(t, m_1^2, m_2^2)$ is given by

$$J_{\mathrm{NR}}(s, m_1^2, m_2^2) = \int_0^\Lambda \frac{\mathrm{d}q\, q^2}{2\pi^2} \frac{2\mu(m_1, m_2)}{q^2 - p^2(s, m_1, m_2) - i\epsilon} \tag{3.27}$$

with the reduced mass

$$\mu(m_1, m_2) = \frac{m_1 m_2}{m_1 + m_2} \tag{3.28}$$

and the center-of-mass momentum

$$p^2(s, m_1, m_2) = 2\mu(m_1, m_2)(\sqrt{s} - m_1 - m_2)\,. \tag{3.29}$$

For $p^2(t, m_1, m_2) \in \mathcal{R}$ and $p^2(t, m_1, m_2) > 0$ and $p^2(t, m_1, m_2) < \Lambda^2$ it can be analytically evaluated to be

$$J_{\mathrm{NR}}(t, m_1^2, m_2^2) = \frac{\mu\Lambda}{\pi^2}\left(1 - \sqrt{\frac{p^2}{\Lambda^2}}\left(\operatorname{arctanh}\left(\sqrt{\frac{p^2}{\Lambda^2}}\right) - \frac{i\pi}{2}\right)\right)\,. \tag{3.30}$$

For any other case it amounts to

$$J_{\mathrm{NR}}(t, m_1^2, m_2^2) = \frac{\mu\Lambda}{\pi^2}\left(1 - \sqrt{-\frac{p^2}{\Lambda^2}}\arctan\left(\frac{\Lambda}{\sqrt{-p^2}}\right)\right)\,. \tag{3.31}$$

In the following we set the cutoff $\Lambda = 1\,\text{GeV}$. Due to the square root in Eq. (3.29) $J_{\text{NR}}(t)$ has a left-hand cut starting from $t = 0$. This is a non-relativistic artifact and unphysical.

The $B^{(\star)}B^{\star} \to \Upsilon(ns)\pi$ scattering amplitude $T_{B^{(\star)}B^{\star}\to\Upsilon(ns)\pi}(t)$ will be modeled through a coupled-channel Lippmann-Schwinger equation as presented in Refs. [223, 238].

Therefore the Z_b and Z_b' resonances are produced as dynamic rescattering effects of the elastic channels $BB^{\star}$ ($\alpha = 1$) and $B^{\star}B^{\star}$ ($\alpha = 2$) denoted by greek indices $\alpha, \beta, \gamma, \ldots$. They gain a width by including further inelastic channels enumerated by latin indices $i, j, k, \ldots$. The considered inelastic ones are $\Upsilon(1S)\pi$ ($i = 1$), $\Upsilon(2S)\pi$ ($i = 2$), $\Upsilon(3S)\pi$ ($i = 3$), $h_b(1P)\pi$ ($i = 4$) and $h_b(2P)\pi$ ($i = 5$).

In this manner the elastic-to-elastic amplitude may be expressed by

$$T_{\alpha\beta} = v_{\alpha\beta} - \sum_{\gamma} v_{\alpha\gamma} J_{\gamma} T_{\gamma\beta} - \sum_{k} v_{\alpha k} J_k T_{k\beta}\,, \tag{3.32}$$

where J_{γ} and J_k are short hand notations for $J_{NR}(t, m_1^2, m_2)$ with the corresponding masses of the elastic and inelastic channels. The elastic potential $v_{\alpha\beta}$ is be approximated as a constant

$$v_{\alpha\beta} = \begin{pmatrix} c_d & c_f \\ c_f & c_d \end{pmatrix} = \begin{pmatrix} -3.3 & -0.06 \\ -0.06 & -3.3 \end{pmatrix}. \tag{3.33}$$

The values of the coupling constants were determined in a fit to the data [223]. On the other hand the elastic-to-inelastic potential may be parametrized as

$$v_{i\alpha} = v_{\alpha i} = g_{i\alpha} k_i^{L_i}\,, \tag{3.34}$$

where k_i is the center-of-mass momentum of the i^{th} inelastic channel, with the masses m_1^i and m_2^i,

$$k_i(t) = \frac{\sqrt{\lambda(t, m_1^i, m_2^i)}}{2\sqrt{t}}\,. \tag{3.35}$$

As the inelastic channel needs to have the same quantum numbers as the Z_B resonance, their angular momenta L_i also need to be included for the transition. Explicitly their values are

$$L_1 = L_2 = L_3 = 0 \quad \text{and} \quad L_4 = L_5 = 1\,. \tag{3.36}$$

The values of $g_{i\alpha}$ are fixed by comparison to Ref. [223] resulting in

$$g_{i\alpha} = \begin{pmatrix} g_{11} & g_{12} \\ g_{21} & g_{22} \\ g_{31} & g_{32} \\ g_{41} & g_{42} \\ g_{51} & g_{52} \end{pmatrix} = \frac{1}{\sqrt{2m_{\pi}}} \begin{pmatrix} 0.30 & -0.30 \\ 1.01 & -1.01 \\ 1.28 & -1.28 \\ 3.29 & 3.29 \\ 11.38 & 11.38 \end{pmatrix}. \tag{3.37}$$

Note that the parameters were rescaled by a factor of $1/\sqrt{2m_{\pi}}$ in order to be consistent with the newer analysis [180]. Notice that g_{i1} and g_{i2} are related by to each other by heavy quark spin symmetry.

The corresponding elastic-to-inelastic transition amplitude is given by the Lippmann-Schwinger equation

$$T_{\alpha i} = T_{i\alpha} = v_{i\alpha} - \sum_{\gamma} v_{i\gamma} J_\gamma T_{\gamma\alpha} - \sum_{k} v_{ik} J_k T_{k\alpha} \,. \tag{3.38}$$

For the inelastic-to-inelastic transition amplitude the equation

$$T_{ij} = v_{ij} - \sum_{\gamma} v_{i\gamma} J_\gamma T_{\gamma j} - \sum_{k} v_{ik} J_k T_{kj} \tag{3.39}$$

holds. As indicated by effective field theories [239] and lattice calculations [240] the transition between the inelastic channels are very weak. Thus we can safely set

$$v_{ij} = 0 \,. \tag{3.40}$$

Since the employed potentials are separable, the Lippmann-Schwinger equations Eqs. (3.32), (3.38) and (3.39) can be solved analytically. Further simplifications can be applied due to the vanishing of the inelastic-to-inelastic potential. Namely

$$T_{\alpha\beta} = v^{\text{eff}}_{\alpha\beta} - \sum_{\gamma} v^{\text{eff}}_{\alpha\gamma} J_\gamma T_{\gamma\beta} \tag{3.41}$$

for the elastic-to-elastic amplitude;

$$T_{i\alpha} = v_{i\alpha} - \sum_{\gamma} v_{i\gamma} J_\gamma T_{\gamma\alpha} \tag{3.42}$$

for the elastic-to-inelastic amplitude and finally for the inelastic-to-inelastic amplitude

$$T_{ij} = - \sum_{\gamma} v_{i\gamma} J_\gamma T_{j\gamma} \,. \tag{3.43}$$

Therefore the elastic-to-elastic equation is reduced to an effective elastic Lippmann-Schwinger equation with the effective potential

$$v^{\text{eff}}_{\alpha\beta} = v_{\alpha\beta} - \sum_{k} v_{\alpha k} J_k v_{k\beta} \,. \tag{3.44}$$

For further consistency with Ref. [223] the real part of J_k is absorbed into the definition of the coupling constants. The imaginary part of J_k is fixed by unitarity to the phase space of the k^{th} channel σ_k. However in order to avoid the continuation of σ_k into the complex plane we choose

$$v^{\text{eff}}_{\alpha\beta} = v_{\alpha\beta} - i \sum_{k} v_{\alpha k}\, v_{k\beta}\, \text{Im}(J_k) \,. \tag{3.45}$$

Note that Ref. [223] replaced $\text{Im}(J_k)$ by the relativistic phase space

$$\text{Im}(J_k(s)) = \frac{4 m_a m_b}{8\pi} \sqrt{\frac{\nu}{s}} \tag{3.46}$$

and

$$\nu = \lambda(s, m_a^2, m_b^2)\,. \tag{3.47}$$

For a proper analytic continuation we keep the relativistic loop function, which is normalized non-relativistically by multiplying with the factor $4m_a m_b$. It reads for real and positive ν

$$\begin{aligned} J(s, m_a, m_b) = \frac{-4m_a m_b}{16\pi^2}\Bigg(&\left(\frac{m_a^2 - m_b^2}{s} - \frac{m_a^2 + m_b^2}{m_a^2 - m_b^2}\right)\log\left(\frac{m_a}{m_b}\right) - 1 \\ &+ \frac{\sqrt{\nu}}{s}\left(\log\left(\frac{s - m_a^2 - m_b^2 + \sqrt{\nu}}{s - m_a^2 - m_b^2 - \sqrt{\nu}}\right) - 2i\pi\Theta(s - (m_a + m_b)^2)\right)\Bigg) \end{aligned} \tag{3.48}$$

and otherwise

$$\begin{aligned} J(s, m_a, m_b) = \frac{-4m_a m_b}{16\pi^2}\Bigg(&\left(\frac{m_a^2 - m_b^2}{s} - \frac{m_a^2 + m_b^2}{m_a^2 - m_b^2}\right)\log\left(\frac{m_a}{m_b}\right) - 1 \\ &+ \frac{\sqrt{-\nu}}{s}\left(\arctan\left(\frac{m_a^2 - m_b^2 + s}{\sqrt{-\nu}}\right) - \arctan\left(\frac{m_a^2 - m_b^2 - s}{\sqrt{-\nu}}\right)\right)\Bigg)\,. \end{aligned} \tag{3.49}$$

Note that due to the non-relativistic loop function in Eqs. (3.24) and (3.25) the single-variable amplitude $\phi(t)$ in Eq. (3.23) also has a left-hand cut starting at $t = 0\,\mathrm{GeV}^2$. The right-hand cut on the other hand starts at $t = (m_{\Upsilon(1S)} + m_\pi)^2$.

As the amplitude in Eq. (3.23) is a superposition of the $B\bar{B}^\star$ and $B^\star\bar{B}^\star$ intermediate states it is possible to separate their contributions by setting $c_{BB^\star} = 1$ and $c_{B^\star B^\star} = 0$ for the $B\bar{B}^\star$ intermediate state or $c_{BB^\star} = 0$ and $c_{B^\star B^\star} = 1$ for the $B^\star\bar{B}^\star$ one. A figure of each of these amplitudes is shown in Fig. 3.4.

Since the potential $v_{\alpha\beta}$ of Eq. (3.33) is almost diagonal and the inelastic channels only produce a small correction, both the $B\bar{B}^\star$ and $B^\star\bar{B}^\star$ channel will mostly decouple. As the Z_b resonances are dynamically generated by rescattering of these channels, the Z_b will predominantly couple to the $B\bar{B}^\star$ channel and the Z_b' to the $B^\star\bar{B}^\star$ channel. This phenomenon is shown in Fig. 3.4 by the two sharp peaks near the corresponding thresholds. As the channels are not entirely decoupled a small contribution of the Z_b' to the $B\bar{B}^\star$ intermediate state and the Z_b to the $B^\star\bar{B}^\star$ intermediate state is still visible. Two other sharp structures show up, which are artifacts of the non-relativistic propagators and are located at $p(t, m_B, m_{B^\star}) = 1\,\mathrm{GeV}^2$ and $p(t, m_{B^\star}, m_{B^\star}) = 1\,\mathrm{GeV}^2$ corresponding to the non-relativistic cutoff at $\Lambda = 1\,\mathrm{GeV}$.

In the present model the transition amplitude between an inelastic state i and the elastic one α is directly proportional to $|v_{i\alpha}|$. On the other hand, its line shape is dictated by the elastic-to-elastic scattering amplitude. Hence we expect that the amplitude $\phi(t)$ has the same line-shape for the different final states $\Upsilon(1S)$, $\Upsilon(2S)$ and $\Upsilon(3S)$. However, they are rescaled to each other according to Eq. (3.37), whose parameters were determined by a fit [223]. Therefore the higher mass final states have a stronger contribution.

3.5. Calculation of the inhomogeneity

In order to evaluate the inhomogeneous dispersion integral of Eq. (3.14) the partial-wave projection of Eq. (3.15) with the in the previous section introduced

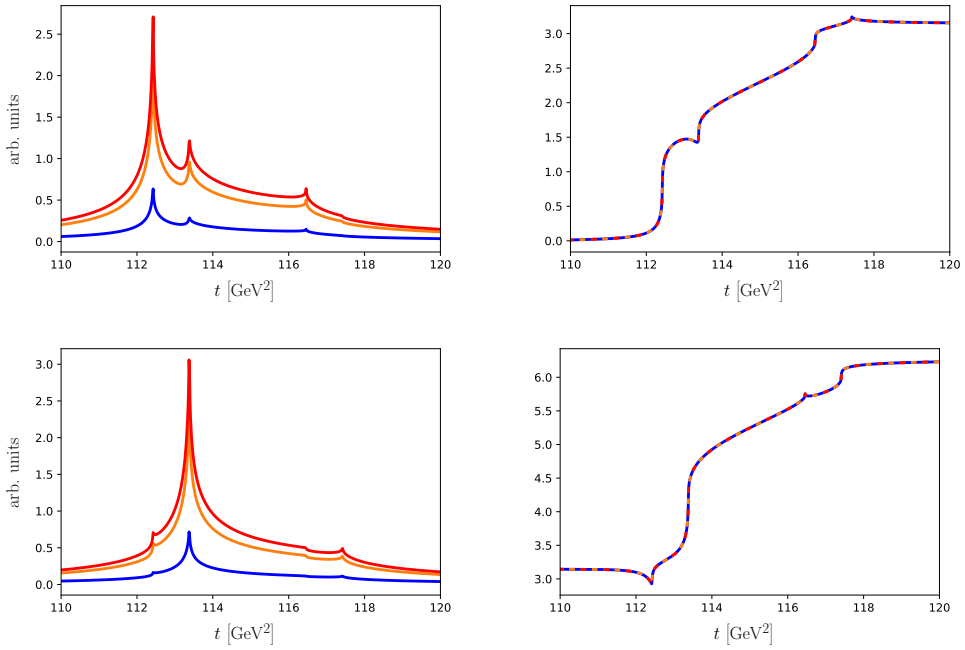

Figure 3.4.: Modulus (left) and phase (right) of $\phi(t)$ using a $BB^\star$ (top) and $B^\star B^\star$ (bottom) intermediate state for the $\Upsilon(1S)$ (blue), $\Upsilon(2S)$ (orange) and $\Upsilon(3S)$ (red) final state.

amplitude needs to be evaluated first.

As explained in Appendix A.1, the integration over the scattering angle $\cos\theta = z$ can be rewritten as an integration over the Mandelstam variables $t(s, \cos\theta)$ or $u(s, \cos\theta)$. In our case the partial-wave projection may therefore be written as

$$K_L(s) = \frac{2}{(2L+1)\kappa(s)} \left(\int_{t_-(s)}^{t_+(s)} \mathrm{d}t\, \phi(t) P_L(z_t) + \int_{u_+(s)}^{u_-(s)} \mathrm{d}u\, \phi(u) P_L(z_u) \right) \tag{3.50}$$

where the scattering angle is given as

$$z_t = \frac{2t - m_i^2 - m_f^2 - 2m_\pi^2 + s}{\kappa(s)} \tag{3.51}$$

and

$$z_u = -\frac{2u - m_i^2 - m_f^2 - 2m_\pi^2 + s}{\kappa(s)}\,. \tag{3.52}$$

Furthermore we use the short hand notation for the endpoints

$$t_\pm = u_\mp = t(s, \pm 1) = u(s, \mp 1)\,. \tag{3.53}$$

For the S-wave projection the t- and u-channel amplitudes contribute equally

and thus the inhomogeneity simplifies to

$$K_0(s) = \frac{4}{\kappa} \int\limits_{t_-(s)}^{t_+(s)} \mathrm{d}t\, \phi(t)\,. \tag{3.54}$$

As the cut in $\phi(t)$ for $\Upsilon(5S) \to \Upsilon(1S)\pi\pi$ starts at $t = (m_{\Upsilon(1S)} + m_\pi)^2$ we may integrate along the Khuri-Treiman path (KT) as explained in Appendix A.2.

For the S-wave this amounts to evaluating the integral

$$K_0(s) = \frac{4}{\kappa(s)} \left[\int\limits_{s}^{4m_\pi^2} \mathrm{d}s' \, \frac{\partial t_-(s')}{\partial s'} \phi(t_-(s')) + \int\limits_{4m_\pi^2}^{s} \mathrm{d}s' \, \frac{\partial t_+(s')}{\partial s'} \phi(t_+(s')) \right] . \tag{3.55}$$

Due to the coupled-channel approach used here (see Sect. 3.4), the right-hand cut for the amplitudes $\Upsilon(5S) \to \Upsilon(nS)\pi\pi$ with $n = 2, 3$ also start at the lowest threshold $(m_{\Upsilon(1S)} + m_\pi)^2$. In a dispersive approach this however leads to the appearance of anomalous thresholds as introduced in Appendix B. Therefore a straight forward integration as for the decay $\Upsilon(5S) \to \Upsilon(1S)\pi\pi$ is not valid, but needs to be modified.

While the KT solution may be modified in order also to describe the higher mass final states, we want to present an alternative approach, which is entirely consistent to the KT path for the decay $\Upsilon(5S) \to \Upsilon(1S)\pi\pi$ but can be applied more easily to $\Upsilon(5S) \to \Upsilon(nS)\pi\pi$ with $n = 2, 3$.

Since $\phi(t)$ falls off fast outside of the Z_B and Z_B' region it may be written as a unsubtracted dispersion integral

$$\phi(t) = \frac{1}{\pi} \int\limits_{m_0^2}^{\infty} \mathrm{d}m^2 \, \frac{\rho(m^2)}{t - m^2 + i\epsilon} \tag{3.56}$$

over the right-hand cut starting at

$$m_0^2 = \left(m_{\Upsilon(1s)} + m_\pi\right)^2 . \tag{3.57}$$

The spectral density $\rho(m^2)$ is related to $\phi(t)$ via

$$\rho(m^2) = -\mathrm{Im}\, \phi(m^2)\,. \tag{3.58}$$

Note that in principle $\phi(t)$ as well as $\rho(m^2)$ are vectors in channel space. However due to our model only the $\pi\pi$ component contributes to the further calculations.

By choosing a proper integration path all singularities are formally avoided. Therefore it is possible to swap the order of integrations in Eq. (3.14), such that the S-wave amplitude of the decay is determined by

$$f_0(s) = \Omega_L(s) \left[P_0(s) + I_0(s) \right] + K_0(s) \tag{3.59}$$

with the full inhomogeneous dispersion integral

$$I_0(s) = \frac{1}{\pi} \int\limits_{m_0^2}^{\infty} \mathrm{d}m^2 \; \tilde{I}_0(s, m^2)\, \rho(m^2) \tag{3.60}$$

and the inhomogeneous dispersion integral for the t-channel exchange of a stable particle with mass m

$$\tilde{I}_0(s, m^2) = \frac{s^n}{\pi} \int\limits_{4m_\pi^2}^{\infty} \frac{\mathrm{d}s'}{(s')^n} \frac{4}{\kappa(s')} \frac{\Omega_0^{-1}(s') t_0(s') \hat{\sigma}(s')}{(s'-s)} A_0(s', m^2)\,. \tag{3.61}$$

The inhomogeneity $A_0(s', m^2)$ of a stable propagator with mass m^2 is defined by

$$A_0(s, m^2) = \int\limits_{t_-(s)}^{t_+(s)} \frac{\mathrm{d}t}{t - m^2}\,. \tag{3.62}$$

Its correct analytical continuation is discussed in detail in Appendix A.4.

For $m^2 < (m_f + m_\pi)^2$ Eq. (3.61) needs to be modified to take the anomalous threshold into account as explained in Appendix B. This amounts to

$$\tilde{I}_0^{\mathrm{mod}}(s, m^2) = \tilde{I}_0(s, m^2) + \xi_{\mathrm{anom}}(s, m^2) \tag{3.63}$$

with

$$\xi_{\mathrm{anom}}(s, m^2) = -\frac{s^n}{2\pi i} \int\limits_0^1 \mathrm{d}x \, \frac{16\pi \Omega_0^{-1}(z(x)) t_0(z(x)) \hat{\sigma}(z(x)) v}{z^n(x) \kappa(z(x))\,(z(x) - s)} \frac{\mathrm{d}z}{\mathrm{d}x}\,. \tag{3.64}$$

As only the inhomogeneity of the $\pi\pi$ channel contributes in our model we introduce the vector v in channel space pointing in the $\pi\pi$ direction. The integration path $z(x)$ should be chosen in order to avoid singularities of the denominator.

This procedure for the evaluation of $\tilde{I}_L(s, m^2)$ has been crossed-checked by comparison to the scalar triangle graph, as explained in Appendix C.

The spectral density dispersion integral (SD) will be our preferred technique since it not only allows for the treatment of anomalous thresholds, but it is universal up to the spectral density and thus can be applied to different decays.

3.5.1. Dispersive construction of the left-hand cut amplitude

As already pointed out in Sect. 3.4 the crossed-channel amplitude $\phi(t)$ does not only have a right-hand cut in the complex t-plane but also inherits an artificial left-hand cut coming from the non-relativistic loop function. As it is a purely non-relativistic artifact we want to remove it, especially since it can have a non-negligible contribution for the full inhomogeneous Omnès problem. We

therefore compare the crossed-channel amplitude $\phi(t)$ as defined in Eq. (3.23) with its dispersive reconstruction with only a right-hand cut

$$\phi_{\text{disp}}(t) = -\frac{1}{\pi} \int\limits_{(m_{\Upsilon(1s)}+m_\pi)^2}^{\infty} \mathrm{d}m^2 \, \frac{\operatorname{Im}\phi(m^2)}{t-m^2} \,. \tag{3.65}$$

As previously shown the amplitude falls off quickly outside of the Z_B region and thus no subtraction is needed.

For the further calculation only the values along the Khuri-Treiman path, which is depicted in Fig. 3.5, are necessary. In order to have a better comparison between $\phi(t_+(s))$ and $\phi_{\text{disp}}(t_+(s))$ we consider three different energy range. Range 1 is restricted to $4m_\pi^2 \leq s \leq (m_i - m_f)^2$ and therefore real and positive values of $t_\pm(s)$. While range 2 with $(m_i - m_f)^2 \leq s \leq (m_i + m_f)^2$ allows also for complex values of $t_\pm(s)$ range 3 with $(m_i + m_f)^2 \leq s$ allows only for real and negative $t_\pm(s)$.

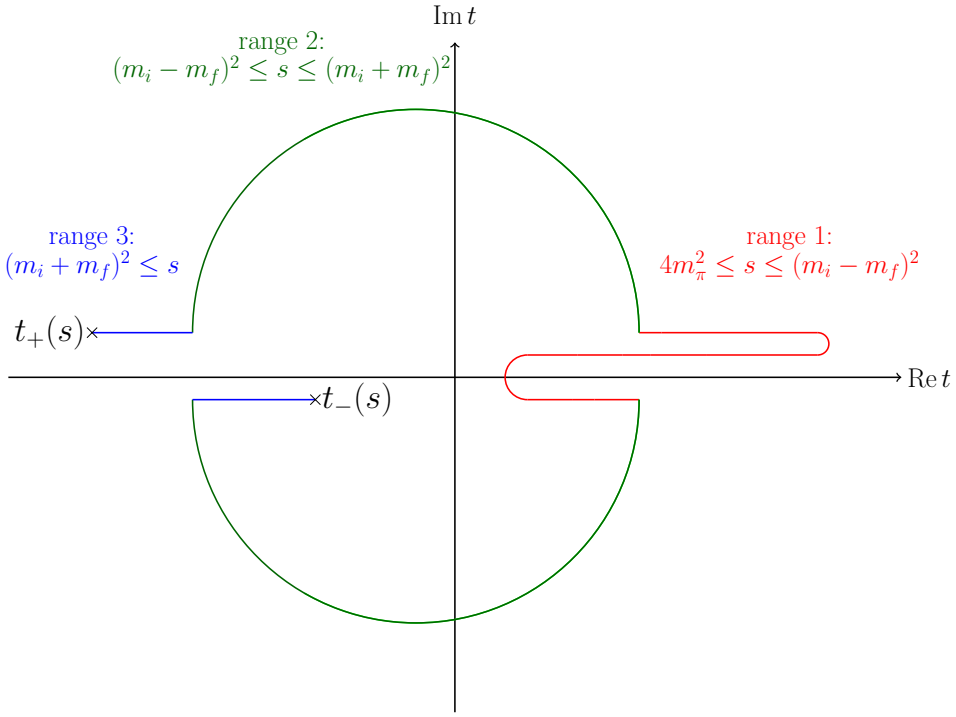

Figure 3.5.: Khuri-Treimann integration path between the endpoints $t_-(s)$ and $t_+(s)$. In the first range $4m_\pi^2 \leq s \leq (m_i - m_f)^2$ the end points will lie on the red path. For $(m_i - m_f)^2 \leq s \leq (m_i + m_f)^2$ they lie on green and for $(m_i + m_f)^2 \leq s$ on the blue path.

In range 1 $t_\pm(s)$ are restricted to values $m_\pi^2 + m_i m_f \leq t_+ \leq (m_i - m_\pi)^2$ and $(m_f + m_\pi)^2 \leq t_- \leq \frac{1}{2}\left(m_i^2 + m_f^2 - 2m_\pi^2\right)$. Hence it is only necessary to calculate $\phi(t)$ and $\phi_{\text{disp}}(t)$ for $(m_f + m_\pi)^2 \leq t \leq (m_i - m_\pi)^2$ which is shown

in Fig. 3.6. Note that we use the $+i\epsilon$-prescription in order to determine values for the real axis. Values for $t_-(s)$ using the $-i\epsilon$-prescription can be determined by the Schwarz reflection principle. As especially this energy range covers the $\pi\pi$ phase space in the decay $\Upsilon(5S) \to \Upsilon(1S)\pi\pi$ it makes sense to illustrate the differences between the crossed-channel amplitude $\phi(t)$ and its dispersive reconstruction with only a right-hand cut $\phi_{\text{disp}}(t)$ in more detail. Therefore we plot their relative difference $2|(\phi(t)-\phi_{\text{disp}}(t))/(\phi(t)+\phi_{\text{disp}}(t))|$ in Fig. 3.7. Thus even at low s, which is equivalent with the largest values of t and therefore the farthest away from the left-hand cut, both functions differ at most to 5%.

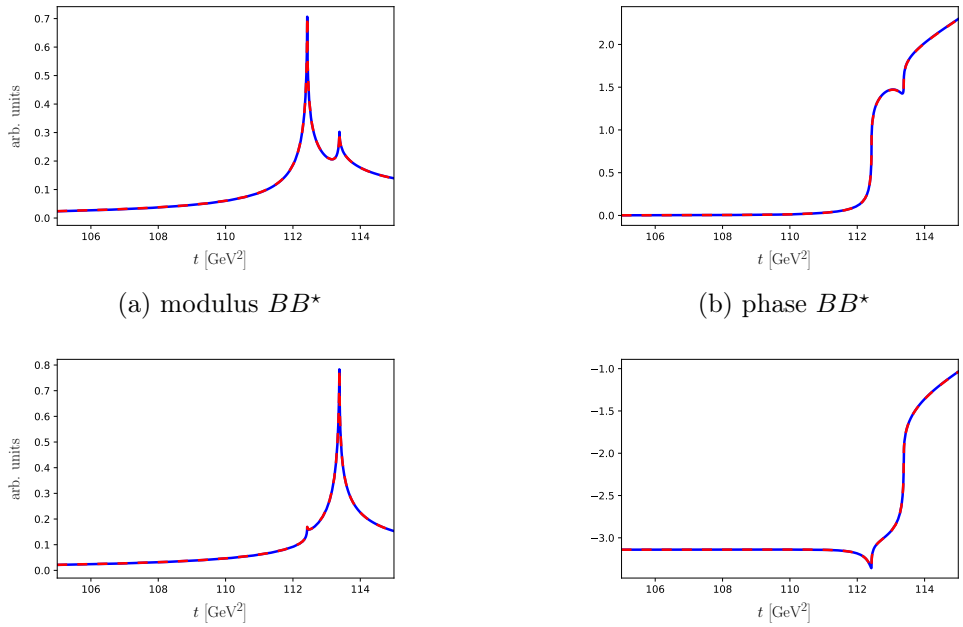

(a) modulus $BB^\star$ (b) phase $BB^\star$

(c) modulus $B^\star B^\star$ (d) phase $B^\star B^\star$

Figure 3.6.: Modulus and phase of $\phi(t)$ (blue) and $\phi_{\text{disp}}(t)$ (red) in range 1 with either the $BB^\star$ or the $B^\star B^\star$ intermediate state.

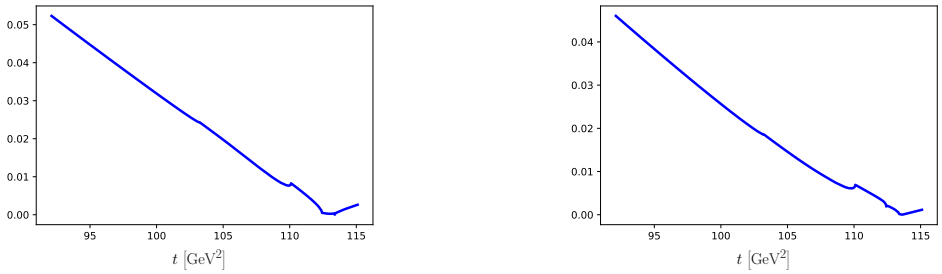

(a) modulus $BB^\star$ (b) modulus $B^\star B^\star$

Figure 3.7.: Modulus of $2|(\phi(t)-\phi_{\text{disp}}(t))/(\phi(t)+\phi_{\text{disp}}(t))|$ in range 1 with either the $BB^\star$ or the $B^\star B^\star$ intermediate state.

Range 2 describes the complex arc of the KT path in the complex t plane. We only need to consider the values of $\phi(t_+(s))$ and $\phi_{\text{disp}}(t_+(s))$ as the lower arc can be inferred by the Schwarz reflection principle. Fig. 3.8 shows both functions. As the energy is increased, $t_\pm(s)$ move closer to the left-hand cut. Therefore the deviation between them quickly becomes large, which is especially apparent in the phase motion at high energies.

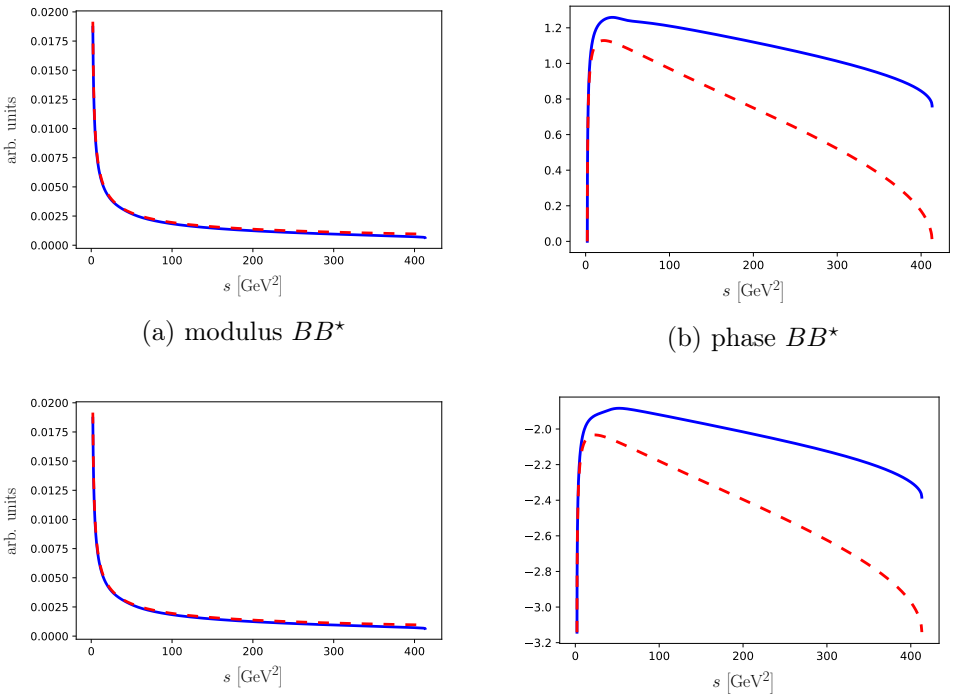

(a) modulus $BB^\star$

(b) phase $BB^\star$

(c) modulus $B^\star B^\star$

(d) phase $B^\star B^\star$

Figure 3.8.: Modulus and phase of $\phi(t_+(s))$ (blue) and $\phi_{\text{disp}}(t_+(s))$ (red) for range 2 with either the $BB^\star$ or the $B^\star B^\star$ intermediate state.

Lastly energy range 3 deals with $s \geq (m_i + m_f)^2$. Hence $t_\pm(s)$ are restricted to $t_+(s) \leq m_\pi^2 - m_i m_f$ and $m_\pi^2 - m_i m_f \leq t_-(s) \leq 0$. The comparison between $\phi(t_+)$ and $\phi_{\text{disp}}(t_+)$ is shown in Fig. 3.9. For $\phi(t_-)$ and $\phi_{\text{disp}}(t_-)$ we refer to Fig. 3.10. The non-trivial phase motion of $\phi(t_\pm)$ clearly shows the presence of a left-hand cut. The dispersive reconstruction $\phi_{\text{disp}}(t_\pm)$ on the other hand has only has real values as required by construction.

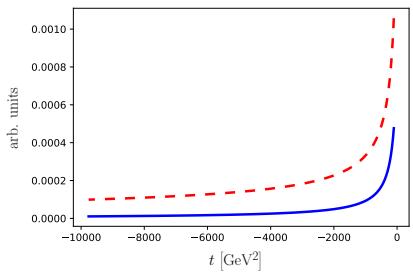

(a) modulus $BB^\star$

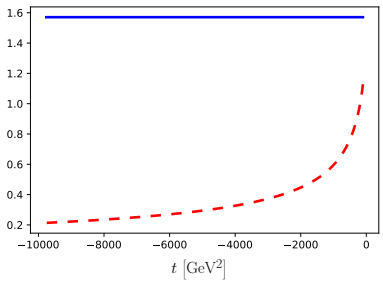

(b) phase $BB^\star$

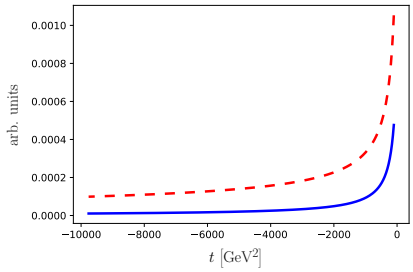

(c) modulus $B^\star B^\star$

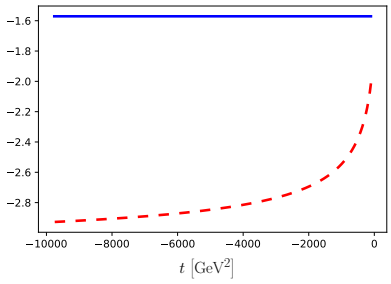

(d) phase $B^\star B^\star$

Figure 3.9.: Modulus and phase of $\phi(t_+)$ (blue) and $\phi_{\text{disp}}(t_+)$ (red) for range 3 with either the $BB^\star$ or the $B^\star B^\star$ intermediate state.

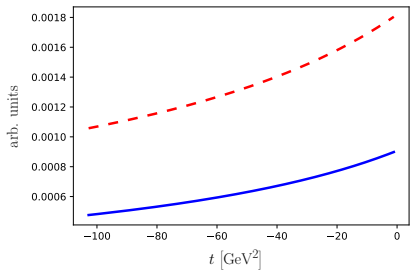

(a) modulus $BB^\star$

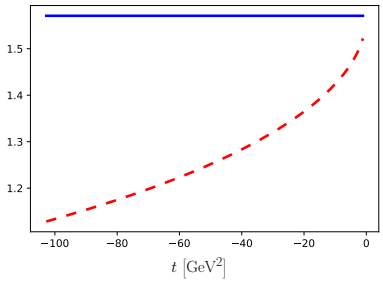

(b) phase $BB^\star$

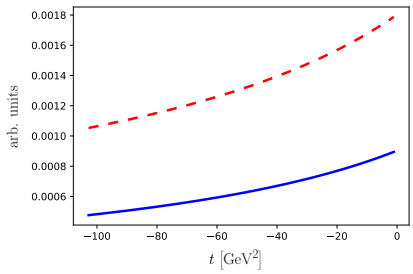

(c) modulus $B^\star B^\star$

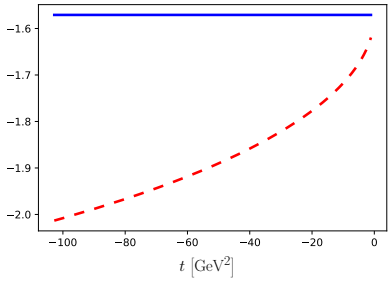

(d) phase $B^\star B^\star$

Figure 3.10.: Modulus and phase of $\phi(t_-)$ (blue) and $\phi_{\text{disp}}(t_-)$ (red) for range 3 with either the $BB^\star$ or the $B^\star B^\star$ intermediate state.

3.5.2. Partial-wave projection of the KT method

While the parametrization of Eq. (3.55) is formally valid for all energies, numerically is proofs to be inefficient because of large cancellations along the integration path. Hence we choose a different parametrization in order to calculate the partial-wave projection $K_0(s)$.

For $4m_\pi^2 < s < \frac{m_\pi(m_i^2-m_f^2)}{m_f+m_\pi}$ the integration between $t_-(s)$ and $t_+(s)$ is entirely on the real axis determined with the $+i\epsilon$ prescription. As the limit

$$\lim_{\epsilon\to 0}\phi(t+i\epsilon) = \phi(t) \tag{3.66}$$

is considered, the inhomogeneity may be written as

$$K_0(s) = \frac{4}{\kappa(s)}\int\limits_{t_-(s)}^{t_+(s)} \mathrm{d}t\,\phi(t)\,. \tag{3.67}$$

For $\frac{m_\pi(m_i^2-m_f^2)}{m_f+m_\pi} < s < (m_i-m_f)^2$ $t_-(s)$ turns around the threshold at $(m_f+m_\pi)^2$ onto the real axis approaching from the lower half t-plane. As $\phi(t)$ fulfills the Schwarz reflection principle the partial-wave projection may be expressed by

$$K_0(s) = \frac{4}{\kappa}\left[\int\limits_{t_-(s)}^{(m_f+m_\pi)^2} \mathrm{d}t\,\phi^\star(t) + \int\limits_{(m_f+m_\pi)^2}^{t_+(s)} \mathrm{d}t\phi(t)\right]. \tag{3.68}$$

Note that for $s=(m_i-m_f)^2$ the real part of both end-points are equal $t_+(s) = t_-(s) = m_\pi^2 + m_i m_f$. Therefore Eq. (3.68) reduces to an integral over the discontinuity of $\phi(t)$

$$K_0((m_i-m_f)^2) = \frac{4}{\kappa}\int\limits_{(m_f+m_\pi)^2}^{m_i m_f+m_\pi^2} \mathrm{d}t\,2i\,\mathrm{Im}\,\phi(t)\,. \tag{3.69}$$

For $(m_i-m_f)^2 < s < (m_i+m_f)^2$ the partial-wave projection also includes the integration along the complex arc. However, since in this energy range $t_+(s) = t_-^\star(s)$ holds it is possible to apply the Schwarz reflection principle again resulting in

$$K_0(s) = \frac{8i}{\kappa}\left[\int\limits_{(m_i-m_f)^2}^{s} \mathrm{d}x\;\mathrm{Im}\left(\frac{\partial t_+(x)}{\partial x}\,\phi(t_+(x))\right) + \int\limits_{(m_f+m_\pi)^2}^{m_i m_f+m_\pi^2} \mathrm{d}t\,\mathrm{Im}\,\phi(t)\right]. \tag{3.70}$$

For larger values $s > (m_i+m_f)^2$ one needs to add an integration below the real axis coming from $t_-(s)$ to $t_-((m_i+m_f)^2) = m_\pi^2 - m_i m_f$ and one above the real axis from $t_+((m_i+m_f)^2) = m_\pi^2 - m_i m_f$ to $t_+(s)$. In this case the

inhomogeneity reads

$$K_0(s) = \frac{8i}{\kappa}\left[\int\limits_{(m_i-m_f)^2}^{(m_i+m_f)^2} \mathrm{d}x\ \mathrm{Im}\left(\frac{\partial t_+(x)}{\partial x}\,\phi(t_+(x))\right) + \int\limits_{(m_f+m_\pi)^2}^{m_i m_f+m_\pi^2} \mathrm{d}t\,\mathrm{Im}\,\phi(t)\right] + \frac{4}{\kappa}\left[\int\limits_{t_-(s)}^{-m_i m_f+m_\pi^2} \mathrm{d}t\,\phi^\star(t) + \int\limits_{-m_i m_f+m_\pi^2}^{t_+(s)} \mathrm{d}t\,\phi(t)\right]. \tag{3.71}$$

The prefactor $1/\kappa(s)$ has singularities arising at $s = 4m_\pi^2$ and $s = (m_i \pm m_f)^2$. They are formally avoided by the prescription $m_i^2 \to m_i^2 + i\epsilon$. In order to analyze the s dependence we define the function

$$\hat{K}_0(s) = \frac{\kappa(s)}{2} K_0(s) \tag{3.72}$$

which is free of the kinematical singularities in $1/\kappa(s)$. A plot is shown in Fig. 3.11. For $s < (m_i - m_f)^2$ it shows both real and imaginary parts. However above that value it is purely imaginary as already expected by the Schwarz reflection principle. It is furthermore interesting that there is a difference between the crossed-channel amplitude $\phi(t)$ and its dispersive reconstruction considering only a right-hand cut $\phi_{\mathrm{disp}}(t)$. For $s < (m_i - m_f)^2$ the deviation tends to be small, but non-negligible. This is an artifact of the previously shown difference between the two (see Sect. 3.5.1). The deviations accumulate upon integration over the KT path and become clearly visible. This is even more severe for $s > (m_i - m_f)^2$, since the integrand is evaluated closer to the left-hand cut in t. However the line shape of both of them looks very similar. Note that the Z_B and Z_B' resonance contribute to the two peaks below $(m_i - m_f)^2$.

Another interesting observation is that $\hat{K}_0(s)$ for the $BB^\star$ and the $B^\star B^\star$ intermediate state almost look the same except for a sign difference. This is a consequence of heavy quark spin symmetry, which is slightly broken by the $BB^\star$ mass difference.

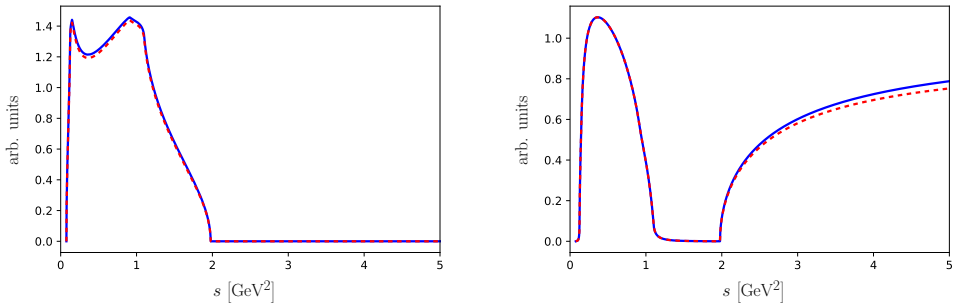

(a) real part $BB^\star$

(b) imaginary part $BB^\star$

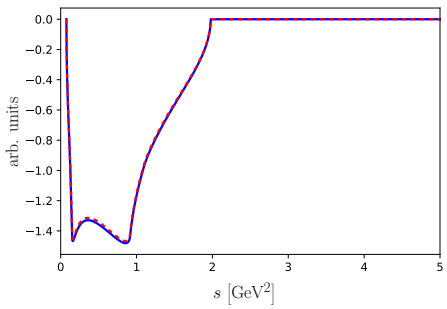

(c) real part $B^\star B^\star$

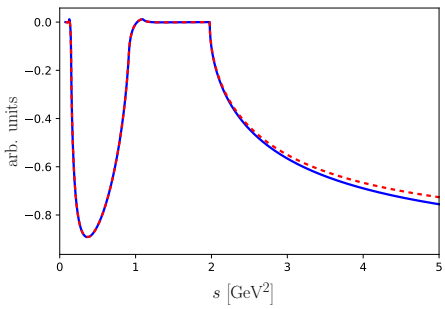

(d) imaginary part $B^\star B^\star$

Figure 3.11.: S-wave projection $\hat{K}_0 = \frac{\kappa(s)}{2} K_0(s)$ of $\phi(t)$ (blue) and $\phi_{\text{disp}}(t)$ (red) for the $BB^\star$ and $B^\star B^\star$ intermediate state.

3.6. Evaluation of the inhomogeneous integral

3.6.1. Omnès matrix

Before solving the inhomogeneous Omnès problem of Eq. (3.21) the Omnès matrix for the isoscalar scalar channel needs to be constructed. As the available dipion energy of the $\Upsilon(5S)$ decay is limited to 0.51 GeV for $\Upsilon(3s)$, 0.84 GeV for $\Upsilon(2S)$ and 1.40 GeV for $\Upsilon(1S)$ in the final state we discuss the Omnès matrices for a single channel (only $\pi\pi$), two channels (including $K\bar{K}$) and a three channels (mimicking the effects at higher energies).

For a single channel the scattering amplitude above the pion-threshold may be expressed as

$$t_0(s) = \frac{e^{2i\delta(s)} - 1}{2i\sigma_\pi(s)} \tag{3.73}$$

whereas $\delta(s)$ is the isoscalar scalar pion-phase shift determined by not only several experiments [210, 211, 220] but also dispersively [124, 184, 185]. Note that most of the mentioned studies do not only include the $\pi\pi$ channel but also further inelasticities coming from e.g. $K\bar{K}$. We will use the phase shifts and inelasticities presented in Ref. [205] not only for the single-channel but also for the two-channel case. The single-channel Omnès function can be calculated analytically as

$$\Omega(s) = \exp\left(\frac{s}{\pi}\int\limits_{4m_\pi^2}^{\infty}\frac{\mathrm{d}z}{z}\,\frac{\delta(z)}{z-s}\right). \tag{3.74}$$

The scattering amplitude for two-channels has been introduced in Eq. (3.16). As shown in Ref. [90] this Muskhelishvili-Omnès problem (MO) cannot be solved analytically anymore but needs to be obtained by solving the integral equation

$$\Omega(s) = \frac{1}{\pi}\int\limits_{4m_\pi^2}^{\infty}\mathrm{d}z\, t_0^\star(z)\hat{\sigma}(z)\Omega(z) \tag{3.75}$$

numerically with the additional requirement

$$\Omega(0) = 1 \tag{3.76}$$

as explained in Sect. 1.3.3.

As above roughly 1.3 GeV further inelastic channels become relevant, we use an effective parametrization [232], introduced in chapter 2, in order to extend the description. Explicitly we take the central values of Fit 1 of that reference with an additional $\rho\rho$-channel.

A comparison between the one-, two- and three-channel scattering matrices are depicted in Figs. 3.12, 3.13 and 3.14. Below the $K\bar{K}$ threshold the single-channel and the two-channel amplitudes are identical as expected, see Fig. 3.12. The three-channel scattering amplitude also has small deviations below 1 GeV. Additionally it shows signs of the $f_0(1500)$ resonance, which both the two- and single-channel solutions lack. These differences also show up in the other

matrix elements as depicted in Fig. 3.13. The additional scattering channels (Fig. 3.14) show strong contributions from the $f_0(1500)$. However due to final state rescattering they also include the lower lying resonances such as $f_0(500)$ and $f_0(980)$.

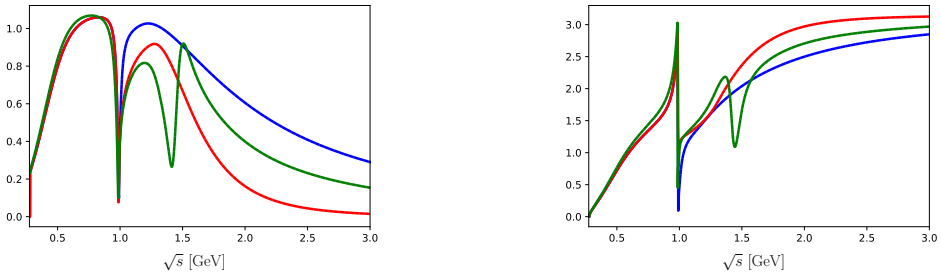

(a) modulus t_0^{11} (b) phase t_0^{11}

Figure 3.12.: Modulus and phase for the one-channel (blue), two-channel (red) and three channel (green) scattering amplitude t_0^{ij}

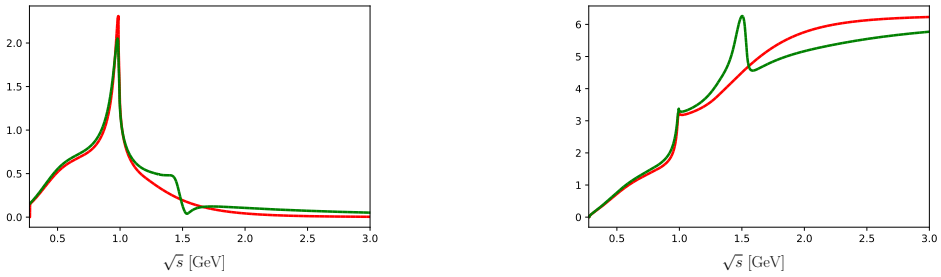

(a) modulus t_0^{12} (b) phase t_0^{12}

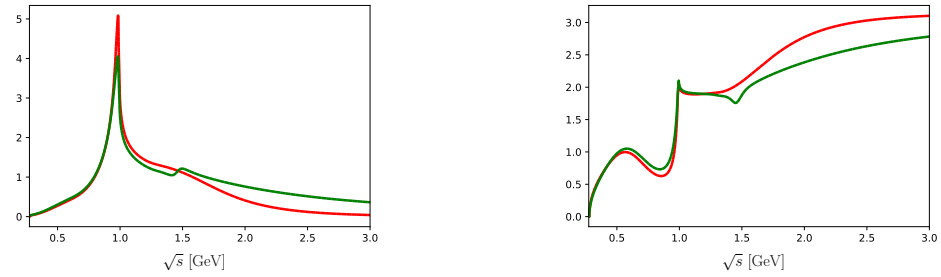

(c) modulus t_0^{22} (d) phase t_0^{22}

Figure 3.13.: Modulus and phase for the two-channel (red) and three-channel (green) scattering amplitude t_0^{ij}

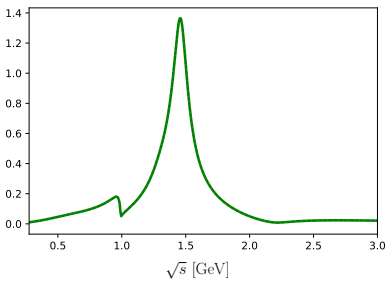

(a) modulus t_0^{13}

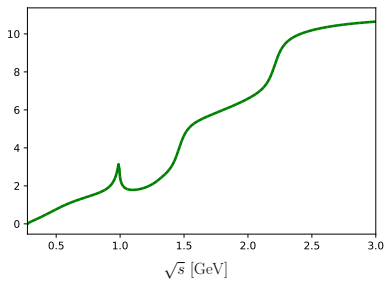

(b) phase t_0^{13}

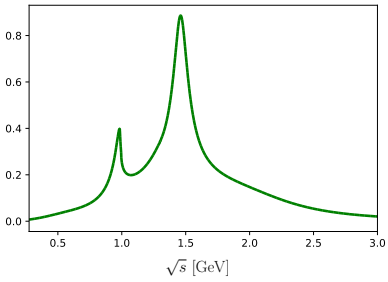

(c) modulus t_0^{23}

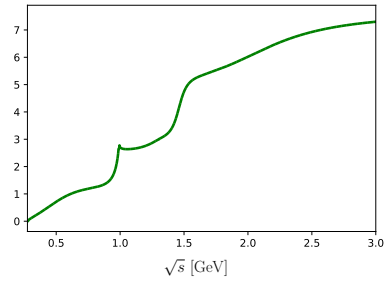

(d) phase t_0^{23}

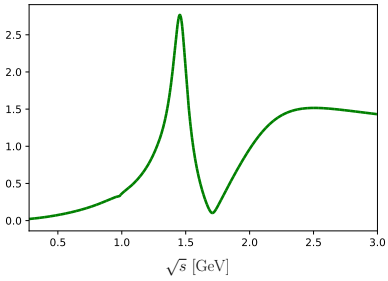

(e) modulus t_0^{33}

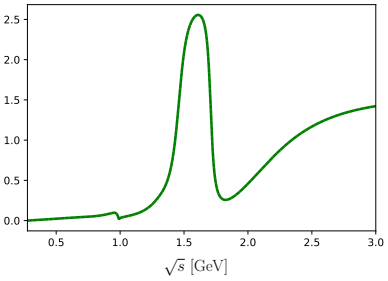

(f) phase t_0^{33}

Figure 3.14.: Modulus and phase of the three-channel scattering amplitude t_0^{ij}

The presented Omnès matrices are computed with these scattering amplitudes as input. Comparing the single-, two- and three-channel Omnès function leads to Fig. 3.15. The three-channel solution is a modification of the two-channel one. As already for the scattering amplitude, it includes the $f_0(1500)$ resonance, allowing to extend the energy range for a possible description. However, there are also deviations below 1 GeV, which propagate from the scattering amplitude. These observations are also visible in the other channels (Fig. 3.16).

The single-channel solution includes a broad $f_0(500)$ and a $f_0(980)$ resonance. The latter shows up as a sharp peak. Since the phase motion still knows about the $K\bar{K}$ threshold, the line shape is distorted from the typical Breit-Wigner resonance. Furthermore, it is not useful to directly compare the single-channel solution to the multi-channel ones. This is because they have a different high energy behavior. The single-channel Omnès function scales as s^{-2} for high energies, while the others follow a s^{-1} behavior by construction. It is possible to construct comparable objects in terms of a homogeneous Omnès problem. If the multi-channel needs a polynomial of order n, then the single-channel one needs one of order $n+1$. This additional parameter would then also allow to include a zero in the amplitude. Therefore the $f_0(980)$ resonance can also show up as dip instead of a peak. To avoid the additional subtraction in the inhomogeneous Omnès problem, we will only consider the two- and three-channel amplitude in the following.

The additional channels in the three-channel parametrization are shown in Fig. 3.17. The visible effects are coming from the $f_0(980)$ and $f_0(1500)$ resonance.

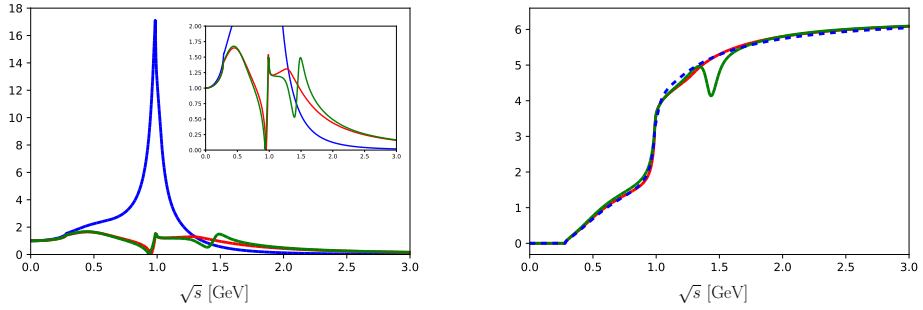

(a) modulus Ω_{11} (b) phase Ω_{11}

Figure 3.15.: Modulus and phase for the one-channel (blue), two-channel (red) and three channel (green) Omnès matrix Ω_{11}

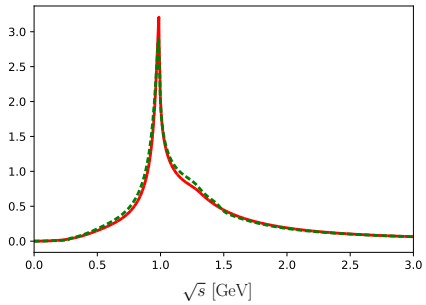

(a) modulus Ω_{12}

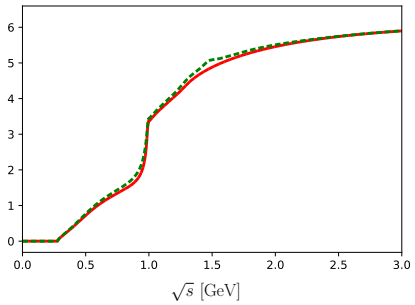

(b) phase Ω_{12}

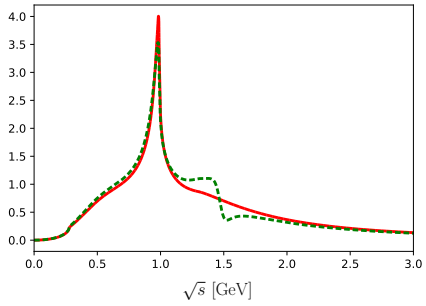

(c) modulus Ω_{21}

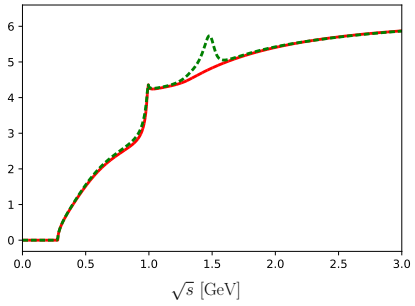

(d) phase Ω_{21}

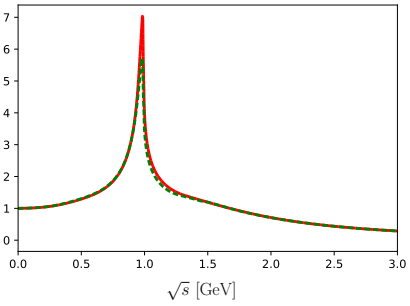

(e) modulus Ω_{22}

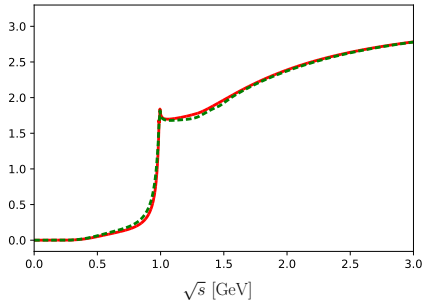

(f) phase Ω_{22}

Figure 3.16.: Modulus and phase for the two-channel (red) and three-channel (green) Omnès matrix Ω_{ij}

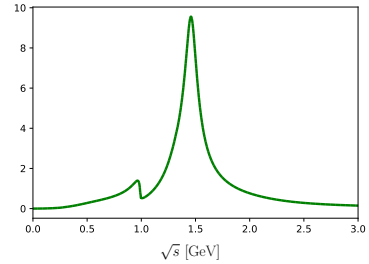

(a) modulus Ω_{13}

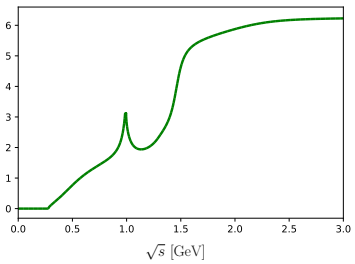

(b) phase Ω_{13}

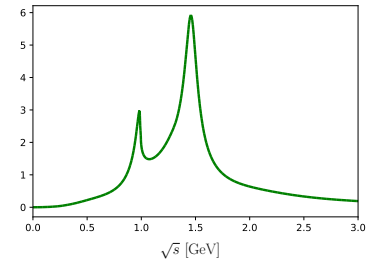

(c) modulus Ω_{23}

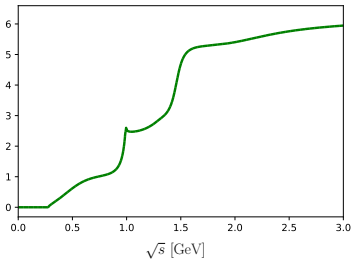

(d) phase Ω_{23}

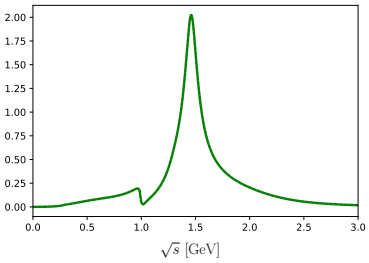

(e) modulus Ω_{31}

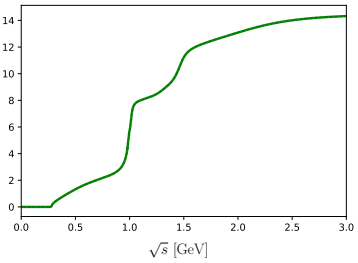

(f) phase Ω_{31}

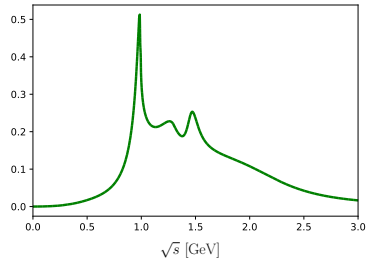

(g) modulus Ω_{32}

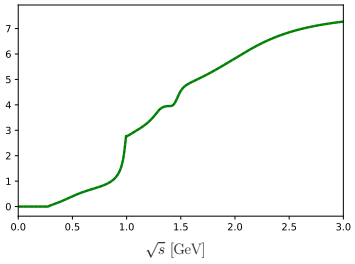

(h) phase Ω_{32}

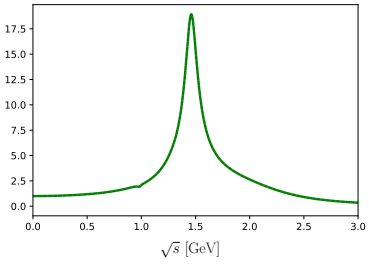

(i) modulus Ω_{33}

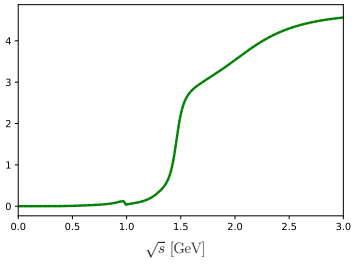

(j) phase Ω_{33}

Figure 3.17.: Modulus and phase of the three-channel Omnès matrix Ω_{ij}

3.6.2. Evaluation of the Khuri-Treiman integral

We first proceed to solve the dispersive integral

$$I_0^{\mathrm{KT}}(s) = \frac{s^n}{\pi} \int\limits_{4m_\pi^2}^{\infty} \frac{\mathrm{d}s'}{(s')^n} \frac{\Omega^{-1}(s') t_0(s') \hat{\sigma}(s') K_0(s')}{s' - s}\,, \tag{3.77}$$

where $K_0(s)$ has been introduced as the S-wave projection of either the crossed-channel amplitude $\phi(t)$ or its dispersive reconstruction with only a right-hand cut $\phi_{\mathrm{disp}}(t)$ in Sect. 3.5.2. For the Omnès matrix $\Omega(s)$ and the scattering amplitude $t_0(s)$ we either take the two- or three-channel amplitude as defined in the Sect. 3.6.1. The number of subtractions n, which are needed to render the dispersion integral convergent, can be determined by the high-energy behavior of $|\Omega^{-1}(s') t_0(s') \hat{\sigma}(s') K_0(s')|$ for $s' \to \infty$.

Since the Omnès matrix is determined by an unsubtracted dispersion relation, each of its elements will behave as s^{-1} for high-energies. Its inverse thus will scale as s for each element.

For the scattering amplitude t_0 we proceed with the conservative estimate $t_0(s) \propto s^{-1}$ for high s. For the two-channel case defined in Eq. (3.16) it is possible to show that for $t_0^{12} \propto s^{-1}$ for high s, $(t_0)_{11}$ and t_0^{22} need to scale as s^{-2}. Numerically we extrapolate the three-channel amplitude in a similar manner.

The high energy behavior of $K_0(s)$ can be estimated through Eq. (3.71). The integral from $t_-(s)$ to $-m_i m_f + m_\pi^2$ converges to a constant for $s \to \infty$ as $\lim\limits_{s\to\infty} t_-(s) = 0$. In order to estimate the high-energy behavior of the integral between $-m_i m_f + m_\pi^2$ and $t_+(s)$ we proceed by assuming $\phi(t) \propto 1/\sqrt{t}$ for $|t| \to \infty$. Overall $K_0(s)$ scales as $\sqrt{(}t_+(s))/\kappa(s)$ and thus $\sqrt{(}s)/\kappa(s)$ for high s.

With $\lim\limits_{s\to\infty} \hat{\sigma}(s) = 1$ the whole integrand scales as $\sqrt{s}/\kappa(s)$ at high energies. Therefore one subtraction is necessary such that the dispersion integral converges.

In order to treat this integral numerically the integral is split into two parts

$$I_0^{\mathrm{KT}}(s) = J_0(s, 4m_\pi^2, \Gamma^2) + J_0(s, \Gamma^2, \infty) \tag{3.78}$$

with

$$J_0(s, a, b) = \int\limits_a^b \mathrm{d}s' \, \frac{F(s')}{\sqrt{s_{pt} - s'}(s' - s)} \tag{3.79}$$

and

$$F(s') = \frac{s^n}{\pi (s')^n} \frac{\Omega^{-1}(s') t_0(s') \hat{\sigma}(s') \hat{K}_0(s')}{\sqrt{1 - \frac{4m_\pi^2}{s}}\sqrt{s_t - s'}}\,. \tag{3.80}$$

Here we introduced the short hand notations

$$s_{pt} = (m_i - m_f)^2 \tag{3.81}$$

and

$$s_t = (m_i + m_f)^2\,. \tag{3.82}$$

Note that $K_0(s)$ is regular at s_t if the left-hand cut in $\phi(t)$ is absent. For our case we choose the separation scale at $\Gamma^2 = 280\,\mathrm{GeV}^2$, which lies above $(m_i - m_f)^2$ and below $(m_i + m_f)^2$. As the pion phase space in the decay $\Upsilon(5S) \to \Upsilon(1S)\pi\pi$ is limited to s_{pt} the cutoff is set to be far away from the interesting region.

In order to estimate the contribution of the high-energy integral we make the assumption

$$J_0(s, \Gamma^2, \infty) \approx \frac{s^n}{\pi} \Omega^{-1}(\Gamma^2) t_0(\Gamma^2) \hat{\sigma}(\Gamma^2) K_0(\Gamma^2) \int\limits_{\Gamma^2}^{\infty} \frac{\mathrm{d}s'}{(s')^n (s' - s)} \,. \tag{3.83}$$

Since $\hat{K}_0\left((m_i - m_f)^2\right)$ is non-vanishing as shown in Eq. (3.69) one needs to avoid the singularity properly by using the prescription $m_i^2 \to m_i^2 + i\epsilon$.

For real values $s < 4m_\pi^2$ or complex ones the other integral can be evaluated through

$$J_0(s, 4m_\pi^2, \Gamma^2) = Q_0(s, 4m_\pi^2, \Gamma^2) \tag{3.84}$$

with

$$Q(s, a, b) = \int\limits_a^b \mathrm{d}s' \, \frac{F(s') - F(s_{pt})}{\sqrt{s_{pt} - s'}(s' - s)} + \hat{Q}(s, a, b) \tag{3.85}$$

and

$$\hat{Q}(s, a, b) = \frac{F(s_{pt})}{\sqrt{s_{pt} - s}} \log \left(\frac{\sqrt{s - s_{pt}} - \sqrt{b - s_{pt}}}{\sqrt{s - s_{pt}} + \sqrt{b - s_{pt}}} \frac{\sqrt{s - s_{pt}} + \sqrt{a - s_{pt}}}{\sqrt{s - s_{pt}} - \sqrt{a - s_{pt}}} \right) . \tag{3.86}$$

Note that the integral in Eq. (3.85) is regular as $F(s')$ can be expanded near s_{pt} in a power series

$$F(s') \approx F(s_{pt}) + c_1 \sqrt{s_{pt} - s'} + c_2 (s_{pt} - s) + \dots \,. \tag{3.87}$$

For real $s > 4m_\pi^2$ also the Cauchy kernel singularity needs to be taken into account. To achieve this goal we split the integral to separate the singularity at $s' = s$ and $s' = s_{pt}$. To this end define

$$s_v = \frac{s_{pt} + s}{2} \,. \tag{3.88}$$

If $s > s_{pt}$ the integral is given as

$$J_0(s, 4m_\pi^2, \Gamma^2) = Q(s, 4m_\pi^2, s_v) + R(s, s_v, \Gamma^2) \tag{3.89}$$

with

$$R(s, a, b) = \int\limits_a^b \mathrm{d}s' \, \frac{F(s') - F(s)}{\sqrt{s_{pt} - s}(s' - s)} + \hat{R}(s, a, b) \tag{3.90}$$

and

$$\hat{R}(s, a, b) = \frac{F(s)}{\sqrt{s_{pt} - s}} \left[\log \left(- \frac{\sqrt{s - s_{pt}} - \sqrt{b - s_{pt}}}{\sqrt{s - s_{pt}} + \sqrt{b - s_{pt}}} \frac{\sqrt{s - s_{pt}} + \sqrt{a - s_{pt}}}{\sqrt{s - s_{pt}} - \sqrt{a - s_{pt}}} \right) + i\pi \right] . \tag{3.91}$$

On the contrary if $s < s_{pt}$ the integral may be evaluated as

$$J_0(s, 4m_\pi^2, \Gamma^2) = Q(s, s_v, \Gamma^2) + R(s, 4m_\pi^2, \Gamma^2)\,. \tag{3.92}$$

The inhomogeneous integral $I_0^{KT}(s)$ is a vector consisting of two entries for the two-channel problem or three for the three-channel. Results of the computation are shown in Figs. 3.18, 3.19 and 3.20.

Overall, the numerical evaluation of the dispersion integral still shows small instabilities, which need to be taken care of in the future. These are especially visible in the energy range between 0.98 GeV and 1 GeV, which lies close to the $K\bar{K}$ threshold. Further instabilities show up close to $\sqrt{s_{pt}} \approx 1.406\,\text{GeV}$ arising from large cancellations in the presented method for the numerical evaluation of the dispersion integral. Some remaining instabilities, such as between 1.28 and 1.32 GeV, which get amplified in the three-channel case by the presence of the $f_0(1500)$ resonance, still need to be understood. Furthermore, it is noteworthy that because the $K\bar{K}$ and 4π components of the $I_0^{KT}(s)$ vector are smaller by orders compared to the $\pi\pi$ component, they are more sensitive to the numerical instabilities. Apart from these numerical problems, the evaluation seems to be plausible.

Assuming a natural size for the subtraction constants, we indeed see that $I_0^{KT}(s)$ is a small correction to the homogeneous Omnès problem. As the inhomogeneity is driven by the $\pi\pi$ channel only, the contributions to I_0^{KT} for the $K\bar{K}$ and 4π channel can only enter via pion-rescattering. Therefore the magnitude of I_0^{KT} is smaller in the other channels.

The integral also contributes a non-vanishing phase motion for small s, which is a consequence of the $\Upsilon(1S)\pi$ rescattering. Since in this energy range, most of the energy is contained in the $\Upsilon(1S)\pi$-system, they can produce the Z_B and Z_B' resonances. For higher energies, the $\Upsilon(1S)$ becomes a spectator, and therefore, the phase goes to a constant.

The main difference between the two- and the three-channel solution shows up especially near the $f_0(1500)$ resonance, which also was already expected by the difference of the scattering as well as the Omnès matrix (see Sect. 3.6.1).

To test if the numerical implementation of the dispersion integral is correct, we not only calculate the once- but also twice-subtracted integral. Their difference for each matrix element is shown in Figs. 3.21, 3.22 and 3.23. Each one of them shows that the deviation between the over-subtracted and the once-subtracted dispersion integral is a linear polynomial with a constant phase. Thus it can be absorbed in a subtraction polynomial, which is fully consistent with the analytical properties of the dispersion integral. Consequently, the numerical implementation appears to be correct.

As already suspected in Sect. 3.5.2 a visible difference shows up between the solution using the crossed-channel amplitude with a left-hand cut $\phi(t)$ and without $\phi_{\text{disp}}(t)$. This also allows us to estimate the influence of the left-hand cut in $\phi(t)$ on the inhomogeneous Omnès problem, which amounts to a few percent. This illustrates that especially for high-precision experiments a proper analytic structure and continuation of the amplitude is essential.

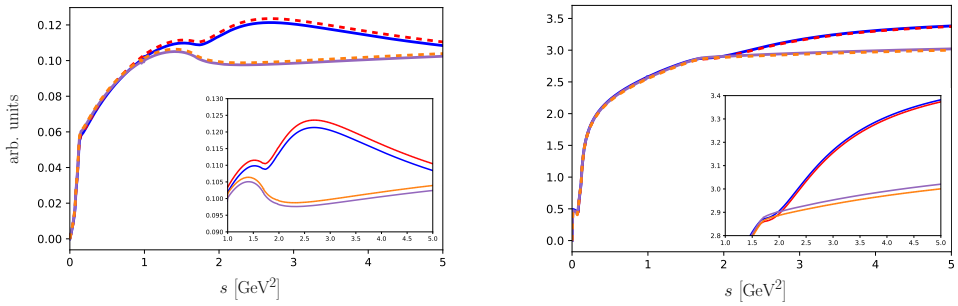

(a) modulus $BB^\star$

(b) phase $BB^\star$

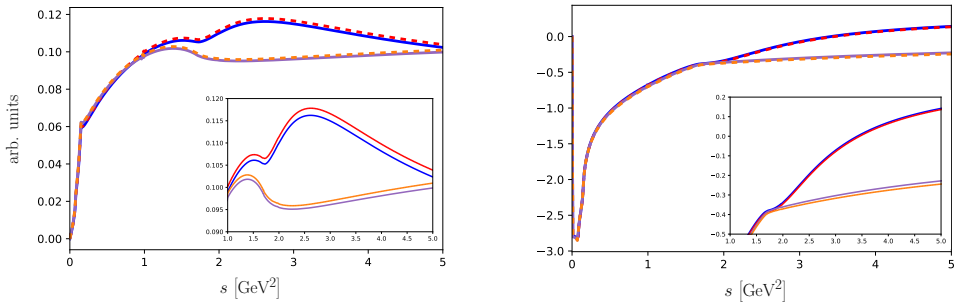

(c) modulus $B^\star B^\star$

(d) phase $B^\star B^\star$

Figure 3.18.: Modulus and phase of the $\pi\pi$-final state component $(I_0^{KT}(s))_1$ with one subtraction. The two-channel solution using $\phi(t)$ is shown in blue, while its dispersive reconstruction with only a right-hand cut $\phi_{\text{disp}}(t)$ is shown in red. Similarly for the three-channel $\phi(t)$ is in purple, while $\phi_{\text{disp}}(t)$ is orange.

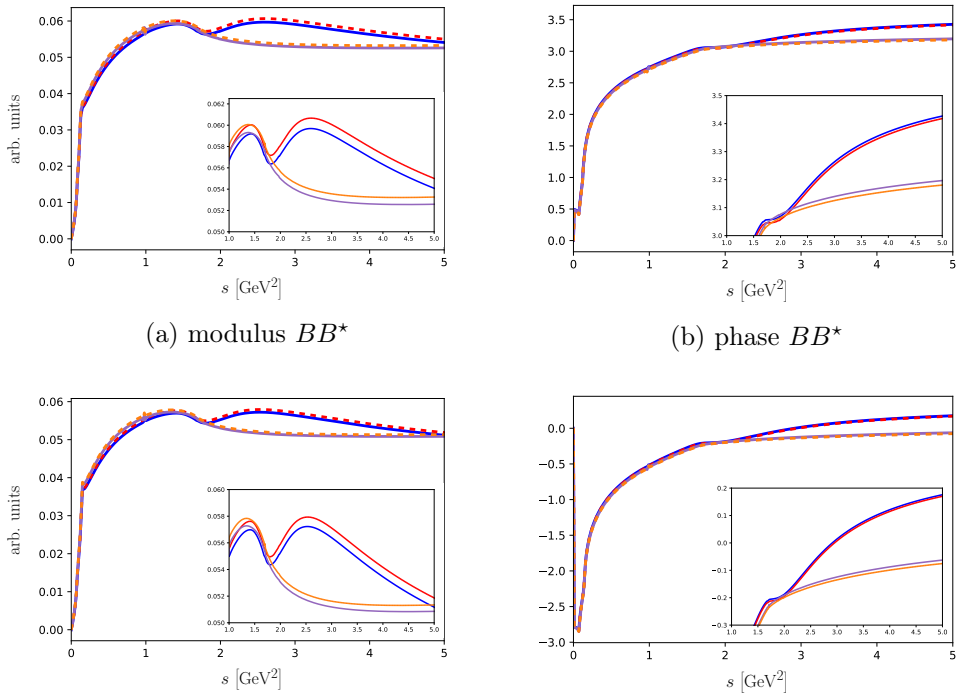

(a) modulus $BB^\star$ (b) phase $BB^\star$

(c) modulus $B^\star B^\star$ (d) phase $B^\star B^\star$

Figure 3.19.: Modulus and phase of the $K\bar{K}$ final-state component $(I_0^{KT}(s))_2$ with one subtraction. The two-channel solution using $\phi(t)$ is shown in blue, while its dispersive reconstruction with only a right-hand cut $\phi_{\text{disp}}(t)$ is shown in red. Similarly for the three-channel $\phi(t)$ is in purple, while $\phi_{\text{disp}}(t)$ is orange.

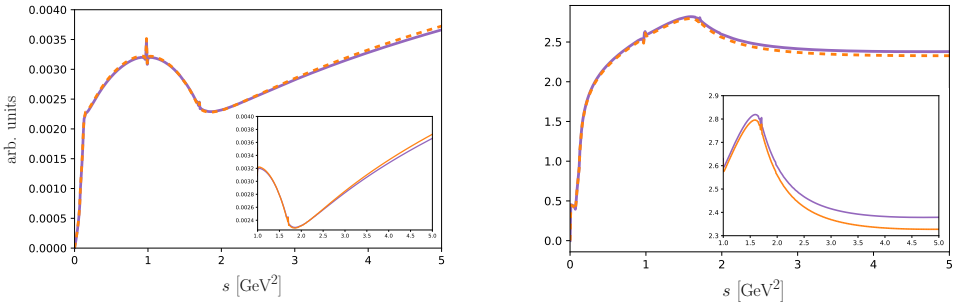

(a) modulus $BB^\star$

(b) phase $BB^\star$

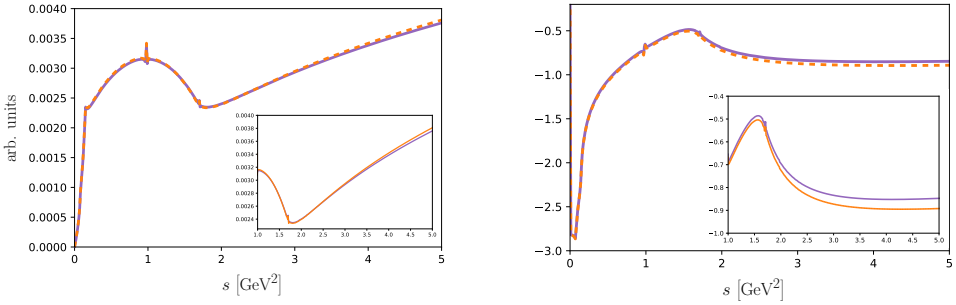

(c) modulus $B^\star B^\star$

(d) phase $B^\star B^\star$

Figure 3.20.: Modulus and phase of the 4π final-state component $(I_0^{KT}(s))_3$ with one subtraction. The three-channel solution shows the solution using $\phi(t)$ in purple, while its dispersive reconstruction with only a right-hand cut $\phi_{\text{disp}}(t)$ is orange.

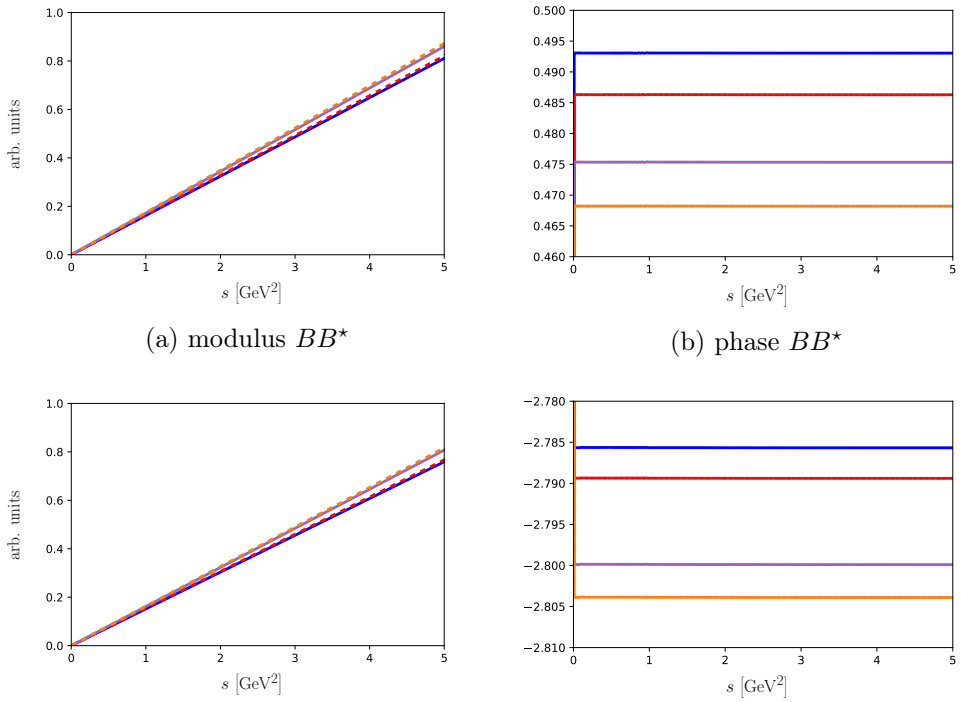

(a) modulus $BB^\star$ (b) phase $BB^\star$

(c) modulus $B^\star B^\star$ (d) phase $B^\star B^\star$

Figure 3.21.: Modulus and phase of the difference between the once- and twice subtracted integral for the $\pi\pi$ final-state component $(I_0^{KT}(s))_1$. The two-channel solution using $\phi(t)$ is shown in blue, while its dispersive reconstruction with only a right-hand cut $\phi_{\text{disp}}(t)$ is shown in red. Similarly for the three-channel $\phi(t)$ is in purple, while $\phi_{\text{disp}}(t)$ is orange.

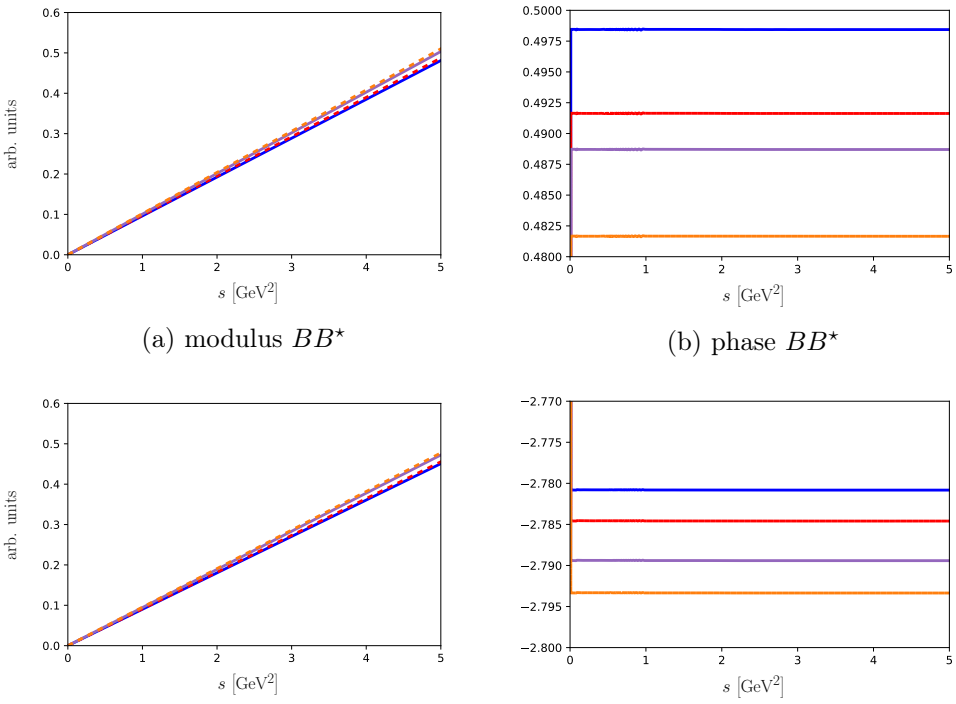

(a) modulus $BB^\star$

(b) phase $BB^\star$

(c) modulus $B^\star B^\star$

(d) phase $B^\star B^\star$

Figure 3.22.: Modulus and phase of the difference between the once- and twice subtracted integral of the $K\bar{K}$ final-state component $(I_0^{KT}(s))_2$. The two-channel solution using $\phi(t)$ is shown in blue, while its dispersive reconstruction with only a right-hand cut $\phi_{\text{disp}}(t)$ is shown in red. Similarly for the three-channel $\phi(t)$ is in purple, while $\phi_{\text{disp}}(t)$ is orange.

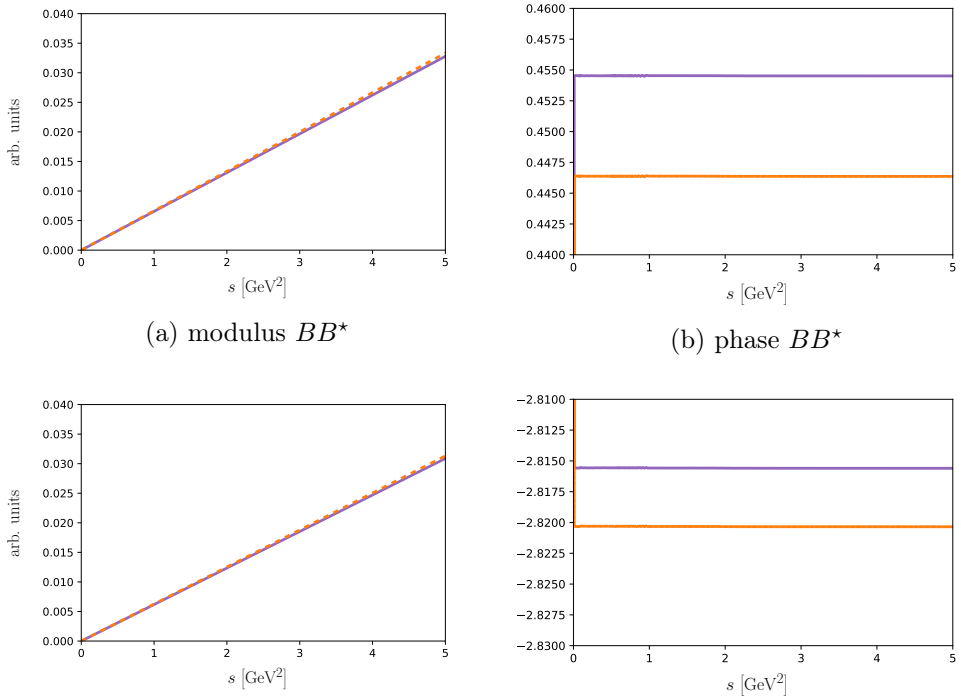

(a) modulus $BB^\star$ (b) phase $BB^\star$

(c) modulus $B^\star B^\star$ (d) phase $B^\star B^\star$

Figure 3.23.: Modulus and phase of the difference between the once- and twice subtracted integral of the 4π final-state component $(I_0^{KT}(s))_3$. The three-channel solution shows the solution using $\phi(t)$ in purple, while its dispersive reconstruction with only a right-hand cut $\phi_{\text{disp}}(t)$ is orange.

3.6.3. Evaluation of the spectral density integral

Consider the spectral density dispersion integral defined by Eq. (3.60). It is a regular integral consisting of the product between the spectral density $\rho(m^2)$ and the inhomogeneous dispersion integral $\tilde{I}_0(s, m^2)$ for a stable particle with mass m. Therefore a restriction of the m^2 integration to the main contributions of the integrand gives a good approximation for the integral.

The spectral density $\rho\left(m^2\right)$ is mostly located in the energy region between $110\,\mathrm{GeV}^2$ and $120\,\mathrm{GeV}^2$ as shown in Fig. 3.24. The strongest contributions come from the Z_b resonances. Due to the nearby threshold, the numerical evaluation needs to take them into account properly. We split the integral with the thresholds as endpoints and integrated each one with a Gauss-Legendre quadrature.

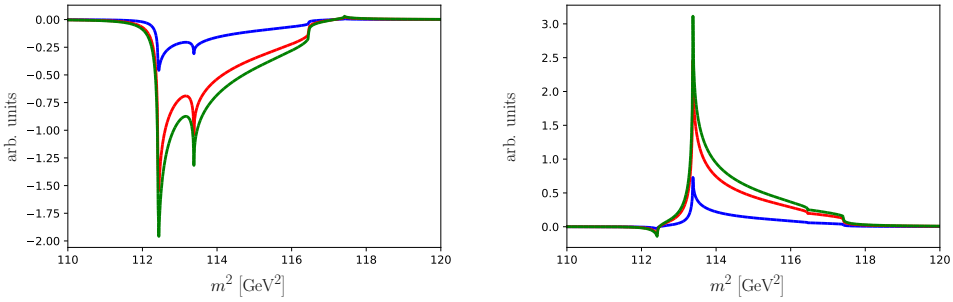

(a) $BB^\star$ (b) $B^\star B^\star$

Figure 3.24.: Spectral density $\rho(m^2)$ with an intermediate $BB^\star$ or $B^\star B^\star$ state for the decay $\Upsilon(5S) \to \Upsilon(1S)\pi\pi$ (blue), $\Upsilon(5S) \to \Upsilon(2S)\pi\pi$ (red) and $\Upsilon(5S) \to \Upsilon(3S)\pi\pi$ (green).

The inhomogeneous dispersion integral $\tilde{I}_0(s, m^2)$ can be evaluated in a similar fashion to Eq. 3.78 in Sect. 3.6.2. The only modification, which is required, is the inclusion of anomalous thresholds for $m^2 < (m_f + m_\pi)^2$ as shown in Eq. (3.63). For this, information about the scattering amplitude t_0 in the complex s-plane is necessary. Since the analytic continuation is very involved, this is problematic. For single-channel problems, it is customary [241] to obtain a scattering amplitude by the inverse amplitude method. Since it is not a valid parametrization for a coupled-channel method, a continuation needs to be done via e.g. Roy-equations, which lies beyond the scope of this thesis. Therefore we want to restrict the range of integration to masses above the crossed-channel thresholds $(m_{\Upsilon(1S)+m_\pi})^2 \approx 92.1\,\mathrm{GeV}^2$, $(m_{\Upsilon(2S)} + m_\pi)^2 \approx 103.2\,\mathrm{GeV}^2$ and $(m_{\Upsilon(3S)+m_\pi})^2 \approx 110.1\,\mathrm{GeV}^2$ and thus avoid anomalous thresholds.

In order to illustrate the behavior of $\tilde{I}_0(s, m^2)$ we show two examples of the first component, where we neglected the anomalous threshold, with $s = 0.5\,\mathrm{GeV}^2$ in Fig. 3.25 and $s = 2.5\,\mathrm{GeV}^2$ in Fig. 3.26.

Three different thresholds show up at $m^2 = (m_i - m_\pi)^2$, $m^2 = m_i m_f + m_\pi^2$ and $m^2 = (m_f + m_\pi)^2$, which we used to distinguish the cases for the inhomogeneity (see Appendix A). The prominent gap in the imaginary part at $m^2 = (m_f + m_\pi)^2$

can be repaired by including an anomalous threshold term.

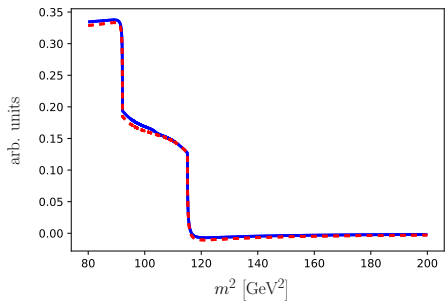

(a) real part with $m_f = m_{\Upsilon(1s)}$

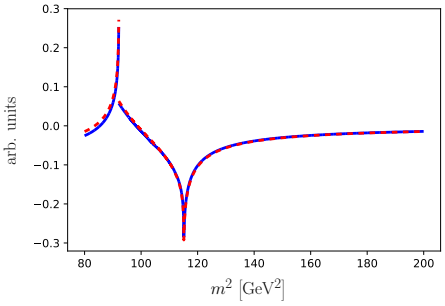

(b) imaginary part with $m_f = m_{\Upsilon(1s)}$

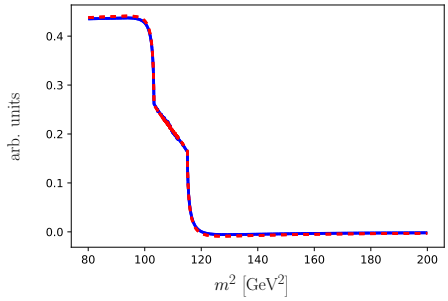

(c) real part with $m_f = m_{\Upsilon(2s)}$

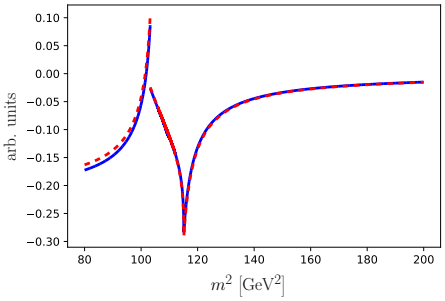

(d) imaginary part with $m_f = m_{\Upsilon(2s)}$

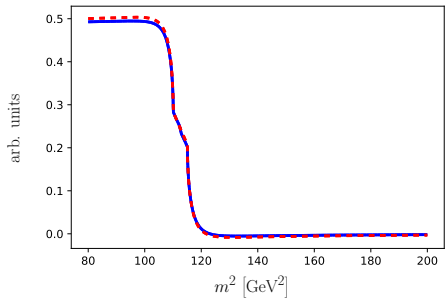

(e) real part with $m_f = m_{\Upsilon(3s)}$

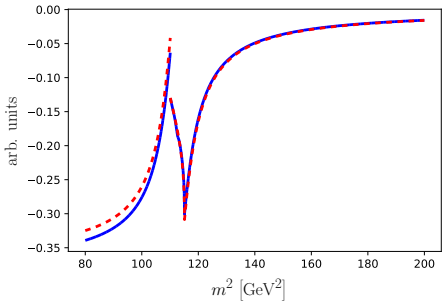

(f) imaginary part with $m_f = m_{\Upsilon(3s)}$

Figure 3.25.: $\pi\pi$ final-state component $(\tilde{I}_0(s, m^2))_1$ for $s = 0.5\,\text{GeV}^2$ coming from a two-channel (blue) or three-channel solution (red).

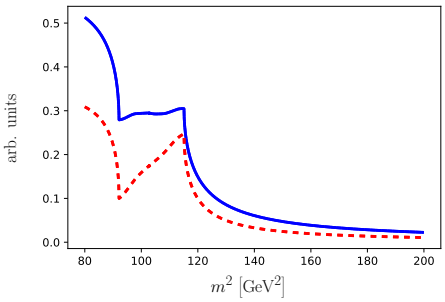

(a) real part with $m_f = m_{\Upsilon(1s)}$

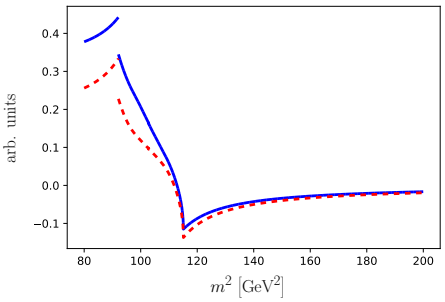

(b) imaginary part with $m_f = m_{\Upsilon(1s)}$

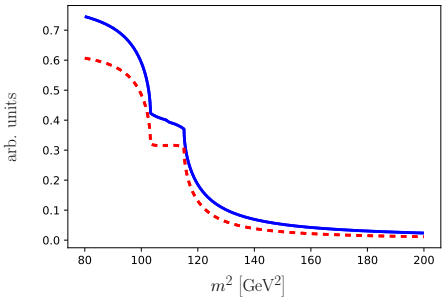

(c) real part with $m_f = m_{\Upsilon(2s)}$

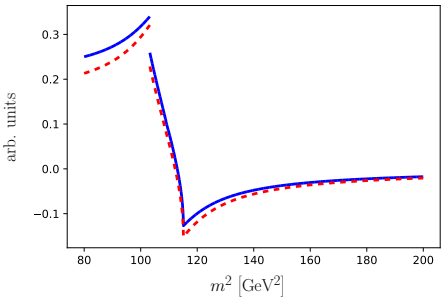

(d) imaginary part with $m_f = m_{\Upsilon(2s)}$

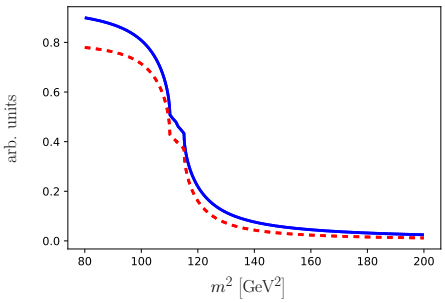

(e) real part with $m_f = m_{\Upsilon(3s)}$

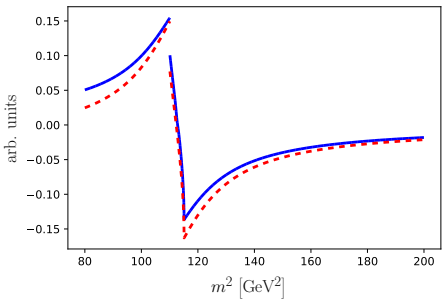

(f) imaginary part with $m_f = m_{\Upsilon(3s)}$

Figure 3.26.: $\pi\pi$ final-state component $(\tilde{I}_0(s, m^2))_1$ for $s = 2.5\,\mathrm{GeV}^2$ coming from a two-channel (blue) or three-channel solution (red).

The support of the spectral density gives the dominant contributions for the integral $I_0(s)$. Hence for the decay $\Upsilon(5S) \to \Upsilon(1S)$ we set the integral limits to $105\,\mathrm{GeV}^2 < m^2 < 125\,\mathrm{GeV}^2$, which ensures that most of the important structure in $\rho(m^2)$ is taken into account. The numerical results of the dispersive reconstruction is shown in Figs. 3.27, 3.28 and 3.29. Up to a few percent difference, the SD solution is consistent with the KT solution. It is in better agreement with the one using $\phi_{\mathrm{disp}}(t)$ rather than $\phi(t)$. Thus the left-hand cut in $\phi(t)$ changes the inhomogeneous Omnès problem by a few percent. However, both the SD as well as the KT solution are consistent with each other. As already seen for the KT solution, the three-channel analysis is in agreement with the two-channel one up to about $1.9\,\mathrm{GeV}^2$.

Numerical instabilities, as discussed for the KT solutions (see Sect. 3.6.2), are also available here and still need to be removed.

With this, we have shown that not only the SD solution is consistent with the KT one, but also that as long as we take into account the dominant parts of $\rho(m^2)$ a restriction in the m^2 integration range is possible.

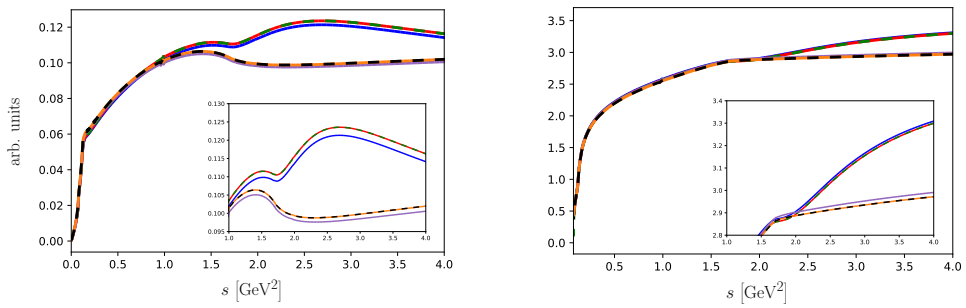

(a) modulus $BB^\star$ (b) phase $BB^\star$

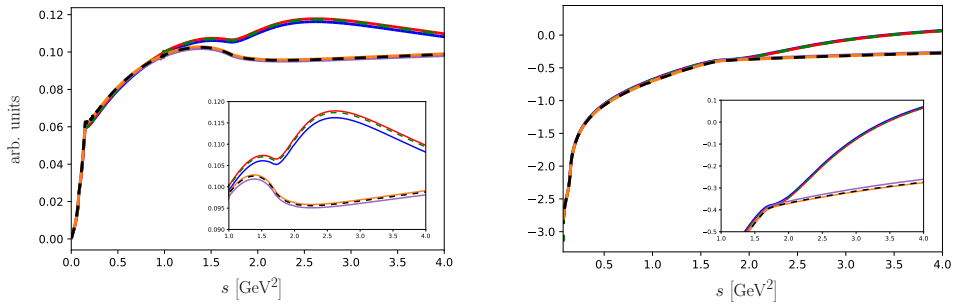

(c) modulus $B^\star B^\star$ (d) phase $B^\star B^\star$

Figure 3.27.: $\pi\pi$ final-state component $(I_0(s))_1$ for $\Upsilon(5S) \to \Upsilon(1S)\pi\pi$. The two-channel solution contains the KT-integral using $\phi(t)$ (blue), its dispersive reconstruction with only a right-hand cut $\phi_{\mathrm{disp}}(t)$ (red) and the SD-integral (green). The three-channel solution shows similarly the KT using $\phi(t)$ (purple), its dispersive reconstruction with only a right-hand cut $\phi_{\mathrm{disp}}(t)$ (orange) and the SD-integral (black).

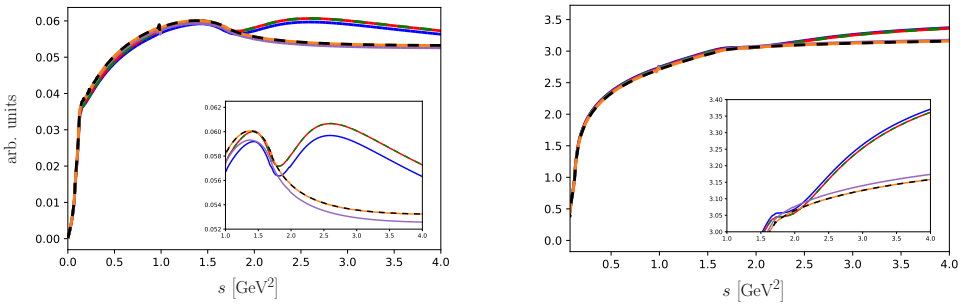

(a) modulus $BB^\star$

(b) phase $BB^\star$

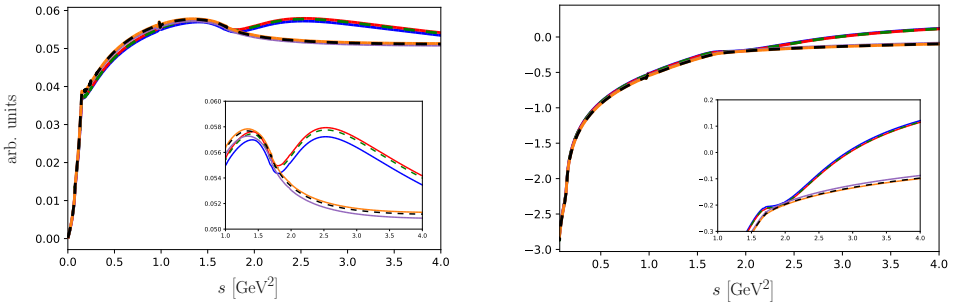

(c) modulus $B^\star B^\star$

(d) phase $B^\star B^\star$

Figure 3.28.: $K\bar{K}$ final-state component $(I_0(s))_2$ for $\Upsilon(5S) \to \Upsilon(1S)\pi\pi$. The two-channel solution contains the KT-integral using $\phi(t)$ (blue), its dispersive reconstruction with only a right-hand cut $\phi_{\text{disp}}(t)$ (red) and the SD-integral (green). The three-channel solution shows similarly the KT using $\phi(t)$ (purple), its dispersive reconstruction with only a right-hand cut $\phi_{\text{disp}}(t)$ (orange) and the SD-integral (black).

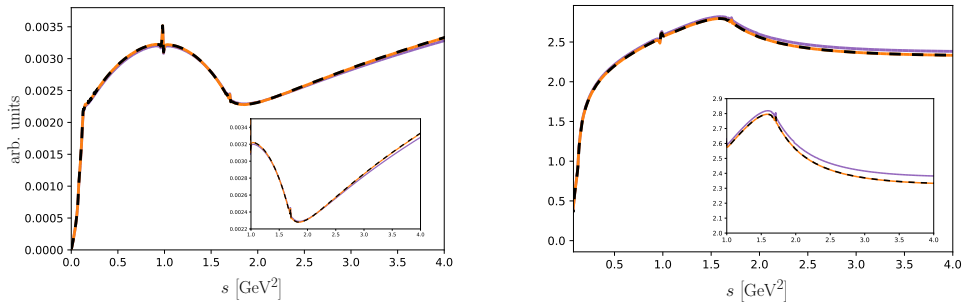

(a) modulus $BB^\star$

(b) phase $BB^\star$

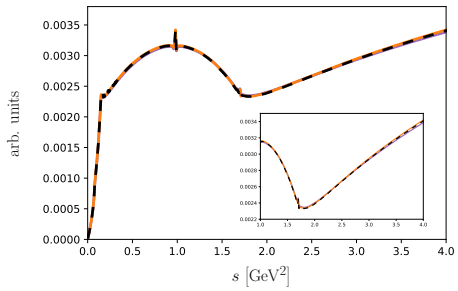

(c) modulus $B^\star B^\star$

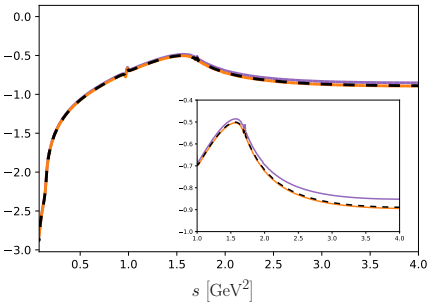

(d) phase $B^\star B^\star$

Figure 3.29.: 4π final-state component $(I_0(s))_3$ for $\Upsilon(5S) \to \Upsilon(1S)\pi\pi$. The three-channel solution contains the KT-integral using $\phi(t)$ (purple), its dispersive reconstruction with only a right-hand cut $\phi_{\text{disp}}(t)$ (orange) and the SD-integral (black).

Therefore we can also apply the SD solution for the decays $\Upsilon(5S) \to \Upsilon(2S)\pi\pi$ and $\Upsilon(5S) \to \Upsilon(3S)\pi\pi$. In order to avoid the anomalous thresholds we have to make sure, that the m^2 integration starts above $(m_f + m_\pi)^2$. Therefore we restrict it to $105\,\mathrm{GeV}^2 < m^2 < 125\,\mathrm{GeV}^2$ for $\Upsilon(2S)$ and $110.2\,\mathrm{GeV}^2 < m^2 < 125\,\mathrm{GeV}^2$ for $\Upsilon(3S)$.

The numerical solutions are shown in Figs. 3.30, 3.31 and 3.32. The lineshapes look very similar, except for a rescaling in favor of the heavier final states as already discussed in Sect. 3.4.

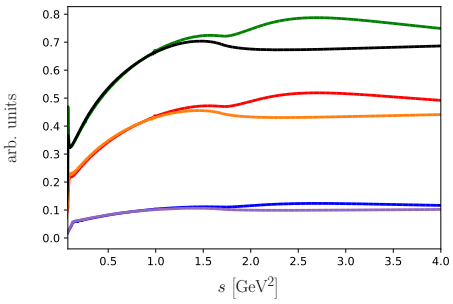

(a) modulus $BB^\star$

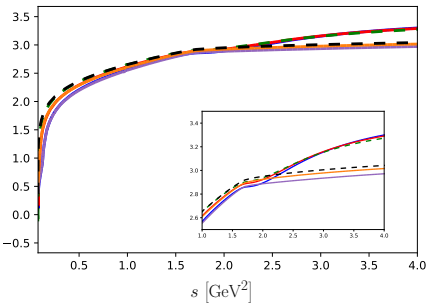

(b) phase $BB^\star$

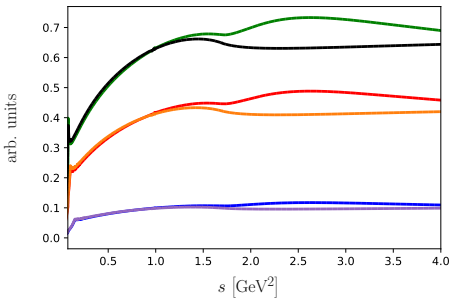

(c) modulus $B^\star B^\star$

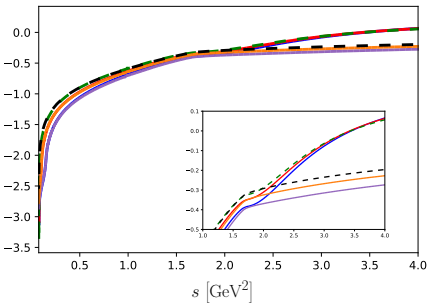

(d) phase $B^\star B^\star$

Figure 3.30.: SD dispersion integral $\pi\pi$ final-state component $(I_0(s))_1$ for $\Upsilon(5S) \to \Upsilon(nS)\pi\pi$ with $n = 1, 2, 3$. The two-channel solutions are given in blue ($\Upsilon(1S)$), red ($\Upsilon(2S)$) and green ($\Upsilon(3S)$). The three-channel solutions on the other hand are in purple ($\Upsilon(1S)$), orange ($\Upsilon(2s)$) and black ($\Upsilon(3S)$).

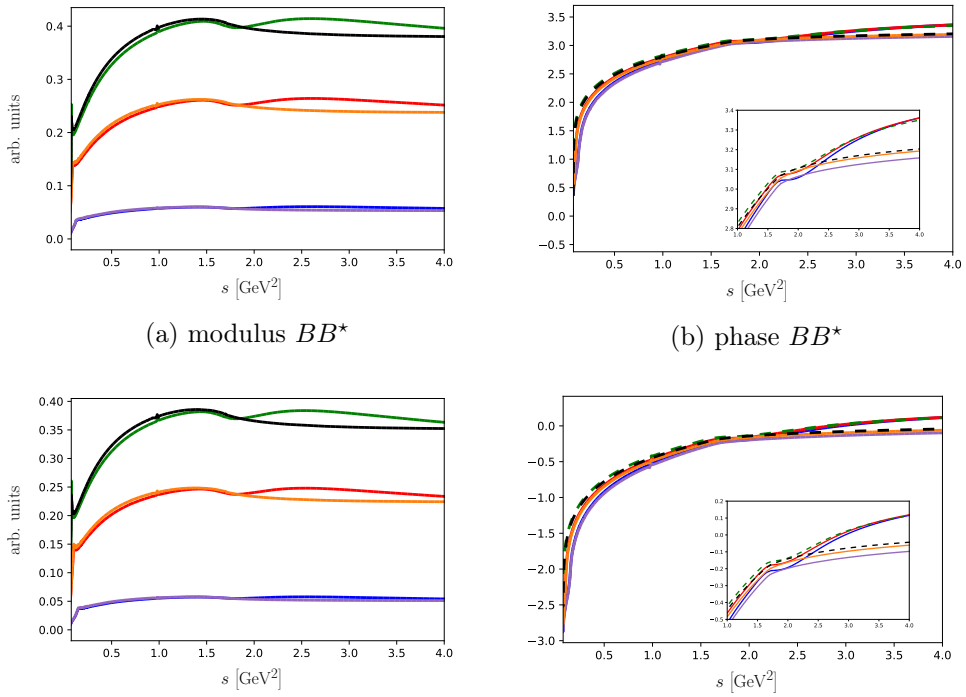

(a) modulus $BB^\star$

(b) phase $BB^\star$

(c) modulus $B^\star B^\star$

(d) phase $B^\star B^\star$

Figure 3.31.: SD dispersion integral $K\bar{K}$ final-state component $(I_0(s))_2$ for $\Upsilon(5S) \to \Upsilon(nS)\pi\pi$ with $n = 1, 2, 3$. The two-channel solutions are given in blue ($\Upsilon(1S)$), red ($\Upsilon(2S)$) and green ($\Upsilon(3S)$). The three-channel solutions on the other hand are in purple ($\Upsilon(1S)$), orange ($\Upsilon(2S)$) and black ($\Upsilon(3S)$).

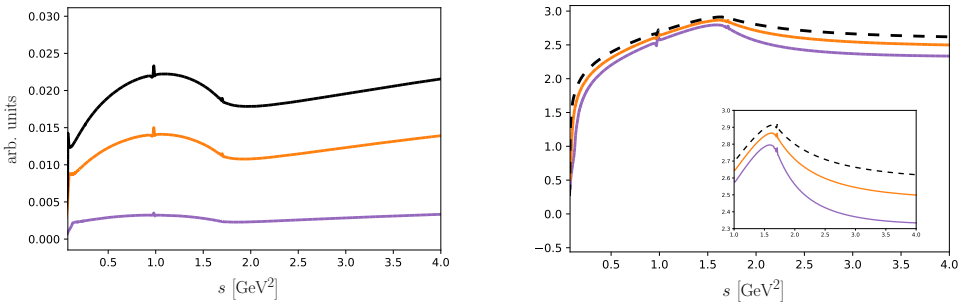

(a) modulus $BB^\star$

(b) phase $BB^\star$

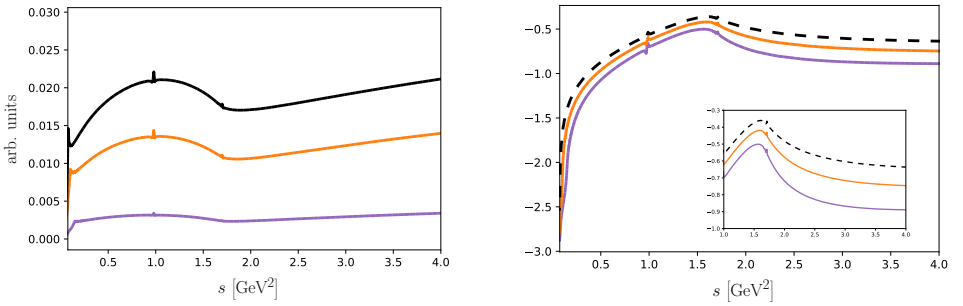

(c) modulus $B^\star B^\star$

(d) phase $B^\star B^\star$

Figure 3.32.: SD dispersion integral 4π final-state component $(I_0(s))_3$ for $\Upsilon(5S) \to \Upsilon(nS)\pi\pi$ with $n = 1, 2, 3$. The three-channel solutions are shown in purple ($\Upsilon(1S)$), orange ($\Upsilon(2S)$) and black ($\Upsilon(3S)$).

3.7. Conclusion and outlook

In this work we showed an application of dispersion theory to decays of heavy meson on the example of $\Upsilon(5S) \to \Upsilon(nS)\pi\pi$ with $n = 1, 2, 3$.

The model for the crossed-channel amplitude is consistent with a hadronic molecule picture. For this, the $B^{(\star)}\bar{B}^{\star}$ amplitudes, that contain the $Z_b(10610)$ and the $Z_b(10650)$, were constructed in such a way that they are analytic in the Mandelstam variable t and fulfill the Schwarz reflection principle. The left-hand cut of the function $\phi(t)$ is an artifact of the non-relativistic propagator and thus is unphysical. As it is an unphysical branch cut, we removed it by a dispersive reconstruction $\phi_{\text{disp}}(t)$ considering only a right-hand cut. The deviation between the inhomogeneous Omnès solutions is a few percent.

In order to describe the $\pi\pi$ interaction under the influence of crossed-channel effects, Omnès matrices need to be calculated. While the two-channel isoscalar scalar Omnès-matrix with $\pi\pi$ and $K\bar{K}$ is well established, we created an effective three-channel solution with additionally a $4\pi(\rho\rho)$ channel, which allows for an extension of the range of application. For this, we used the results of our previous work (see chapter 2). However, not only an uncertainty estimation still needs to be done, but also an application to other decays is necessary in order to show the validity of this matrix. Note that the application of the formalism in chapter 2 to the decay $\bar{B}_s^0 \to \psi(2S)\pi\pi$ is in progress [242]. This allows us to test the universality of the parameters.

The dispersion integral for the final state $\Upsilon(1S)$ was solved in two different ways. The first one is the KT solution, where the partial-wave projection is calculated by integrating the crossed-channel amplitude along the Khuri-Treiman path. The second solution, which we denoted as SD, rewrites the crossed-channel amplitude as a dispersion integral over a stable propagator with mass m^2, which will be weighted by the corresponding spectral density. Due to the correct analytical continuation of the partial-wave projection for a stable propagator with $m^2 > 0$, which has been cross-checked by applying it to the well-known scalar triangle graph, the order of integrations can be interchanged, thus allowing for evaluating the m^2 integral at last. After removing the left-hand cut in t from the crossed-channel amplitude, the SD solution is consistent with the well established KT up to numerical artifacts. In order to treat, or in our case avoid, anomalous thresholds, the SD method can also be applied for the decays $\Upsilon(5S) \to \Upsilon(nS)\pi\pi$ with $n = 2, 3$.

The advantages of the SD method is three-fold. Firstly it is well established how to include anomalous thresholds for stable propagators. Therefore it can be applied directly to the present case here. Secondly, the model dependence for the crossed-channel amplitude only comes in through the spectral density $\rho(m^2)$ while the rest of the dispersion integral is universal. This is especially important if the amplitude contains exotic resonances, as here many different models can be employed. Hence the SD method will help to discern the nature of those exotics by allowing the description of them in a decay involving light meson rescattering effects. The third advantage is that it is better applicable for a fit involving free parameters in $\rho(m^2)$. Since the integration over m^2 is done at last, it is possible to calculate the rest of the dispersion integral outside

of the fit, which speeds up the computation time immensely.

The goal of this work has been to show that the KT solution and SD solution are consistent with each other, such that the latter can also be applied in a broader context. To obtain a proper uncertainty estimate of e.g. the Omnès matrix or crossed-channel amplitude model parameters, a Dalitz plot fit of the decay $\Upsilon(5S) \to \Upsilon(nS)\pi\pi$ is still necessary.

4. Thesis summary and outlook

In this thesis we provided a toolkit based on dispersion relations, which is suitable to analyze heavy meson decays involving the rescattering of light mesons such as pions. With it, amplitudes can be constructed that are consistent with the constraints from unitarity and analyticity. Dispersion theory depends only on the scattering phases of the final and intermediate states employing analyticity and unitarity. It is a model-independent way to describe strong final state interactions. However, it is only applicable if the scattering amplitudes are known. Fully analytic and unitary amplitudes for light mesons are provided by dispersive integrals, e.g. for the S-waves of the channels $\pi\pi$ [124, 184, 243], πK and $K\bar{K}$ [185, 186, 244, 245] and $\pi\eta$ [246, 247]. However, their dispersive application is not only limited by the range of applicability of each extracted partial-wave amplitude but also the opening of multi-particle intermediate channels such as 4π. For heavy meson rescattering such a dispersive analysis is unfeasible, as it requires multiple channels from the beginning. Hence effective models are required, which allow for the introduction of additional resonances and channels and are consistent with the low energy constraints by the previously mentioned dispersive analysis. Therefore good models, which are analytic and unitary, are necessary. Effective field theories such as heavy meson chiral perturbation theory provide amplitudes, which can be unitarized by e.g. a Lippmann-Schwinger equation, thus providing the required construction [180]. Therefore both in the light and heavy meson sector, an analytic continuation of the amplitude is possible to extract pole parameters of previously badly determined resonances. Identifying the QCD bound states then helps us to understand the QCD spectrum and its interaction as well.

We generalized the effective parametrization of pion rescattering at higher energies [95] to the S-wave. The formalism considered a single-channel dispersive approach as input, which is coupled to additional channels by s-channel resonance exchange. It was extended by allowing a two-channel dispersive approach as input. In order to test the framework the decays $\bar{B}_s^0 \to J/\psi\pi^+\pi^-$ and $\bar{B}_s^0 \to J/\psi K\bar{K}$ have been analyzed. These decays are in particular suitable as the $J/\psi\pi^+$ and $J/\psi K$ invariant mass spectra do not show any structure [196, 209] and they provide a dipion phase space up to about 2.2 GeV. Furthermore the decay $\bar{B}_s^0 \to J/\psi\pi^+\pi^-$ shows a strong S-wave contribution. The D-wave contributions to the decay are modeled in analogy to the LHCb analysis as Breit-Wigner functions. On the other hand, the process $\bar{B}_s^0 \to J/\psi K\bar{K}$ is less clean, as it contains not only a S-wave but also strong P- and D-wave contributions, which are also modeled as Breit-Wigner amplitudes. However, the inherent coupled-channel approach helps us to determine the free parameters contained in the new parameterization for the S-wave.

In comparison to a previous dispersive analysis [190], which was valid up to

a dipion energy of about 1.05 GeV, this new work allows for the description of the whole energy range of the decay. This however came at the cost of introducing several new free parameters. While the number of free parameters is larger than for a sum of single-channel Breit-Wigner functions, it is comparable to a multi-channel K-matrix and allows for a coupled-channel description. In order to estimate the systematic uncertainty introduced by the parameterization, six different fits to the angular moments $\langle Y_0^0 \rangle$ and $\langle Y_2^0 \rangle$ were performed. Fit 1 considers two additional resonances, Fit 2 allows for a linear subtraction polynomial and Fit 3 contains three additional resonances and a constant subtraction polynomial. Each of the fits has an effective four pion channel modeled by either $\rho\rho$ or by $\sigma\sigma$. The fit improves for every additional degree of freedom and prefers the $\rho\rho$ inelastic channel.

The framework does not only provide an analytic parameterization for the form factor, which was used for the fit, but with the same set of parameters also a scattering amplitude. Hence in principle, it can be analytically continued onto different Riemann sheets, allowing for the extraction of resonance poles. This however needs information about the input scattering amplitude $T_0(s)$ in the complex s-plane. As it contains left- and right-hand cuts, this task was beyond the scope of this thesis and thus an analytic continuation of the form factor via Padé approximants has been performed. As a cross-check for the validity of our extraction we compared the pole parameters for the $f_0(500)$ and $f_0(980)$ to Ref. [127]. Except for a deviation of about 5% of the strange $f_0(500)$ coupling strength, they are consistent within the uncertainties. The deviation might be reduced by including further subtractions of the resonance exchange potential, which still remains to be shown. The extraction of the $f_0(1500)$ gives a similar pole position to the LHCb Breit-Wigner one. However, our fit prefers a significantly shifted pole for the $f_0(2020)$, which was identified by LHCb as a $f_0(1790)$. We also observed that while the parameters for the $f_0(1500)$ were stable, stronger uncertainties for the $f_0(2020)$ were found. In order to alleviate this problem, it is necessary to include data for further inelastic channels in the fit.

Another interesting property of the parameterization is that the scattering amplitude parameters are independent of the decay. This universality is currently being tested for example in the decay $\bar{B}_s^0 \to \psi(2S)\pi\pi$ [242]. For this, the scattering amplitude parameters, such as bare resonance masses and resonance-channel couplings, are adapted from Ref. [232], whereas the source dependent parameters are adjusted by a fit. For an easy application the pion form factor is given as

$$F_\pi(s) = \sum_{i=1}^{N_c} (c_i + l_i s)\, \Gamma_i(s) + \sum_{r=1}^{N_R} \alpha_r X_r(s)\,. \tag{4.1}$$

Here N_c are the number of channels and N_R the number of additional resonances. The source parameters c_i, l_i and α_r are obtained by a Dalitz plot fit, whereas the basis functions are fixed by the previous analysis.

With the extracted scattering matrix as input, it is possible to calculate a multi-channel Omnès matrix, as shown in this thesis. While several tests for the validity of the matrix and uncertainty estimation are still necessary, it

matches smoothly onto the two-channel solution with a deviation starting near the $f_0(1500)$ resonance. Hence we assume that it provides a reasonable high energy extension for pion-pion rescattering to higher energies.

Therefore it is also possible to analyze heavy meson decays involving pion-pion rescattering where the additional complication of a a left-hand cut amplitude coming from crossed-channel resonances arises. Here we consider the decay of $\Upsilon(5S)$ into $\Upsilon(nS)\pi\pi$ with $n = 1, 2, 3$. Two exotic resonances Z_b and Z_b' show up in the $\Upsilon(nS)\pi$ invariant mass distribution. Due to their closeness to the $B\bar{B}^\star$ and $B^\star\bar{B}^\star$ thresholds, respectively, they can be modeled as dynamically produced resonance in B-meson rescattering [180]. While the model works exceptionally well for $B\bar{B}^\star$ and $B^\star\bar{B}^\star$ scattering as well as the decay amplitudes $\Upsilon(5S) \to h_b(mP)\pi\pi$ with $m = 1, 2$ problems for the decays $\Upsilon(5S) \to \Upsilon(nS)\pi\pi$, since here $\pi\pi$-rescattering cannot be neglected, a full Dalitz plot analysis is required.

In order to find the inhomogeneous multi-channel Omnès solution for the $\pi\pi$-S-wave, it is necessary to first calculate the inhomogeneity by partial-wave projection of the crossed-channel amplitude. This proceeds in two different approaches. The first method denotes as KT, involves integrating the crossed-channel amplitude along the Khuri-Treiman path. The second option is to first write the crossed-channel amplitude as an integral over the spectral density denoted by SD. By reversing the order of integration, it involves the analytically correct partial-wave projection of a crossed-channel stable resonance exchange. We have provided this analytic continuation for decays involving exchanged resonances with arbitrary positive masses. Depending on the mass range, it also involves anomalous thresholds, which can be treated in this approach. This procedure was verified by applying it to the dispersive reconstruction of the scalar triangle diagram. The remaining integrals can be solved in the standard procedure. We showed for the decay $\Upsilon(5S) \to \Upsilon(1S)\pi\pi$ that the KT and SD method are consistent with each other, such that either one can be applied.

We especially want to advocate the SD method. It can be easily generalized in order to include anomalous thresholds, such as required for the decays $\Upsilon(5S) \to \Upsilon(nS)\pi\pi$ with $n = 2, 3$. However, depending on the kinematical situation, anomalous thresholds might be required. This requires knowledge of the scattering amplitude in the complex plane. Furthermore, it should be suited for fits, as all the crossed-channel model parameters are contained in the spectral density integral, which is evaluated in the last step.

This work has been a proof of principle and a real application to the Dalitz plot data still needs to be performed. While we considered only the simplest model for the crossed-channel amplitude, a generalization to more advanced models is straightforward. This procedure will allow one to test different models for the nature of the Z_b states, while correctly describing light meson rescattering. The first extension is the inclusion of one-pion exchange potentials in the Lippmann-Schwinger equation for $B\bar{B}^\star$-$B^\star\bar{B}^\star$ scattering[223]. Compared to the study in this thesis, only the spectral density in the SD approach needs to be adjusted. Also the inclusion of a Z_b with strangeness content is possible. For this, the Lippmann-Schwinger equation in the presented crossed-channel amplitude has to include strange B-meson channels. The resonance would primarily contribute

to the inhomogeneity of the $K\bar{K}$ channel. The SD method needs to be slightly adjusted due to the different kinematics of the $\pi\pi$ and $K\bar{K}$ final states. In order to constrain the model parameters a coupled-channel fit of the Dalitz plots $\Upsilon(5S) \to \Upsilon(nS)\pi\pi$ with $n = 1, 2, 3$ and $\Upsilon(5S) \to \Upsilon(1S)K\bar{K}$ would be preferred.

A similar analysis can also be applied in the charm sector to the decay $Y(4260) \to J/\psi\pi\pi$ [169]. It shows the exotic $Z_c(3900)$ resonance in the $J/\psi\pi$ invariant mass spectrum. As pointed out in Ref. [248], triangle singularities in the crossed-channel amplitude might play a significant role in the production of the Z_c. For this, the SD method needs to be adjusted to take these singularities into account.

Furthermore, data on the decay of the $\Upsilon(6S)$ is expected to be published by the Belle collaboration in the future. Due to the larger phase space, it might show further exotic resonances. However, this also means that improved methods for $\pi\pi$ rescattering at higher energies are necessary. The framework we have provided in this thesis is especially suited for this endeavor.

To summarize, we provided a dispersive toolkit which not only allows an analytic and unitary extension of light meson scattering to higher energies but also their application to heavy meson decays with a non-vanishing left-hand cut.

A. Analytic partial-wave projections

A.1. General considerations about the partial-wave projection

Consider the decay of a particle with mass m_i into one with mass m_f as well as two with mass m_π. The kinematics has already been introduced in Sect. 3.2.

This chapter aims to introduce a valid partial-wave projection for an amplitude $K(t)$ with only a right-hand cut in the t-plane. The following reasoning can be applied analogously to a function depending on u only.

Since $K(t)$ is fully analytic in the complex t-plane except for a right-hand cut starting at m_0^2 it can be written as

$$K(t) = \frac{1}{\pi} \int_{m_0^2}^{\infty} \mathrm{d}m_r^2 \, \frac{\rho(m_r^2)}{t - m_r^2} \,. \tag{A.1}$$

The spectral density is given by

$$\rho(m_r^2) = -\mathrm{Im}\, K(m_r^2) \,. \tag{A.2}$$

In the case that $\rho(t)$ does not fall fast enough for $|t| \to \infty$ subtraction can be introduced. However these do not change the analytic structure and are thus irrelevant for the following discussion.

The partial-wave projection of this amplitude is given by

$$K_\ell(s) = \frac{1}{2\ell + 1} \int_{-1}^{1} \mathrm{d}\cos\theta \, P_\ell(\cos\theta) \, K(t(s, \cos\theta)) \,, \tag{A.3}$$

where $t(s, \cos\theta)$ was already introduced in Eq. (3.4).

By properly constructing the analytic continuation of the partial-wave projection in the external masses it is possible to switch the order of integration

$$K_\ell(t) = \frac{1}{\pi} \int_{m_0^2}^{\infty} \mathrm{d}m_r^2 \, \rho(m_r^2) \, \frac{1}{2\ell + 1} \int_{-1}^{1} \mathrm{d}\cos\theta \, \frac{P_\ell(\cos\theta)}{t(s, \cos\theta) - m_r^2} \,. \tag{A.4}$$

The angular integral

$$A_\ell(s, m_r^2) = \frac{1}{2\ell + 1} \int_{-1}^{1} \mathrm{d}\cos\theta \, \frac{P_\ell(\cos\theta)}{t(s, \cos\theta) - m_r^2} \tag{A.5}$$

can be transformed to a path integral in the complex t plane via variable transformation

$$A_\ell(s, m_r^2) = \frac{2}{(2\ell+1)\kappa(s)} \int\limits_{t_-(s)}^{t_+(s)} \mathrm{d}t \frac{F_\ell(t)}{t - m_r^2} \tag{A.6}$$

with

$$t_\pm(s) = \frac{1}{2}(m_i^2 + m_f^2 + 2m_\pi^2 - s \pm \kappa(s)z) \tag{A.7}$$

and

$$F_\ell(t) = P_\ell\left(\frac{2t + s - m_i^2 - m_f^2 - 2m_\pi^2}{\kappa(s)}\right). \tag{A.8}$$

Choose now m_r^2 to be large enough that for all $s > s_0 = 4m_\pi^2$ it never interferes with the integration in the complex t-plane. Each direct path between $t_+(s)$ and $t_-(s)$ as well as their contour deformations consistent with Cauchy's theorem are valid in order to evaluate the integration.

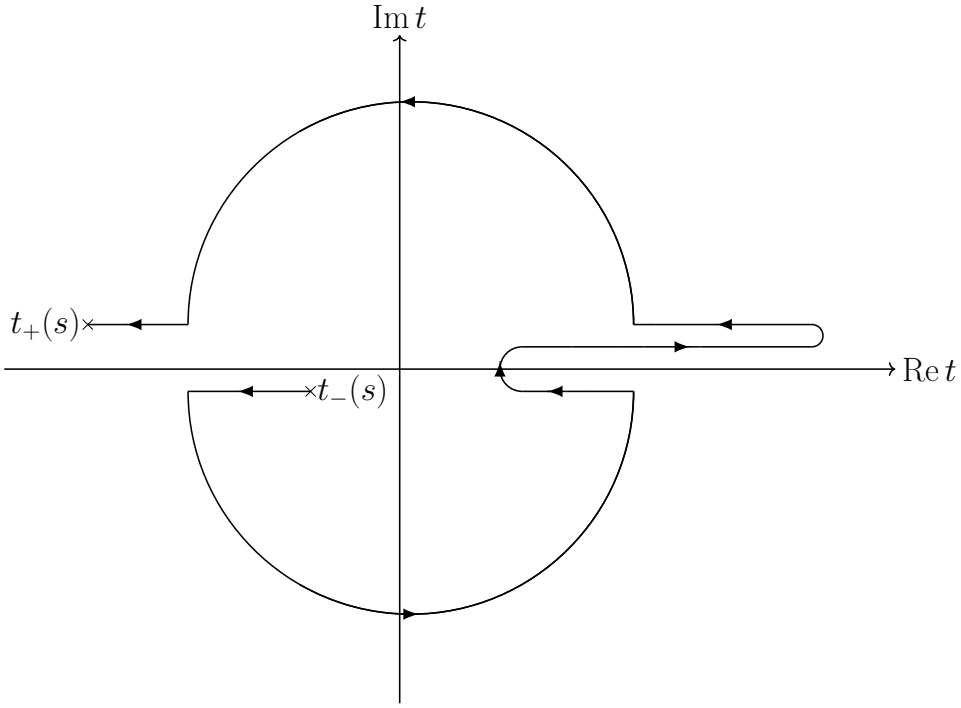

Figure A.1.: Example for a Khuri-Treimann path.

A particular choice is the integration along the end-points of the integral

$$A_\ell(s, m_r^2) = \frac{2}{(2\ell+1)\kappa(s)} \int_{\mathrm{KT}} \mathrm{d}t \frac{F_\ell(t)}{t - m_r^2} \tag{A.9}$$

with

$$\int_{\mathrm{KT}} \mathrm{d}t \frac{F_\ell(\ell)}{t-m_r^2} = \int_s^{s_0} \mathrm{d}s' \, \frac{\partial t_-(s')}{\partial s'} \, \frac{F_\ell(t_-(s'))}{t_-(s')-m_r^2} + \int_{s_0}^{s} \mathrm{d}s' \, \frac{\partial t_+(s')}{\partial s'} \, \frac{F_\ell(t_+(s'))}{t_+(s')-m_r^2} \,, \tag{A.10}$$

which we will call Khuri-Treiman path (KT). An example for such a path is shown in Fig. A.1.

A.2. More on the Khuri-Treiman path

In the following we want to describe the KT path as a function of the Mandelstam variable s. For this note, that it is important to treat $t_\pm(s)$ as analytic functions in the external masses. This can be illustrated by e.g. adding a small imaginary part to the decay particle mass

$$m_i^2 \to m_i^2 + i\epsilon \,. \tag{A.11}$$

With this it is possible to describe the KT path as follows:

- $4m_\pi^2 \leq s \leq (m_i - m_f)^2$:
  In this case we have

  $$\mathrm{Re}\, t_\pm(s) = \frac{1}{2}\left(m_i^2 + m_f^2 + 2m_\pi^2 - s \pm \kappa(s) \right) \tag{A.12}$$

  and

  $$\mathrm{Im}\, t_\pm(s) = \frac{\epsilon}{2} \left(1 \pm \frac{\sqrt{1-\frac{4m_\pi^2}{s}}(m_i^2 - m_f^2 - s)}{\sqrt{(m_i+m_f)^2 - s}\sqrt{(m_i-m_f)^2 - s}} \right) . \tag{A.13}$$

  We immediately see that $\mathrm{Re}\, t_-(s) \leq \mathrm{Re}\, t_+(s)$ as well as $\mathrm{Im}\, t_+(s) > 0$.

  Solving $\mathrm{Im}\, t_-(s_n) = 0$ we obtain two points

  $$s_n = -\frac{(m_i^2 - m_f^2)m_\pi}{m_f - m_\pi} \quad \text{and} \quad s_n = \frac{(m_i^2 - m_f^2)m_\pi}{m_f + m_\pi} \,. \tag{A.14}$$

  As we consider only $s \geq 4m_\pi^2 > 0$ we discard the first solution. Thus for $s < s_n = (m_i^2 - m_f^2)m_\pi/(m_f + m_\pi)$ the imaginary part of $t_-(s)$ is positive, while for $s > s_n$ it is negative.

  We may also calculate the extrema of $\mathrm{Re}\, t_\pm(s)$ by solving

  $$\frac{\mathrm{dRe}\, t_\pm(s)}{\mathrm{d}s} = 0 \,. \tag{A.15}$$

  The solutions are given by

  $$s_{1/2} = \pm\frac{(m_i^2 - m_f^2)m_\pi}{m_f \pm m_\pi} \quad \text{and} \quad s_{3/4} = \pm\frac{(m_i^2 - m_f^2)m_\pi}{m_i \mp m_\pi} \,. \tag{A.16}$$

Discarding the negative solutions we only consider s_1 and s_3. Under the assumption $m_i > m_f + 2m_\pi$ we also see that $s_1 > s_3$. Reinserting s_1 in $t_\pm(s)$ we obtain

$$\mathrm{Re}\, t_+(s_1) = \frac{m_i^2 m_f - m_f^2 m_\pi - m_f m_\pi^2 + m_\pi^3}{m_f + m_\pi} \quad \text{with} \quad \mathrm{Im}\, t_+(s_1) > 0 \tag{A.17}$$

and

$$\mathrm{Re}\, t_-(s_1) = (m_f + m_\pi)^2 \quad \text{with} \quad \mathrm{Im}\, t_-(s_1) = 0\,. \tag{A.18}$$

A similar inspection for s_3 gives

$$\mathrm{Re}\, t_-(s_3) = \frac{m_f^2 + m_\pi m_i^2 - m_i m_\pi^2 - m_\pi^3}{m_i - m_\pi} \quad \text{with} \quad \mathrm{Im}\, t_-(s_3) > 0 \tag{A.19}$$

and

$$\mathrm{Re}\, t_+(s_3) = (m_i - m_\pi)^2 \quad \text{with} \quad \mathrm{Im}\, t_+(s_3) > 0\,. \tag{A.20}$$

- $(m_i - m_f)^2 \le s \le (m_i + m_f)^2$:
  In this case we see that

$$\mathrm{Re}\, t_\pm(s) = \frac{1}{2}(m_i^2 + m_f^2 + 2m_\pi^2 - s) \tag{A.21}$$

and

$$\mathrm{Im}\, t_\pm(s) = \pm\frac{1}{2}\sqrt{1 - \frac{4m_\pi^2}{s}}\sqrt{s - (m_i - m_f)^2}\sqrt{(m_i + m_f)^2 - s}\,. \tag{A.22}$$

Therefore $\mathrm{Im}\, t_+(s) > 0$ and $\mathrm{Im}\, t_-(s) < 0$. Furthermore we see that

$$\mathrm{Re}\, t_\pm(s) \le \mathrm{Re}\, t_\pm((m_i - m_f)^2) = m_i m_f + m_\pi^2\,. \tag{A.23}$$

- $s > (m_i + m_f)^2$:
  We obtain

$$\mathrm{Re}\, t_\pm(s) = \frac{1}{2}(m_i^2 + m_f^2 + 2m_\pi^2 - s \mp \kappa(s)) \tag{A.24}$$

and

$$\mathrm{Im}\, t_\pm(s) = \frac{1}{2}\left(1 \pm \frac{\sqrt{1 - \frac{4m\pi^2}{s}}(s - (m_i + mf)(m_i - mf))}{\sqrt{s - (m_i + m_f)^2}\sqrt{s - (m_i - m_f)^2}}\right)\,. \tag{A.25}$$

It is obvious that $\mathrm{Re}\, t_+(s)$ is bounded from above by

$$\mathrm{Re}\, t_-((m_i + m_f)^2) = \mathrm{Re}\, t_+((m_i + m_f)^2) = -m_i m_f + m_\pi^2 \tag{A.26}$$

with a positive imaginary part. For $t_-(s)$ we obtain a maximum from Eq. (A.2). As there are no solutions for $s > (m_i + m_f)^2$ it follows, that

$\mathrm{Re}\, t_-(s)$ needs to be a monotonous function. It starts from $t_-((m_i+m_f)^2)$ and goes to 0. Its imaginary part can be estimated by

$$\mathrm{Im}\, t_-(s) \leq \tilde{\epsilon}(s - m_i^2 - m_f^2)\left(1 - \sqrt{1 - \frac{4m_\pi^2}{s}}\right) \leq 0 \tag{A.27}$$

with

$$\tilde{\epsilon} = \frac{\epsilon}{2\sqrt{s-(m_i+m_f)^2}\sqrt{s-(m_i-m_f)^2}}\,. \tag{A.28}$$

Fig. A.2 depicts KT paths for different energies. In the following, this path will be the starting point of our discussion. Its analytic continuation for different m_r^2 will include residues of the encountered poles, as discussed in the following section.

A.3. Analytic continuation in the exchange mass

As the exchange masses m_r^2 are in reality not necessarily too heavy, we now perform an analytic continuation within this variable.

For $m_r^2 \gg (m_i - m_\pi)^2$ the pole of the propagator never interferes with the KT path as shown in Fig. A.3a. Even for masses $m_r^2 \geq (m_f + m_\pi)^2$ the KT path does not need to be deformed as shown in Fig. A.3b and Fig. A.3c.

However for $m_r^2 < (m_f + m_\pi)^2$ the pole drags along the contour as seen in Fig. A.4a. Using the residue theorem, it is possible to express the analytic continuation in terms of the previous KT path as well as the residue at m_r^2 (Fig. A.4b). Note that the pole is enclosed in clockwise orientation, which is why the residue contributes with a negative sign.

To summarize for $m_r^2 > (m_f + m_\pi)^2$ the partial-wave projection is given by

$$A_\ell(s, m_r^2) = \frac{2}{(2\ell+1)\kappa(s)} \int_{\mathrm{KT}} \mathrm{d}t \frac{F_\ell(t)}{t - m_r^2}\,. \tag{A.29}$$

For $0 < m_r^2 < (m_f + m_\pi)^2$ we obtain

$$A_\ell(s, m_r^2) = \frac{2}{(2\ell+1)\kappa(s)} \left(\int_{\mathrm{KT}} \mathrm{d}t \frac{F_\ell(t)}{t - m_r^2} - 2\pi i F_\ell(m_r^2) \right)\,. \tag{A.30}$$

This result may also be generalized by replacing $F_\ell(t)$ with any analytic function $\Psi(t)$ in the complex t-plane

$$(2\ell+1)A_\ell(s, m_r^2) = \frac{2}{\kappa} \left(\int_{KT} \mathrm{d}t \frac{\Psi(t)}{t - m_r^2} - 2\pi i \Psi(m_r^2)\Theta(0 < m_r^2 < (m_f + m_\pi)^2) \right) \tag{A.31}$$

Furthermore it is possible to use the position of m_r^2 within this path to distinguish the different cases. Namely **case a)** corresponds to $m_r^2 > (m_i - m_\pi)^2$, **case b)** to $m_i m_f + m_\pi^2 < m_r^2 < (m_i - m_\pi)^2$, **case c)** to $(m_f + m_\pi)^2 < m_r^2 < m_i m_f + m_\pi^2$ and **case d)** to $0 < m_r^2 < (m_f + m_\pi)^2$.

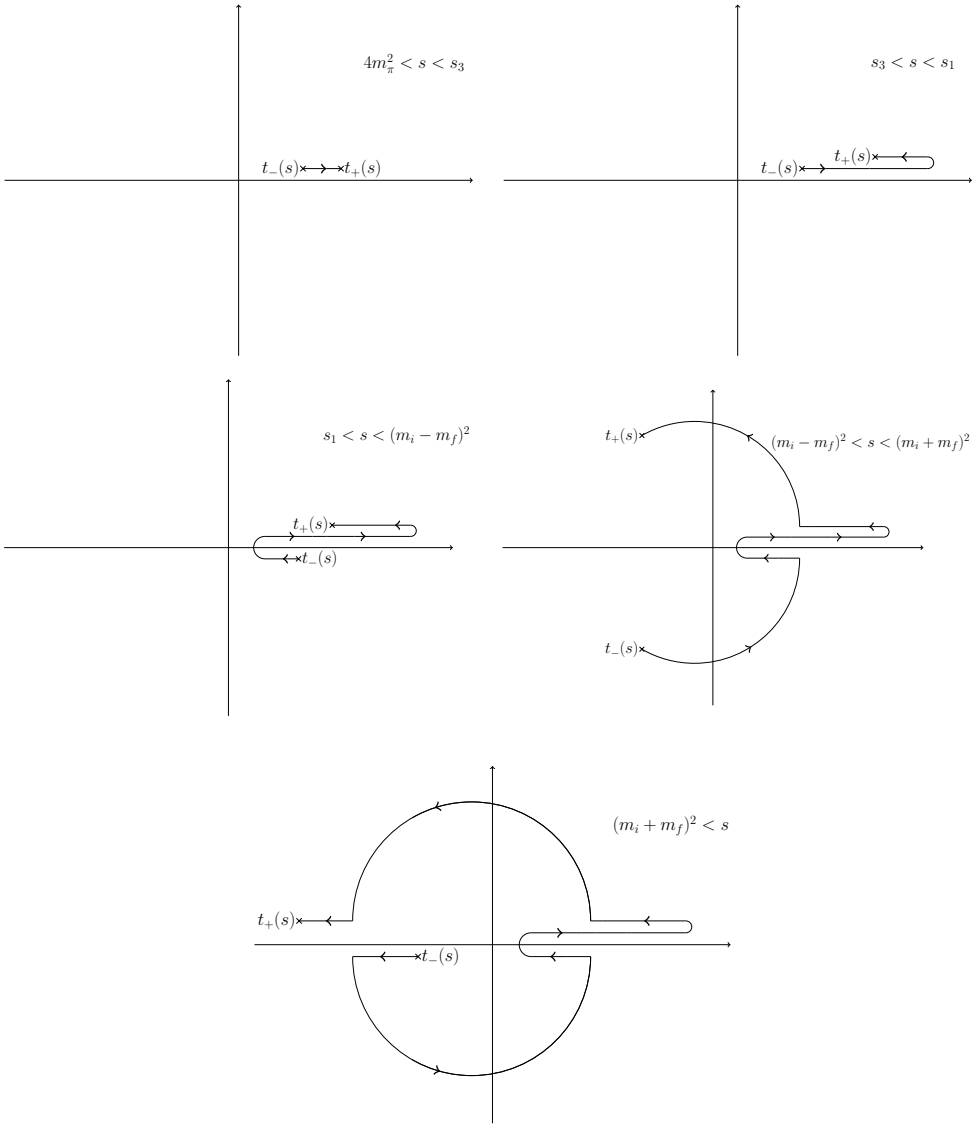

Figure A.2.: Integration path in the complex t-plane for real values of s in different energy regions.

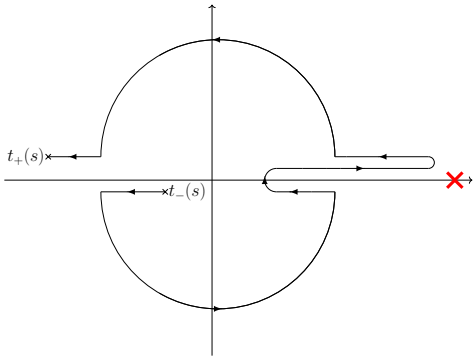

(a) $(m_i - m_\pi)^2 < m_r^2$

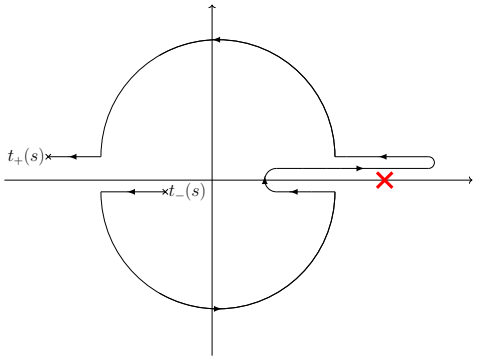

(b) $m_i m_f + m_\pi^2 < m_r^2 < (m_i - m_\pi)^2$

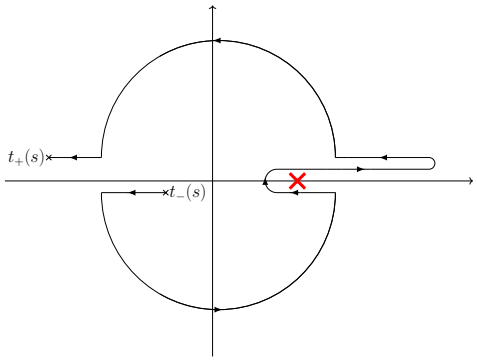

(c) $(m_f + m_\pi)^2 < m_r^2 < m_i m_f + m_\pi^2$

Figure A.3.: Analytic continuation of the partial-wave projection in $m_r^2 \geq (m_f + m_\pi)^2$ without path deformation.

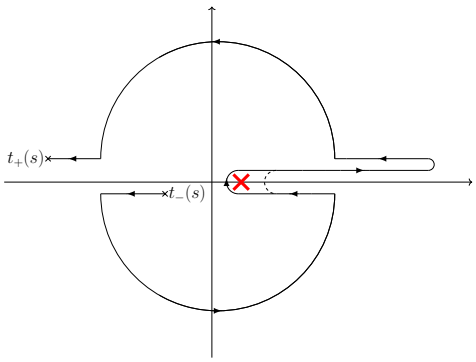

(a) Analytic continuation

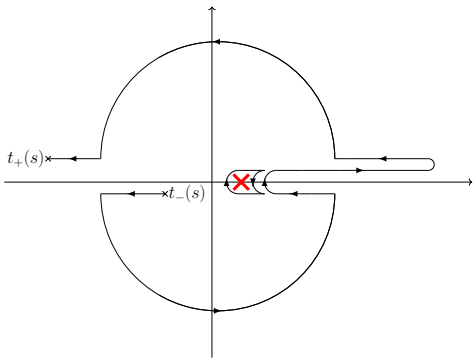

(b) KT path

Figure A.4.: Analytic continuation of the partial-wave projection in $m_r^2 < (m_f + m_\pi)^2$ with a required path deformation.

A.4. Analytic evaluation of the partial-wave projection

As the evaluation of the KT path is involved and time consuming it is advantageous to use the residue theorem to express it in terms of a direct integration $\mathcal{D}$ between $t_-(s)$ and $t_+(s)$. In case of a stable propagator the integration will give logarithms, whereas the residue determines the correct sheet. However, the following ideas are universal and can be applied to more general structures as long as they only involve branch cuts or poles on the real axis.

Case (a): $(\mathbf{m_i} - \mathbf{m}_\pi)^\mathbf{2} < \mathbf{m_r^2}$

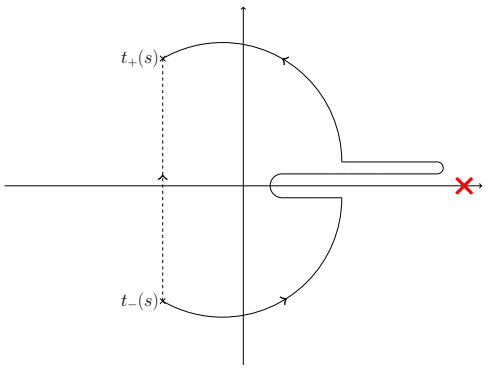

Figure A.5.: Deformed integral for case (a).

We see that for every $s > 4m_\pi^2$ we can use Cauchy's theorem to deform the path into a straight line (see Fig. A.5). Thus we can write

$$(2\ell+1)A_\ell(s) = \frac{2}{\kappa}\int_{KT} \mathrm{d}t \frac{\Psi(t)}{t-m_r^2} = \frac{2}{\kappa}\int_{\mathcal{D}} \mathrm{d}t\, \frac{\Psi(t)}{t-m_r^2}\,. \tag{A.32}$$

For the projection of the stable propagator on the S-wave it reads

$$A_0(s) = \frac{2}{\kappa}\int_{t_-(s)}^{t_+(s)} \mathrm{d}t\, \frac{1}{t-m_r^2} = \frac{2}{\kappa}\log\left(\frac{t_+(s)-m_r^2}{t_-(s)-m_r^2}\right)\,. \tag{A.33}$$

Case (b): $\mathbf{m_i m_f} + \mathbf{m_\pi^2} < \mathbf{m_r^2} < (\mathbf{m_i} - \mathbf{m}_\pi)^\mathbf{2}$

Whereas it is still possible to connect $t_\pm(s)$ with each other via a straight line for every $s > 4m_\pi^2$ (see Fig. A.6) we need to treat the singularity at $t = m_r^2$ for $\epsilon \to 0$ properly.

The pole only contributes for $4m_\pi^2 < s < (m_i - m_f)^2$ since otherwise we can deform the path in order to avoid the singularity entirely. In this case the projection is given by Eq. (A.33). We solve $\mathrm{Re}\, t_\pm(s_\pm) = m_r^2$ which results in

$$s_\pm = \frac{(m_i-m_f)^2 - \left(\sqrt{\lambda(m_i^2,m_r^2,m_\pi^2)} \mp \sqrt{\lambda(m_f^2,m_r^2,m_\pi^2)}\right)^2}{4m_r^2}\,. \tag{A.34}$$

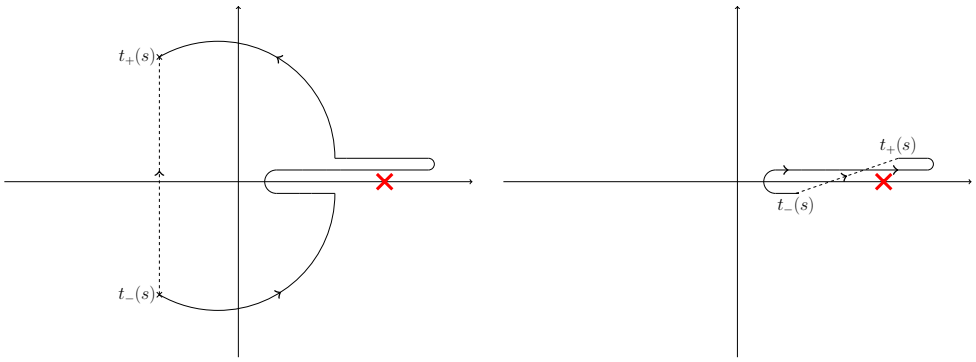

(a) $s_+ < s$ (b) $s_- < s < s_+$

Figure A.6.: Deformed integral for case (b).

Consider now $s_- < s < s_+$. In this case we can evaluate the partial-wave projection as a straight line integral with a positive imaginary part

$$(2\ell+1)A_\ell(s) = \frac{2}{\kappa}\int\limits_{t_-(s)}^{t_+(s)} \mathrm{d}t\, \frac{\Psi(t+i\epsilon)}{t-m_r^2+i\epsilon} \tag{A.35}$$

For the S-wave projection of a stable propagator this reduces to

$$A_0(s) = \frac{2}{\kappa}\int\limits_{t_-(s)}^{t_+(s)} \frac{\mathrm{d}t}{t-m_r^2+i\epsilon}\,. \tag{A.36}$$

Using the Sokhotski-Plemelj theorem we can evaluate it to be

$$\begin{aligned} A_0(s) &= \frac{2}{\kappa}\fint_{t_-(s)}^{t_+(s)} \frac{\mathrm{d}t}{t-m_r^2} - \frac{2i\pi}{\kappa}\int_{t_-(s)}^{t_+(s)} \mathrm{d}t\,\delta(t-m_r^2) \\ &= \frac{2}{\kappa}\left[\log\left(-\frac{t_+(s)-m_r^2}{t_-(s)-m_r^2}\right) - i\pi\right]. \end{aligned} \tag{A.37}$$

Summarizing for all energy regions the solution is given by

$$(2\ell+1)A_\ell(s) = \begin{cases} \frac{2}{\kappa}\int\limits_{t_-(s)}^{t_+(s)} \mathrm{d}t\, \frac{\Psi(t+i\epsilon)}{t-m_r^2+i\epsilon} & , \quad s_- \le s \le s_+ \\ \\ \frac{2}{\kappa}\int_{\mathcal{D}} \mathrm{d}t\, \frac{\Psi(t)}{t-m_r^2} & , \quad \text{else} \end{cases}. \tag{A.38}$$

For a S-wave projection of a stable propagator it reads

$$A_0(s) = \begin{cases} \frac{2}{\kappa}\left[\log\left(-\frac{t_+(s)-m_r^2}{t_-(s)-m_r^2}\right) - i\pi\right] & , \quad s_- \le s \le s_+ \\ \\ \frac{2}{\kappa}\log\left(\frac{t_+(s)-m_r^2}{t_-(s)-m_r^2}\right) & , \quad \text{else} \end{cases}. \tag{A.39}$$

Case (c): $\mathbf{(m_f + m_\pi)^2 < m_r^2 < m_i m_f + m_\pi^2}$

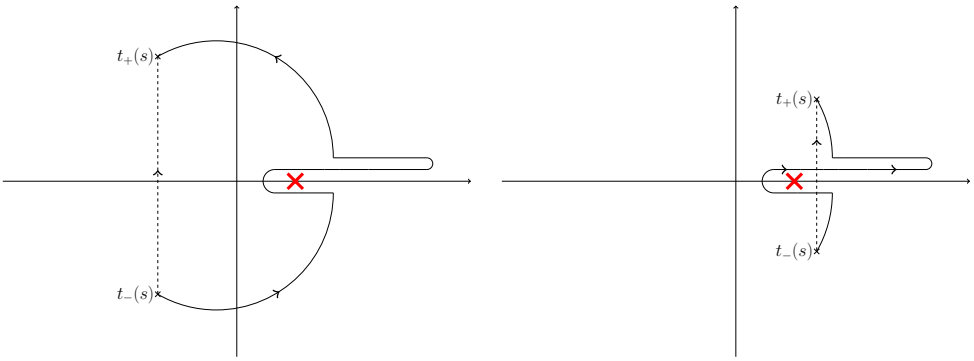

(a) $s_f < s$ (b) $s_+ < s < s_f$

Figure A.7.: Deformed integral for case (c).

Additionally to a proper regularization of the pole as seen in **case (b)**, we also need to consider that the closed integration contour can encircle the pole entirely, as shown in Fig. A.7b. Increasing the energy s then leads to an enclosure of the pole.

For $s_- < s < s_+$ we have to avoid the pole by using the $+i\epsilon$ prescription. Thus in this region, the partial-wave projection is given by Eq. (A.37).

For $s > s_+$ we see that the pole gets enclosed by the integration contour. Hence the residue needs to be taken into account until

$$\operatorname{Re} t_\pm(s_f) = m_r^2 \,. \tag{A.40}$$

Notice that in the corresponding energy region κ is purely imaginary. Thus we can determine s_f to be

$$s_f = m_i^2 + m_f^2 + 2m_\pi^2 - 2m_r^2 \,. \tag{A.41}$$

Restricting ourselves to the energy region $s_+ < s < s_f$ allows us to calculate

$$(2\ell+1)A_\ell(s) = \frac{2}{\kappa}\left[\int_{\mathcal{D}} \mathrm{d}t\, \frac{\Psi(t)}{t - m_r^2} - 2\pi i\, \Psi(m_r^2)\right] . \tag{A.42}$$

and for the S-wave projection of a stable propagator

$$A_0(s) = \frac{2}{\kappa}\left[\log\left(\frac{t_+(s) - m_r^2}{t_-(s) - m_r^2}\right) - 2\pi i\right] . \tag{A.43}$$

Overall we thus obtain

$$(2\ell+1)A_\ell(s) = \begin{cases} \frac{2}{\kappa}\int\limits_{t_-(s)}^{t_+(s)} \mathrm{d}t\, \frac{\Psi(t+i\epsilon)}{t - m_r^2 + i\epsilon} & , \quad s_- \le s \le s_+ \\ \frac{2}{\kappa}\left[\int_{\mathcal{D}} \mathrm{d}t\, \frac{\Psi(t)}{t-m_r^2} - 2\pi i \Psi(m_r^2)\right] & , \quad s_+ < s \le s_f \\ \frac{2}{\kappa}\int_{\mathcal{D}} \mathrm{d}t\, \frac{\Psi(t)}{t-m_r^2} & , \quad \text{else} \end{cases} \tag{A.44}$$

and for the S-wave projection

$$A_0(s) = \begin{cases} \frac{2}{\kappa}\left[\log\left(-\frac{t_+(s)-m_r^2}{t_-(s)-m_r^2}\right) - i\pi\right] & , \quad s_- \leq s < s_+ \\ \frac{2}{\kappa}\left[\log\left(\frac{t_+(s)-m_r^2}{t_-(s)-m_r^2}\right) - 2i\pi\right] & , \quad s_+ \leq s < s_f \\ \frac{2}{\kappa}\log\left(\frac{t_+(s)-m_r^2}{t_-(s)-m_r^2}\right) & , \quad \text{else} \end{cases} \tag{A.45}$$

Case (d): $\mathbf{0 < m_r^2 < (m_f + m_\pi)^2}$

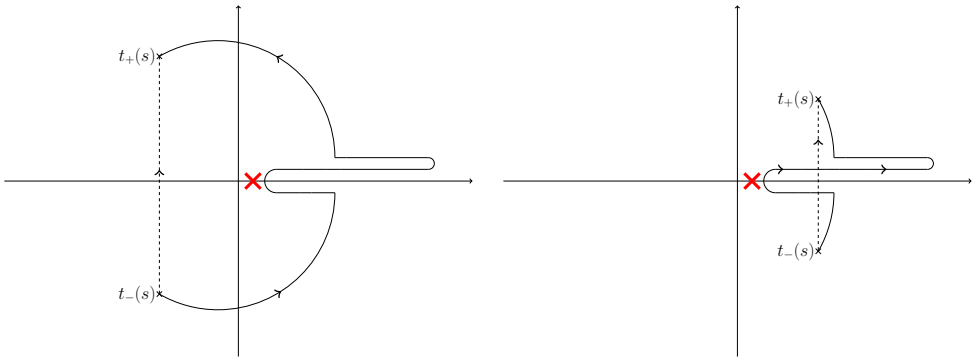

(a) $s_f < s$ (b) $s < s_f$

Figure A.8.: Deformed integral for case (d).

The last case can be treated in analogy to the other three. However as previously shown the partial-wave projection is given by

$$(2\ell+1)A_\ell(s) = \frac{2}{\kappa}\left(-2\pi i\Psi(m_r^2) + \int_{KT} \mathrm{d}t\, \frac{\Psi(t)}{t-m_r^2}\right). \tag{A.46}$$

Compared to **case (b)** the $\epsilon \to 0$ prescription does not pose any problem for the integration. For $s < s_f$ we see that

$$(2\ell+1)A_\ell(s) = \frac{2}{\kappa}\left(-2\pi i\Psi(m_r^2) + \int_{\mathcal{D}} \mathrm{d}t\, \frac{\Psi(t)}{t-m_r^2}\right) \tag{A.47}$$

as the pole lies outside of the integration contour.

For $s \geq s_f$ the pole is encircled in a counterclockwise direction. Therefore the residue cancels out and we obtain

$$(2\ell+1)A_\ell(s) = \frac{2}{\kappa}\int_{\mathcal{D}} \mathrm{d}t\, \frac{\Psi(t)}{t-m_r^2}. \tag{A.48}$$

Therefore the partial-wave projection reads

$$(2\ell+1)A_\ell(s) = \begin{cases} \frac{2}{\kappa}(-2\pi i\Psi(m_r^2) + \int_{\mathcal{D}} \mathrm{d}t\, \frac{\Psi(t)}{t-m_r^2}) & , \quad s < s_f \\ \frac{2}{\kappa}\int_{\mathcal{D}} \mathrm{d}t\, \frac{\Psi(t)}{t-m_r^2} & , \quad \text{else} \end{cases} \tag{A.49}$$

and explicitly for the S-wave of a stable propagator

$$A_0(s) = \begin{cases} \frac{2}{\kappa}\left[\log\left(\frac{t_+(s)-m_r^2}{t_-(s)-m_r^2}\right) - 2i\pi\right] & , \quad s \leq s_f \\ \\ \frac{2}{\kappa}\log\left(\frac{t_+(s)-m_r^2}{t_-(s)-m_r^2}\right) & , \quad \text{else} \end{cases} . \tag{A.50}$$

B. Anomalous thresholds

Consider the S-wave projections defined by Eqs. (A.33), (A.39), (A.45), (A.50). They have a branch cut lying between the branch points $s_\pm$ from Eq. (A.34). In this section we will show their influence on the inhomogeneous Omnès problem.

Assume first m_f to be fixed in a range such that $m_f < m_r + m_\pi$ and $m_r < m_f + m_\pi$. This assumption is equivalent with $(m_r - m_\pi)^2 \leq m_f^2 \leq (m_r + m_\pi)^2$, which guarantees that m_r cannot go on-shell. In order to ensure that $s_\pm$ do not lie on the integration path $s' \in [s_0, \infty)$, we make m_i sufficiently small. In this case the inhomogeneous Omnès solution defined in Sect. 1.3.4

$$\zeta_\ell(s) = P(s) + \frac{s^n}{\pi} \int\limits_{s_0}^{\infty} \frac{\mathrm{d}s'}{(s')^n} (\Omega_\ell^{-1})(s') \frac{t_\ell(s') \hat{\sigma}(s') K_\ell(s')}{s' - s - i\epsilon} \tag{B.1}$$

is well defined.

Using the discontinuity

$$\mathrm{disc}_R\, \zeta_\ell = 2i \Omega_\ell^{-1} t_\ell \hat{\sigma} K_\ell \,. \tag{B.2}$$

it is possible do an analytic continuation of ζ_ℓ onto the second Riemann sheet by

$$\zeta_\ell^{II}(s) = \zeta_\ell(s) - \mathrm{disc}_R\, \zeta_\ell(s) = \zeta_\ell(s) + 2i(\Omega^{-1}) t_\ell \hat{\sigma} K_\ell \,. \tag{B.3}$$

An interesting observation is that $\zeta_\ell^{II}(s)$ additionally has the logarithmic branch cut coming from K_ℓ.

As soon as this function is analytically continued in m_i, the logarithmic branch points $s_\pm$ move through the complex plane and may go though the unitarity cut onto the first Riemann sheet. In order to illustrate this further we first search the solution of

$$4m_\pi^2 = s_\pm((\tilde{m}_i)^2) = \frac{(\tilde{m}_i^2 - m_f^2)^2 - \left(\sqrt{\lambda(\tilde{m}_i^2, m_r^2, m_\pi^2)} \mp \sqrt{\lambda(m_f^2, m_r^2, m_\pi^2)}\right)^2}{4m_r^2} \tag{B.4}$$

which is given by

$$\tilde{m}_i^2 = 2m_\pi^2 + 2m_r^2 - m_f^2 \,. \tag{B.5}$$

Using this solution for $s_\pm(\tilde{m}_i^2)$ we obtain

$$s_+(\tilde{m}_i^2) = \frac{(m_\pi^2 - m_f^2 + m_r^2)^2}{m_r^2} \quad \text{and} \quad s_-(\tilde{m}_i^2) = 4m_\pi^2 \,. \tag{B.6}$$

In order to better understand the motion of $s_\pm(m_i^2)$ near the unitarity cut, we expand them up to second order in m_i^2.

While the first derivative is given by

$$\left.\frac{\mathrm{d}s_+}{\mathrm{d}m_i^2}\right|_{m_i^2=\tilde{m}_i^2} = \frac{m_\pi^2 - m_f^2 + m_r^2}{m_r^2} \quad , \quad \left.\frac{\mathrm{d}s_-}{\mathrm{d}m_i^2}\right|_{m_i^2=\tilde{m}_i^2} = 0 \tag{B.7}$$

the second derivative is evaluated to be

$$\left.\frac{\mathrm{d}^2 s_+}{\mathrm{d}(m_i^2)^2}\right|_{m_i^2=\tilde{m}_i^2} = -\frac{2m_\pi^2}{\lambda(m_f^2, m_r^2, m_\pi^2)} \quad , \quad \left.\frac{\mathrm{d}^2 s_-}{\mathrm{d}(m_i^2)^2}\right|_{m_i^2=\tilde{m}_i^2} = \frac{2m_\pi^2}{\lambda(m_f^2, m_r^2, m_\pi^2)} \,. \tag{B.8}$$

Using the $+i\epsilon$ prescription for m_i^2 we can calculate

$$\begin{aligned} s_+(\tilde{m}_i^2 + i\epsilon + \delta m_i^2) = {} & \frac{(m_\pi^2 - m_f^2 + m_r^2)^2}{m_r^2} + \frac{m_\pi^2 \epsilon^2}{\lambda(m_f^2, m_r^2, m_\pi^2)} + \frac{m_\pi^2 - m_f^2 + m_r^2}{m_r^2}\, i\epsilon \\ & + \delta m_i^2 \left[\frac{m_\pi^2 - m_f^2 + m_r^2}{m_r^2} - \frac{m_\pi^2 \delta m_i^2}{\lambda(m_f^2, m_r^2, m_\pi^2)}\right] \\ & - \frac{m_\pi^2}{\lambda(m_f^2, m_r^2, m_\pi^2)}\, 2i\epsilon\delta m_i^2 + \mathcal{O}(\epsilon^3) \end{aligned} \tag{B.9}$$

and

$$\begin{aligned} s_-(\tilde{m}_i^2 + i\epsilon + \delta m_i^2) = {} & 4m_\pi^2 - \frac{m_\pi^2 \epsilon^2}{\lambda(m_f^2, m_r^2, m_\pi^2)} + \frac{m_\pi^2 (\delta m_i^2)^2}{\lambda(m_f^2, m_r^2, m_\pi^2)} \\ & + \frac{m_\pi^2}{\lambda(m_f^2, m_r^2, m_\pi^2)} 2i\epsilon\delta m_i^2 + \mathcal{O}(\epsilon^3) \,. \end{aligned} \tag{B.10}$$

Varying now δm_i^2 from negative to positive values we see that $s_+(m_i^2)$ does not cross the unitarity cut, as it still has a nonvanishing imaginary part at $\delta m_i^2 = 0$. However $s_-(m_i^2)$ will pass the unitarity cut if $\lambda(m_f^2, m_r^2, m_\pi^2) < 0$.

Thus $s_-(m_i^2)$ goes to the physical Riemann sheet if

$$m_i^2 > 2m_\pi^2 + 2m_r^2 - m_f^2 \quad \text{and} \quad \lambda(m_f^2, m_r^2, m_\pi^2) < 0 \,. \tag{B.11}$$

The second restriction will be lifted by an additional analytic continuation within m_f. Therefore an additional branch point appears on the physical sheet when

$$m_i^2 > 2m_\pi^2 + 2m_r^2 - m_f^2 \,. \tag{B.12}$$

The additional logarithmic branch point on the first Riemann sheet is called anomalous threshold.

It follows, that the inhomogeneous Omnès problem needs to be adjusted. Additionally to the unitarity cut the anomalous logarithmic cut between s_- and s_+ coming from $K_\ell(s)$ needs to be avoided. Therefore the anomalous discontinuity is given by

$$\mathrm{disc}_{\mathrm{anom}}\, \zeta_\ell(s) = 2i(\Omega_L^{-1}) t_\ell \hat{\sigma}\, \mathrm{disc}\, K_\ell \,. \tag{B.13}$$

For the S-wave projection of a stable propagator the anomalous discontinuity is produced by the logarithmic branch cut leading to the discontinuity

$$\operatorname{disc} K_0 = \operatorname{disc} A_0 = \frac{4i\pi}{\kappa(s)} \tag{B.14}$$

with $A_0(s)$ as in Appendix A.4. Note that K_0 is in general a vector in channel space. Assume that only one channel contributes to the inhomogeneity, which we call for simplicity $\pi\pi$. Then the anomalous discontinuity can be written as

$$\operatorname{disc}_{\text{anom}} \zeta_L(s) = -\frac{8\pi}{\kappa(s)} \Omega_0^{-1}(s) t_0(s) \hat{\sigma}(s) \vec{v}\,, \tag{B.15}$$

where $\vec{v}$ is a unit vector in channel space pointing in the $\pi\pi$ direction. The branch cut between s_- on the first Riemann sheet and s_+ on the second sheet is parametrized by a straight line from s_- to the unitarity branch point s_0 and from there to s_+. Therefore the inhomogeneous Omnès problem is modified to

$$\zeta_0(s) = P(s) + \frac{s^n}{\pi} \int\limits_{s_0}^{\infty} \frac{\mathrm{d}s'}{(s')^n} \Omega_0^{-1}(s') \frac{t_0(s') \hat{\sigma}(s') K_0(s')}{s' - s} + \zeta_{\text{anom}}(s) \tag{B.16}$$

with

$$\zeta_{\text{anom}}(s) = -\frac{s^n}{2\pi i} \int\limits_0^1 \mathrm{d}x \frac{8\pi\, \Omega_0^{-1}(z(x)) t_0(z(x)) \hat{\sigma}(z(x)) \vec{v}}{z^n(x) \kappa(z(x)) (z(x) - s)} \frac{\mathrm{d}z(x)}{\mathrm{d}x} \tag{B.17}$$

and

$$z(x) = (1 - x) s_- + x s_0\,. \tag{B.18}$$

This form is equivalent to

$$M_0(s) = \Omega_0(s) \left[P(s) + \frac{s^n}{\pi} \int\limits_{s_0}^{\infty} \frac{\mathrm{d}s'}{(s')^n} \Omega_0^{-1}(s') \frac{t_0(s') \sigma(s') K_0(s')}{s' - s} + \zeta_{\text{anom}}(s) \right]. \tag{B.19}$$

Note that in principle singularities in this integration can show up at the zeros of $\kappa(z(s))$. Therefore one can choose the logarithmic cut between s_- and s_0 in the complex plane such that these singularities are avoided.

C. Dispersive reconstruction of the scalar triangle

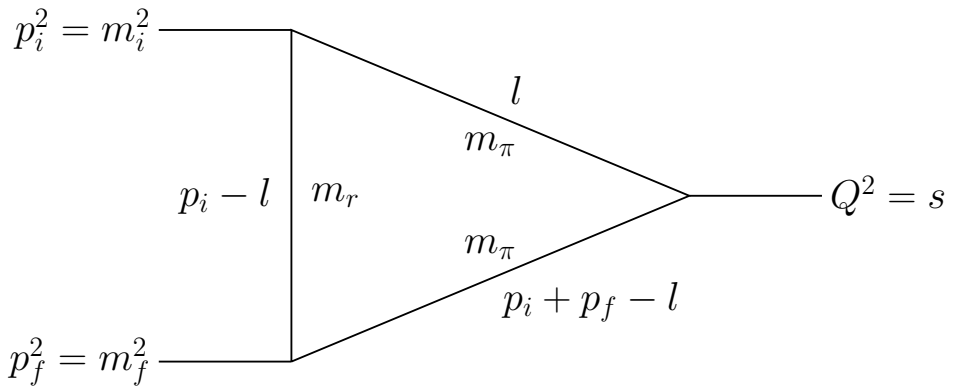

Figure C.1.: Scalar triangle graph.

The scalar triangle graph as shown in Fig. C.1 and is defined by the external momenta p_i, p_f and $Q = p_i + p_f$. Their corresponding masses are given as $p_i^2 = m_i^2$, $p_f^2 = m_f^2$ and $Q^2 = s$. The internal masses are denoted by m_r and m_π. Additionally the diagram contains one free loop momentum l. With these definitions the standard scalar triangle reads

$$C_0 = \frac{1}{i\pi^2} \int \mathrm{d}^4 l \, \frac{1}{(p_i - l)^2 - m_r^2} \, \frac{1}{l^2 - m_\pi^2} \, \frac{1}{(p_i + p_f - l)^2 - m_\pi^2} \,. \tag{C.1}$$

A standard procedure for the evaluation of the integral is defined by the use of Feynman-parameters. There are also many available libraries, which allow for the numerical evaluation of loop integrals such as Looptools [249] or the X-package [250].

Since the scalar triangle graph is a well-known function it allows us to test the viability of our considerations in Appendix A and B. A dispersive reconstruction of C_0 as already discussed in Refs. [69, 251, 252, 253] will be applied here.

By restricting m_i and m_r to the regions $m_r - m_\pi < m_i < m_r + m_\pi$ and $m_f - m_\pi < m_r < m_f + m_\pi$ the resonance with mass m_r cannot go on-shell. Therefore the only cut, which is operative is the dipion cut. Its discontinuity can be calculated using the Cutkosky rules [254]

$$\mathrm{disc}\, C_0 = \frac{1}{i\pi^2} \int \mathrm{d}^4 l \, \frac{(-2\pi i \delta(l^2 - m_\pi^2))}{(p_i - l)^2 - m_r^2} \, (-2\pi i \delta((p_i + p_f - l)^2 - m_\pi^2)) \,. \tag{C.2}$$

Due to the δ-distribution each internal pion momentum will be set on-shell. In this manner the kinematics of this process is similar to a 2-2 scattering process. Thus define the Mandelstam variables in the dipion center-of-mass frame

$$(p_i + p_f)^2 = Q^2 = s \tag{C.3}$$

and

$$(p_i - l)^2 = t = \frac{1}{2}\left(m_i^2 + m_f^2 + 2m_\pi^2 - s + \kappa(s)\cos\theta\right) \tag{C.4}$$

as already defined in Eq. (3.4). The scattering angle θ is defined by the product

$$\vec{p_i} \cdot \vec{l} = |\vec{p}||\vec{l}|\cos\theta\,. \tag{C.5}$$

An evaluation of the δ distributions leads to

$$\operatorname{disc} C_0(s) = 2\pi i \frac{\sigma_\pi(s)}{2} \int_{-1}^{1} \mathrm{d}\cos\theta\, \frac{1}{t(s,\cos\theta) - m_r^2} = 2\pi i\, \frac{\sigma_\pi(s)}{2} A_0(s, m_r^2) \tag{C.6}$$

with the pion phase space

$$\sigma_\pi(s) = \sqrt{1 - \frac{4m_\pi^2}{s}}\,. \tag{C.7}$$

The most general analytic continuation in m_i and m_r does not only involve the function $A_0(s, m_r^2)$ as already discussed in the Appendix A.4 but also anomalous thresholds of Appendix B.

Summarizing the discontinuity can be differentiated with four cases. **Case a** considers $m_r^2 > (m_i - m_\pi)^2$ with a discontinuity

$$\operatorname{disc} C_0^a(s) = 2\pi i\, \frac{\sigma_\pi(s)}{\kappa(s)} \log\left(\frac{t_+(s) - m_r^2}{t_-(s) - m_r^2}\right)\,. \tag{C.8}$$

Case b, with $m_i m_f + m_\pi^2 < m_r^2 < (m_i - m_\pi)^2$ on the other hand gives

$$\operatorname{disc} C_0^b(s) = 2\pi i\, \frac{\sigma_\pi(s)}{\kappa(s)} \begin{cases} \left[\log\left(-\frac{t_+(s)-m_r^2}{t_-(s)-m_r^2} - i\pi\right)\right] & , s_- \le s \le s_+ \\ \log\left(\frac{t_+(s)-m_r^2}{t_-(s)-m_r^2}\right) & , \text{else} \end{cases}\,. \tag{C.9}$$

The logarithmic branch points $s_\pm$ are defined in Eq. (A.34).

Case c extends the describtion to $(m_i + m_\pi)^2 < m_r^2 < m_i m_f + m_\pi^2$. Its discontinuity is given by

$$\operatorname{disc} C_0^c(s) = 2\pi i\, \frac{\sigma_\pi(s)}{\kappa(s)} \begin{cases} \left[\log\left(-\frac{t_+(s)-m_r^2}{t_-(s)-m_r^2} - i\pi\right)\right] & , s_- \le s \le s_+ \\ \left[\log\left(\frac{t_+(s)-m_r^2}{t_-(s)-m_r^2}\right) - 2i\pi\right] & , s_+ < s < s_f \\ \log\left(\frac{t_+(s)-m_r^2}{t_-(s)-m_r^2}\right) & , \text{else} \end{cases}\,, \tag{C.10}$$

where s_f is defined in Eq. (A.41).

Each of these three cases can be reconstructed dispersively without an anomalous threshold, as the logarithmic branch points lie on the second Riemann-sheet

$$C_0^{a,b,c} = \frac{1}{2\pi i} \int\limits_{4m_\pi^2}^{\infty} \frac{\mathrm{d}z}{z-s} \operatorname{disc} C_0^{a,b,c}(z)\,. \tag{C.11}$$

For $m_r^2 < (m_f + m_\pi)^2$, denoted as **case d**, the discontinuity is given as

$$\operatorname{disc} C_0^d(s) = 2\pi i \, \frac{\sigma_\pi(s)}{\kappa(s)} \begin{cases} \left[\log\left(\frac{t_+(s)-m_r^2}{t_-(s)-m_r^2}\right) - 2i\pi\right] & , \, s < s_f \\ \log\left(\frac{t_+(s)-m_r^2}{t_-(s)-m_r^2}\right) & , \text{ else} \end{cases} . \tag{C.12}$$

It can be reconstructed dispersively by

$$C_0^d(s) = \frac{1}{2\pi i} \int\limits_{4m_\pi^2}^{\infty} \frac{\mathrm{d}z}{z-s} \operatorname{disc} C_0^d(z) + I_{\text{anom}}(s) \tag{C.13}$$

with

$$I_{\text{anom}}(s) = \frac{1}{2\pi i} \int\limits_{0}^{1} \mathrm{d}x \, \frac{4\pi^2 \sigma_\pi(z(x))}{\kappa(z(x))(z(x)-s)} \, \frac{\mathrm{d}z(x)}{\mathrm{d}x} \tag{C.14}$$

and $z(x)$ defined in Eq. (B.18).

Exemplary plots for the evaluation in the four different cases are shown in Fig. C.2. It shows that the reconstruction works perfectly and thus signifies the correctness of our approach. However, we want to point out again that this approach only has been calculated for decay processes with $s > 4m_\pi^2$ as well as $m_r^2 > 0$. An extension to other energy regions remains to be shown.

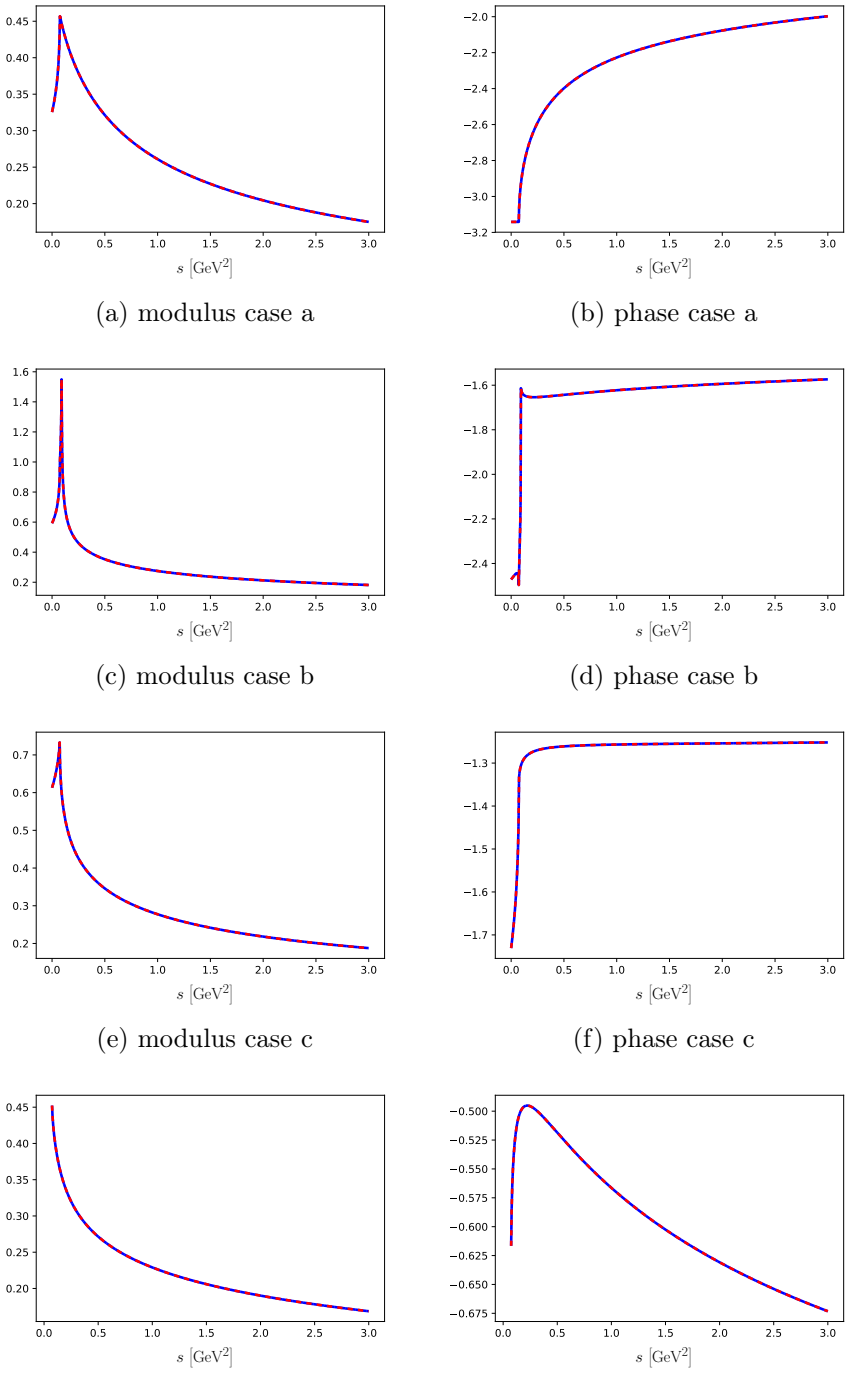

(a) modulus case a (b) phase case a

(c) modulus case b (d) phase case b

(e) modulus case c (f) phase case c

(g) modulus case d (h) phase case d

Figure C.2.: Exemplary evaluation for C_0 with $m_i = m_{\Upsilon(5s)}$ and $m_f = m_{\Upsilon(1s)}$. The Looptools evaluation is shown blue and the dispersive reconstruction in orange. The resonance mass is given by $m_r^2 = 120\,\mathrm{GeV}^2$ (case a), $m_r^2 = 110\,\mathrm{GeV}^2$ (case b), $m_r^2 = 95\,\mathrm{GeV}^2$ (case c) and $m_r^2 = 80\,\mathrm{GeV}^2$ (case d).

Bibliography

[1] S. L. Glashow, Nucl. Phys. **22**, 579 (1961).

[2] S. Weinberg, Phys. Rev. Lett. **19**, 1264 (1967).

[3] A. Salam, Conf. Proc. **C680519**, 367 (1968).

[4] H. Fritzsch, M. Gell-Mann, and H. Leutwyler, Phys. Lett. **47B**, 365 (1973).

[5] F. Englert and R. Brout, Phys. Rev. Lett. **13**, 321 (1964).

[6] P. W. Higgs, Phys. Rev. Lett. **13**, 508 (1964).

[7] G. Aad *et al.* [ATLAS Collaboration], Phys. Lett. **B716**, 1 (2012) [arXiv:1207.7214 [hep-ex]].

[8] S. Chatrchyan *et al.* [CMS Collaboration], Phys. Lett. **B716**, 30 (2012) [arXiv:1207.7235 [hep-ex]].

[9] Z. Maki, M. Nakagawa, and S. Sakata, Prog. Theor. Phys. **28**, 870 (1962).

[10] B. Pontecorvo, Sov. Phys. JETP **26**, 984 (1968), [Zh. Eksp. Teor. Fiz.53,1717(1967)].

[11] K. S. Hirata *et al.* [Kamiokande-II Collaboration], Phys. Lett. **B205**, 416 (1988).

[12] D. J. Gross and F. Wilczek, Phys. Rev. **D8**, 3633 (1973).

[13] K. Ottnad, B. Kubis, U.-G. Meißner, and F. K. Guo, Phys. Lett. **B687**, 42 (2010) [arXiv:0911.3981 [hep-ph]].

[14] M. Tanabashi *et al.* [Particle Data Group], Phys. Rev. **D98**, 030001 (2018).

[15] S. Weinberg, Physica **A96**, 327 (1979).

[16] S. Weinberg, PoS **CD09**, 001 (2009) [arXiv:0908.1964 [hep-th]].

[17] J. Gasser and H. Leutwyler, Annals Phys. **158**, 142 (1984).

[18] J. Gasser and H. Leutwyler, Nucl. Phys. **B250**, 465 (1985).

[19] V. Bernard, N. Kaiser, and U.-G. Meißner, Int. J. Mod. Phys. E **4**, 193 (1995) [arXiv:hep-ph/9501384].

[20] S. Scherer, Adv. Nucl. Phys. **27**, 277 (2003) [arXiv:hep-ph/0210398], [,277(2002)].

[21] B. Kubis, "An Introduction to chiral perturbation theory," in *Workshop on Physics and Astrophysics of Hadrons and Hadronic Matter Shantiniketan, India, November 6-10, 2006*. 2007. arXiv:hep-ph/0703274 [HEP-PH].

[22] A. Manohar and H. Georgi, Nucl. Phys. **B234**, 189 (1984).

[23] C. Vafa and E. Witten, Nucl. Phys. **B234**, 173 (1984).

[24] S. Weinberg, Physica A: Statistical Mechanics and its Applications **96**, 327 (1979), `http://www.sciencedirect.com/science/article/pii/0378437179902231`.

[25] M. Gell-Mann, R. J. Oakes, and B. Renner, Phys. Rev. **175**, 2195 (1968).

[26] G. Muller and U.-G. Meißner, Nucl. Phys. B **492**, 379 (1997) [arXiv:hep-ph/9610275].

[27] U.-G. Meißner, G. Muller, and S. Steininger, Annals Phys. **279**, 1 (2000) [arXiv:hep-ph/9809446].

[28] N. Isgur and M. B. Wise, Phys. Lett. **B232**, 113 (1989).

[29] H. Georgi, Phys. Lett. **B240**, 447 (1990).

[30] B. Grinstein, Nucl. Phys. **B339**, 253 (1990).

[31] H. D. Politzer and M. B. Wise, Phys. Lett. **B206**, 681 (1988).

[32] M. B. Voloshin and M. A. Shifman, Sov. J. Nucl. Phys. **45**, 292 (1987), [Yad. Fiz.45,463(1987)].

[33] M. Neubert, Subnucl. Ser. **34**, 98 (1997) [arXiv:hep-ph/9610266].

[34] R. Casalbuoni, A. Deandrea, N. Di Bartolomeo, R. Gatto, F. Feruglio, and G. Nardulli, Phys. Rept. **281**, 145 (1997) [arXiv:hep-ph/9605342].

[35] H. Georgi, "Heavy quark effective field theory," in *Theoretical Advanced Study Institute in Elementary Particle Physics (TASI 91): Perspectives in the Standard Model*, pp. 0589–630. 8, 1991.

[36] T. Mannel, W. Roberts, and Z. Ryzak, Nucl. Phys. **B368**, 204 (1992).

[37] E. E. Jenkins and A. V. Manohar, Phys. Lett. **B255**, 558 (1991).

[38] U.-G. Meißner, ed., *Effective field theories of the standard model. Proceedings, Workshop, Dobogoko, Hungary, August 22-26, 1991*. 1992.

[39] J. Gasser, Annals Phys. **136**, 62 (1981).

[40] J. Gasser and H. Leutwyler, Phys. Rept. **87**, 77 (1982).

[41] M. E. Luke, Phys. Lett. **B252**, 447 (1990).

[42] H. Georgi, B. Grinstein, and M. B. Wise, Phys. Lett. **B252**, 456 (1990).

[43] A. F. Falk, B. Grinstein, and M. E. Luke, Nucl. Phys. **B357**, 185 (1991).

[44] E. Eichten and B. R. Hill, Phys. Lett. **B243**, 427 (1990).

[45] T. Mannel and G. A. Schuler, Phys. Lett. **B349**, 181 (1995) [arXiv:hep-ph/9412337].

[46] A. F. Falk, Nucl. Phys. **B378**, 79 (1992).

[47] S. R. Coleman, J. Wess, and B. Zumino, Phys. Rev. **177**, 2239 (1969).

[48] C. G. Callan, Jr., S. R. Coleman, J. Wess, and B. Zumino, Phys. Rev. **177**, 2247 (1969).

[49] M. B. Wise, Phys. Rev. **D45**, R2188 (1992).

[50] T.-M. Yan, H.-Y. Cheng, C.-Y. Cheung, G.-L. Lin, Y. C. Lin, and H.-L. Yu, Phys. Rev. **D46**, 1148 (1992), [Erratum: Phys. Rev.D55,5851(1997)].

[51] G. Burdman and J. F. Donoghue, Phys. Lett. **B280**, 287 (1992).

[52] G. Burdman and J. F. Donoghue, Phys. Rev. Lett. **68**, 2887 (1992).

[53] A. F. Falk, H. Georgi, B. Grinstein, and M. B. Wise, Nucl. Phys. **B343**, 1 (1990).

[54] E. E. Jenkins, M. E. Luke, A. V. Manohar, and M. J. Savage, Nucl. Phys. **B390**, 463 (1993) [arXiv:hep-ph/9204238].

[55] T. Mannel and R. Urech, Z. Phys. **C73**, 541 (1997) [arXiv:hep-ph/9510406].

[56] Y.-H. Chen, J. T. Daub, F.-K. Guo, B. Kubis, U.-G. Meißner, and B.-S. Zou, Phys. Rev. **D93**, 034030 (2016) [arXiv:1512.03583 [hep-ph]].

[57] M. Cleven, F.-K. Guo, C. Hanhart, and U.-G. Meißner, Eur. Phys. J. **A47**, 120 (2011) [arXiv:1107.0254 [hep-ph]].

[58] J. S. Schwinger, Phys. Rev. **73**, 416 (1948).

[59] J. S. Schwinger, Phys. Rev. **74**, 1439 (1948).

[60] J. S. Schwinger, Phys. Rev. **75**, 651 (1948).

[61] J. S. Schwinger, Phys. Rev. **76**, 790 (1949).

[62] H. Fukuda, Y. Miyamoto, and S.-i. Tomonaga, Progress of Theoretical Physics **4**, 47 (03, 1949) [https://academic.oup.com/ptp/article-pdf/4/1/47/5257519/4-1-47.pdf], https://doi.org/10.1143/PTP.4.47.

[63] R. P. Feynman, Phys. Rev. **74**, 1430 (1948).

[64] R. P. Feynman, Phys. Rev. **76**, 769 (1949).

[65] F. J. Dyson, Phys. Rev. **75**, 486 (1949).

[66] F. J. Dyson, Phys. Rev. **75**, 1736 (1949).

[67] D. J. Gross and F. Wilczek, Phys. Rev. **D9**, 980 (1974).

[68] H. D. Politzer, Phys. Rept. **14**, 129 (1974).

[69] L. Landau, Nucl. Phys. **13**, 181 (1960).

[70] G. F. Chew, Rev. Mod. Phys. **34**, 394 (1962).

[71] H. P. Stapp, Phys. Rev. **125**, 2139 (1962).

[72] J. Gunson, Journal of Mathematical Physics **6**, 827 (1965).

[73] J. Gunson, Journal of Mathematical Physics **6**, 845 (1965).

[74] J. Gunson, Journal of Mathematical Physics **6**, 852 (1965).

[75] R. J. Eden, P. V. Landshoff, D. I. Olive, and J. C. Polkinghorne, *The analytic S-matrix*, Cambridge Univ. Press, 1966.

[76] A. R. White [arXiv:hep-ph/0002303].

[77] D. Iagolnitzer, *Scattering in quantum field theories: The Axiomatic and constructive approaches*, Princeton University Press, 1994.

[78] H. Lehmann, K. Symanzik, and W. Zimmermann, Nuovo Cim. **1**, 205 (1955).

[79] H. Lehmann, K. Symanzik, and W. Zimmermann, Nuovo Cim. **6**, 319 (1957).

[80] H. Epstein, "Some Analytic Properties of Scattering Amplitudes in Quantum Field Theory," in *Axiomatic Field Theory, Volume 1*, M. Chrétien and S. Deser, eds., vol. 1, p. 1. Jan., 1966.

[81] H. Epstein, V. Glaser, and R. Stora, "General Properties of the n Point Functions in Local Quantum Field Theory," in *Institute on Structural Analysis of Multiparticle Collision Amplitudes in Relativistic Quantum Theory*, pp. 5–93. 1, 1975.

[82] D. I. Olive, Il Nuovo Cimento **37**, 1422 (1965).

[83] S. Mandelstam, Phys. Rev. **112**, 1344 (1958).

[84] M. Jacob and G. C. Wick, Annals Phys. **7**, 404 (1959), [Annals Phys.281,774(2000)].

[85] J. S. Schwinger, Phys. Rev. **82**, 914 (1951).

[86] G. Luders, Kong. Dan. Vid. Sel. Mat. Fys. Med. **28N5**, 1 (1954).

[87] W. Pauli, L. Rosenfeld, and V. Weisskopf, *Niels Bohr and the Development of Physics*, Pergamon Press, 1955.

[88] J. S. Bell, PhD thesis, Birmingham University (1954).

[89] R. Omnes, Nuovo Cim. **8**, 316 (1958).

[90] N. Muskhelishvili, *Singular integral equations:*, P. Noordhoff, 1953.

[91] J. F. Donoghue, J. Gasser, and H. Leutwyler, Nucl. Phys. **B343**, 341 (1990).

[92] J. Gasser and U.-G. Meißner, Nucl. Phys. **B357**, 90 (1991).

[93] J. F. De Troconiz and F. J. Yndurain, Phys. Rev. **D65**, 093001 (2002) [arXiv:hep-ph/0106025].

[94] F.-K. Guo, C. Hanhart, F. J. Llanes-Estrada, and U.-G. Meißner, Phys. Lett. **B678**, 90 (2009) [arXiv:0812.3270 [hep-ph]].

[95] C. Hanhart, Phys. Lett. **B715**, 170 (2012) [arXiv:1203.6839 [hep-ph]].

[96] J. Niecknig, PhD thesis, University of Bonn (2018).

[97] K. M. Watson, Phys. Rev. **95**, 228 (1954).

[98] B. Moussallam, Eur. Phys. J. **C14**, 111 (2000) [arXiv:hep-ph/9909292].

[99] S. Descotes-Genon, PhD thesis, Université de Paris-Sud (2000).

[100] M. Hoferichter, C. Ditsche, B. Kubis, and U.-G. Meißner, JHEP **06**, 063 (2012) [arXiv:1204.6251 [hep-ph]].

[101] J. Daub, Diploma thesis, University of Bonn (2013).

[102] M. Galassi, J. Davies, J. Theiler, B. Gough, and G. Jungman, *GNU Scientific Library - Reference Manual, Third Edition, for GSL Version 1.12 (3. ed.).*, Network Theory Ltd, 2009.

[103] M. Mikhasenko [arXiv:1507.06552 [hep-ph]].

[104] M. Gell-Mann, Phys. Lett. **8**, 214 (1964).

[105] G. Zweig, *An SU(3) model for strong interaction symmetry and its breaking. Version 2*, pp. 22–101. Hadronic Press, 2, 1964.

[106] M. Aghasyan *et al.* [COMPASS Collaboration], Phys. Rev. **D98**, 092003 (2018) [arXiv:1802.05913 [hep-ex]].

[107] M. Alekseev *et al.* [COMPASS Collaboration], Phys. Rev. Lett. **104**, 241803 (2010) [arXiv:0910.5842 [hep-ex]].

[108] C. Adolph *et al.* [COMPASS Collaboration], Phys. Lett. **B740**, 303 (2015) [arXiv:1408.4286 [hep-ex]].

[109] R. Aaij *et al.* [LHCb Collaboration], Phys. Rev. Lett. **115**, 072001 (2015) [arXiv:1507.03414 [hep-ex]].

[110] M. H. Alston, L. W. Alvarez, P. Eberhard, M. L. Good, W. Graziano, H. K. Ticho, and S. G. Wojcicki, Phys. Rev. Lett. **6**, 698 (1961).

[111] F.-K. Guo, C. Hanhart, U.-G. Meißner, Q. Wang, Q. Zhao, and B.-S. Zou, Rev. Mod. Phys. **90**, 015004 (2018) [arXiv:1705.00141 [hep-ph]].

[112] S. Weinberg, Phys. Rev. **137**, B672 (1965).

[113] A. Filin, A. Romanov, V. Baru, C. Hanhart, Y. Kalashnikova, A. Kudryavtsev, U.-G. Meißner, and A. Nefediev, Phys. Rev. Lett. **105**, 019101 (2010) [arXiv:1004.4789 [hep-ph]].

[114] F.-K. Guo and U.-G. Meißner, Phys. Rev. D **84**, 014013 (2011) [arXiv:1102.3536 [hep-ph]].

[115] V. Baru, J. Haidenbauer, C. Hanhart, Y. Kalashnikova, and A. E. Kudryavtsev, Phys. Lett. B **586**, 53 (2004) [arXiv:hep-ph/0308129].

[116] D. Morgan, Nucl. Phys. **A543**, 632 (1992).

[117] C. Hanhart, J. R. Pelaez, and G. Rios, Phys. Lett. **B739**, 375 (2014) [arXiv:1407.7452 [hep-ph]].

[118] W.-J. Lee and D. Weingarten, Phys. Rev. **D61**, 014015 (2000) [arXiv:hep-lat/9910008].

[119] G. S. Bali, K. Schilling, A. Hulsebos, A. C. Irving, C. Michael, and P. W. Stephenson [UKQCD Collaboration], Phys. Lett. **B309**, 378 (1993) [arXiv:hep-lat/9304012].

[120] C. J. Morningstar and M. J. Peardon, Phys. Rev. **D56**, 4043 (1997) [arXiv:hep-lat/9704011].

[121] Y. Chen *et al.*, Phys. Rev. **D73**, 014516 (2006) [arXiv:hep-lat/0510074].

[122] S. Gardner and U.-G. Meißner, Phys. Rev. **D65**, 094004 (2002) [arXiv:hep-ph/0112281].

[123] G. Colangelo, J. Gasser, and H. Leutwyler, Nucl. Phys. **B603**, 125 (2001) [arXiv:hep-ph/0103088].

[124] R. Garcia-Martin, R. Kaminski, J. R. Pelaez, J. Ruiz de Elvira, and F. J. Yndurain, Phys. Rev. **D83**, 074004 (2011) [arXiv:1102.2183 [hep-ph]].

[125] I. Caprini, G. Colangelo, and H. Leutwyler, Phys. Rev. Lett. **96**, 132001 (2006) [arXiv:hep-ph/0512364].

[126] R. Garcia-Martin, R. Kaminski, J. R. Pelaez, and J. Ruiz de Elvira, Phys. Rev. Lett. **107**, 072001 (2011) [arXiv:1107.1635 [hep-ph]].

[127] B. Moussallam, Eur. Phys. J. **C71**, 1814 (2011) [arXiv:1110.6074 [hep-ph]].

[128] J. R. Pelaez, Phys. Rept. **658**, 1 (2016) [arXiv:1510.00653 [hep-ph]].

[129] J. Nebreda, J. Pelaez, and G. Rios, Phys. Rev. D **84**, 074003 (2011) [arXiv:1107.4200 [hep-ph]].

[130] A. V. Anisovich, V. V. Anisovich, and A. V. Sarantsev, Phys. Rev. **D62**, 051502 (2000) [arXiv:hep-ph/0003113].

[131] C. Amsler and N. Tornqvist, Phys. Rept. **389**, 61 (2004).

[132] R. L. Jaffe, Phys. Rev. **D15**, 267 (1977).

[133] M. G. Alford and R. L. Jaffe, Nucl. Phys. **B578**, 367 (2000) [arXiv:hep-lat/0001023].

[134] L. Maiani, F. Piccinini, A. D. Polosa, and V. Riquer, Phys. Rev. Lett. **93**, 212002 (2004) [arXiv:hep-ph/0407017].

[135] L. Maiani, A. D. Polosa, and V. Riquer, Phys. Lett. **B651**, 129 (2007) [arXiv:hep-ph/0703272].

[136] G. 't Hooft, G. Isidori, L. Maiani, A. D. Polosa, and V. Riquer, Phys. Lett. **B662**, 424 (2008) [arXiv:0801.2288 [hep-ph]].

[137] J. D. Weinstein and N. Isgur, Phys. Rev. **D41**, 2236 (1990).

[138] A. Abele *et al.* [Crystal Barrel Collaboration], Eur. Phys. J. **C19**, 667 (2001).

[139] A. Abele *et al.* [CRYSTAL BARREL Collaboration], Eur. Phys. J. **C21**, 261 (2001).

[140] D. Barberis *et al.* [WA102 Collaboration], Phys. Lett. **B471**, 440 (2000) [arXiv:hep-ex/9912005].

[141] C. Amsler and F. E. Close, Phys. Rev. **D53**, 295 (1996) [arXiv:hep-ph/9507326].

[142] F. E. Close and A. Kirk, Eur. Phys. J. **C21**, 531 (2001) [arXiv:hep-ph/0103173].

[143] T. Barnes, F. E. Close, and H. J. Lipkin, Phys. Rev. **D68**, 054006 (2003) [arXiv:hep-ph/0305025].

[144] E. E. Kolomeitsev and M. F. M. Lutz, Phys. Lett. **B582**, 39 (2004) [arXiv:hep-ph/0307133].

[145] A. Faessler, T. Gutsche, V. E. Lyubovitskij, and Y.-L. Ma, Phys. Rev. **D76**, 014005 (2007) [arXiv:0705.0254 [hep-ph]].

[146] M. F. M. Lutz and M. Soyeur, Nucl. Phys. **A813**, 14 (2008) [arXiv:0710.1545 [hep-ph]].

[147] L. Liu, K. Orginos, F.-K. Guo, C. Hanhart, and U.-G. Meißner, Phys. Rev. **D87**, 014508 (2013) [arXiv:1208.4535 [hep-lat]].

[148] H.-Y. Cheng and W.-S. Hou, Phys. Lett. **B566**, 193 (2003) [arXiv:hep-ph/0305038].

[149] K. Terasaki, Phys. Rev. **D68**, 011501 (2003) [arXiv:hep-ph/0305213].

[150] L. Maiani, F. Piccinini, A. D. Polosa, and V. Riquer, Phys. Rev. **D71**, 014028 (2005) [arXiv:hep-ph/0412098].

[151] V. Dmitrasinovic, Phys. Rev. Lett. **94**, 162002 (2005).

[152] G. S. Bali, Phys. Rept. **343**, 1 (2001) [arXiv:hep-ph/0001312].

[153] N. Brambilla, S. Eidelman, C. Hanhart, A. Nefediev, C.-P. Shen, C. E. Thomas, A. Vairo, and C.-Z. Yuan [arXiv:1907.07583 [hep-ex]].

[154] R. Aaij *et al.* [LHCb Collaboration], Phys. Rev. Lett. **110**, 222001 (2013) [arXiv:1302.6269 [hep-ex]].

[155] R. Aaij *et al.* [LHCb Collaboration], Phys. Rev. **D92**, 011102 (2015) [arXiv:1504.06339 [hep-ex]].

[156] N. A. Tornqvist [arXiv:hep-ph/0308277].

[157] A. Esposito, A. L. Guerrieri, F. Piccinini, A. Pilloni, and A. D. Polosa, Int. J. Mod. Phys. **A30**, 1530002 (2015) [arXiv:1411.5997 [hep-ph]].

[158] S. Chatrchyan *et al.* [CMS Collaboration], Phys. Lett. **B727**, 57 (2013) [arXiv:1309.0250 [hep-ex]].

[159] F.-K. Guo, C. Hidalgo-Duque, J. Nieves, and M. P. Valderrama, Phys. Rev. **D88**, 054007 (2013) [arXiv:1303.6608 [hep-ph]].

[160] F.-K. Guo, U.-G. Meißner, W. Wang, and Z. Yang, Eur. Phys. J. **C74**, 3063 (2014) [arXiv:1402.6236 [hep-ph]].

[161] M. Karliner and J. L. Rosner, Phys. Rev. **D91**, 014014 (2015) [arXiv:1410.7729 [hep-ph]].

[162] B. Aubert *et al.* [BaBar Collaboration], Phys. Rev. **D71**, 031501 (2005) [arXiv:hep-ex/0412051].

[163] F. E. Close and P. R. Page, Phys. Lett. **B628**, 215 (2005) [arXiv:hep-ph/0507199].

[164] M. Berwein, N. Brambilla, J. Tarrús Castellà, and A. Vairo, Phys. Rev. **D92**, 114019 (2015) [arXiv:1510.04299 [hep-ph]].

[165] E. Kou and O. Pene, Phys. Lett. **B631**, 164 (2005) [arXiv:hep-ph/0507119].

[166] Yu. S. Kalashnikova and A. V. Nefediev, Phys. Rev. **D77**, 054025 (2008) [arXiv:0801.2036 [hep-ph]].

[167] Q. Wang, C. Hanhart, and Q. Zhao, Phys. Rev. Lett. **111**, 132003 (2013) [arXiv:1303.6355 [hep-ph]].

[168] A. Ali, L. Maiani, A. V. Borisov, I. Ahmed, M. Jamil Aslam, A. Ya. Parkhomenko, A. D. Polosa, and A. Rehman, Eur. Phys. J. **C78**, 29 (2018) [arXiv:1708.04650 [hep-ph]].

[169] M. Ablikim *et al.* [BESIII Collaboration], Phys. Rev. Lett. **110**, 252001 (2013) [arXiv:1303.5949 [hep-ex]].

[170] M. Ablikim *et al.* [BESIII Collaboration], Phys. Rev. Lett. **112**, 022001 (2014) [arXiv:1310.1163 [hep-ex]].

[171] P. Krokovny *et al.* [Belle Collaboration], Phys. Rev. **D88**, 052016 (2013) [arXiv:1308.2646 [hep-ex]].

[172] A. Bondar *et al.* [Belle Collaboration], Phys. Rev. Lett. **108**, 122001 (2012) [arXiv:1110.2251 [hep-ex]].

[173] A. Garmash *et al.* [Belle Collaboration], Phys. Rev. Lett. **116**, 212001 (2016) [arXiv:1512.07419 [hep-ex]].

[174] Y.-H. Chen, M. Cleven, J. T. Daub, F.-K. Guo, C. Hanhart, B. Kubis, U.-G. Meißner, and B.-S. Zou, Phys. Rev. **D95**, 034022 (2017) [arXiv:1611.00913 [hep-ph]].

[175] A. E. Bondar, A. Garmash, A. I. Milstein, R. Mizuk, and M. B. Voloshin, Phys. Rev. **D84**, 054010 (2011) [arXiv:1105.4473 [hep-ph]].

[176] A. Ali, L. Maiani, A. D. Polosa, and V. Riquer, Phys. Rev. **D91**, 017502 (2015) [arXiv:1412.2049 [hep-ph]].

[177] M. B. Voloshin, Phys. Rev. **D84**, 031502 (2011) [arXiv:1105.5829 [hep-ph]].

[178] T. Mehen and J. W. Powell, Phys. Rev. **D84**, 114013 (2011) [arXiv:1109.3479 [hep-ph]].

[179] V. Baru, E. Epelbaum, A. A. Filin, C. Hanhart, and A. V. Nefediev, JHEP **06**, 158 (2017) [arXiv:1704.07332 [hep-ph]].

[180] V. Baru, E. Epelbaum, A. A. Filin, C. Hanhart, A. V. Nefediev, and Q. Wang, Phys. Rev. **D99**, 094013 (2019) [arXiv:1901.10319 [hep-ph]].

[181] E. Klempt and A. Zaitsev, Phys. Rept. **454**, 1 (2007) [arXiv:0708.4016 [hep-ph]].

[182] W. Ochs, J. Phys. **G40**, 043001 (2013) [arXiv:1301.5183 [hep-ph]].

[183] B. Ananthanarayan, G. Colangelo, J. Gasser, and H. Leutwyler, Phys. Rept. **353**, 207 (2001) [arXiv:hep-ph/0005297].

[184] I. Caprini, G. Colangelo, and H. Leutwyler, Eur. Phys. J. **C72**, 1860 (2012) [arXiv:1111.7160 [hep-ph]].

[185] P. Buettiker, S. Descotes-Genon, and B. Moussallam, Eur. Phys. J. **C33**, 409 (2004) [arXiv:hep-ph/0310283].

[186] J. R. Pelaez and A. Rodas, Eur. Phys. J. **C78**, 897 (2018) [arXiv:1807.04543 [hep-ph]].

[187] S. Descotes-Genon, JHEP **03**, 002 (2001) [arXiv:hep-ph/0012221].

[188] J. T. Daub, H. K. Dreiner, C. Hanhart, B. Kubis, and U.-G. Meißner, JHEP **01**, 179 (2013) [arXiv:1212.4408 [hep-ph]].

[189] A. Celis, V. Cirigliano, and E. Passemar, Phys. Rev. **D89**, 013008 (2014) [arXiv:1309.3564 [hep-ph]].

[190] J. T. Daub, C. Hanhart, and B. Kubis, JHEP **02**, 009 (2016) [arXiv:1508.06841 [hep-ph]].

[191] M. W. Winkler, Phys. Rev. **D99**, 015018 (2019) [arXiv:1809.01876 [hep-ph]].

[192] F. Niecknig, B. Kubis, and S. P. Schneider, Eur. Phys. J. **C72**, 2014 (2012) [arXiv:1203.2501 [hep-ph]].

[193] B. Hu, R. Molina, M. Döring, M. Mai, and A. Alexandru, Phys. Rev. **D96**, 034520 (2017) [arXiv:1704.06248 [hep-lat]].

[194] V. Baru, J. Haidenbauer, C. Hanhart, A. E. Kudryavtsev, and U.-G. Meißner, Eur. Phys. J. **A23**, 523 (2005) [arXiv:nucl-th/0410099].

[195] R. Aaij *et al.* [LHCb Collaboration], Phys. Rev. **D89**, 092006 (2014) [arXiv:1402.6248 [hep-ex]].

[196] R. Aaij *et al.* [LHCb Collaboration], JHEP **08**, 037 (2017) [arXiv:1704.08217 [hep-ex]].

[197] R. Kaminski, L. Lesniak, and B. Loiseau, Phys. Lett. **B413**, 130 (1997) [arXiv:hep-ph/9707377].

[198] R. Molina, D. Nicmorus, and E. Oset, Phys. Rev. **D78**, 114018 (2008) [arXiv:0809.2233 [hep-ph]].

[199] L. S. Geng and E. Oset, Phys. Rev. **D79**, 074009 (2009) [arXiv:0812.1199 [hep-ph]].

[200] D. Gülmez, U.-G. Meißner, and J. A. Oller, Eur. Phys. J. **C77**, 460 (2017) [arXiv:1611.00168 [hep-ph]].

[201] M.-L. Du, D. Gülmez, F.-K. Guo, U.-G. Meißner, and Q. Wang, Eur. Phys. J. **C78**, 988 (2018) [arXiv:1808.09664 [hep-ph]].

[202] J. M. Blatt and V. F. Weisskopf, *Theoretical nuclear physics*, Springer, 1952.

[203] R. Aaij *et al.* [LHCb Collaboration], Phys. Rev. **D86**, 052006 (2012) [arXiv:1204.5643 [hep-ex]].

[204] K. Nakano, Phys. Rev. **C26**, 1123 (1982).

[205] L.-Y. Dai and M. R. Pennington, Phys. Rev. **D90**, 036004 (2014) [arXiv:1404.7524 [hep-ph]].

[206] I. J. R. Aitchison, Nucl. Phys. **A189**, 417 (1972).

[207] M. Albaladejo, J. T. Daub, C. Hanhart, B. Kubis, and B. Moussallam, JHEP **04**, 010 (2017) [arXiv:1611.03502 [hep-ph]].

[208] L. Zhang and S. Stone, Phys. Lett. **B719**, 383 (2013) [arXiv:1212.6434 [hep-ph]].

[209] R. Aaij *et al.* [LHCb Collaboration], Phys. Rev. Lett. **112**, 091802 (2014) [arXiv:1310.2145 [hep-ex]].

[210] V. V. Anisovich and A. V. Sarantsev, Eur. Phys. J. **A16**, 229 (2003) [arXiv:hep-ph/0204328].

[211] B. Hyams *et al.*, Nucl. Phys. **B100**, 205 (1975).

[212] D. H. Cohen, D. S. Ayres, R. Diebold, S. L. Kramer, A. J. Pawlicki, and A. B. Wicklund, Phys. Rev. **D22**, 2595 (1980).

[213] A. Etkin *et al.*, Phys. Rev. **D25**, 1786 (1982).

[214] P. Masjuan and J. J. Sanz-Cillero, Eur. Phys. J. **C73**, 2594 (2013) [arXiv:1306.6308 [hep-ph]].

[215] P. Masjuan, J. Ruiz de Elvira, and J. J. Sanz-Cillero, Phys. Rev. **D90**, 097901 (2014) [arXiv:1410.2397 [hep-ph]].

[216] I. Caprini, P. Masjuan, J. Ruiz de Elvira, and J. J. Sanz-Cillero, Phys. Rev. **D93**, 076004 (2016) [arXiv:1602.02062 [hep-ph]].

[217] K. Maltman, Phys. Lett. **B462**, 14 (1999) [arXiv:hep-ph/9906267].

[218] D. Morgan and M. R. Pennington, Z. Phys. **C48**, 623 (1990).

[219] R. Aaij *et al.* [LHCb Collaboration], Phys. Rev. **D87**, 052001 (2013) [arXiv:1301.5347 [hep-ex]].

[220] D. V. Bugg, B. S. Zou, and A. V. Sarantsev, Nucl. Phys. **B471**, 59 (1996).

[221] L. Maiani, A. D. Polosa, and V. Riquer, Phys. Lett. **B778**, 247 (2018) [arXiv:1712.05296 [hep-ph]].

[222] A. Ali, C. Hambrock, and W. Wang, Phys. Rev. **D85**, 054011 (2012) [arXiv:1110.1333 [hep-ph]].

[223] Q. Wang, V. Baru, A. A. Filin, C. Hanhart, A. V. Nefediev, and J. L. Wynen, Phys. Rev. **D98**, 074023 (2018) [arXiv:1805.07453 [hep-ph]].

[224] J. Nieves and M. P. Valderrama, Phys. Rev. **D84**, 056015 (2011) [arXiv:1106.0600 [hep-ph]].

[225] J.-R. Zhang, M. Zhong, and M.-Q. Huang, Phys. Lett. **B704**, 312 (2011) [arXiv:1105.5472 [hep-ph]].

[226] Y. Yang, J. Ping, C. Deng, and H.-S. Zong, J. Phys. **G39**, 105001 (2012) [arXiv:1105.5935 [hep-ph]].

[227] Z.-F. Sun, J. He, X. Liu, Z.-G. Luo, and S.-L. Zhu, Phys. Rev. **D84**, 054002 (2011) [arXiv:1106.2968 [hep-ph]].

[228] S. Ohkoda, Y. Yamaguchi, S. Yasui, K. Sudoh, and A. Hosaka, Phys. Rev. **D86**, 014004 (2012) [arXiv:1111.2921 [hep-ph]].

[229] M. T. Li, W. L. Wang, Y. B. Dong, and Z. Y. Zhang, J. Phys. **G40**, 015003 (2013) [arXiv:1204.3959 [hep-ph]].

[230] H.-W. Ke, X.-Q. Li, Y.-L. Shi, G.-L. Wang, and X.-H. Yuan, JHEP **04**, 056 (2012) [arXiv:1202.2178 [hep-ph]].

[231] J. M. Dias, F. Aceti, and E. Oset, Phys. Rev. **D91**, 076001 (2015) [arXiv:1410.1785 [hep-ph]].

[232] S. Ropertz, C. Hanhart, and B. Kubis, Eur. Phys. J. **C78**, 1000 (2018) [arXiv:1809.06867 [hep-ph]].

[233] J. Kambor, C. Wiesendanger, and D. Wyler, Nucl. Phys. **B465**, 215 (1996) [arXiv:hep-ph/9509374].

[234] B. Moussallam, Eur. Phys. J. C **73**, 2539 (2013) [arXiv:1305.3143 [hep-ph]].

[235] J. Plenter, Master thesis, University of Bonn (2017).

[236] S. Holz, Master thesis, University of Bonn (2018).

[237] A. Anisovich and H. Leutwyler, Phys. Lett. B **375**, 335 (1996) [arXiv:hep-ph/9601237].

[238] C. Hanhart, Yu. S. Kalashnikova, P. Matuschek, R. V. Mizuk, A. V. Nefediev, and Q. Wang, Phys. Rev. Lett. **115**, 202001 (2015) [arXiv:1507.00382 [hep-ph]].

[239] X.-H. Liu, F.-K. Guo, and E. Epelbaum, Eur. Phys. J. **C73**, 2284 (2013) [arXiv:1212.4066 [hep-ph]].

[240] W. Detmold, S. Meinel, and Z. Shi, Phys. Rev. **D87**, 094504 (2013) [arXiv:1211.3156 [hep-lat]].

[241] O. Junker, S. Leupold, E. Perotti, and T. Vitos, Phys. Rev. **C101**, 015206 (2020) [arXiv:1910.07396 [hep-ph]].

[242] J. Grabowski, PHD thesis, to appear.

[243] J. Pelaez, A. Rodas, and J. Ruiz De Elvira, Eur. Phys. J. C **79**, 1008 (2019) [arXiv:1907.13162 [hep-ph]].

[244] J. Pelaez and A. Rodas, Phys. Rev. D **93**, 074025 (2016) [arXiv:1602.08404 [hep-ph]].

[245] J. Peláez and A. Rodas, PoS **Hadron2017**, 139 (2018) [arXiv:1711.07861 [hep-ph]].

[246] M. Albaladejo and B. Moussallam, Eur. Phys. J. **C75**, 488 (2015) [arXiv:1507.04526 [hep-ph]].

[247] J. Lu and B. Moussallam [arXiv:2002.04441 [hep-ph]].

[248] F.-K. Guo [arXiv:2001.05884 [hep-ph]].

[249] T. Hahn and M. Perez-Victoria, Comput. Phys. Commun. **118**, 153 (1999) [arXiv:hep-ph/9807565].

[250] H. H. Patel, Comput. Phys. Commun. **197**, 276 (2015) [arXiv:1503.01469 [hep-ph]].

[251] R. Karplus, C. M. Sommerfield, and E. H. Wichmann, Phys. Rev. **111**, 1187 (1958).

[252] C. Fronsdal and R. E. Norton, Journal of Mathematical Physics **5**, 100 (1964).

[253] R. E. Norton, Phys. Rev. **135**, B1381 (Sep, 1964), `https://link.aps.org/doi/10.1103/PhysRev.135.B1381`.

[254] R. Cutkosky, J. Math. Phys. **1**, 429 (1960).

[255] W. Lucha, D. Melikhov, and S. Simula, Phys. Rev. D **75**, 016001 (Jan, 2007), `https://link.aps.org/doi/10.1103/PhysRevD.75.016001`.

Acknowledgements

Finally, I want to thank several people who supported me during my Ph.D. studies not only technically but also emotionally.

I would like to first thank my supervisor Christoph Hanhart for the opportunity to work with him on the presented topics. I am very thankful for countless fruitful discussions and his patience with my projects, especially when they showed unexpected complications. Furthermore, he was great in advocating my projects, allowing me to get in touch with many people who were interested in them.

Next, I would like to thank Bastian Kubis. He not only helped me very much with the projects but also a lot of organization in the university. Although I did not belong to his working group, he allowed me to participate in several of their social events.

On this occasion, I would like to thank the working group Kubis for making me feel welcome. I would like to especially thank Bai-Long Hoid and Tobias Isken, whom I have known for the longest. Together with Malwin Niehus, Simon Holz and Marvin Zanke, we did have not only interesting physical discussions but also shared many laughs. The board game evenings with Tobias, Maximilian Dax, Frederic Noel and Dominik Stamen were always fun and a welcome distraction. I am thankful for the time I spend with my office colleges Andria Agadjanov, Falk Zimmermann and Ingrid Dax. We did share not only a lot of stories with each other but also a lot of snacks.

Furthermore, I want to thank my parents Dagmar and Norbert Ropertz, brother Thorsten Ropertz and grandmother Sigrid Kujat for emotional support. Without their backing, my studies would not have been possible as they helped me to endure especially the dark times.

I appreciate my sport friends, who helped my to vent frustration not only with sports but also board games.

Also, I want to thank my good friends I met during my undergraduate studies. Mathias Weiß has always been a good friend with whom I spend many times laughing. I thank Stephan Kürten for the hourlong movie sessions weekends and evenings. I especially cherish the family Leuteritz, Till, Yasmine and Anton, who gave me not only a lot of emotional support but also a free lunch here and then.

I greatly appreciate the fundings offered by the CRC 110 Symmetries and the Emergence of Structure in QCD.